Structure and Function in Single-Chain Nanoparticles

Author: Julen de la Cuesta Leone

Supervisor: Prof. José A. Pomposo

Donostia - San Sebastián, 2021

eman ta zabal zazu

Universidad del País Vasco

Euskal Herriko Unibertsitatea

Contents

Chapter 1: Introduction

1.1. Motivation

Trying to mimic the outstanding functionalities of enzymes and intrinsically disordered proteins (IDPs) the research field of folding functionalized synthetic polymers to single-chain polymer nanoparticles (SCNPs) has flourished in recent years. The folded conformations of SCNPs produce robust SCNPs when stabilized by covalent interactions. Conversely, when folding results from noncovalent interactions such as hydrogen bonds, host-guest interactions, metal complexation, π-π stacking and hydrophobic interactions, dynamic SCNPs are obtained. Even if current single-chain technology still lacks the nature´s exquisite degree of control to generate 3D-proteins, some SCNPs already mimic the outstanding properties of antimicrobial polypeptides, as well as both the size and function of structural proteins, IDPs and metallo-enzymes.

The motivation of this Thesis is to deepen the understanding of single-chain polymer nanoparticles (SCNPs) as complex soft nano-objects with potential applications in a variety of fields, specially catalysis and sensing. In particular, this work covers different aspects related to the structure and properties of SCNPs such as: i) the development of a theoretical model of elastic SCNPs allowing to understand the behavior of these nanoparticles in solution and on surfaces; ii) the design of SCNPs as advanced nanoreactors for the synthesis of a relevant intrinsically conducting polymer such as poly(ethylenedioxythiophene), PEDOT; iii) the design of highly fluorescent SCNPs by photoactivation of copolymers containing diazo functional groups and an aggregation induced emission (AIE) fluorophore decorated with azide moieties; and iv) the synthesis of SCNPs containing orthogonal fluorophores for self-reporting intramolecular compaction and, when present or externally induced, intermolecular aggregation.

Since the research carried out in this Thesis is a multidisciplinary research that covers different disciplines such as polymer chemistry, polymer physics, nanoscience, nanotechnology and luminescence, in next sections we briefly introduce several concepts relevant to understand the results reported in Chapters 3 - 6. Additionally, all the experimental techniques employed in this work are described in Chapter 2.

1.2. Polymers

Polymers are large molecules (macromolecules) formed by the repetition of smaller subunits (monomers) [1]. Polymers include synthetic materials like plastics, natural compounds like rubber and biopolymers like proteins and DNA. They are synthetized by the polymerization reaction of their constituent units.

Polymers are classified according to their architecture. Linear polymers consist of a single chain with two ends. Branched polymers include side chains, or branches, attached to the main chain. Sometimes these branches are cross-linked forming a network polymer.

Copolymers are polymers formed by 2 or more different monomers. They have different structures based on how the monomers are arranged in the chain. Alternating copolymers have regularly alternating monomers. Periodic copolymers have the monomer units arranged in a repeating sequence. Random copolymers have different monomers distributed randomly. Block copolymers have homopolymer subunits. Grafted copolymers have side chains of different composition than the main chain.

The structure of polymers can be amorphous or semi-crystalline. Amorphous polymers lack long range order and are arranged randomly. Semi-crystalline polymers are partially ordered with crystalline structures separated by amorphous regions. A polymer cannot be 100% crystalline.

In polymers individual chains do not have the same number of repeating units and in consequence they have different molar masses. Normally an average is calculated. The molar mass distribution describes the relation between the number of polymer chains and the mass of the polymer. The most common methods to calculate the average are the number average and the weight average.

The number average molar mass (M_n) is the arithmetic mean of the molar masses. It is calculated by dividing the sum of all polymer masses by the number of polymer chains.

(1.1)

$$M_n = \frac{\sum N_i M_i}{\sum N_i}$$

The weight average molar mass (M_w) represents an average over the weight of the polymer. Larger molecules have a larger contribution than smaller molecules. Some properties are dependent on molecular size.

(1.2)

$$M_w = \frac{\sum N_i M_i^2}{\sum N_i M_i}$$

The dispersity index $Đ > 1$ is the ratio between M_w and M_n. If $Đ$ is high the polymer has a broad size distribution.

The hydrodynamic radius (R_h) of a solute particle is the radius of a hypothetical equivalent hard sphere that diffuses at the same speed than the solute. The movement of the solute particles is resisted by the viscosity of the solution. The hydrodynamic radius takes into account all the molecules attracted to the solute and solvating it. These molecules hinder the mobility of the particle.

The radius of gyration (R_g) of a polymer is the average distance from any point in the polymer to its centre of mass. The value of R_g depends on the molar mass, the architecture and the quality of the solvent. It is worth mentioning that polymers swell in good solvents and shrink in bad ones.

1.3. Polymer conformations

Polymers are made of repeating units. A simple model of polymers consists of a chain of N repeating segments of length l. In an ideal chain the segments can be oriented in any direction and the parts of the chain units do not interact with each other. In this case the polymer can be described as a random walk in three dimensions [1, 2].

The end-to-end distance vector is given by the sum of the vectors corresponding to all individual segments.

<div align="right">(1.3)</div>

$$\vec{R} = \sum \{\vec{r_1}, \ldots \ldots, \vec{r_n}\}$$

The length and number of the individual segments of the model does not necessarily correspond with the length and number of monomers.

The end-to-end distance in a random walk can be approximated by the following scaling law:

<div align="right">(1.4)</div>

$$R \sim N^{\nu}$$

Where the ν is the Flory exponent, which is $\nu = 1/2$ for an ideal chain. However, in real chains the excluded volume must be taken into account, and the chain is best modelled as a self-avoiding random walk. In this case the value of the exponent is $\nu = 3/5$.

The Flory exponent of a polymer depends on its solubility. In a good solvent the chain swells to maximize interaction with the solvent, corresponding to the self-avoiding random walk with $\nu = 3/5$. Meanwhile, in a poor solvent the polymer chain collapsed into a solid sphere where $\nu = 1/3$. In the so-called θ-solvent the polymer behaves as an ideal chain with $\nu = 1/2$.

1.4. Polymer synthesis

Many methods have been developed along time for the synthesis of (co)polymers with narrow molecular weight distribution ($Đ \rightarrow 1$) such as anionic, cationic, and controlled radical polymerization techniques. Among them, the most useful, versatile and easy to use is the reversible addition fragmentation chain transfer (RAFT) polymerization technique.

1.4.1. RAFT polymerization

Reversible addition fragmentation chain transfer polymerization is a type of reversible deactivation radical polymerization. It uses a chain transfer agent, normally a thiocarbonylthio compound, to control the molecular weight and the polydispersity of the polymer chain during synthesis [3]. It was first reported in the Commonwealth Scientific and Industrial Research Organization (CSIRO) of Australia in 1998 [4] and it has since become one of the most versatile and powerful polymerization techniques for the synthesis of complex polymeric architectures.

A RAFT polymerization system consists of an initiator, a chain transfer agent (CTA), the monomers and the solvent. The mechanism consists of six steps: In step 1 the initiator reacts

with the monomer forming a radical. This radical reacts with more monomer molecules, propagating a growing polymer-radical chain (step 2). In step 3, the propagating polymer chain reacts reversibly with the CTA, stopping the growth of the chain and releasing a radical. In step 4, the released radical adds new monomers to a propagating polymer chain. In the next step the main equilibrium is reached, where the CTA agent is exchanged between polymer chains allowing chains that have not undergone termination to share the radicals, allowing equal opportunities for growth. The last step involves the reaction of two radicals terminating chain growth [5].
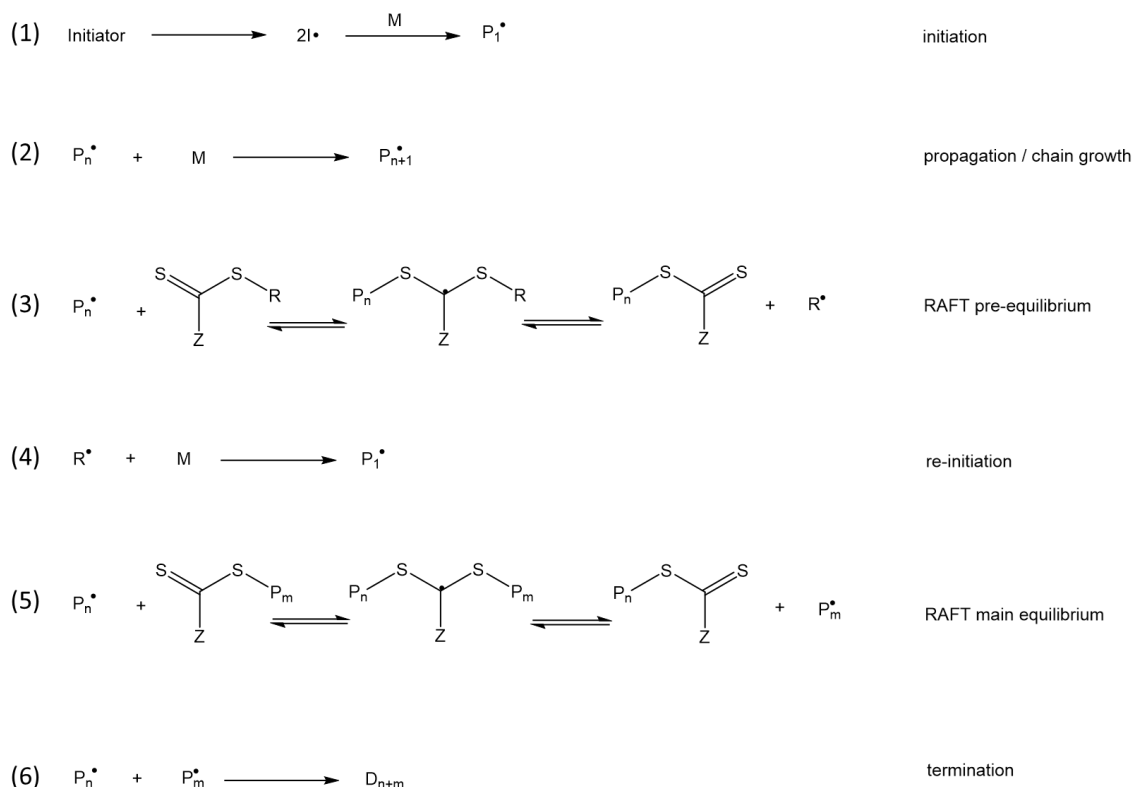
Scheme 1.1. *Schematic representation of the RAFT polymerization mechanism with a thiocarbonylthio chain-transfer agent [6].*

1.5. Intrinsically conducting polymers

Conductive polymers or intrinsically conducting polymers are organic polymers that conduct electricity [7]. Electrical conductivity is the fundamental property of materials that quantify how strongly it conducts electric currents. A high conductivity means that a material allows electric currents. Conductivity is the inverse of electrical resistivity. Electrical resistance is the opposition an object shows to the flow of an electrical current and its SI unit is the ohm (Ω). It depends on the properties of the material and it is proportional to the length of the conductor and inversely proportional to its cross section. Resistivity is defined as the electrical resistance produced by an object of unit cross section per unit length.

$$\rho = R\frac{A}{l}$$

Where ρ is the resistivity, R is the resistance, A the cross section area and l the length. The SI unit of the resistivity is the ohm metre ($\Omega\cdot$m). This means that resistivity (like its reciprocal conductivity) is an intrinsic property of the conducting material and does not depend on the shape of the conducting object. Conductivity (σ) is given as the inverse of resistivity and its SI unit is the Siemens per metre (S/m).

$$\sigma = \frac{1}{\rho}$$

Historically, polymers were considered insulators of electricity. Later it was discovered that some conjugated polymers could conduct electricity nearly as well as metals. These conducting polymers combine the electrical properties of metals with advantages of polymers such as lighter weight, greater workability, resistance to corrosion and lower cost. Polymers are more easily processed than metals: large surfaces can be covered by spin coated polymers, they can be deformed reversibly and they can be shaped into complex multi polymer architectures. Some of their potential applications are organic light emitting diodes, organic solar cells and biosensors [8].

The first breakthrough in the field of electrically conducting polymers happened in 1977 when Alan J. Heeger, Alan G. MacDiarmid and Hideki Shirakawa [9] demonstrated that polyacetylene increased its electrical conductivity after treatment with oxidizing or reducing agents. They were awarded the Nobel Prize in Chemistry in 2000 for the discovery and study of conducting polymers. That discovery led to the research and study of conducting polymers.

Electrically conducting polymers have a molecular character and lack long range order. This character causes the electronic motion across macromolecules to be one-dimensional. In traditional polymers the valence electrons form molecular bonds between sp^3 hybridized electronic orbitals. These sigma bonds have low mobility and do not contribute to the electrical conductivity of the polymer. In conjugated polymers, with a backbone of alternating single and double bonds, it is different. The backbone of the polymer is formed by sp^2 hybridized carbon atoms. These atoms have a valence electron in a p_z orbital orthogonal to the sigma bonds. These p_z orbitals form π bonds between them. When π bonds are conjugated the electrons are delocalized. The conducting properties of these polymers arise from this π-conjugation after the introduction of an electrical charge. When the polymer is doped by oxidation (or reduction) these electrons (or holes) become highly mobile and the polymer becomes conductive.
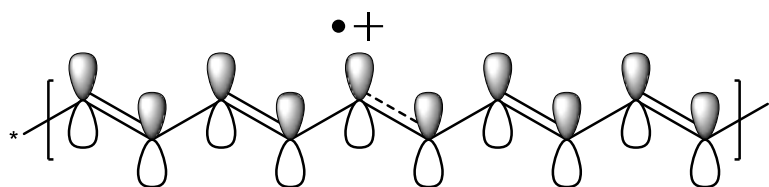
Figure 1.1. *Scheme of conducting polymer p-doped polyacetylene.*

The conductivity of conducting polymers is similar to that of semiconductors. The main difference is the susceptibility of conducting polymers to structural distortion. The dopant, normally a charged molecule, stabilizes the backbone and neutralizes the charge. The dopant introduces a charge carrier in the system by removing or adding electrons from the polymer chain. It is energetically favourable to localize the charge and surround it with a relaxation or structural distortion, forming a polaron and stabilizing the structure. The structure change displaces the valence and conductivity bands of the molecule, shifting the Highest Occupied Molecular Orbital (HOMO) upward and the Lowest Unoccupied Molecular Orbital (LUMO) downward and increasing the conductivity. The polaron can travel through the polymer chain, conducting electricity. If two polarons are near each other they can lower their energy sharing their lattice distortion. If the attraction becomes large enough they become bound and surrounded by the distortion, forming a bipolaron [10].

There are two types of doping processes: p-doping, where the polymer is oxidized and has a positive charge because of the loss of electrons, and n-doping, where the polymer is reduced and has a negative charge due to the acceptance of electrons. There is a proportional relationship between the amount of dopant used and the conductivity of the doped polymer. The doping is reversible and an electrical potential applied through the system causes the polymer to switch between conductive and insulating redox states.

Dopants can be separated into two categories according to their molecular size: small dopants like Cl^- and large dopants like poly(sodium 4-styrenesulfonate), PSS. Small dopants leave and re-enter the polymer with electrical stimulation. Large dopants affect the material properties dramatically and they are immobile and more integrated with the polymer [10, 11].

1.6. Nanoscience and nanotechnology

Nanoscience is the science of structures and materials at the nanoscale level, with sizes intermediate between the largest molecules and the smallest structures that can be fabricated by photolithography, that is, objects with dimensions ranging between 1 nm and 100 nm [12]. The prefix nano in nanoscience and nanotechnology comes from the Greek word for dwarf and is the SI prefix for one billionth (10^{-9}). One nanometre is 10^{-9} meters [13].

The first reference to the concepts associated with nanoscience was the talk by physicist Richard Feynman "There's plenty of room at the bottom" in 1959, where he discussed the possibility of manipulation of individual atoms.

Properties at the nanometric scale differ significantly from those at larger scales [14], resulting in many promising applications. Nanoscience has important applications in the

fields of physics, chemistry and biology. In chemistry the nanoscale is associated with micelles, colloids, polymer molecules or phase separated regions of block copolymers. Meanwhile in physics nanoscience is associated with quantum effects and the behaviour of photons and electrons on nanostructures. In the field of biology and biochemistry nanostructures such as the components of the cell (DNA, proteins) or viruses are important. Structures considered nanostructures include buckyballs, nanotubes, quantum dots, colloids, etc.

On the other hand, nanotechnology is the building and manipulation of these nanostructures for practical applications.

1.6.1. Nanoparticles

Nanoparticles (NPs) are one of the most important applications of nanotechnology. They are defined by IUPAC as particulate materials of any size which have at least two dimensions below 100 nm [15]. Due to their small size and high surface area to volume ratio they have physical, chemical and optical properties different from those of bulk materials. Those properties are dependent on the shape and size of the nanoparticle.

Nanoparticles can be classified into various categories [16], including "hard" inorganic NPs and "soft" organic NPs. Hard nanoparticles include carbon based NPs (fullerenes, carbon nanonotubes), metallic NPs (gold NPs), ceramic NPs, and semiconductor NPs (quantum dots), while soft nanoparticles include polymeric NPs and lipid-based NPs.

1.6.2. Single-chain technology

In recent years, inside the field of nanoscience, a new discipline has emerged: single chain technology. This field consists of soft nanoparticles based on polymers with ultra-small sizes in the range of 3 to 30 nm. The ability to control the synthesis of soft nanoparticles appeared at the beginning of the 21st century. Since then, the discipline has expanded and many different applications have been found [17].

Single chain technology deals with the synthesis of soft nano-objects from single polymers chains. These structures are inspired by natural macromolecules [18]. Nano-objects synthesized in this way include dynamic [19], letter-shaped [20] or unsymmetrical [21] single rings, and complex multi-ring objects. Moreover, copolymer chains of different sizes and masses have been folded into single-chain nanoparticles [22], tadpoles [23] (monotailed SCNPs), dumbbells [24] and hairpins [25].

1.7. Single chain nanoparticles (SCNPs)

The most important products of single-chain technology are single-chain polymeric nanoparticles (SCNPs). SCNPs are a class of nanoparticles that consist of a single polymer chain folded by crosslinking between reactive pendant groups [26, 27]. Intramolecular cross-linking in linear single polymer chains was first reported by Kuhn and Balmer in 1962 [28]. SCNPs are the smallest nano-objects that can be prepared from a linear polymer

through intra-chain collapse. They have potential applications as enzyme mimics, sensors, catalytic systems, etc. These SCNPs are synthesized by the folding and collapse of a single polymer chain into a nanoparticle via covalent or non-covalent bonds.

SCNPs can show sparse or globular morphologies. Sparse SCNPs are synthesized in dilute good solvent conditions, where compaction is relatively inefficient, since it involves cross-linking events separated by short distances. Globular SCNPs have a high degree of compaction caused by cross-links forming long-range loops [25]. These are synthesized by the folding/collapse of amphiphilic random copolymers or by the addition of relatively long cross-linkers.

1.7.1. Synthesis of SCNPs

The synthesis of SCNPs often consists of 3 steps: the synthesis of a precursor polymer from monomers, the functionalization of the polymer with functional groups suitable for the reaction, and the folding or collapse of the polymer chain [29].

1.7.1.1. Precursor synthesis

Precursor synthesis consists of the addition of complementary (reactive and inert) monomers into a polymer chain in a controlled manner forming a linear chain. For the synthesis of precursor polymers, it is important to find a polymerization technique that results in polymers with a narrow molar mass (and size) distribution. In chain growth polymerizations the occurrence of irreversible termination reactions in propagating chains results in "dead" polymer chains with very different chain lengths [30]. Controlled Radical Polymerization (CRP), also known as living radical polymerization or reversible deactivation radical polymerization (RDRP), processes allow a facile construction of polymers with low dispersity values and controlled architectures (stars, branches, dendrimers…) even in the presence of a broad range of monomer functional groups. A common feature in CRP is the existence of an equilibrium between free radical and deactivated species. The exchange between active and growing radicals and dormant species results in a slow but simultaneous growth of all chains [29]. As the reaction with a chain transfer agent is reversible the propagating chains are considered as "living". Some of the most common CPR techniques employed in the synthesis of precursor polymers are reversible addition fragmentation chain transfer (RAFT) [4], atom transfer radical polymerization (ATRP) [31], nitroxide mediated radical polymerization (NMP) [32] or ring opening polymerization (ROP) [33].

The precursor polymers used in the experiments carried out in this thesis were synthesized by RAFT polymerization.

1.7.1.2. Precursor functionalization

Sometimes precursor polymers lack the functional groups necessary for the intra-chain cross-linking that forms SCNPs. In these cases an additional step called polymer functionalization is needed. In this step the functional groups of the polymer are modified to produce suitable functional groups for cross-linking [29]. The aim of polymer

functionalization is the selective modification of a polymer under mild conditions avoiding side-reactions.

Some of the most efficient and used polymer functionalization reactions are the following: thiol-ene/thiol-yne additions (click reactions); modification of epoxides, anhydrides, oxazolines and isocyanates by reaction with amines/alcohols/thiols [34] (click reactions); modification of active esters by reaction with amines; thiol-disulphide exchange [35]; Diels-Alder reaction [36] (click reaction); Michael-type addition; Copper-catalyzed azide alkyne cycloaddition (CuAAC); Modification of ketones and aldehydes with amines / alkoxyamines / hydrazines; azidation [37] (nucleophilic substitution); and the transfer of diazo groups [38].

1.7.1.3. Intra-chain folding/collapse

The final step in the synthesis of SCNPs is the folding/collapse of the polymer. The formation of SCNPs is achieved by collapsing the polymer chain and stabilizing the resulting nanoparticle by intramolecular cross-linking in a process analogous to many folding processes of natural biomacromolecules. Reactive functional groups from the polymer chain react with each other to form cross-links. The cross-linking reactions are normally carried out at low concentrations to avoid intermolecular cross-linking and the formation of aggregates.

There are several approaches to generate intra-chain collapse. The bonding interactions of the crosslinks can be classified as covalent or non-covalent [39, 40].

Covalent folding

SCNPs are cross-linked irreversibly by covalent bonds. Many of these reactions follow the "click-chemistry" approach, where simple, specific and high-yield reactions form carbon heteroatom bonds [41]. There are three main strategies to form intramolecular covalent bonds: intra-chain homocoupling, intra-chain heterocoupling or cross-linker induced collapse.

Intra-chain homocoupling

In the homofunctional chain collapse method the chain is functionalized with self-complementary groups like double bonds. These functional groups react with each other (e.g. via radical-radical coupling reactions) collapsing the chain.

Intra-chain heterocoupling

The heterobifunctional chain collapse approach is similar to homocoupling but requires two different complementary functional groups on the same chain instead of a single one. Copper-catalyzed azide alkyne cycloaddition (CuAAC, click chemistry) [42] is a good example.

Cross-linker-induced Collapse

In the cross-linker mediated chain collapse strategy, functional groups in the polymer chain do not react directly with one another. The polymer is functionalized with suitable functional groups to react with the end-groups of a small cross-linker molecule. When the external cross-linker is added it reacts with 2 or more polymer functional groups, forming a bridge [43]. Examples include SCNP synthesis via Michael addition [44, 45], amide formation [46] and thiol-ene/thiol-yne additions [47].

Non-covalent folding

Non-covalent interactions, also called supramolecular interactions, are interactions between atoms of an intensity much weaker than covalent bonds. Non-covalent bonds are responsible for the structure of biomacromolecules such as proteins and they can be used in the construction of artificial macromolecular structures [48]. Some examples are hydrogen bonds, hydrophobic interactions, π-π stacking, metal coordination [49-51], van der Waals forces or ionic interactions. These interactions are reversible and the strength of the bonds is dependent on many factors such as temperature, pressure, concentration, etc. A result of this is that the structure of the complexes they form depends on solvent polarity, concentration, pH, temperature, etc. [52]. This versatility allows the formation of complex, dynamic and responsive structures.

Dynamic covalent bonds

Dynamic covalent bonds are covalent bonds that are stable under certain conditions but can be broken and reformed under specific external factors such as temperature, pH, light or catalysts [53, 54]. They combine the strength of covalent bonds and the reversibility of non-covalent bonds under certain conditions. For example, disulphides are stable under acidic and neutral conditions and exchange under basic conditions while hydrazones are stable under neutral and basic conditions and hydrolyse under acidic conditions [55]. Examples of dynamic covalent interactions include disulphide bonds [56], imine derivatives [56, 57], hydrazones [58], enamines [59], acetals/hemiacetals [60], etc. Dynamic covalent bonds are common in natural macromolecules (e.g. disulphide bonds in proteins) and are promising for the fabrication of artificial nanoparticles that change their structure in response to external stimuli [58].

1.8. Applications of SCNPs

SCNPs have potential applications in a wide range of fields [39, 61]. Despite the field being relatively recent, the experiments that have been carried out show promising results.

1.8.1. Catalysis

One of the most promising applications of SCNPs is their use as catalysts. The folding of bioinspired polymers is reminiscent of the folding of proteins and SCNPs mimic roughly their structure [29]. Proteins are constituted by one or several folded peptides that function under unique conformations. A complex and delicate self-folded structure and dynamic adaptability endows proteins with various functions. One of the most important of these

functions is enzyme catalysis, where the reaction time is increased up to a factor of 10^9, which means enzymes are the most efficient catalysts known in nature. Many enzymes have an active site that consists of a hydrophobic nano-cavity stabilized by hydrophobic interactions where catalysis takes place. The folded structure of the enzyme provides a unique environment for the catalytic site and is responsible for its specificity. This structure is maintained by hydrogen bonds, hydrophobic interactions and disulphide bonds. As a result, the design of artificial enzymes with high catalytic efficiency has been subject to many studies and they are the source of inspiration for artificial SCNPs with catalytic properties [62, 63].

There are two approaches to build artificial enzymes. The first approach consists on copying the structure of the active catalytic centres of the enzyme. Sparse SCNPs mimic the morphology of Intrinsically Disordered Proteins (IDPs). The structure of IDPs is a "pearl necklace" conformation consisting of many small active pockets that can bind several ligands, such as ions, small molecules, other proteins or nucleic acids. Sparse SCNPs with this conformation are endowed with transient-binding activity.

The second approach is to mimic the morphology of proteins. The spatial conformation of the active centre is very important in enzymatic catalysis and, in consequence, the strategy of imitating the structure has attracted much attention. Globular SCNPs mimic native proteins by creating a large hydrophobic pocket by self-assembly of amphiphilic copolymers [61]. Metal ions can be placed in the pocket to provide it with catalytic activity [64].

Those characteristics of proteins are mimicked by self-folding polymers, which take the form of SCPNs. SCPNs mimic the whole enzyme taking into account both the conformation and the chemical entity of the reactive centre [65].

SCNPs that mimic the catalytic activity of carboxylases [66], polymerases [67], reductases [67], oxidases [49], etc. have been synthesized.

1.8.2. Sensing

SCNPs have promising applications as sensors and biosensors. Changes in the optical properties of SCNP solutions in the presence substances such as metal ions [68] or proteins [69] allow their easy, visual detection.

1.8.3. Nanomedicine

Nanomedicine is the application of nanotechnology for diagnosis monitoring and therapy of physical and pathological processes [70].

1.8.3.1. Drug delivery

SCNPs are promising nanomaterials for drug delivery applications. Nanoparticles can protect drugs from the action of enzymes and their size is large enough to avoid rapid clearance in the kidneys and be retained in the body in a range of physiological media long enough to have the desired effect. Insoluble or toxic drugs could be encapsulated into

biocompatible SCNPs, providing several advantages [71]. Functionalized polymers would deliver the encapsulated drug to their target before releasing it in a controlled way, reducing the toxicity of the drug and improving its effectivity. Experiments have been performed with SCNPs as drug delivery nanocarriers for amino acids [72], peptides [73], vitamins [44] and anti-cancer drugs [74].

1.8.3.2. Imaging

Nanoparticles have promising applications in the medical imaging field as contrast agents or luminescent markers. For example, metal-complexed SCNPs have been used as contrast agents for Magnetic Resonance Imaging [75].

Fluorescence has long been used in many applications in biology, biochemistry and medicine; for example, biomarker analysis, immunoassays and diagnostic imaging. Small organic molecules suffer from limitations regarding their wavelength range, brightness, photo-stability and fluorescence self-quenching. The toxicity of some organic fluorophores has limited their application for *in vitro* and *in vivo* optical imaging.

Fluorescent nanoparticles are a possible solution to the limitations of small organic fluorescent dyes. Fluorescent nanoparticles often contain multiple fluorophores, leading to brighter photoluminescent emission compared to the low absorption coefficients of individual organic fluorophore molecules. The encapsulation of the fluorophore into the nanoparticle increases its stability and reduces photo-bleaching and toxicity. Proper selection of the nature of the particle can improve biocompatibility compared to small organic fluorescent molecules. The possibility to combine imaging and drug delivery in the same system is a unique characteristic of fluorescent nanoparticles.

Fluorescent nanoparticle systems based on block copolymer micelles and cross-linked polymer networks, quantum dots (QDs), π-conjugated polymers, and dendrimers have been evaluated as optical imaging systems. However, despite the successful use of fluorescent nanoparticles for optical imaging, some problems remain to be solved. The large size of these particles prevents them from traversing intact cell membranes efficiently, appropriate tuning of absorption and photoluminescence emission wavelengths is difficult and, in the case of inorganic nanoparticles, the issue is non-degradability and in vivo accumulation of large particles [76].

In recent years, several methods have been developed to endow SCNPs with fluorescent characteristics. The folding of linear polymer chains into a collapsed state provides dense zones where π-conjugated fluorophore molecules can be packed.

Four different pathways have been developed to endow SCNPs with fluorescent properties: precursor pre-functionalization with fluorophore, fluorophore entrapment / *in situ* generation, SCNP post-functionalization with fluorophore, and fluorophore generation through SCNP formation [77].

Precursor pre-functionalization with fluorophore: The precursor polymer is functionalized with a fluorescent moiety before crosslinking into an SCNP.

Fluorophore entrapment / in situ generation: Fluorophore molecules are entrapped into the dense local packaging zones of the polymer or fluorophores are synthesized in the packaging zones taking advantage of the local environment.

SCNP post-functionalization with fluorophore: Cross-linked SCNPs are functionalized by reacting with fluorescent moieties.

Fluorophore generation through SCNP formation: The cross-linking reaction generates fluorophores inside the SCNP. For example synthesis of fluorescent SCNPs via photoinduced nitrile imine mediated tetrazole-ene cycloaddition [78].

1.9. Luminescence

Luminescescence is the emission of light by a substance not resulting from heat. It can be caused by chemical reactions (chemoluminescence), ionizing radiation (radioluminescence), mechanical action (mechanoluminescence), electric currents (electroluminescence) or light (photoluminescence) [79].

Photoluminescence is caused by the absorption of photons by a molecule. It is initiated when the absorption of photons causes the excitation of electrons to a higher energy level in an atom. This phenomenon is known as photoexcitation. The electrons then return to the ground state via several relaxation processes that include the emission of photons. Part of the energy can be dissipated through non-radiative pathways such as vibrations, resulting in the emission of lower energy, and longer wavelength, photons. The phenomena that produce this result are fluorescence and phosphorescence.

Phosphorescence is a process where the electronic spin changes and electrons are promoted to a triplet excited state. The only transitions back to the ground singlet state are through "forbidden" mechanisms. These "forbidden" transitions can happen but are kinetically unfavoured, resulting in a slower decay to the ground state. The lifetime of the excited state is of the order of seconds to minutes, which means that phosphorescence persists after the exciting source is removed as an afterglow.

1.9.1. Fluorescence

Fluorescence was first described by George Gabriel Stokes [80] in 1852, when he observed the ability of fluorspar and uranium glass to change invisible ultraviolet light into visible blue light. Fluorescence is a type of photoluminescence where an electron in the singlet ground state is promoted to the singlet-excited state. The electronic transition does not change the electron spin and the transition back to the ground state is allowed. The excited state is short lived ($<10^{-5}$ s). Vibrations dissipate part of the energy and the electron returns to the ground state emitting a longer wavelength photon. Fluorescence ceases immediately after the photoexcitation of the fluorescent material stops [81].

Fluorescence is common in nature. It appears in many different animals and some plants. It can also be seen in some minerals and in atmospheric phenomena like auroras. Among the practical applications of fluorescence are fluorescent lamps, the use of fluorescent dyes (fluorophores) in sensing [82] and imaging, as markers in biological applications [83], and fluorescence spectroscopy.

Fluorophores are chemical compounds that emit light under light excitation. Usually they contain aromatic rings or conjugated double bonds with conjugated π electrons in them.

Intrinsically fluorescent molecules can be used alone as tracers, dyes or indicators, while others can be bound covalently to otherwise non-fluorescent systems as markers for spectroscopy and imaging applications. The emission range of organic fluorophores goes from UV light to the near infrared. Some of the most common fluorophores include fluorescein, rhodamine, coumarin or cyanine [84].

The fluorescence quantum yield is the parameter used to measure the efficiency of fluorescent emission. It is defined as the ratio of the number of photons emitted by a fluorophore to the number of photons absorbed. It represents the probability that a given excited fluorophore will produce an emitted photon.

(1.7)

$$Quantum\ Yield\ = \frac{Number\ of\ photons\ emitted}{Number\ of\ photons\ absorbed}$$

The quantum yield of a fluorophore is calculated by building a calibration curve using multiple standards of a compound with known fluorescence quantum yield. The integrated area of fluorescence is plotted against the absorbance for different concentrations of the fluorophore [85].

1.10. Aggregation Induced Emission

In most biomedical applications luminophores are used in aqueous media in physiological environments where the intrinsically hydrophobic aromatic components like phenyl rings responsible for the luminescence are insoluble, causing the formation of nanoaggregates [86]. Aggregation can result in changes in the emissivity of the molecule.

In 1954 Förster and Kasper discovered that the fluorescence of pyrene was weakened with increasing solute concentration [87]. This phenomenon is known as aggregation caused quenching (ACQ). This effect is common in simple aromatic compounds according to the summary Photophysics of Aromatic Molecules (Birks, 1970) [88]. These conventional fluorescent molecules emit strongly in the isolated state. In the aggregated state, however, fluorophores interact with adjoining molecules in their immediate vicinity. The aromatic rings of adjoining molecules experience intermolecular π-π stacking interactions, causing these fluorophores to decay from the excited state to the ground state via non-radiative pathways, resulting in the quenching of fluorescent emission [86].

Fluorescence is caused mostly by electronic conjugation of π bands. One strategy to increase the yield of organic luminescence has been to increase π conjugation by adding more aromatic rings. The resulting molecules have increased fluorescence efficiency but often suffer a severe ACQ effect [89]. ACQ is detrimental to most applications. In biological applications for example, these molecules are in an aqueous medium (physiological medium) resulting in aggregation. Even when attaching polar functional groups to the fluorophore to increase their solubility and make them hydrophilic, the resulting compounds -despite being water soluble- tend to form aggregates due to the intrinsic hydrophobicity of the luminescent part, filled with π conjugated aromatic rings [89]. As ACQ is deleterious on most practical applications, different strategies were followed to deal with

this problem. Most of them tried to avoid aggregation, but some followed a different strategy.

In 2001, Tang and co-workers discovered a luminogen system in which aggregation resulted in an increase of fluorescence rather than a decrease [90]. These compounds were non emissive in dilute solutions but became fluorescent in concentrated solutions or solid films. Because the emission was induced by aggregates, the process was named Aggregation Induced Emission (AIE).

1.10.1. Mechanism

The first AIE luminogen was hexaphenyl silole (HPS). Unlike conventional luminophores, such as disk-shaped perylene [89], HPS is propeller shaped and non-planar. In a diluted solution the aromatic rings of the luminophore rotate freely, dissipating the energy of the excited state and causing the molecule to return to the ground state via non-radiative ways, rendering it non-luminescent. In the aggregate state the π-π stacking that causes ACQ is avoided by the propeller shape of HPS, while intramolecular rotations are restricted by steric hindrance caused by the presence of other molecules in a crowded space. As a result HPS is emissive in the aggregated state [89].
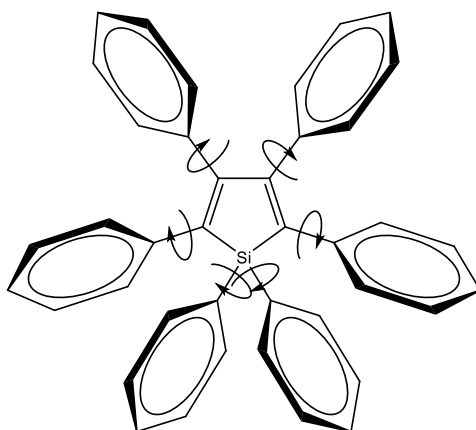
Scheme 1.2. Representation of the 3D structure of aggregation induced emission luminophore hexaphenyl silole.

1.11. Structure of this thesis

The present Chapter has summarized several concepts relevant for the understanding of the results reported in Chapters 3-6.

Chapter 2 explains the techniques and instruments used in the characterization of polymers, SCNPs, and products used or synthesized in this thesis.

Chapter 3 introduces a new model for the calculation of the size, apparent molar mass, and shrinking factor of elastic SCNPs based on the length of the polymer chain, the monomer

fraction and the solvent quality. The model is used to understand the size of SCNPs on different surfaces.

In Chapter 4 we present the synthesis of enzyme-mimicking, iron containing, water soluble SCNPs comprised of poly (oligo (ethylene glycol) methyl ether methacrylate-*co*-2-acetoacetoxy ethyl methacrylate) [poly(OEGMA-co-AEMA)] copolymers by metal coordination. These SCNPs will be used -for the first time- as catalysts for the synthesis of intrinsically conducting polymer PEDOT: PSS dispersions *via* oxidative polymerization.

Chapter 5 shows the synthesis and characterization of fluorescent SCNPs by photoactivation of poly (methyl methacrylate-co-2-acetoacetoxy ethyl methacrylate) [poly(MMA-co-AEMA)] copolymers functionalized with diazo functional groups. Fluorescence emission is produced by the addition of an aggregation induced emission (AIE) fluorophore with azide moieties. Crosslinking in the SCNP is achieved by the cleavage of azide and diazo groups by irradiating them with UV light.

Chapter 6 presents a route for synthesis and characterization of fluorescent poly(MMA-co-AEMA) SCNPs based on the Hantzsch pyridine synthesis reaction. Orthogonal fluorophores will allow for the reporting of both the folding and the aggregation of these SCNPs. Intramolecular compaction and SCNP formation is identified by the formation of fluorescent Hantzsch esters, while the addition of AIE luminophores with fluorescence at redshifted wavelengths allows for the detection of intermolecular aggregation.

Finally, Chapter 7 summarizes the major conclusions of this thesis.

1.12. References

[1] P.J. Flory, Principles of polymer chemistry, Cornell University Press1953.
[2] S.M. Bhattacharjee, A. Giacometti, A. Maritan, Flory theory for polymers, Journal of Physics: Condensed Matter, 25 (2013) 503101.
[3] S. Perrier, 50th Anniversary Perspective: RAFT Polymerization—A User Guide, Macromolecules, 50 (2017) 7433-7447.
[4] J. Chiefari, Y.K. Chong, F. Ercole, J. Krstina, J. Jeffery, T.P.T. Le, R.T.A. Mayadunne, G.F. Meijs, C.L. Moad, G. Moad, Living free-radical polymerization by reversible addition—fragmentation chain transfer: the RAFT process, Macromolecules, 31 (1998) 5559-5562.
[5] G. Moad, J. Chiefari, Y.K. Chong, J. Krstina, R.T.A. Mayadunne, A. Postma, E. Rizzardo, S.H. Thang, Living free radical polymerization with reversible addition – fragmentation chain transfer (the life of RAFT), Polymer International, 49 (2000) 993-1001.
[6] G. Moad, Y.K. Chong, A. Postma, E. Rizzardo, S.H. Thang, Advances in RAFT polymerization: the synthesis of polymers with defined end-groups, Polymer, 46 (2005) 8458-8468.
[7] G. Inzelt, Conducting polymers: a new era in electrochemistry, Springer Science & Business Media2012.
[8] A.K. Bakhshi, G. Bhalla, Electrically conducting polymers: Materials of the twentyfirst century, Journal of Scientific and Industrial Research, 63(09) (2004) 715-728.
[9] H. Shirakawa, E.J. Louis, A.G. MacDiarmid, C.K. Chiang, A.J. Heeger, Synthesis of electrically conducting organic polymers: halogen derivatives of polyacetylene, (CH), Journal of the Chemical Society, Chemical Communications, (1977) 578-580.
[10] P. Chandrasekhar, Conducting polymers, fundamentals and applications, Springer1999.

[11] R. Balint, N.J. Cassidy, S.H. Cartmell, Conductive polymers: Towards a smart biomaterial for tissue engineering, Acta Biomaterialia, 10 (2014) 2341-2353.

[12] G.M. Whitesides, Nanoscience, Nanotechnology, and Chemistry, Small, 1 (2005) 172-179.

[13] C.P. Poole Jr, F.J. Owens, Introduction to nanotechnology, John Wiley & Sons2003.

[14] A.P. Dowling, Development of nanotechnologies, Materials Today, 7 (2004) 30-35.

[15] M. Vert, Y. Doi, K.-H. Hellwich, M. Hess, P. Hodge, P. Kubisa, M. Rinaudo, F. Schué, Terminology for biorelated polymers and applications (IUPAC Recommendations 2012), Pure and Applied Chemistry, 84 (2012) 377-410.

[16] I. Khan, K. Saeed, I. Khan, Nanoparticles: Properties, applications and toxicities, Arabian Journal of Chemistry, 12 (2019) 908-931.

[17] J.A. Pomposo, Single-Chain Polymer Nanoparticles: Synthesis, Characterization, Simulations, and Applications, John Wiley & Sons2017.

[18] M. Gonzalez-Burgos, A. Latorre-Sanchez, J.A. Pomposo, Advances in single chain technology, Chemical Society Reviews, 44 (2015) 6122-6142.

[19] Y. Inoue, P. Kuad, Y. Okumura, Y. Takashima, H. Yamaguchi, A. Harada, Thermal and Photochemical Switching of Conformation of Poly(ethylene glycol)-Substituted Cyclodextrin with an Azobenzene Group at the Chain End, Journal of the American Chemical Society, 129 (2007) 6396-6397.

[20] B.V.K.J. Schmidt, N. Fechler, J. Falkenhagen, J.-F. Lutz, Controlled folding of synthetic polymer chains through the formation of positionable covalent bridges, Nature Chemistry, 3 (2011) 234-238.

[21] Z. Ge, Y. Zhou, J. Xu, H. Liu, D. Chen, S. Liu, High-Efficiency Preparation of Macrocyclic Diblock Copolymers via Selective Click Reaction in Micellar Media, Journal of the American Chemical Society, 131 (2009) 1628-1629.

[22] D. Mecerreyes, V. Lee, C.J. Hawker, J.L. Hedrick, A. Wursch, W. Volksen, T. Magbitang, E. Huang, R.D. Miller, A Novel Approach to Functionalized Nanoparticles: Self-Crosslinking of Macromolecules in Ultradilute Solution, Advanced Materials, 13 (2001) 204-208.

[23] J. Tao, G. Liu, Polystyrene-block-poly(2-cinnamoylethyl methacrylate) Tadpole Molecules, Macromolecules, 30 (1997) 2408-2411.

[24] R.K. Roy, J.-F. Lutz, Compartmentalization of Single Polymer Chains by Stepwise Intramolecular Cross-Linking of Sequence-Controlled Macromolecules, Journal of the American Chemical Society, 136 (2014) 12888-12891.

[25] J. Romulus, M. Weck, Single-Chain Polymer Self-Assembly Using Complementary Hydrogen Bonding Units, Macromolecular Rapid Communications, 34 (2013) 1518-1523.

[26] A.M. Hanlon, C.K. Lyon, E.B. Berda, What Is Next in Single-Chain Nanoparticles?, Macromolecules, 49 (2016) 2-14.

[27] R. Chen, E.B. Berda, 100th Anniversary of Macromolecular Science Viewpoint: Re-examining Single-Chain Nanoparticles, ACS Macro Letters, 9 (2020) 1836-1843.

[28] W. Kuhn, G. Balmer, Crosslinking of single linear macromolecules, Journal of Polymer Science, 57 (1962) 311-319.

[29] A. Sanchez-Sanchez, I. Pérez-Baena, J.A. Pomposo, Advances in Click Chemistry for Single-Chain Nanoparticle Construction, Molecules, 18 (2013) 3339-3355.

[30] N. Corrigan, K. Jung, G. Moad, C.J. Hawker, K. Matyjaszewski, C. Boyer, Reversible-deactivation radical polymerization (Controlled/living radical polymerization): From discovery to materials design and applications, Progress in Polymer Science, 111 (2020) 101311.

[31] J.-S. Wang, K. Matyjaszewski, Controlled/"living" radical polymerization. atom transfer radical polymerization in the presence of transition-metal complexes, Journal of the American Chemical Society, 117 (1995) 5614-5615.

[32] C.J. Hawker, A.W. Bosman, E. Harth, New Polymer Synthesis by Nitroxide Mediated Living Radical Polymerizations, Chemical Reviews, 101 (2001) 3661-3688.

[33] D.M. Lynn, S. Kanaoka, R.H. Grubbs, Living Ring-Opening Metathesis Polymerization in Aqueous Media Catalyzed by Well-Defined Ruthenium Carbene Complexes, Journal of the American Chemical Society, 118 (1996) 784-790.

[34] J.B. Beck, K.L. Killops, T. Kang, K. Sivanandan, A. Bayles, M.E. Mackay, K.L. Wooley, C.J. Hawker, Facile Preparation of Nanoparticles by Intramolecular Cross-Linking of Isocyanate Functionalized Copolymers, Macromolecules, 42 (2009) 5629-5635.

[35] J.-H. Ryu, R.T. Chacko, S. Jiwpanich, S. Bickerton, R.P. Babu, S. Thayumanavan, Self-Cross-Linked Polymer Nanogels: A Versatile Nanoscopic Drug Delivery Platform, Journal of the American Chemical Society, 132 (2010) 17227-17235.

[36] T.A. Croce, S.K. Hamilton, M.L. Chen, H. Muchalski, E. Harth, Alternative o-Quinodimethane Cross-Linking Precursors for Intramolecular Chain Collapse Nanoparticles, Macromolecules, 40 (2007) 6028-6031.

[37] M. González-Burgos, A. Alegría, A. Arbe, J. Colmenero, J.A. Pomposo, An unexpected route to aldehyde-decorated single-chain nanoparticles from azides, Polymer Chemistry, 7 (2016) 6570-6574.

[38] G.M. Green, N.P. Peet, W.A. Metz, Polystyrene-Supported Benzenesulfonyl Azide: A Diazo Transfer Reagent That Is Both Efficient and Safe, The Journal of Organic Chemistry, 66 (2001) 7930-7930.

[39] C.K. Lyon, A. Prasher, A.M. Hanlon, B.T. Tuten, C.A. Tooley, P.G. Frank, E.B. Berda, A brief user's guide to single-chain nanoparticles, Polymer Chemistry, 6 (2015) 181-197.

[40] O. Altintas, C. Barner-Kowollik, Single Chain Folding of Synthetic Polymers by Covalent and Non-Covalent Interactions: Current Status and Future Perspectives, Macromolecular Rapid Communications, 33 (2012) 958-971.

[41] H.C. Kolb, M.G. Finn, K.B. Sharpless, Click Chemistry: Diverse Chemical Function from a Few Good Reactions, Angewandte Chemie International Edition, 40 (2001) 2004-2021.

[42] L. Oria, R. Aguado, J.A. Pomposo, J. Colmenero, A Versatile "Click" Chemistry Precursor of Functional Polystyrene Nanoparticles, Advanced Materials, 22 (2010) 3038-3041.

[43] M.K. Aiertza, I. Odriozola, G. Cabañero, H.-J. Grande, I. Loinaz, Single-chain polymer nanoparticles, Cellular and Molecular Life Sciences, 69 (2012) 337-346.

[44] A. Sanchez-Sanchez, S. Akbari, A. Etxeberria, A. Arbe, U. Gasser, A.J. Moreno, J. Colmenero, J.A. Pomposo, "Michael" Nanocarriers Mimicking Transient-Binding Disordered Proteins, ACS Macro Letters, 2 (2013) 491-495.

[45] O. Galant, M. Davidovich-Pinhas, C.E. Diesendruck, The Effect of Intramolecular Cross-Linking on Polymer Interactions in Solution, Macromolecular Rapid Communications, 39 (2018) 1800407.

[46] A. Sanchez-Sanchez, J.A. Pomposo, Efficient Synthesis of Single-Chain Polymer Nanoparticles <i>via</i> Amide Formation, Journal of Nanomaterials, 2015 (2015) 723492.

[47] I. Perez-Baena, I. Asenjo-Sanz, A. Arbe, A.J. Moreno, F. Lo Verso, J. Colmenero, J.A. Pomposo, Efficient Route to Compact Single-Chain Nanoparticles: Photoactivated Synthesis via Thiol–Yne Coupling Reaction, Macromolecules, 47 (2014) 8270-8280.

[48] J.-M. Lehn, Dynamers: dynamic molecular and supramolecular polymers, Progress in Polymer Science, 30 (2005) 814-831.

[49] A. Sanchez-Sanchez, A. Arbe, J. Colmenero, J.A. Pomposo, Metallo-Folded Single-Chain Nanoparticles with Catalytic Selectivity, ACS Macro Letters, 3 (2014) 439-443.

[50] A. Sanchez-Sanchez, A. Arbe, J. Kohlbrecher, J. Colmenero, J.A. Pomposo, Efficient Synthesis of Single-Chain Globules Mimicking the Morphology and Polymerase Activity of Metalloenzymes, Macromolecular Rapid Communications, 36 (2015) 1592-1597.

[51] S. Mavila, C.E. Diesendruck, S. Linde, L. Amir, R. Shikler, N.G. Lemcoff, Polyclooctadiene Complexes of Rhodium(I): Direct Access to Organometallic Nanoparticles, Angewandte Chemie International Edition, 52 (2013) 5767-5770.

[52] A. Sanchez-Sanchez, J.A. Pomposo, Single-Chain Polymer Nanoparticles via Non-Covalent and Dynamic Covalent Bonds, Particle & Particle Systems Characterization, 31 (2014) 11-23.

[53] T. Maeda, H. Otsuka, A. Takahara, Dynamic covalent polymers: Reorganizable polymers with dynamic covalent bonds, Progress in Polymer Science, 34 (2009) 581-604.
[54] P. Chakma, D. Konkolewicz, Dynamic Covalent Bonds in Polymeric Materials, Angewandte Chemie International Edition, 58 (2019) 9682-9695.
[55] A. Wilson, G. Gasparini, S. Matile, Functional systems with orthogonal dynamic covalent bonds, Chemical Society Reviews, 43 (2014) 1948-1962.
[56] B.T. Tuten, D. Chao, C.K. Lyon, E.B. Berda, Single-chain polymer nanoparticles via reversible disulfide bridges, Polymer Chemistry, 3 (2012) 3068-3071.
[57] A.W. Jackson, D.A. Fulton, Making polymeric nanoparticles stimuli-responsive with dynamic covalent bonds, Polymer Chemistry, 4 (2013) 31-45.
[58] B.S. Murray, D.A. Fulton, Dynamic Covalent Single-Chain Polymer Nanoparticles, Macromolecules, 44 (2011) 7242-7252.
[59] A. Sanchez-Sanchez, D.A. Fulton, J.A. Pomposo, pH-responsive single-chain polymer nanoparticles utilising dynamic covalent enamine bonds, Chemical Communications, 50 (2014) 1871-1874.
[60] D. Drahoňovský, J.-M. Lehn, Hemiacetals in Dynamic Covalent Chemistry: Formation, Exchange, Selection, and Modulation Processes, The Journal of Organic Chemistry, 74 (2009) 8428-8432.
[61] A. Latorre-Sánchez, J.A. Pomposo, Recent bioinspired applications of single-chain nanoparticles, Polymer International, 65 (2016) 855-860.
[62] J.A. Pomposo, Bioinspired single-chain polymer nanoparticles, Polymer International, 63 (2014) 589-592.
[63] J. Rubio-Cervilla, E. González, J.A. Pomposo, Advances in Single-Chain Nanoparticles for Catalysis Applications, Nanomaterials, 7 (2017) 341.
[64] H. Rothfuss, N.D. Knöfel, P.W. Roesky, C. Barner-Kowollik, Single-Chain Nanoparticles as Catalytic Nanoreactors, Journal of the American Chemical Society, 140 (2018) 5875-5881.
[65] M. Huo, N. Wang, T. Fang, M. Sun, Y. Wei, J. Yuan, Single-chain polymer nanoparticles: Mimic the proteins, Polymer, 66 (2015) A11-A21.
[66] R. Zeng, L. Chen, Q. Yan, CO2-Folded Single-Chain Nanoparticles as Recyclable, Improved Carboxylase Mimics, Angewandte Chemie International Edition, 59 (2020) 18418-18422.
[67] I. Perez-Baena, F. Barroso-Bujans, U. Gasser, A. Arbe, A.J. Moreno, J. Colmenero, J.A. Pomposo, Endowing Single-Chain Polymer Nanoparticles with Enzyme-Mimetic Activity, ACS Macro Letters, 2 (2013) 775-779.
[68] M.A.J. Gillissen, I.K. Voets, E.W. Meijer, A.R.A. Palmans, Single chain polymeric nanoparticles as compartmentalised sensors for metal ions, Polymer Chemistry, 3 (2012) 3166-3174.
[69] A. Latorre-Sanchez, J.A. Pomposo, A simple, fast and highly sensitive colorimetric detection of zein in aqueous ethanol via zein–pyridine–gold interactions, Chemical Communications, 51 (2015) 15736-15738.
[70] A.K. Mishra, Nanomedicine for drug delivery and therapeutics, John Wiley & Sons2013.
[71] J. Rubio-Cervilla, E. González, J.A. Pomposo, Applications of Single-Chain Polymer Nanoparticles, in: J.A. Pomposo (Ed.) Single-Chain Polymer Nanoparticles: Synthesis, Characterization, Simulations, and Applications., Wiley-VCH, Weinheim, Germany, 2017, pp. 341-400.
[72] G. Njikang, G. Liu, L. Hong, Chiral Imprinting of Diblock Copolymer Single-Chain Particles, Langmuir, 27 (2011) 7176-7184.
[73] S.K. Hamilton, E. Harth, Molecular Dendritic Transporter Nanoparticle Vectors Provide Efficient Intracellular Delivery of Peptides, ACS Nano, 3 (2009) 402-410.
[74] R.J. Passarella, D.E. Spratt, A.E. van der Ende, J.G. Phillips, H. Wu, V. Sathiyakumar, L. Zhou, D.E. Hallahan, E. Harth, R. Diaz, Targeted Nanoparticles That Deliver a Sustained, Specific Release of Paclitaxel to Irradiated Tumors, Cancer Research, 70 (2010) 4550.

[75] I. Perez-Baena, I. Loinaz, D. Padro, I. García, H.J. Grande, I. Odriozola, Single-chain polyacrylic nanoparticles with multiple Gd(iii) centres as potential MRI contrast agents, Journal of Materials Chemistry, 20 (2010) 6916-6922.

[76] X. Zhang, S. Wang, L. Xu, L. Feng, Y. Ji, L. Tao, S. Li, Y. Wei, Biocompatible polydopamine fluorescent organic nanoparticles: facile preparation and cell imaging, Nanoscale, 4 (2012) 5581-5584.

[77] J. De-La-Cuesta, J.A. Pomposo, Photoactivation of Aggregation-Induced Emission Molecules for Fast and Efficient Synthesis of Highly Fluorescent Single-Chain Nanoparticles, ACS Omega, 3 (2018) 15193-15199.

[78] J. Willenbacher, K.N.R. Wuest, J.O. Mueller, M. Kaupp, H.-A. Wagenknecht, C. Barner-Kowollik, Photochemical Design of Functional Fluorescent Single-Chain Nanoparticles, ACS Macro Letters, 3 (2014) 574-579.

[79] B. Valeur, M.N. Berberan-Santos, A Brief History of Fluorescence and Phosphorescence before the Emergence of Quantum Theory, Journal of Chemical Education, 88 (2011) 731-738.

[80] G.G. Stokes, XXX. On the change of refrangibility of light, Philosophical Transactions of the Royal Society of London, 142 (1852) 463-562.

[81] J.R. Lakowicz, Introduction to Fluorescence, in: J.R. Lakowicz (Ed.) Principles of Fluorescence Spectroscopy, Springer US, Boston, MA, 2006, pp. 1-26.

[82] J.R. Lakowicz, Fluorescence Sensing, in: J.R. Lakowicz (Ed.) Principles of Fluorescence Spectroscopy, Springer US, Boston, MA, 2006, pp. 623-673.

[83] M. Chalfie, Green Fluorescent Protein, Photochemistry and Photobiology, 62 (1995) 651-656.

[84] J. Rietdorf, Microscopy techniques, 2005.

[85] A.M. Brouwer, Standards for photoluminescence quantum yield measurements in solution (IUPAC Technical Report), Pure and Applied Chemistry, 83 (2011) 2213-2228.

[86] J. Mei, N.L.C. Leung, R.T.K. Kwok, J.W.Y. Lam, B.Z. Tang, Aggregation-Induced Emission: Together We Shine, United We Soar!, Chemical Reviews, 115 (2015) 11718-11940.

[87] T. Förster, K. Kasper, Ein Konzentrationsumschlag der Fluoreszenz des Pyrens, Zeitschrift für Elektrochemie, Berichte der Bunsengesellschaft für physikalische Chemie, 59 (1955) 976-980.

[88] J.B. Birks, Photophysics of aromatic molecules, 1970.

[89] Y. Hong, J.W.Y. Lam, B.Z. Tang, Aggregation-induced emission, Chemical Society Reviews, 40 (2011) 5361-5388.

[90] J. Luo, Z. Xie, J.W.Y. Lam, L. Cheng, H. Chen, C. Qiu, H.S. Kwok, X. Zhan, Y. Liu, D. Zhu, B.Z. Tang, Aggregation-induced emission of 1-methyl-1,2,3,4,5-pentaphenylsilole, Chemical Communications, (2001) 1740-1741.

Chapter 2: Experimental Techniques

2.1. Motivation

In this Chapter, the techniques and instruments used in the characterization of polymers, single-chain polymer nanoparticles, and products used or synthesized in this thesis are explained.

2.2. Size exclusion chromatography / Gel permeation chromatography

Size exclusion chromatography (SEC) is a chromatographic method that separates molecules according to their size. It was first developed in 1955 by Lathe and Ruthven [1]. Gel permeation chromatography (GPC) is a type of SEC introduced by J.C. Moore of the Dow Chemical Company in 1964 [2] to separate polymers. Soon it was discovered that this method provided good molar mass distribution (M_w) information for polymers. Because of this GPC is widely used for polymer characterization.

GPC is used primarily for the analysis of large molecules such as polymers and proteins. This technique separates molecules based on the hydrodynamic radius of the analyte. The differentiation takes place in a porous column which typically consists of a hollow tube tightly packed with polymer beads containing microscopic pores of different sizes called the stationary phase. The smaller molecules become trapped in the pores more easily and spend more time there, needing longer times to elute. This increases their retention time. Large molecules are too big to enter the pores and are eluted quickly, separating them from the smaller ones.

Theoretically, in the SEC mode of separation the analyte molecules do not interact with the surface of the stationary phase. Due to this lack of interactions, the separation of the analyte depends only on the hydrodynamic volume of the solute rather than the chemical or electrostatic interactions between the phases.

The concentration by weight of the polymer is monitored continuously with a detector. The concentration in each part of the chromatogram can be measured by refractive index (RI), UV or light scattering detectors. The molar mass of the polymer is measured either directly by a multi-angle laser light scattering (MALLS) detector or indirectly by calibrating the column. A chromatogram is generated, which consists of a weight distribution of the polymer as a function of the retention time. The shape of the peak depends on the dispersity ($Ð$) of the polymer: disperse samples ($Ð \gg 1$) form wide peaks, while when the peaks are narrow the sample is near monodisperse ($Ð \approx 1$).

Refractive index detectors measure changes in the refractive index of the solution. Changes in the refractive index of the solution (n) are proportional to the solute concentration (c) according to

$$(2.1)$$

$$n \propto n_0 + c(n_p - n_0)$$

where n_p is the refractive index of the solute and n_0 the refractive index of the solvent.

A method to calculate the molecular mass distribution of polymer samples is to construct a calibration curve, which is created by plotting the molar mass of monodisperse standards of known molecular weight vs. the retention time in the column. Using this curve, the molecular weight of the sample can be interpolated from its retention time.

MALLS is used to determine the absolute molecular weight of polymers. This technique allows to measure the mass and size of molecules independently of the retention time and without need for calibration. The intensity of the scattered light (I_s) is dependent on the molar mass (M), the solute concentration (c), and the differential refractive index (dn/dc) of the solute

(2.2)

$$I_s \propto Mc \left(\frac{dn}{dc}\right)^2$$

The hydrodynamic volume (V_h) and the hydrodynamic radius (R_h) of the polymer can be measured with the help of viscometers according to the Einstein viscosity relation [3]

(2.3)

$$V_h = \frac{M[\eta]}{2.5N_A}$$

where $[\eta]$ is the viscosity of the solution and N_A is Avogadro's number.

The relation between viscosity and molar mass is given by the Mark-Howink-Sakurada equation

(2.4)

$$[\eta] = KM^\alpha$$

where K and α are constants specific to the solvent- polymer system that give information about the conformation of the polymer. These parameters be calculated plotting $[\eta]$ and M.

GPC can be used for the monitoring of the formation of SCNPs. Polymeric nanoparticles have a smaller hydrodynamic radius compared to the precursor polymer due to the collapse of the polymer chain upon intra-chain crosslinking. The formation of SCNPs is indicated by an increase in the retention time compared to the precursor polymer [4].

The samples were dissolved in THF and filtered before injecting them in the chromatograph.

GPC measurements were performed in an Agilent 1200 GPC-SEC Analysis system equipped with Wyatt light scattering miniDawnTreos, a ViscoStar II differential viscometer and a Optilab rEX Refractive Index Detector (Figure 2.1).

Figure 2.1. *GPC equipment used in this work.*

2.3. Nuclear magnetic resonance

Nuclear magnetic resonance (NMR) is a spectroscopic technique in which atomic nuclei in a strong magnetic field are perturbed by a weak oscillating magnetic field, resulting in the production of an electromagnetic signal with a frequency dependent on the magnetic field on the nucleus.

Nuclear particles like protons and neutrons have a spin. In nuclei with an odd number of protons or neutrons the spins pf the particles are not cancelled, resulting in an overall nuclear spin. In the absence of an external magnetic field, all spin states have the same energy. However, when an external magnetic field is applied, spin states aligned with the magnetic field are more stable and have less energy than anti-aligned states. The difference between both energy levels is proportional to the intensity of the magnetic field.

A weak oscillating magnetic field in the form of radio waves induces the excitation of the nuclei and a transition between the spin energy levels, producing an electromagnetic signal. The resonance frequency is directly proportional to the magnetic field around the nucleus. This magnetic field is shielded by the magnetic fields induced by other nuclei and electrons in the molecule, giving information about the chemical environment of atoms.

The resonant frequency of the signals change with the intensity of the applied magnetic field. To eliminate this dependence a reference frequency is employed, that corresponds to that observed for tetramethylsilane. The chemical shift (δ) of the analyte relative to the reference frequency is calculated in equation (2.5), where ν is the resonant frequency of the analyte and ν_0 the frequency of the reference [5].

$$(2.5)$$

$$\delta = \frac{\nu - \nu_0}{\nu_0}$$

The nuclei most commonly used in NMR are ^{1}H and ^{13}C.

^{1}H NMR spectra were recorded at r.t. on a Bruker spectrometer operating at 400 MHz (Figure 2.2), using $CDCl_3$ as a solvent and tetramethylsilane as internal reference.
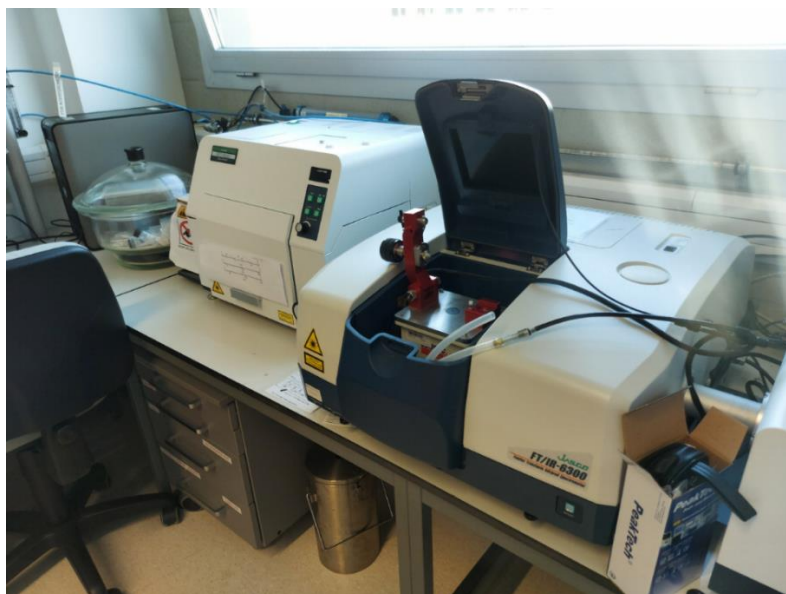
Figure 2.2. NMR equipment used in this work.

2.4. Fourier transform infrared spectroscopy

Fourier transform infrared spectroscopy (FTIR) is a spectroscopy technique used to measure the absorption of a sample in the infrared (IR) range of the spectrum. Absorption in the IR range is due to the transition between different vibrational energy levels of the molecule. Only the vibration modes that change the dipole moment are active. The frequencies of the vibrations are related to the strength of the bond and the mass of the atoms forming the bond.

In FTIR measurements, the sample is irradiated simultaneously with the entire range of frequencies, reducing the time needed for the experiment. The sample is commonly mixed with a non-absorbing salt (usually KBr) to form a pellet that is crossed by the light beam. The development of attenuated total reflection (ATR) allowed to simplify the sample preparation procedure. In ATR the sample is placed in direct contact with a crystal. The light passes through the crystal reflecting on the sample and producing evanescent waves that extend into the sample, and after multiple reflections the light is collected. After collection the light passes through an interferometer (normally a Michelson interferometer), where the beam is separated into 2 by a beam-splitter, reflected back by 2 mirrors and directed toward the detector. One of the mirrors is fixed while the other is moving, resulting in a difference in the optical path length that changes with time. This produces an interferogram where each wavelength is periodically blocked or transmitted due to wave interference, with a maximum at the zero retardation position where interference is constructive in all wavelengths. The detector receives a different spectrum each moment and a computer converts the raw data into the actual spectrum through a Fourier transform mathematical process [6].

FTIR spectra were recorded in a FT-IR JASCO 6360 (130-400K) infrared spectrometer (Figure 2.3).

Figure 2.3. *FTIR equipment used in this work.*

2.5. Ultraviolet-visible spectroscopy

Ultraviolet-visible spectroscopy (UV-Vis) is a spectroscopy technique that measures the absorption of light in the visible and adjacent near-UV and near-IR ranges. Absorption in the ultraviolet (UV) and visible range is due to the transitions of electrons from low energy to high energy atomic or molecular orbitals. Such transitions occur in transition metal ions, including d-d transitions and metal-ligand chain transfers, and inorganic and organic molecules, especially n-π* and π-π* orbital transitions in double bonds from conjugated organic compounds. Electrons with small energy gaps between the Highest Occupied Molecular Orbital (HOMO) and the Lowest Unoccupied Molecular Orbital (LUMO), and therefore easily excited to higher orbitals, absorb light at longer wavelengths than those with larger gaps. The absorption in the visible range is responsible for the colour of the sample [7].

According to the Beer-Lambert law [Equation (2.6)] the absorbance of a solution (A) is directly proportional to the concentration of the solute (c) and the path length (L).

(2.6)

$$A = \log_{10}(I_0/I) = \varepsilon c L$$

where I_0 is the intensity of the incident light, I is the transmitted intensity and ε is the extinction coefficient, which is an intrinsic property of the sample. Beer-Lambert law is often only valid for values of $A < 1$.

UV-Vis spectra were recorded in an Agilent 8453A UV-Vis spectrometer with Peltier thermostatic cell holder T-controller 89096A (Figure 2.4).

Figure 2.4. UV-Vis equipment used in this work.

2.6. Fluorescence spectroscopy

Fluorescence spectroscopy is a spectroscopic technique that analyses samples based on their fluorescent properties.

Fluorescence spectroscopy, like UV-Vis spectroscopy, is based on the electronic transitions, but it is focused on the emission rather than the absorption of light. Within each electronic level there are different vibrational levels. When a fluorescent molecule absorbs a photon of a certain wavelength an electron is promoted to a higher energy level and the molecule adopts a higher vibrational energy state. Then the molecules collide with other molecules causing them to lose energy and return to the lowest vibrational energy state inside the excited state. When the excited molecule returns to the ground state it emits a photon with a longer wavelength than the absorbed one. This process can be visualized in a Jablonsky energy diagram (Figure 2.5) [8].
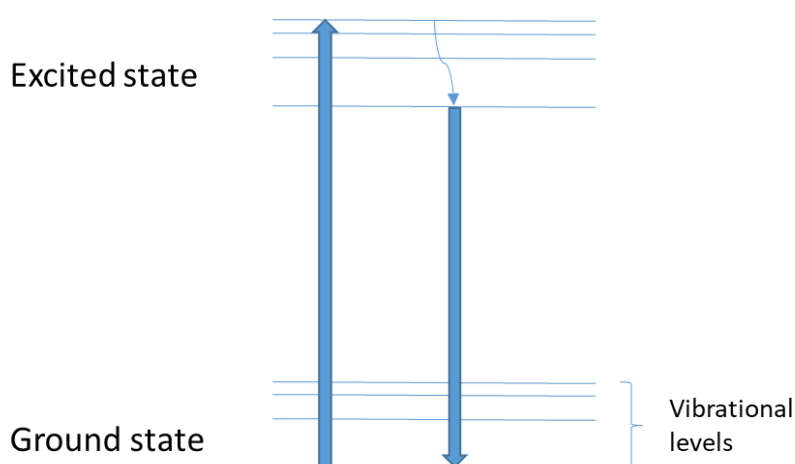
Figure 2.5. Representation of a Jablonsky diagram.

This change in the frequency of emitted photons is called Stokes shift and occurs in most fluorophore solutions. It is caused by the rapid decay of excited electrons to the lowest vibrational level of the excited state. The shift is measured as the difference between the wavelengths of the maxima of the excitation and emission spectra. This phenomenon blocks excitation light from reaching the detector, allowing higher precision measurements.

Excitation of a fluorophore with a single wavelength of maximum absorption while scanning all wavelengths produces the emission spectrum and scanning through the absorption spectrum while recording the emission intensity at a single wavelength (usually the wavelength of maximum emission intensity) generates the excitation spectrum. The emission spectrum for many common fluorophores looks like the mirror image of the excitation spectrum due to the similarity of the vibrational levels of the ground state and the excited state. The emission spectrum is independent of the excitation energy (wavelength) as a consequence of rapid internal conversion from higher initial excited states to the lowest vibrational energy level of the excited state [9].

In a fluorescence spectrometer, a light from the source passes through a monochromator to select the excitation wavelength. The light is directed toward the fluorophore sample producing fluorescence. The intensity of fluorescence is measured by a detector placed at a 90º angle to avoid interference from the excitation light [10].

Fluorescence spectra were recorded at r.t. on an Agilent Cary Eclipse spectrometer at an excitation wavelength of 365 nm (Figure 2.6).

Figure 2.6. Fluorescence spectroscopy equipment used in this work.

2.7. Dynamic light scattering

Dynamic light scattering (DLS) is a technique used to determine the distribution of sizes of small particles in suspension and polymer solutions, dispersions and emulsions.

In order to measure the sample a monochromatic light source, normally a laser, is shot through the sample. When the light hits small particles it scatters in all directions if the particles are small in relation to the wavelength. The diffracted light from all the molecules interferes, either constructively or destructively, creating interference patterns. Then, this scattered light is recorded by a detector at a fixed angle. The Brownian motion of the small molecules in the sample causes the scattering intensities of a monochromatic light to vary with time, giving information about the time scale of movement of the scatters. These fluctuations are then recorded by the autocorrelator that compares the intensity of light at each point over time and from this information a correlation function is created. After a short time interval the intensity is virtually unchanged and the correlation remains high. At longer time delays, however, the correlation decays exponentially, meaning that after a long period there is no correlation between the intensity of the initial and final states. Small particles cause the intensity of the scattered light to fluctuate in shorter time-scales, while larger particles have more difficulty for diffusion and change the intensity slower [11]. According to the Stokes-Einstein equation [equation (2.7)], the diffusion coefficient (D) is inversely proportional to the radius (R) of the particle.

(2.7)

$$D = \frac{k_B T}{6\pi\eta R}$$

Where η is the viscosity, k_B the Boltzmann constant and T the absolute temperature [12].

DLS measurements were performed in a Malvern Zetasizer Nano apparatus (Figure 2.7).

Figure 2.7. *DLS equipment used in this work.*

2.8. Transmission electron microscopy

Transmission electron microscopy (TEM) is a microscopy technique in which a beam of electrons is transmitted through a thin sample to form an image. The transmission electron microscope was developed by Knoll and Ruska in 1932, for which Ruska was awarded the Nobel Prize in 1986. In TEM, electrons from an electron gun are focused into a narrow beam by magnetic lenses and directed toward the sample. Transmitted electrons reach a fluorescent screen where an image is projected. The image contrasts depends on the density of the sample material. High atom densities and atoms with high atomic numbers produce more scattering events that result in fewer electrons reaching the detector. TEM allows to take images with a resolution much higher than that of optical microscopes due to electrons having a De Broglie wavelength orders of magnitude smaller than that of visible light, allowing them to take images with atom level resolution [13].

TEM measurements were performed using a high-resolution transmission electron microscope TECNAI G220 TWIN (Figure 2.8). The measurements were carried out using an accelerating voltage of 200 kV under low dose conditions.

Figure 2.8. TEM equipment used in this work.

2.9. Elemental Analysis

Elemental Analysis (EA) is a process where presence and the proportions of chemical elements present in a sample are measured. In organic chemistry, the most common type of EA is CHNS analysis, where mass fractions of carbon, hydrogen, nitrogen, and sulphur are determined. The technique for CHNS analysis is usually combustion analysis, where the sample is burned and the combustion products; CO_2, H_2O, NO, and SO_2; are collected and weighted. The composition of the sample is calculated from the obtained product masses [14].

EA measurements were performed in a Euro EA3000 elemental analyser (CHNS) (Figure 2.9).

Figure 2.9. *EA equipment used in this work.*

2.10. X-ray scattering

X-ray scattering is a family of techniques used to study the structure, composition and physical properties of materials. Scattering is produced by the movement of the electronic cloud in atoms caused by incident electromagnetic waves, resulting in the re-radiation of these waves. These techniques are based on the observation and measurement of the scattering intensity of an X-ray beam hitting a sample as a function of the incident and scattering angle.

X-ray scattering can be elastic, where the energy of incident and scattered photons does not change, or inelastic, where energy is transferred from the X-rays to the sample. Elastic X-ray scattering techniques are classified according to their scattering angle. As the scattering angle provides information about the reciprocal space, the variation of electronic density at nanometre length scales cause the beams to scatter at low angles, while at atomic size scales it scatters at high angles [15].

2.10.1. Small angle X-ray scattering

Small angle X-Ray scattering (SAXS) is a small angle scattering technique used to characterize nanostructures with a resolution of nanometres. It can be used to determine the size, distribution and shape of nanoparticles and macromolecules [16]. It measures the

scattering caused on an X-ray beam when travelling through the sample at small angles (0.1º to 10º).

The first principles of SAXS were developed by Guinier in the 1930s for the study of metallic alloys [17]. In 1955 Guinier and Fournet demonstrated that the method yields not just information on the sizes and shapes of particles but also on the internal structure of disordered and partially ordered systems [18]. In the 1960s the method become important for the study of biological macromolecules and in the 1970s a breakthrough was achieved with the use of synchrotron radiation as the X-ray source, which provided a higher X-ray flux [19].

In a SAXS instrument a monochromatic beam of X-rays travels through the sample. Most of the X-rays do not interact with the sample, but some are scattered. A scattering pattern is formed in the detector, which is situated behind the sample. The high intensity produced by the main beam is blocked in order to detect the weak scattered intensity. The 2D data collected on the detector is reduced by converting the position of each pixel in the image into scattering angle 2θ or scattering vector q according to

(2.8)

$$q = (4\pi \sin\theta)/\lambda$$

where λ is the wavelength of the X-rays. The intensity of the scattering is plotted as a function of q [15]. The scattering intensity $I(q)$ is the product of the from factor $P(q)$, which depends on the size and shape of the particles, and the structure factor $S(q)$, which depends on the interactions between particles. In the case of SCNPs in solution, SAXS is employed for a precise determination of the values of radius of gyration, R_g, and scaling exponent, ν.
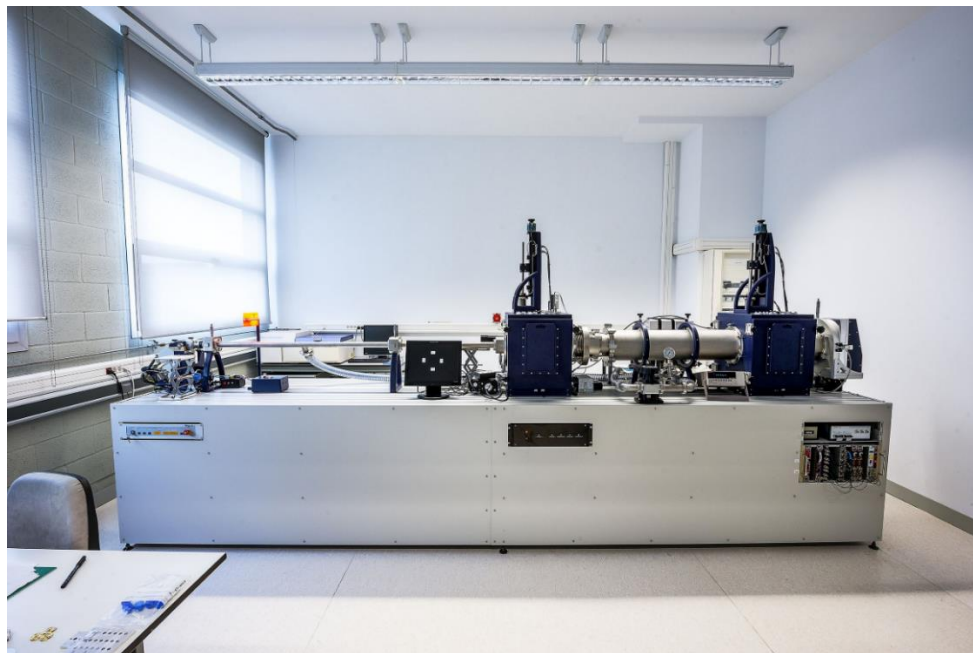
If $U = \frac{(2\nu+1)(2\nu+2)}{6} q^2 R_g^2$

and $\gamma(a, x) = \int_0^x t^{a-1} exp(-t)dt$

the generalized Gaussian coil function [20] is given by:

(2.9)

$$P(q) = \frac{1}{\nu U^{1/2\nu}} \gamma\left(\frac{1}{2\nu}, U\right) - \frac{1}{\nu U^{1/\nu}} \gamma\left(\frac{1}{\nu}, U\right)$$

SAXS measurements were performed on a Rigaku PSAXS-L SAXS instrument (Figure 2.10).

Figure 2.10. *SAXS equipment used in this work*

2.11. Thermogravimetric analysis

Thermogravimetric analysis (TGA) is a technique that measures the mass change of a material as a result of changes in temperature. It is used to determine characteristics of a materials that loss or gain mass due to decomposition, oxidation or loss of volatiles. Its applications are the analysis of degradation mechanisms and kinetics, and the determination of organic and inorganic content of a sample [21].

TGA measurements were performed in a Q500, TA Instruments Thermogravimetric analyser (Figure 2.11).

Figure 2.11. TGA equipment used in this work.

2.12. Inductively coupled plasma atomic emission spectroscopy

Inductively coupled plasma atomic emission spectroscopy (ICP-AES) is an analytical technique used for the detection of chemical elements, often metal atoms in solution. This technique uses inductively coupled plasma to excite atoms and ions that then emit light at characteristic wavelengths.

In a plasma source, a gas (usually argon) is ionized forming a plasma. The free electrons are accelerated by an electromagnetic field, producing more ions and heating the plasma to 6000-10000K. Then, the sample is introduced into the flame. The heat of the plasma breaks the chemical bonds of the sample molecules, and the free atoms are excited into excited electronic states. When the excited electrons return to the ground state, they emit photons of a frequency characteristic to each element. This light is detected by a spectrometer [22].

ICP-AES was performed on an Agilent 7700X spectrometer (Figure 2.12).
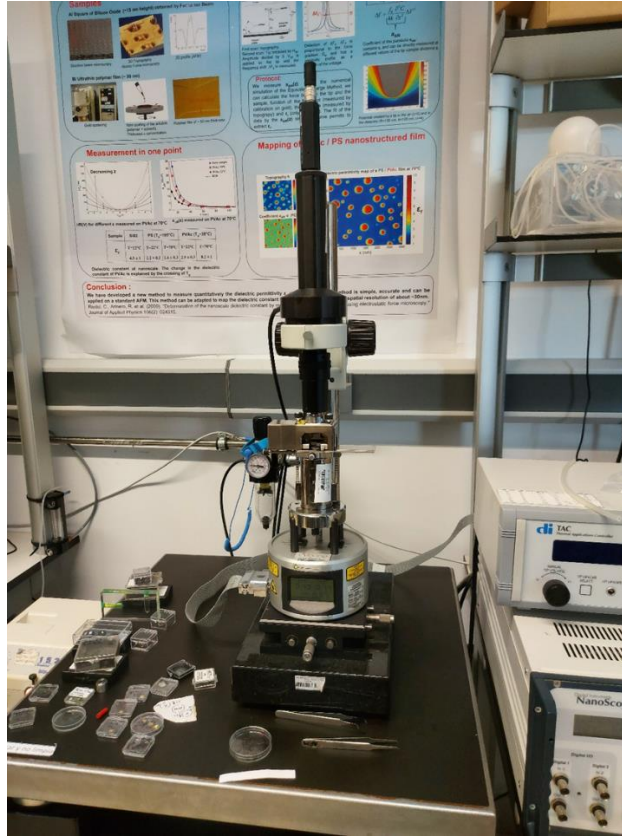
Figure 2.12. ICP-AES equipment used in this work.

2.13. Atomic force microscopy

Atomic force microscopy (AFM) is a type of scanning probe microscopy that allows to see surfaces with a resolution in the order of fractions of a nanometre.

The atomic force microscope was developed by Binnig, Quate, and Gerber at IBM labs in 1985 [23]. AFM consists of a cantilever with a very sharp tip. This tip scans the surface of the sample. When the tip approaches a surface interactions (Van der Waals, electric…) between the tips and the sample cause the cantilever to deflect toward or away from the sample. A laser beam is reflected on the cantilever towards a detector. Cantilever deflections cause the direction of the reflected beam to change. These changes allow a feedback-loop mechanism to adjust the height of the tip over the surface, creating a topographic map of the surface [24, 25].

AFM measurements were performed using a Multimode AFM, equipped with a Nanoscope V controller (Bruker) (Figure 2.13).

Figure 2.13. *AFM equipment used in this work.*

2.14. Conductivity measurements

The 4-point-probe is the standard method for the measurement of electric resistivity in thin films. The probe consists in four equally spaced conducting tips placed on a line on the sample film. An electric current is applied between the outer probes and the current is measured by a voltmeter connected to the inner probes [26, 27].

Conductivity of thin films was measured using a 4-point probe setup (HFS600-P, Linkam) (Figure 2.14) and an Alpha impedance analyser (Novocontrol).

Figure 2.14. *A 4-point probe setup.*

2.15. UV irradiation

UV irradiation experiments were performed with UV irradiation experiments were performed in i) a Hamamatsu LightningCure spot light source Model LC8 L9588 (Figure 2.15) and ii) a Penn PhD Photoreactor M2 (Penn Photon Devices, LLC). The equipment consisted of a Hg−Xe Lamp equipped with an A9616-05 filter (the transmittance wavelength was 300−400 nm with the maximum at 365 nm; the transmitted intensity was 80%) and the corresponding UV-light guide. The intensity of the UV light was 3.5 W/cm^2.

Figure 2.15. *UV light source equipment used in this work.*

2.16. References

[1] G.H. Lathe, C.R.J. Ruthven, The separation of substances and estimation of their relative molecular sizes by the use of columns of starch in water, Biochemical Journal, 62 (1956) 665-674.

[2] J.C. Moore, Gel permeation chromatography. I. A new method for molecular weight distribution of high polymers, Journal of Polymer Science Part A: General Papers, 2 (1964) 835-843.

[3] M.P.J. Dohmen, A.M. Pereira, J.M.K. Timmer, N.E. Benes, J.T.F. Keurentjes, Hydrodynamic Radii of Polyethylene Glycols in Different Solvents Determined from Viscosity Measurements, Journal of Chemical & Engineering Data, 53 (2008) 63-65.

[4] A. Latorre-Sánchez, A. Alegría, F. Lo Verso, A.J. Moreno, A. Arbe, J. Colmenero, J.A. Pomposo, A Useful Methodology for Determining the Compaction Degree of Single-Chain Nanoparticles by Conventional SEC, Particle & Particle Systems Characterization, 33 (2016) 373-381.

[5] R.K. Harris, Nuclear magnetic resonance spectroscopy, John Wiley and Sons Inc.,New York, NY, United States, 1986.

[6] O. Faix, Fourier Transform Infrared Spectroscopy, in: S.Y. Lin, C.W. Dence (Eds.) Methods in Lignin Chemistry, Springer Berlin Heidelberg, Berlin, Heidelberg, 1992, pp. 83-109.

[7] B.M. Weckhuysen, Ultraviolet-visible spectroscopy, in: J. van Bokhoven, T. Ressler, F.M. de Groot, A. Knop-Gericke (Eds.) In-situ Spectroscopy of Catalysts, American Scientific Publishers2004, pp. 255-270.

[8] J.R. Lakowicz, Introduction to fluorescence, Principles of fluorescence spectroscopy, Springer1999, pp. 1-23.

[9] B. Herman, V.E. Centonze Frohlich, J.R. Lakowicz, D.B. Murphy, K.R. Spring, M.W. Davidson, Fluorescence microscopy: basic concepts in fluorescence, Florida State University, 2003, pp. 2017.

[10] A. Sharma, S.G. Schulman, Introduction to fluorescence spectroscopy, Wiley Analytical Science, New York, 1999.

[11] W.I. Goldburg, Dynamic light scattering, American Journal of Physics, 67 (1999) 1152-1160.

[12] M. Sartor, Dynamic light scattering to determine the radius of small beads in Brownian motion in a solution, University of California San Diego, 2003, pp. 1-21.

[13] D.B. Williams, C.B. Carter, The Transmission Electron Microscope, in: D.B. Williams, C.B. Carter (Eds.) Transmission Electron Microscopy: A Textbook for Materials Science, Springer US, Boston, MA, 1996, pp. 3-17.

[14] F. Pregl, Quantitative micro-analysis of organic substances, Nobel Lectures, World Scientific Publishing Co., 1923.

[15] T. Li, A.J. Senesi, B. Lee, Small Angle X-ray Scattering for Nanoparticle Research, Chemical Reviews, 116 (2016) 11128-11180.

[16] B. Chu, B.S. Hsiao, Small-Angle X-ray Scattering of Polymers, Chemical Reviews, 101 (2001) 1727-1762.

[17] A. Guinier, La diffraction des rayons X aux très petits angles : application à l'étude de phénomènes ultramicroscopiques, Ann. Phys., 11 (1939) 161-237.

[18] A. Guinier, G. Fournet, K.L. Yudowitch, Small-angle scattering of X-rays, (1955).

[19] D.I. Svergun, M.H.J. Koch, Small-angle scattering studies of biological macromolecules in solution, Reports on Progress in Physics, 66 (2003) 1735-1782.

[20] B. Hammouda, Small-Angle Scattering From Branched Polymers, Macromolecular Theory and Simulations, 21 (2012) 372-381.

[21] S. Vyazovkin, Thermogravimetric Analysis, Characterization of Materials2012, pp. 1-12.

[22] T.J. Manning, W.R. Grow, Inductively coupled plasma-atomic emission spectrometry, The chemical educator, 2 (1997) 1-19.

[23] G. Binnig, C.F. Quate, C. Gerber, Atomic Force Microscope, Physical Review Letters, 56 (1986) 930-933.

[24] D. Rugar, P. Hansma, Atomic force microscopy, Physics today, 43 (1990) 23-30.

[25] P. Eaton, P. West, Atomic force microscopy, Oxford university press2010.

[26] J.C. Li, Y. Wang, D.C. Ba, Characterization of Semiconductor Surface Conductivity by Using Microscopic Four-Point Probe Technique, Physics Procedia, 32 (2012) 347-355.

[27] A.P. Schuetze, W. Lewis, C. Brown, W.J. Geerts, A laboratory on the four-point probe technique, American Journal of Physics, 72 (2004) 149-153.

Chapter 3: Size of Elastic Single-Chain Nanoparticles in Solution and on Surfaces

3.1. Motivation

To understand the complexity of single-chain polymer nanoparticles (SCNPs) as intricate soft nano-objects with potential applications in a variety of fields we can make use of physical models of different complexity degrees. In this Chapter, a simple model of SCNPs that allows one to reproduce the structure of these nano-objects both in solution and on surfaces is developed. The model deals with SCNPs with covalent (permanent) intra-chain bonds.

3.2. Introduction

The folding of individual synthetic polymer chains (precursors) to single-chain polymer nanoparticles (SCNPs) is reminiscent of protein folding to its functional, native state and is attracting significant interest in recent years [1-3]. The self-folding process can be driven by different intramolecular interactions such as noncovalent, covalent, and dynamic covalent bonds by using well-defined precursors decorated with appropriate functional groups and experimental conditions such that inter-chain coupling events are minimized to a large extent [4-13]. The resulting SCNPs are useful soft nano-objects with potential applications in nanomedicine [14-17], biosensing [18, 19], and catalysis [20-23], among other different fields. [24-39] Theoretical models providing a connection between both the amount of functional groups, x, and precursor molar mass, M, with the size of the resulting SCNPs are of great interest to establish useful structure—property relationships. In particular, relevant parameters for end-use applications such as surface area, intrinsic viscosity, and diffusion coefficient do depend on SCNP size.

Recently, a model providing the expected size reduction upon folding single chains of size R0 to SCNPs of size R by means of reversible interactions (noncovalent bonds) as a function of x and M has been introduced [40]. This simple model affords a valuable a priori estimation of the size reduction upon folding single chains to conventional SCNPs via reversible interactions (~7% of average deviation of calculated data from experimental ones; 72 SCNPs and 22 reversible interactions analysed). In spite of such advance in providing useful structure-property relationships for developing practical applications of responsive SCNPs, to the best of our knowledge no equivalent model has been yet reported for the case of covalent-bonded SCNPs.

When compared to reversible SCNPs, the structure of covalent-bonded SCNPs includes permanent intramolecular cross-links that affect to a large extent the final compaction degree achieved [40, 41] and provide them with superior thermal stability. Hence, covalent-bonded SCNPs in solution with similar nature, M, and x than reversible SCNPs do display, on average, a higher level of chain compaction [40]. In this work, we introduce a simple model of covalent-bonded SCNPs by considering these intra-chain cross-linked nano-objects as elastic unimolecular networks composed of elastic strands connected by cross-links [42]. We derive scaling law expressions for the size, diffusion coefficient, apparent molar mass, and shrinking factor of elastic SCNPs in good, theta, and bad solvents. Also, we obtain scaling laws for the height of elastic SCNPs deposited on both low- and high-surface free energy substrates.

3.3. Theoretical section

3.3.1. Model of elastic single-chain nanoparticles

We consider a SCNP precursor of total degree of polymerization N and root-mean-square size R_0 containing two different monomers distributed randomly along the chain: reactive monomers of type A and unreactive monomers of type B. The number fraction of A monomers in the precursor is x. Let us assume that the precursor follows a scaling law such as [42]:

(3.1)

$$R_0 \approx a_0 N^{\nu_0}$$

where a_0 is proportional to the monomer size and ν_0 is the corresponding scaling exponent. For the precursor in good solvent conditions, $\nu_0 = \nu_F = 3/5 = 0.6$ (0.588 according to renormalization group theory) [42].

Upon SCNP formation in a solvent at high dilution via intra-chain covalent bonds, the A monomers are expected to dimerise to produce cross-links of type A-A. By working at very high dilution, the nature of the cross-linking should be intramolecular due to isolation of each individual chain under such conditions. Each resulting SCNP can be regarded as a network of elastic strands connected by cross-links (see Figure 3.1).
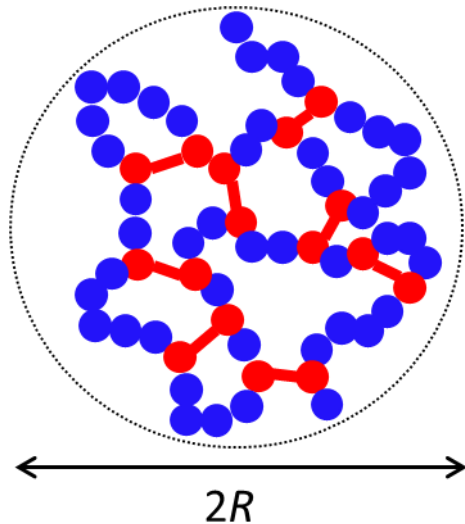
Figure 3.1. *Schematic illustration of an elastic single-chain nanoparticle (SCNP) regarded as a network of elastic strands connected by crosslinks.*

The free energy (F) of such SCNP of size R is decomposed into two contributions: (i) an elastic free energy (F_{el}) arising from the presence of the elastic strands and (ii) an excluded volume contribution (F_{ex}) from the balance of monomer$-$monomer and monomer$-$solvent interactions, such as:

(3.2)

$$F = F_{el} + F_{ex}$$

The elastic free energy can be expressed as:

(3.3)

$$\frac{F_{el}}{k_B T} \approx \frac{3}{2} \frac{R^2}{R_0^2} + KR^2 = \left(\frac{3}{2R_0} + Ax \right) R^2$$

where k_B is the Boltzmann constant, T the absolute temperature, and K an effective constant related to the elasticity of the unimolecular network. We assume that K is proportional to x where A is the corresponding proportionality constant.

When $x \to 0$, equation (3.3) reduces to the Flory expression for a linear chain [42]. For elastic SCNPs equation (3.3) becomes:

(3.4)

$$\frac{F_{el}}{k_B T} \approx KR^2 = AxR^2$$

by assuming $K \gg 3/(2R_0^2)$, which is a good approximation (see section 3.4.4). An expression similar to equation (3.4) was originally introduced by Vilgis [44] for the case of soft micro-gels in the presence of excluded volume interactions.

The excluded volume contribution to the free energy can be expressed as a virial expansion of ρ [43]:

(3.5)

$$\frac{F_{ex}}{k_B T} \approx \frac{N}{2} (\rho B + \rho^2 C + \cdots)$$

where $\rho \propto N/R^3$ and B, C, ... are effective second, third, ... virial coefficients of the monomer interaction. The first term in equation (3.5) corresponds to the excluded volume coefficient ($B > 0$ in a good solvent, $B = 0$ in a θ-solvent, and $B < 0$ in a bad solvent). The second term in equation (3.5) accounts for three-body interactions ($C > 0$).

The equilibrium configuration of the elastic SCNP is obtained by minimizing equation (3.2) with respect to R, so:

(3.6)

$$2AxR - 3 \left(\frac{BN^2}{2R^4} + \frac{CN^3}{R^7} \right) = 0$$

Equation (3.6) will be used in next section to derive useful expressions relating the relative amount of reactive monomers, x, and precursor molecular weight, M, with the size, R, and diffusion coefficient, D, of elastic SCNPs in solvents of different quality.

3.3.2. Size, diffusion coefficient, apparent molar mass, and shrinking factor of elastic single-chain nanoparticles in solution

3.3.2.1. Good solvent conditions

Size

In good solvent ($B > 0$) the third term in equation (3.6) can be neglected, so we obtain the following scaling law for the size of the elastic SCNP:

(3.7)

$$R = a_1 x^{-1/5} N^{2/5} = b_1 x^{-1/5} M^{2/5} = b_1 x^{\omega_1} M^{\nu_1}$$

where $a_1 \equiv \left(\frac{3B}{4A}\right)^{1/5}$, $b_1 \equiv \left(\frac{3B}{4Am_0^2}\right)^{1/5}$, $m_0 = \frac{M}{N}$, and M is the molar mass. Consequently, the elastic SCNP has a scaling exponent ($\nu_1 = 2/5 = 0.4$) smaller than that of a linear chain in a good solvent ($\nu_0 \approx 3/5 = 0.6$). The same value of scaling exponent was previously derived for the case of soft micro-gels in the presence of excluded volume interactions [44]. A ratio of radius of gyration (R_g) to hydrodynamic radius (R_h) very close to 1 is expected for chains having $\nu = 0.4$ (see Figure 3.2).

The R_g/R_h ratio as a function of ν can be estimated from [45, 46]:

(3.8)

$$R_g = \frac{b}{\sqrt{(2\nu + 1)(2\nu + 2)}} N^\nu$$

(3.9)

$$R_h = \frac{\pi(1 - \nu)(2 - \nu)b}{2\sqrt{6}\pi} N^\nu$$

(3.10)

$$\frac{R_g}{R_h} = \frac{2\sqrt{6}}{(1 - \nu)(2 - \nu)\sqrt{\pi(2\nu + 1)(2\nu + 2)}}$$

where b is the segment length. It is worth of mention that for compact globules ($\nu = 1/3$) the exact value of R_g/R_h is $3/5 \approx 0.775$.

Figure 3.2 illustrates the values of R_g/R_h ratio for $\nu = 3/5$, $\nu = 1/2$, and $\nu = 1/3$. Both for $\nu = 2/5 = 0.4$ and $\nu = 3/8 = 0.375$ a value of R_g/R_h ratio very close to 1 is expected.
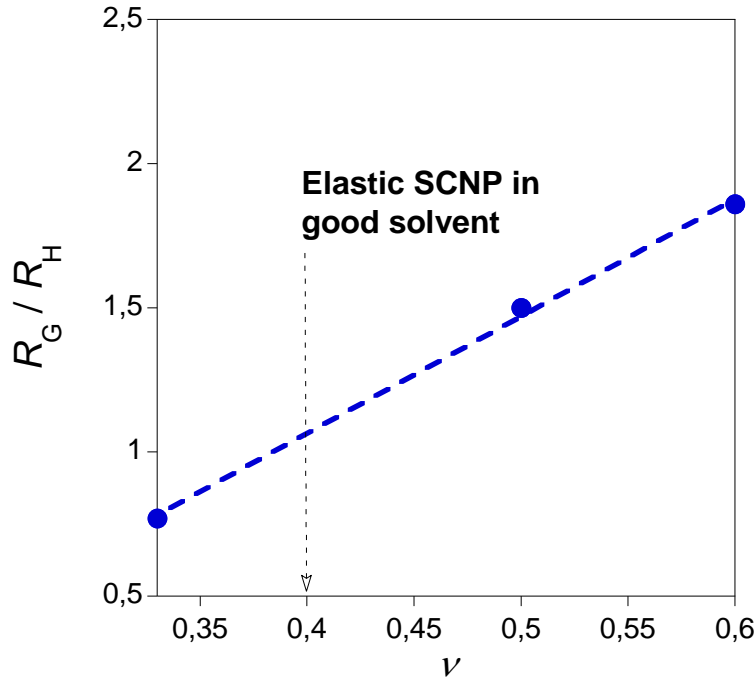

Figure 3.2. R_g/R_h ratio as a function of the scaling exponent ν.

Hence, equation (3.7) should be valid for R_g as well as for R_h data. It is worth of mention that the size of elastic SCNPs scales with the relative amount of reactive monomers, x, with an exponent $\omega_1 = -1/5 = -0.2$. According to equation (3.7), the size of the elastic SCNP depends on the ratio of the excluded volume coefficient B to the effective elastic constant A, with a value of scaling exponent of 1/5.

Diffusion coefficient

By assuming $R_g/R_h \approx 1$, we can use the Stokes-Einstein equation [42] to obtain an expression for the diffusion coefficient (D) of elastic SCNPs in good solvent as a function of x and M, such as:

(3.11)

$$D = \frac{k_B T}{6\pi\eta R} = d_1 x^{1/5} N^{-2/5} = e_1 x^{1/5} M^{-2/5}$$

where $d_1 \equiv \left(\frac{k_B T}{6\pi\eta a_1}\right)$, $e_1 \equiv \left(\frac{k_B T}{6\pi\eta b_1}\right)$, and η is the viscosity of the solvent.

Apparent molar mass

Size exclusion chromatography (SEC) allows determining the apparent molar mass of SCNPs, referred to the molar mass of linear polymer standards. In SEC experiments, macromolecules are separated according to their respective hydrodynamic radius [47]. The hydrodynamic size of a linear polymer standard is related to its molar mass according to:

(3.12)

$$R_h \approx c_0 M^{\nu_0}$$

where c_0 is a constant. According to equations (3.7) and (3.12), an elastic SCNP of size R prepared from a precursor of molar mass M and relative amount of reactive monomers x will have a SEC apparent molecular weight (M_{app}) given by [48]:

(3.13)

$$b_1 x^{\omega_1} M^{\nu_1} \approx c_0 M_{app}^{\nu_0}$$

and hence:

(3.14)

$$M_{app} = f_1 x^{\alpha_1} M^{\beta_1}$$

where $f_1 \equiv \left(\frac{b_1}{c_0}\right)^{1/\nu_0}$, $\alpha_1 = \omega_1/\nu_0$, and $\beta_1 = \nu_1/\nu_0$. For $\nu_0 = 3/5$, we obtain $\alpha_1 = -1/3 \approx -0.33$ and $\beta_1 = 2/3 \approx 0.67$ so equation (3.14) becomes:

(3.15)

$$M_{app} = f_1 x^{-1/3} M^{2/3}$$

Shrinking factor

The shrinking factor is defined as $\langle G \rangle = M_{app}/M$. Consequently, by using equation (3.14), we obtain:

(3.16)

$$\langle G \rangle = f_1 x^{\alpha_1} M^{\beta_1 - 1}$$

For $\nu_0 = 3/5$ equation (3.16) becomes:

(3.17)

$$\langle G \rangle = f_1 x^{-1/3} M^{-1/3}$$

3.3.2.2. Theta solvent conditions

Size

In a theta solvent, the second term in equation (3.6) vanishes ($B = 0$) so we obtain the following expression for the size of the elastic SCNP:

(3.18)

$$R = a_2 x^{-1/8} N^{3/8} = b_2 x^{-1/8} M^{3/8} = b_2 x^{\omega_2} M^{\nu_2}$$

where $a_2 \equiv \left(\frac{3C}{2A}\right)^{1/8}$ and $b_2 \equiv \left(\frac{3C}{2Am_0{}^3}\right)^{1/8}$. As expected, a smaller scaling law exponent (ν_2 = 3/8 = 0.375) is obtained for the elastic SCNP in theta solvent than that in good solvent. In this case, the size of elastic SCNPs scales with x with a smaller exponent $\omega_2 = 1/8 = -0.125$. Equation (3.18) should be also valid for R_g as well as for R_h data (see Figure 3.2). In this case, the size of the elastic SCNP depends on the ratio of the coefficient of three-body interactions C to the effective elastic constant A, with a value of scaling exponent of 1/8.

Diffusion coefficient

By assuming $R_g/R_h \approx 1$, the diffusion coefficient of an elastic SCNP in theta solvent is given by:

(3.19)

$$D = \frac{k_B T}{6\pi\eta R} = d_2 x^{1/8} N^{-3/8} = e_2 x^{1/8} M^{-3/8}$$

where $d_2 \equiv \left(\frac{k_B T}{6\pi\eta a_2}\right)$ and $e_2 \equiv \left(\frac{k_B T}{6\pi\eta b_2}\right)$.

Apparent molar mass

For an elastic SCNP in theta solvent, M_{app} is given by:

(3.20)

$$M_{app} = f_2 x^{\alpha_2} M^{\beta_2}$$

where $f_2 \equiv \left(\frac{b_2}{c_0}\right)^{1/\nu_0}$, $\alpha_2 = \omega_2/\nu_0$, and $\beta_2 = \nu_2/\nu_0$. For $\nu_0 = 3/5$, we obtain α_2 = -5/24 ≈ -0.21 and β_2 = 5/8 ≈ 0.63 so equation (3.20) becomes:

(3.21)

$$M_{app} = f_2 x^{-5/24} M^{5/8}$$

Shrinking factor

The shrinking factor of an elastic SCNP in theta solvent is given by:

(3.22)

$$\langle G \rangle = f_2 x^{\alpha_2} M^{\beta_2 - 1}$$

For $\nu_0 = 3/5$ equation (3.22) becomes:

(3.23)

$$\langle G \rangle = f_2 x^{-5/24} M^{-3/8}$$

3.3.2.3. Bad solvent conditions
Size
In bad solvent $B < 0$, so the size of the elastic SCNP can be approximated by:

(3.24)

$$R = a_3 N^{1/3} = b_3 M^{1/3} = b_3 M^{\nu_3}$$

where $a_3 \equiv \left(\frac{3C}{|B|}\right)^{1/3}$ and $b_3 \equiv \left(\frac{3C}{|B|m_0}\right)^{1/3}$. In this case, the size of elastic SCNPs scales with N with the expected exponent for globules ($\nu_3 = 1/3 \approx 0.33$), and no dependence of R on x is predicted.

Diffusion coefficient
It is well-known that for compact globules $R_g/R_h = \sqrt{3/5} \approx 0.775$, so the diffusion coefficient of an elastic SCNP in bad solvent becomes:

(3.25)

$$D = \frac{k_B T}{6\pi\eta R} = d_3 N^{-1/3} = e_3 M^{-1/3}$$

where $d_3 \equiv \left(\frac{\sqrt{3}k_B T}{6\sqrt{5}\pi\eta a_3}\right)$ and $e_3 \equiv \left(\frac{\sqrt{3}k_B T}{6\sqrt{5}\pi\eta b_3}\right)$.

Apparent molar mass
For an elastic SCNP in bad solvent, M_{app} is given by:

(3.26)

$$M_{app} = f_3 M^{\beta_3}$$

where $f_3 \equiv \left(\frac{b_3}{c_0}\right)^{1/\nu_0}$ and $\beta_3 = \nu_3/\nu_0$. For $\nu_0 = 3/5$, we obtain $\beta_3 = 5/9 \approx 0.56$ so equation (3.26) becomes:

$$(3.27)$$

$$M_{app} = f_3 M^{5/9}$$

<u>*Shrinking factor*</u>

The shrinking factor of an elastic SCNP in bad solvent is given by:

$$(3.28)$$

$$\langle G \rangle = f_3 M^{\beta_3 - 1}$$

For $\nu_0 = 3/5$ equation (3.28) becomes:

$$(3.29)$$

$$\langle G \rangle = f_3 M^{-4/9}$$

3.3.3. Size of elastic single-chain nanoparticles on surfaces

3.3.3.1. Low-surface free energy substrate

Let us consider the case of an elastic SCNP deposited onto a very low-surface free energy substrate. The SCNP is expected to take a compact, globular conformation onto this surface, which allows minimizing the contact between the SCNP and the low-surface energy substrate. The volume of the SCNP should be:

$$(3.30)$$

$$V = \frac{M}{\rho_0 N_A} = \frac{4}{3} \pi R^3$$

where ρ_0 is the bulk density. Consequently, the height ($H = 2R$) of the SCNP will be given by [49]:

$$(3.31)$$

$$H = b_4 M^{1/3}$$

where $b_4 = \left(\frac{6}{\pi \rho_0 N_A} \right)^{1/3}$.

3.3.3.2. High-surface free energy substrate

When compared to the previous case, now the elastic SCNP is expected to spread to some extent over the surface. Let us assume that the SCNP over the substrate adopt a conformation equivalent to that in the melt [50, 51]. Generalization of equation (3.2) to d dimensions for melt and theta solvent conditions gives:

(3.32)

$$\frac{F}{k_B T} \approx AxR^2 + \frac{CN^3}{2R^{2d}}$$

and by minimization of equation (3.32) to:

(3.33)

$$2AxR - \frac{dCN^3}{2R^{2d+1}} = 0$$

Consequently,

(3.34)

$$R = \left(\frac{dC}{2A}\right)^{1/(2d+2)} x^{-1/(2d+2)} N^{3/(2d+2)}$$

We obtain an estimation of the lateral spreading by using equation (3.18) in two dimensions ($d = 2$) such as:

(3.35)

$$R_{II} \propto x^{-1/(2d+2)} M^{3/(2d+2)} \propto x^{1/6} M^{3/6}$$

Since the volume of the elastic SCNP in the high-surface free energy substrate, $V \approx H\,(\pi R_{II}^2)$, should be equal to the volume of the SCNP in a low-surface free energy substrate [equation (3.30)], we obtain:

(3.36)

$$H = g_1\, x^{1/3}$$

where $g_1 \equiv \left[\frac{m_0}{\pi \rho_0 N_A}\left(\frac{C}{A}\right)^{1/3}\right]$ is a constant.

3.3.3.3. Single-chain nanoparticle stretching
From equation (3.4) we obtain the force (f) versus stretching (z) equation of elastic SCNPs such as:

(3.37)

$$f = \frac{\partial F_{el}}{\partial z} \approx (2k_B TAx)z = K_s z$$

where K_s is the effective (x-dependent) spring coefficient. Equation (3.37 could be used to determine the constant A from experimental f vs z curves by AFM of covalent-bonded SCNPs with different amount of reactive groups, x. To the best of our knowledge, such experiments have not been performed yet. For the case of a linear chain ($x \to 0$), the classical result corresponding to the freely jointed chain (FJC) model [52] is obtained from equation (3.3):

(3.38)

$$f = \frac{\partial F_{\text{el}}}{\partial z} \approx \left(\frac{3k_{\text{B}}T}{R_0{}^2} \right) z$$

3.3.4. Summary of scaling laws for elastic single-chain nanoparticles

A summary of the scaling law expressions for elastic SCNP in solution and on solid substrates is given in Table 3.1, as derived by assuming $\nu_0 = 3/5$.

Table 3.1. *Summary of Scaling Law Expressions for Elastic SCNPs (See Text).*

Solution			
Magnitude	**Good solvent**	**Theta solvent**	**Bad solvent**
Size	$R \propto x^{-1/5}M^{2/5}$	$R \propto x^{-1/8}M^{3/8}$	$R \propto M^{1/3}$
Diffusion coefficient	$D \propto x^{1/5}M^{-2/5}$	$D \propto x^{1/8}M^{-3/8}$	$D \propto M^{-1/3}$
Apparent molar mass	$M_{app} \propto x^{-1/3}M^{2/3}$	$M_{app} \propto x^{-5/24}M^{5/8}$	$M_{app} \propto M^{5/9}$
Shrinking factor	$\langle G \rangle \propto x^{-1/3}M^{-1/3}$	$\langle G \rangle \propto x^{-5/24}M^{-3/8}$	$\langle G \rangle \propto M^{-4/9}$
Solid Substrate			
	Low Surface Free Energy		**High Surface Free Energy**
Height	$H \propto M^{1/3}$		$H \propto x^{1/3}$
Nanoparticle Stretching			
Spring Coefficient	$K_s \propto x$		

3.4. Results and discussion

3.4.1. Comparison to experimental results

The most accurate compilation of size data for covalent-bonded SCNPs is due to Hawker and co-workers [49, 53] corresponding to polystyrene (PS)-SCNPs (see Table 3.2 and Table 3.3). The intra-chain cross-linking process was carried out at high temperature (250 °C) by using precursors with highly reactive benzocyclobutene functional groups. In particular, a large set of size data in solution (THF as solvent) was reported corresponding to precursors of narrow molecular weight distribution ($1.09 \leq Đ \leq 1.26$), different amount of reactive groups ($0.025 \leq x \leq 0.3$), and varying precursor molar mass ($44 \leq M \leq 235$ kDa) [53]. Size characterization of the resulting covalent-bonded PS-SCNPs was carried out by SEC in THF. Moreover, the absolute molar mass by static light scattering (SLS) of the PS-SCNPs of higher molar mass ($M = 230$ kDa) was found to be in agreement, within experimental error, with the molar mass by SEC of the corresponding linear precursor ($M = 234$ kDa), supporting the formation of discrete nanoparticles each composed of a single chain. Concerning size data on surfaces (mica and silanized wafer substrates), they cover data from precursors of $Đ$ between 1.04 and 1.91, molar mass between 33.0 and 211 kDa, and amount of reactive groups between 0.025 and 0.60 [49].

In section 3.4.2, we perform a comparison of the experimental data from Table 3.2 with model predictions corresponding to elastic SCNPs in good, theta, and bad solvent conditions. For the same system, a similar comparison of experimental and theoretical H data corresponding to SCNPs deposited on low and high-energy substrates (Table 3.3) is carried out in section 3.4.3. Comparison of model predictions to experimental data for SCNPs different from those given in Table 3.2 and Table 3.3 is performed in section 3.4.5. Relevant information about the conformation of SCNPs in solution and on solid substrates can be found in refs [41] and [49], respectively.

3.4.2. Size, diffusion coefficient, apparent molar mass, and shrinking factor of polystyrene single-chain nanoparticles in tetrahydrofuran

We investigate the ability of the elastic SCNP model corresponding to good, theta, and bad solvent conditions [equations (3.14), (3.20) and (3.26), respectively] to reproduce the M_{app} data from Table 3.2 as a function of x and M, by using the values in equation (3.12) corresponding to PS standards in THF ($c_0 = 1.44 \times 10^{-2}$, $v_0 = 0.561$) [54]. Best fitting of the M_{app} data to equation (3.14) corresponding to elastic SCNPs in good solvent gives $f_1 = 5.95$, $b_1 = c_0 f_1^{v_0} = 3.92 \times 10^{-2}$, and $B/A = (4/3)(b_1^5 m_0^2) = 1.33 \times 10^{-3}$. Average deviation of data calculated from $M_{app} = 5.95 x^{-0.357} M^{0.713}$ and experimental M_{app} data was only 4.2% (see Figure 3.3 A). Conversely, best-fitting the M_{app} data to equations (3.20) and (3.26), corresponding to theta and bad solvent conditions, gives average deviation of calculated and experimental M_{app} data of 13.0% and 33.4%, respectively (Figure 3.3 B, C). Hence, as illustrated in Figure 3.3, the observed experimental trend is only reproduced with reasonable accuracy by the elastic SCNP model for the case of good solvent conditions, as it is expected for the case of THF solutions. The description is fairly achieved in terms of a single model parameter (the ratio of the excluded volume coefficient B to the effective elastic constant A).

Table 3.2. Summary of Size Data for PS–SCNPs in THF [53].

Precursors			SCNPs			
x	M (kDa)	$Đ$	M_{app} (kDa)	$<G>$	R^a (nm)	D^b (nm²/ s)
0.025	44.0	1.09	41.7	0.95	5.6	85
0.050	44.5	1.08	38.2	0.86	5.4	88
0.10	45.5	1.09	29.1	0.64	4.6	103
0.15	43.5	1.10	20.7	0.48	3.8	125
0.20	44.0	1.07	18.5	0.42	3.6	132
0.0125	110.5	1.15	103.0	0.93	9.3	51
0.025	113.0	1.12	94.5	0.84	8.9	53
0.050	109.0	1.14	79.3	0.73	8.1	59
0.075	108.0	1.15	59.8	0.55	6.9	69
0.10	112.0	1.10	56.0	0.50	6.6 (6.2)	72 (77)
0.15	110.0	1.16	44.2	0.40	5.8	82
0.20	111.0	1.11	42.8	0.39	5.7	83
0.25	112.0	1.12	40.5	0.36	5.5	86
0.0125	231.0	1.23	189.8	0.82	13.2	36
0.025	235.0	1.25	174.0	0.74	12.5	38
0.050	228.0	1.22	109.0	0.48	9.6	49
0.075	230.0	1.19	98.0	0.43	9.1	52
0.10	233.0	1.26	91.5	0.39	8.7 (9.5)	55 (50)
0.125	231.0	1.24	81.0	0.35	8.2	58
0.15	235.0	1.23	80.3	0.34	8.1	59
0.20	230.0	1.21	66.0	0.29	7.3	65

Precursors			SCNPs			
x	M (kDa)	$Đ$	M_{app} (kDa)	$<G>$	R^a (nm)	D^b (nm²/ s)
0.25	229.0	1.24	62.0	0.27	7.0 (6.4)	68 (74)
0.3	234.0	1.23	63.5	0.27	7.1	32

[a]Calculated from [53]. R_h (nm) = 1.44 × 10^{-2} $M^{0.561}$. Data from DLS are shown in parentheses.

[b]Calculated from $D = k_B T/6\pi\eta R_h$. Data from DLS are shown in parentheses.
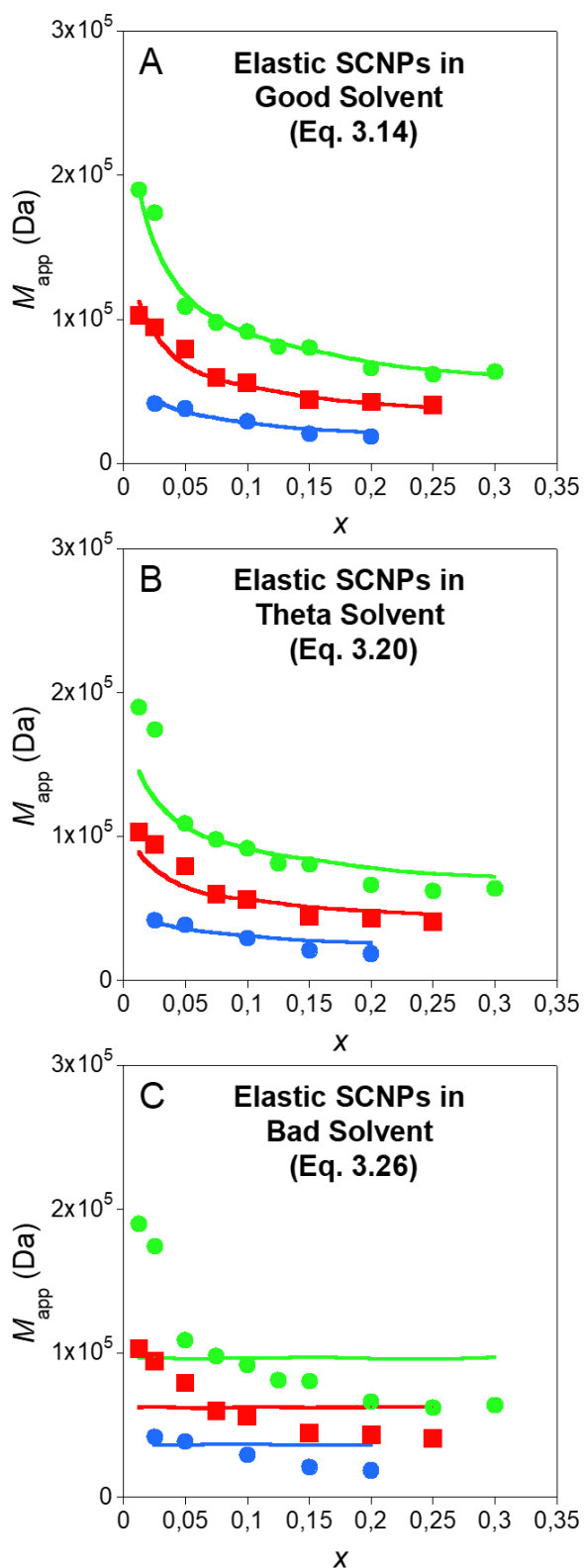
Figure 3.3. M_{app} data of PS-SCNPs in THF (solid green circles: M = 232 kDa; solid red squares: M = 111 kDa; and solid blue circles: M = 44 kDa).[53] The same data are described by the elastic SCNPs model (solid green, red, and blue lines, respectively), assuming the case of good solvent conditions (**A**), theta solvent conditions (**B**), and bad solvent conditions (**C**). The experimental trend is only reproduced by the elastic SCNP model for good solvent conditions in terms of a single model parameter.

Figure 3.4 provides a comparison of calculated size, diffusion coefficient, and shrinking factor to experimental data reported in Table 3.2 according to the elastic SCNP model for good solvent conditions.
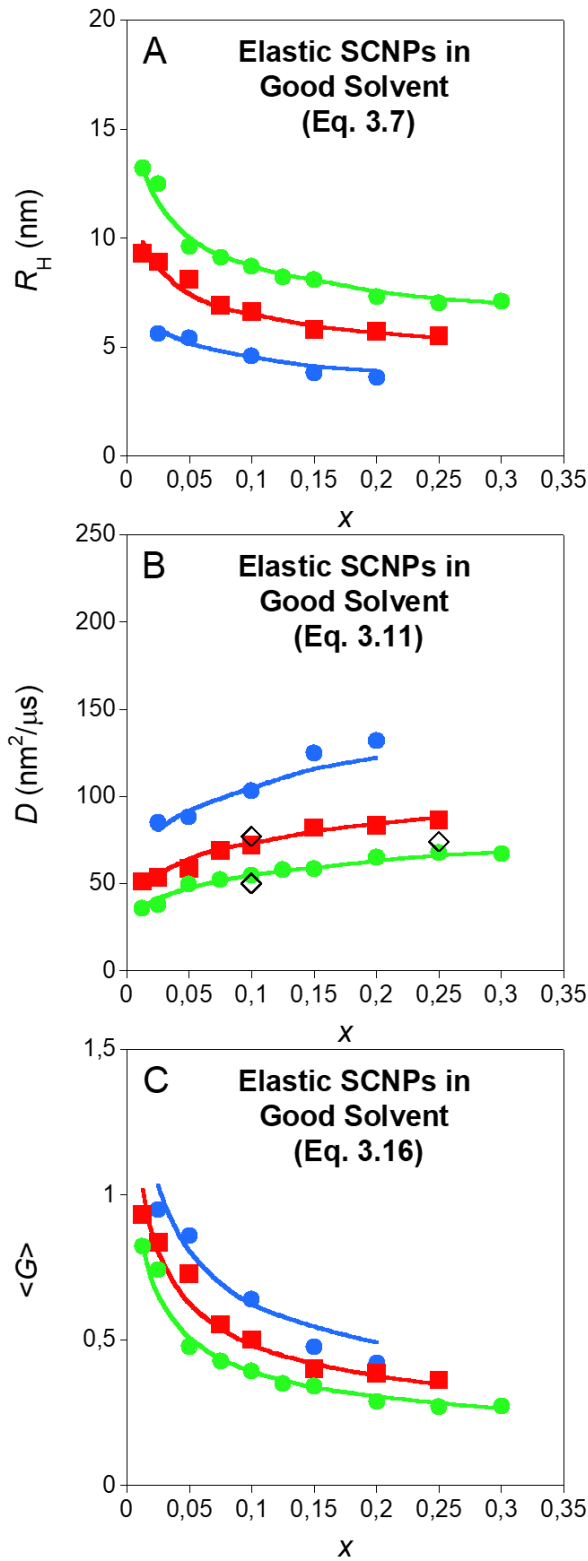
Figure 3.4. *Comparison of calculated size (R_h) **(A)**, diffusion coefficient (D) **(B)**, and shrinking factor (⟨G⟩) **(C)** from the elastic SCNP model corresponding to good solvent conditions to experimental data from Table 3.2.[53] Closed symbols and continuous lines have the same meaning as in Figure 3.3. Open symbols correspond to data from dynamic light scattering (DLS) experiments.*
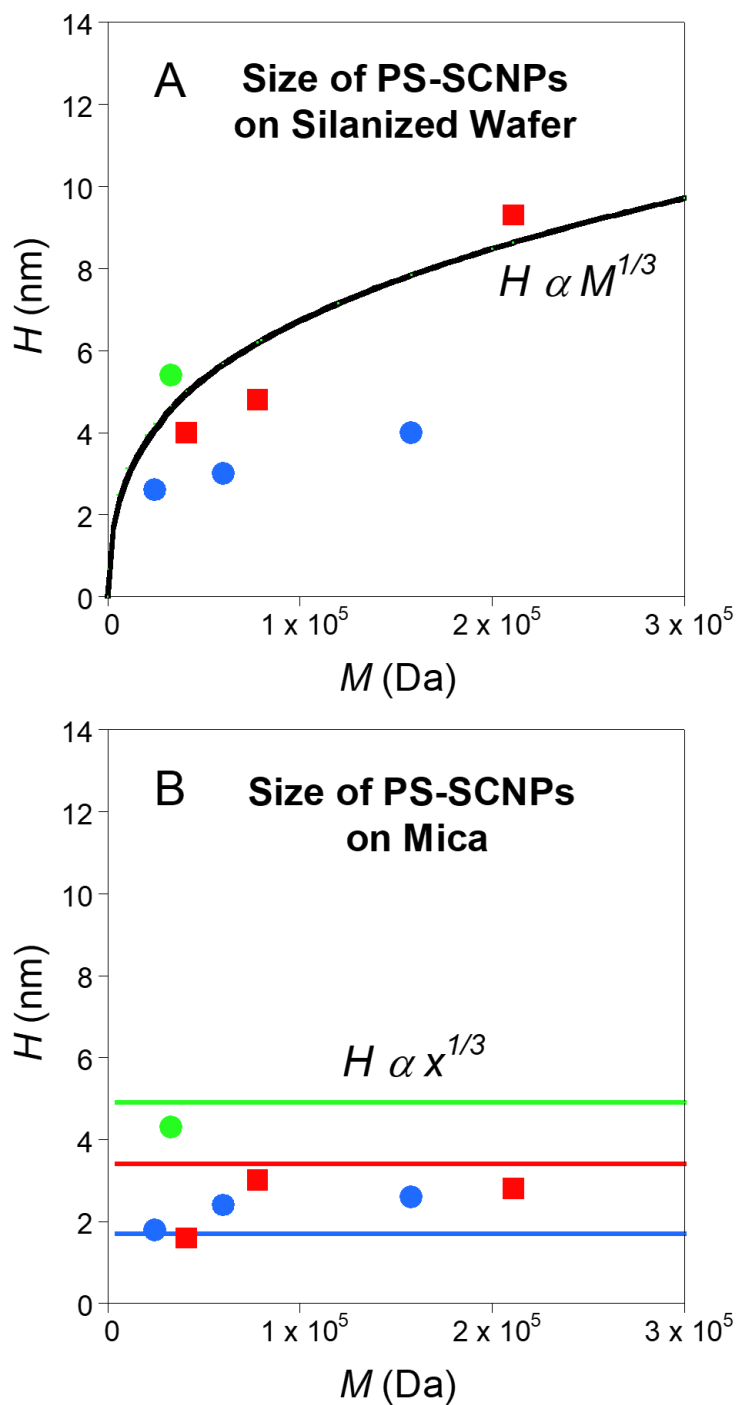
3.4.3. Size of polystyrene single-chain nanoparticles on silanized wafer and mica substrates

A comparison of predictions from the elastic SCNP model and experimental size data for PS-SCNPs [48] deposited onto substrates of different surface free energy is illustrated in Figure 3.5. On a low-free energy substrate such as the silanized wafer surface, PS-SCNPs with $x =$ 0.2 and 0.6 behave as solid globules, a result previously reported by Dukette *et al.* [49]. It is worth of mention that departure from the globular conformation is observed for PS-SCNPs with very low amount of reactive functional groups ($x = 0.025$).

Table 3.3. Summary of Size Data for PS–SCNPs on Silanized Wafer and Mica Substrates [49].

PS-SCNPs			H (nm)	
x	M (kDa)	$Đ$	Silanized Wafer Substrate	Mica Substrate
0.025	24.5	1.14	2.6	1.8
0.025	60.1	1.16	3.0	2.4
0.025	158	1.40	4.0	2.6
0.20	41.0	1.04	4.0	1.6
0.20	78.0	1.14	4.8	3.0
0.20	211	1.32	9.3	2.8
0.60	33.0	1.91	5.4	4.3

Figure 3.5 B shows the ability of the elastic SCNP model to reproduce the experimental behaviour of PS-SCNPs deposited onto a high-surface energy substrate such as mica [49] in terms of a single parameter (related to the ratio of the third virial coefficient C to the effective elastic constant A). Best fitting of the data in Figure 3.5 B to equation (3.36) gives $g_1 = 5.81$, $C/A = 7.3 \times 10^{-7}$, and $C \approx 3.47 \times 10^{-5}$ by using $A \approx 47.6$ (see section 3.4.4).

Figure 3.5. *Comparison of theoretical predictions from the elastic SCNP model to experimental size data of PS-SCNPs48 (solid blue circles: x = 0.025; solid red squares: x = 0.20; and solid green circles: x = 0.60) on **(A)** low-and **(B)** high-surface free energy substrates (see text and Table 4). Solid green, red, and blue lines are the predicted behaviour for x = 0.025, 0.20, and 0.60, respectively.*

3.4.4. Stretching of polystyrene single-chain nanoparticles

Here we use the elastic SCNP model to estimate the force (f) versus stretching (z) curves for PS-SCNPs at low values of z.

From equations (3.3) (with $x = 0$) and (3.5) ($B > 0$) and taking into account that $R_g/R_h \approx$ 1.86 for $\nu = 3/5$, we obtain:

$$(3.39)$$

$$B \approx \frac{2}{b^2}(1.86 \times c_0)^5 m_0{}^3$$

where $b \approx 0.7$ [55], $c_0 = 1.44 \times 10^{-2}$, and $m_0 = 104$ so $B \approx 6.33 \times 10^{-2}$ for PS in THF.

By using $B/A = 1.33 \times 10^{-3}$ (see section 3.4.2) and $B \approx 6.33 \times 10^{-2}$, the estimated value of A is 47.6, which guarantees the condition $K = Ax \gg 3/(2R_0^2)$ [see equation (3.4)] even for the lower values of M and x of Table 3.2 and Table 3.3.

Figure 3.6 shows the predicted force (f) versus stretching (z) curves for PS-SCNPs of different values of x in the regime of low deformations according to equation (3.37). The corresponding values of the effective spring constant are $K_s = 9.8$, 19.6, 39.2, 117.5, and 235.0 for $x = 0.025$, 0.05, 0.10, 0.30, and 0.60, respectively.
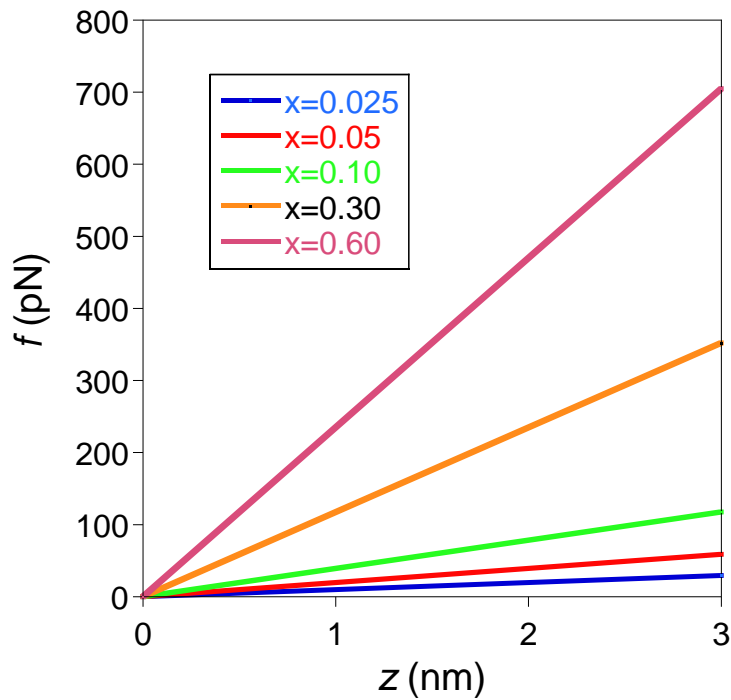
Figure 3.6. *Predicted force (f) versus stretching (z) curves for PS− SCNPs of different values of x at low deformation.*

3.4.5. Comparison of model predictions to experimental data for other covalent-bonded SCNPs

3.4.5.1. SCNP Size in Good Solvent Conditions

We are interested to investigate the predictive possibilities of the model for covalent-bonded PS-SCNPs obtained from other different cross-linking techniques and also for

covalent-bonded SCNPs of other chemical composition (e.g., methacrylate- and acrylate-based SCNPs).

Figure 3.7 provides a comparison of experimental R_h data and calculated ones from R_h (nm) = $3.92 \times 10^{-2}\ x^{-1/5}M^{2/5}$ (see section 3.4.2.) for SCNPs in good solvent conditions. Experimental R_H data were taken from ref. [41] corresponding to covalent-bonded PS-SCNPs obtained by several crosslinking techniques different from benzocyclobutene dimerization as well as covalent-bonded poly(methyl methacrylate) (PMMA)- and poly(alkyl acrylate) (PAA)-based SCNPs. The overall average standard deviation between calculated and experimental size data is 11%, which is quite reasonable by taking into account that both the effective excluded volume coefficient B and the effective elastic constant A could change depending on the specific chemical nature of the reactive functional groups and monomer repeat units (styrene vs (meth)acrylate), the overall chain rigidity, etc. When only PS-SCNPs are compared, the average standard deviation between calculated and experimental data reduces to 8.5%.
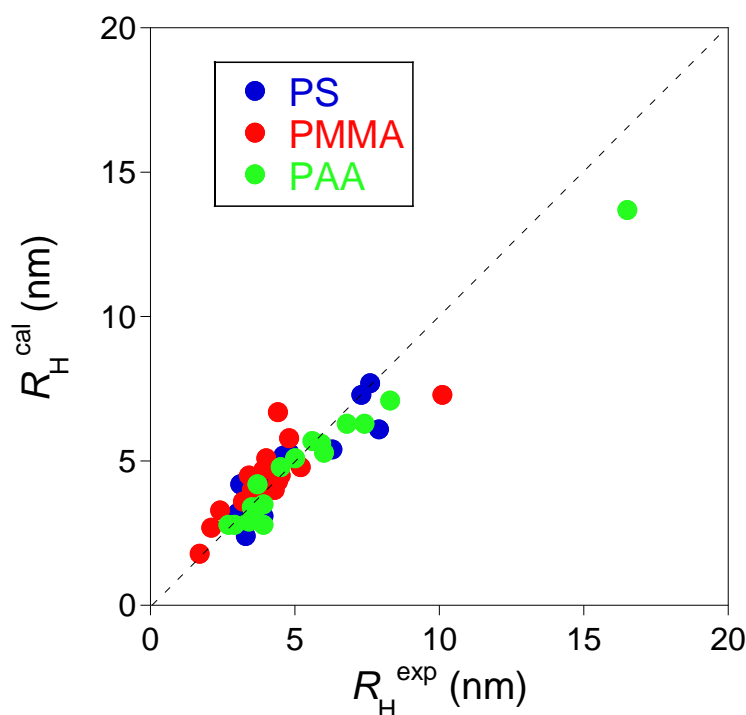
Figure 3.7. *Comparison of experimental R_h data [40] and calculated ones (R_h (nm) = $3.92x^{-1/5}M^{2/5}$, see text) for covalent-bonded PS-SCNPs obtained from several cross-linking techniques different from benzocyclobutene dimerization, as well as covalent-bonded polymethyl methacrylate (PMMA)- and polyalkyl acrylate (PAA)-based SCNPs.*

3.4.5.2. SCNP size on high-surface free energy substrates

A comparison of experimental H data from AFM experiments over mica substrate and calculated ones from H (nm) = $5.81x^{1/3}$ (see section 3.4.3.) is provided in Table 3.4. It is worth of mention that only a reduced number of covalent-bonded SCNPs have been investigated by AFM on mica substrate [16, 49, 56-59]. In spite of the scarce data available, a reasonable agreement is found between predictions and experimental results for covalent-bonded PS-SCNPs obtained by cross-linking techniques different from

benzocyclobutene dimerization [56-58] as well as for covalent-bonded poly(tert-butyl methacrylate) (PtBMA) [59] and poly(methacrylic acid) (PMAA) [16] SCNPs.

Table 3.4. *Comparison of Experimental H Data (H$_{exp}$) and Calculated Ones (H$_{cal}$) for Covalent-Bonded PS–SCNPs Obtained from Cross-Linking Techniques Different from Benzocyclobutene Dimerization as Well as for Covalent-Bonded PtBMA– and PMAA–SCNPs.*

SCNP Type[a]	x	H_{exp}(nm)	H_{cal}(nm)[b]	Ref.
PS	0.09	3.0	2.6	[56]
PS	0.10	1.6, 3.8	2.7	[57]
PS	0.10	1.7	2.7	[58]
PMAA	0.10	2.0	2.7	[16]
PtBMA	0.17	3.5	3.2	[59]

[a]PtBMA = poly(*tert*-butyl methacrylate); PMAA = poly(methacrylic acid).

[b]Calculated from H (nm) = 5.81$x^{1/3}$ (see text).

3.5. Concluding remarks

A simple model of covalent-bonded SCNPs has been developed by considering these soft nano-objects as a network of strands, which behave as elastic springs, connected by crosslinks. Based on this model, scaling law expressions for the size, diffusion coefficient, apparent molar mass, and shrinking factor of elastic SCNPs in good, theta, and bad solvents have been derived as well as scaling laws for the height of elastic SCNPs deposited on both low- and high-surface free energy substrates.

The elastic SCNP model for good solvent conditions reproduces with reasonable accuracy the experimental size, diffusion coefficient, apparent molar mass, and shrinking factor of PS SCNPs in THF as a function of x and M, in terms of a single model parameter (the ratio of the effective excluded volume coefficient B to the effective elastic constant A). The predictions of the elastic SCNP model are found to be in excellent agreement with (i) the approximately constant height of PS-SCNPs of different M on high-surface energy substrates and (ii) the dependence of the height of PS-SCNPs on x, with a theoretical exponent of 1/3 for the case of low-surface energy substrates. Force versus stretching curves for PS-SCNPs of different values of x at low deformation would allow determining experimentally the effective elastic constant A.

To summarize, the simple elastic SCNP model introduced in this Chapter provides a useful framework for connecting the amount of reactive groups and precursor molar mass with the size upon intra-chain cross-linking for a variety of covalent-bonded SCNPs both in solvents of different quality and on substrates of different surface free energy.

3.6. References

[1] J.A. Pomposo, Single-Chain Polymer Nanoparticles: Synthesis, Characterization, Simulations, and Applications, John Wiley & Sons2017.

[2] M. Huo, N. Wang, T. Fang, M. Sun, Y. Wei, J. Yuan, Single-chain polymer nanoparticles: Mimic the proteins, Polymer, 66 (2015) A11-A21.

[3] J.A. Pomposo, Bioinspired single-chain polymer nanoparticles, Polymer International, 63 (2014) 589-592.

[4] S. Mavila, O. Eivgi, I. Berkovich, N.G. Lemcoff, Intramolecular Cross-Linking Methodologies for the Synthesis of Polymer Nanoparticles, Chemical Reviews, 116 (2016) 878-961.

[5] A.M. Hanlon, C.K. Lyon, E.B. Berda, What Is Next in Single-Chain Nanoparticles?, Macromolecules, 49 (2016) 2-14.

[6] O. Altintas, C. Barner-Kowollik, Single-Chain Folding of Synthetic Polymers: A Critical Update, Macromolecular Rapid Communications, 37 (2016) 29-46.

[7] M. Gonzalez-Burgos, A. Latorre-Sanchez, J.A. Pomposo, Advances in single chain technology, Chemical Society Reviews, 44 (2015) 6122-6142.

[8] C.K. Lyon, A. Prasher, A.M. Hanlon, B.T. Tuten, C.A. Tooley, P.G. Frank, E.B. Berda, A brief user's guide to single-chain nanoparticles, Polymer Chemistry, 6 (2015) 181-197.

[9] A. Sanchez-Sanchez, J.A. Pomposo, Single-Chain Polymer Nanoparticles via Non-Covalent and Dynamic Covalent Bonds, Particle & Particle Systems Characterization, 31 (2014) 11-23.

[10] M. Artar, E. Huerta, E.W. Meijer, A.R.A. Palmans, Dynamic Single Chain Polymeric Nanoparticles: From Structure to Function, Sequence-Controlled Polymers: Synthesis, Self-Assembly, and Properties, American Chemical Society2014, pp. 313-325.

[11] A. Sanchez-Sanchez, I. Pérez-Baena, J.A. Pomposo, Advances in Click Chemistry for Single-Chain Nanoparticle Construction, Molecules, 18 (2013) 3339-3355.

[12] O. Altintas, C. Barner-Kowollik, Single Chain Folding of Synthetic Polymers by Covalent and Non-Covalent Interactions: Current Status and Future Perspectives, Macromolecular Rapid Communications, 33 (2012) 958-971.

[13] M.K. Aiertza, I. Odriozola, G. Cabañero, H.-J. Grande, I. Loinaz, Single-chain polymer nanoparticles, Cellular and Molecular Life Sciences, 69 (2012) 337-346.

[14] Y. Bai, H. Xing, G.A. Vincil, J. Lee, E.J. Henderson, Y. Lu, N.G. Lemcoff, S.C. Zimmerman, Practical synthesis of water-soluble organic nanoparticles with a single reactive group and a functional carrier scaffold, Chemical Science, 5 (2014) 2862-2868.

[15] A. Sanchez-Sanchez, S. Akbari, A.J. Moreno, F.L. Verso, A. Arbe, J. Colmenero, J.A. Pomposo, Design and Preparation of Single-Chain Nanocarriers Mimicking Disordered Proteins for Combined Delivery of Dermal Bioactive Cargos, Macromolecular Rapid Communications, 34 (2013) 1681-1686.

[16] I. Perez-Baena, I. Loinaz, D. Padro, I. García, H.J. Grande, I. Odriozola, Single-chain polyacrylic nanoparticles with multiple Gd(iii) centres as potential MRI contrast agents, Journal of Materials Chemistry, 20 (2010) 6916-6922.

[17] S.K. Hamilton, E. Harth, Molecular Dendritic Transporter Nanoparticle Vectors Provide Efficient Intracellular Delivery of Peptides, ACS Nano, 3 (2009) 402-410.

[18] A. Latorre-Sanchez, J.A. Pomposo, A simple, fast and highly sensitive colorimetric detection of zein in aqueous ethanol via zein–pyridine–gold interactions, Chemical Communications, 51 (2015) 15736-15738.

[19] M.A.J. Gillissen, I.K. Voets, E.W. Meijer, A.R.A. Palmans, Single chain polymeric nanoparticles as compartmentalised sensors for metal ions, Polymer Chemistry, 3 (2012) 3166-3174.

[20] C.A. Tooley, S. Pazicni, E.B. Berda, Toward a tunable synthetic [FeFe] hydrogenase mimic: single-chain nanoparticles functionalized with a single diiron cluster, Polymer Chemistry, 6 (2015) 7646-7651.

[21] I. Perez-Baena, F. Barroso-Bujans, U. Gasser, A. Arbe, A.J. Moreno, J. Colmenero, J.A. Pomposo, Endowing Single-Chain Polymer Nanoparticles with Enzyme-Mimetic Activity, ACS Macro Letters, 2 (2013) 775-779.

[22] E. Huerta, P.J.M. Stals, E.W. Meijer, A.R.A. Palmans, Consequences of Folding a Water-Soluble Polymer Around an Organocatalyst, Angewandte Chemie International Edition, 52 (2013) 2906-2910.

[23] T. Terashima, T. Mes, T.F.A. De Greef, M.A.J. Gillissen, P. Besenius, A.R.A. Palmans, E.W. Meijer, Single-Chain Folding of Polymers for Catalytic Systems in Water, Journal of the American Chemical Society, 133 (2011) 4742-4745.

[24] D. Mecerreyes, V. Lee, C.J. Hawker, J.L. Hedrick, A. Wursch, W. Volksen, T. Magbitang, E. Huang, R.D. Miller, A Novel Approach to Functionalized Nanoparticles: Self-Crosslinking of Macromolecules in Ultradilute Solution, Advanced Materials, 13 (2001) 204-208.

[25] B. Zhu, J. Ma, Z. Li, J. Hou, X. Cheng, G. Qian, P. Liu, A. Hu, Formation of polymeric nanoparticles via Bergman cyclization mediated intramolecular chain collapse, Journal of Materials Chemistry, 21 (2011) 2679-2683.

[26] J.A. Kaitz, C.M. Possanza, Y. Song, C.E. Diesendruck, A.J.H. Spiering, E.W. Meijer, J.S. Moore, Depolymerizable, adaptive supramolecular polymer nanoparticles and networks, Polymer Chemistry, 5 (2014) 3788-3794.

[27] G. Li, F. Tao, L. Wang, Y. Li, R. Bai, A facile strategy for preparation of single-chain polymeric nanoparticles by intramolecular photo-crosslinking of azide polymers, Polymer, 55 (2014) 3696-3702.

[28] Y. Liu, T. Pauloehrl, S.I. Presolski, L. Albertazzi, A.R.A. Palmans, E.W. Meijer, Modular Synthetic Platform for the Construction of Functional Single-Chain Polymeric Nanoparticles: From Aqueous Catalysis to Photosensitization, Journal of the American Chemical Society, 137 (2015) 13096-13105.

[29] M. González-Burgos, A. Alegría, A. Arbe, J. Colmenero, J.A. Pomposo, An unexpected route to aldehyde-decorated single-chain nanoparticles from azides, Polymer Chemistry, 7 (2016) 6570-6574.

[30] W. Fan, X. Tong, Q. Yan, S. Fu, Y. Zhao, Photodegradable and size-tunable single-chain nanoparticles prepared from a single main-chain coumarin-containing polymer precursor, Chemical Communications, 50 (2014) 13492-13494.

[31] D.E. Whitaker, C.S. Mahon, D.A. Fulton, Thermoresponsive Dynamic Covalent Single-Chain Polymer Nanoparticles Reversibly Transform into a Hydrogel, Angewandte Chemie International Edition, 52 (2013) 956-959.

[32] M.E. Mackay, T.T. Dao, A. Tuteja, D.L. Ho, B. Van Horn, H.-C. Kim, C.J. Hawker, Nanoscale effects leading to non-Einstein-like decrease in viscosity, Nature Materials, 2 (2003) 762-766.

[33] L. Oria, R. Aguado, J.A. Pomposo, J. Colmenero, A Versatile "Click" Chemistry Precursor of Functional Polystyrene Nanoparticles, Advanced Materials, 22 (2010) 3038-3041.

[34] M.E. Mackay, A. Tuteja, P.M. Duxbury, C.J. Hawker, B. Van Horn, Z. Guan, G. Chen, R.S. Krishnan, General Strategies for Nanoparticle Dispersion, Science, 311 (2006) 1740.

[35] A. Tuteja, P.M. Duxbury, M.E. Mackay, Multifunctional Nanocomposites with Reduced Viscosity, Macromolecules, 40 (2007) 9427-9434.

[36] J.K. Mistry, M.R. Van De Mark, Aziridine cure of acrylic colloidal unimolecular polymers (CUPs), Journal of Coatings Technology and Research, 10 (2013) 453-463.

[37] J.A. Pomposo, A.R. de Luzuriaga, I. García, A. Etxeberria, J. Colmenero, A Nanotechnology Pathway to Arresting Phase Separation in Soft Nanocomposites, Macromolecular Rapid Communications, 32 (2011) 573-578.

[38] A. Arbe, J.A. Pomposo, I. Asenjo-Sanz, D. Bhowmik, O. Ivanova, J. Kohlbrecher, J. Colmenero, Single Chain Dynamic Structure Factor of Linear Polymers in an All-Polymer Nano-Composite, Macromolecules, 49 (2016) 2354-2364.

[39] Y. Zhang, H. Zhao, Surface-tunable colloidal particles stabilized by mono-tethered single-chain nanoparticles, Polymer, 64 (2015) 277-284.

[40] J.A. Pomposo, J. Rubio-Cervilla, A.J. Moreno, F. Lo Verso, P. Bacova, A. Arbe, J. Colmenero, Folding Single Chains to Single-Chain Nanoparticles via Reversible Interactions: What Size Reduction Can One Expect?, Macromolecules, 50 (2017) 1732-1739.

[41] J.A. Pomposo, I. Perez-Baena, F. Lo Verso, A.J. Moreno, A. Arbe, J. Colmenero, How Far Are Single-Chain Polymer Nanoparticles in Solution from the Globular State?, ACS Macro Letters, 3 (2014) 767-772.

[42] M. Rubinstein, R.H. Colby, Polymer physics, Oxford University Press, New York, 2003.

[43] P.G. De Gennes, Collapse of a polymer chain in poor solvents, J. Physique Lett., 36 (1975) 55-57.

[44] T.A. Vilgis, Crosslinked polymer chains with excluded volume: A new class of branched polymers?, Macromolecular Theory and Simulations, 7 (1998) 59-63.

[45] A.Z. Akcasu, M. Benmouna, Concentration Effects on the Dynamic Structure Factor in Polymer Solutions, Macromolecules, 11 (1978) 1193-1198.

[46] B. Hammouda, SANS from homogeneous polymer mixtures: A unified overview, Polymer Characteristics, Springer Berlin Heidelberg, Berlin, Heidelberg, 1993, pp. 87-133.

[47] S. Podzimek, Light scattering, size exclusion chromatography and asymmetric flow field flow fractionation: powerful tools for the characterization of polymers, proteins and nanoparticles, John Wiley & Sons2011.

[48] J.A. Pomposo, I. Perez-Baena, L. Buruaga, A. Alegría, A.J. Moreno, J. Colmenero, On the Apparent SEC Molecular Weight and Polydispersity Reduction upon Intramolecular Collapse of Polydisperse Chains to Unimolecular Nanoparticles, Macromolecules, 44 (2011) 8644-8649.

[49] T.E. Dukette, M.E. Mackay, B. Van Horn, K.L. Wooley, E. Drockenmuller, M. Malkoch, C.J. Hawker, Conformation of Intramolecularly Cross-Linked Polymer Nanoparticles on Solid Substrates, Nano Letters, 5 (2005) 1704-1709.

[50] P.-G. De Gennes, Scaling concepts in polymer physics, Cornell university press1979.

[51] J. Kumaki, Observation of polymer chain structures in two-dimensional films by atomic force microscopy, Polymer Journal, 48 (2016) 3-14.

[52] P.J. Flory, Principles of polymer chemistry, Cornell University Press1953.

[53] E. Harth, B.V. Horn, V.Y. Lee, D.S. Germack, C.P. Gonzales, R.D. Miller, C.J. Hawker, A Facile Approach to Architecturally Defined Nanoparticles via Intramolecular Chain Collapse, Journal of the American Chemical Society, 124 (2002) 8653-8660.

[54] L.J. Fetters, N. Hadjichristidis, J.S. Lindner, J.W. Mays, Molecular Weight Dependence of Hydrodynamic and Thermodynamic Properties for Well-Defined Linear Polymers in Solution, Journal of Physical and Chemical Reference Data, 23 (1994) 619-640.

[55] A. Latorre-Sánchez, A. Alegría, F. Lo Verso, A.J. Moreno, A. Arbe, J. Colmenero, J.A. Pomposo, A Useful Methodology for Determining the Compaction Degree of Single-Chain Nanoparticles by Conventional SEC, Particle & Particle Systems Characterization, 33 (2016) 373-381.

[56] O. Altintas, J. Willenbacher, K.N.R. Wuest, K.K. Oehlenschlaeger, P. Krolla-Sidenstein, H. Gliemann, C. Barner-Kowollik, A Mild and Efficient Approach to Functional Single-Chain Polymeric Nanoparticles via Photoinduced Diels–Alder Ligation, Macromolecules, 46 (2013) 8092-8101.

[57] P. Wang, H. Pu, M. Jin, Single-chain nanoparticles with well-defined structure via intramolecular crosslinking of linear polymers with pendant benzoxazine groups, Journal of Polymer Science Part A: Polymer Chemistry, 49 (2011) 5133-5141.

[58] P. Wang, H. Pu, J. Ge, M. Jin, H. Pan, Z. Chang, D. Wan, Fluorescence-labeled hydrophilic nanoparticles via single-chain folding, Materials Letters, 132 (2014) 102-105.

[59] A. Ruiz de Luzuriaga, I. Perez-Baena, S. Montes, I. Loinaz, I. Odriozola, I. García, J.A. Pomposo, New Route to Polymeric Nanoparticles by Click Chemistry Using Bifunctional Cross-Linkers, Macromolecular Symposia, 296 (2010) 303-310.

Chapter 4: Enzyme-Mimetic Single-Chain Nanoparticles for the Synthesis of PEDOT

4.1. Motivation

The use of single-chain polymer nanoparticles (SCNPs) as enzyme-mimic constructs has attracted significant interest in recent years. In this Chapter, we investigate the design of SCNPs as artificial iron-containing pseudo-enzymes for the synthesis of a relevant intrinsically conducting polymer (ICP) such as poly(3,4-ethylenedioxythiophene), PEDOT. This is the first report of the use of SCNPs as enzyme-mimetic nano-objects for the synthesis of ICPs.

4.2. Introduction

Intrinsically conducting poly(3,4-ethylenedioxythiophene): polystyrenesulfonate (PEDOT: PSS) films prepared upon water removal from PEDOT: PSS dispersions have attracted significant interest for the development of transparent electrodes [1], as functional layers in light emitting diodes [2], electrochromic devices [3] and solar cells [4], as well as for biosensing [5] and regenerative medicine [6] applications.

Poly(3,4-ethylenedioxythiophene) (PEDOT) is a conjugated polymer. It is a polythiophene derivative. It is formed by the polymerization of bicyclic monomer 3,4-ethylenedioxythiophene (EDOT). The EDOT molecule consists of a thiophene ring and a dioxyethylene group bridging across the 3 and 4 positions of the heterocyclic ring. PEDOT is insoluble in water. In its oxidative state, PEDOT has a positive charge roughly every third repeating unit, thus the conductivity is produced through hole transport.

PEDOT:PSS is a polymer mixture made of 2 polymers: PEDOT and PSS. It is a successful conducting polymer with many practical applications (Scheme 4.1).
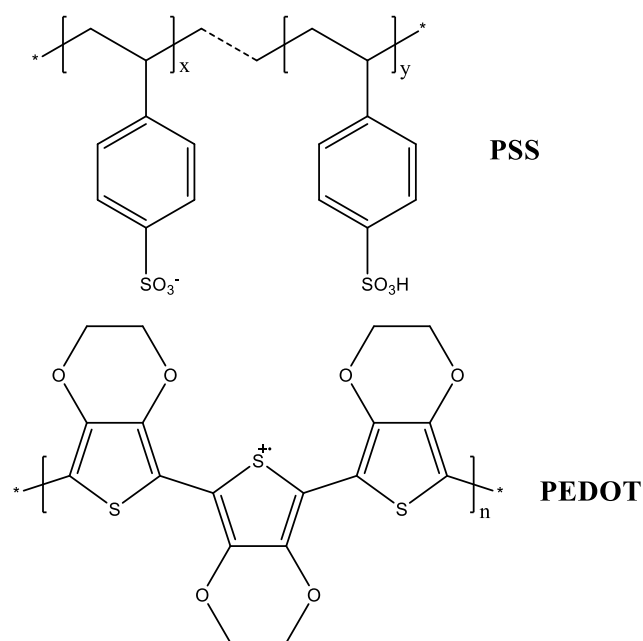
Scheme 4.1. Chemical structure of PEDOT: PSS

PEDOT:PSS consists of positively charged conjugated PEDOT and negatively charged polystyrene sulfonate (PSS) [7]. PEDOT: PSS, unlike pure PEDOT, is dispersible in water and forms a deep-blue opaque solution. It forms a continuous thin film on rigid or flexible substrates by various solution processing techniques. PEDOT: PSS films are smooth and thin films are almost transparent in the visible range. PEDOT: PSS exhibits a wide range of electrical conductivities that range from 10^{-2} to 10^3 S cm^{-1}. These conductivities of the polymer are influenced by the conditions of the synthesis, processing additives and post-treatment. PEDOT: PSS possesses good photo stability and electrical stability.

PEDOT:PSS has been utilized in a wide range of applications like antistatic coating, as electrode in light-emitting diodes (LEDs), photovoltaics, memories, sensors, electrochromic devices, field effect transistors and circuits in general [8]. One potential application is as electrode in organic solar cells (OSC). The electrodes are the bottleneck of the processing of OSCs. At least one electrode needs to be transparent in order to collect light. Currently the standard transparent electrode is made of doped indium tin oxide (ITO). The high cost and brittleness if ITO demands an alternative. PEDOT:PSS is promising as a substitute because of its transparency in the visible range, high mechanical flexibility, excellent thermal stability and can be produced through conventional solution processing [9].

However, PEDOT: PSS has a conductivity much lower than that of ITO (3000 S cm^{-1}) but it can be enhanced. Several treatments have been performed to enhance the conductivity by 3 orders of magnitude. These treatments include hydrophilic solvents like sorbitol [8], methanol [9], DMSO [10], ethylene glycol, glycerol… and thermal annealing [8]. Screening by polar solvents causes the excess PSS to dissolve and the system is rearranged forming a higher PEDOT concentration film with higher conductivity. It has also been suggested that increasing the crystallinity of PEDOT:PSS increases its conductivity [11].

There are two conduction mechanisms in PEDOT: PSS. One of them is dominated by polarons and the other by bipolarons. Bipolarons are more efficient charge carriers and PEDOT: PSS films have different conductivities according to which charge carrier dominates. The higher charge density provided by bipolarons leads to higher conductivity. Absorption of light by polarons produces a peak in the spectrum centered at ~795 nm. Bipolarons produce a broad absorption in the near infrared that is centered at ~3600 cm^{-1} [12].

The first enzyme-mediated synthesis of a PEDOT: PSS dispersion was reported in 2007, through the use of horseradish peroxidase in the presence of PSS as both water-soluble template and charge-balancing dopant [13]. Traditional synthesis of PEDOT: PSS dispersions involves the use of iron-containing salts and oxidants such as ammonium persulfate. With the aim to introduce environmentally friendly alternatives over conventional chemical catalyst, a variety of enzyme mediated synthesis of PEDOT: PSS have been developed in recent years by introducing proteins containing iron in a heme complex (horseradish peroxidase [1], soybean peroxidase [14], catalase and hemoglobin [12], cytochrome c [15]) and hydrogen peroxide as an oxidant. The properties of the resulting PEDOT: PSS films depend on the specific enzyme employed during the synthesis [16]. Interestingly, as demonstrated by Hira and Payne [17], even simple iron-binding proteins showing non-enzymatic activity (e.g., transferrin) can been used as oxidants for the synthesis of PEDOT: PSS dispersions. This fact significantly expands the library of biomolecular oxidants available for the synthesis of PEDOT based films with a desired set of properties, since nowadays over 800 different heme proteins are known [18].

Recently, the use of single-chain polymer nanoparticles (SCNPs) as enzyme-mimic constructs has attracted significant interest [19-22]. It is worth mentioning that SCNPs endowed with enzyme-mimetic morphology and activity often show increased stability against thermal changes and reduced degradability when compared to natural enzymes [23]. SCNPs are constructed via self-folding of a single linear polymer chain by means of intra-chain covalent bonds or supramolecular interactions (e.g., hydrogen bonding, dynamic covalent bonds, metal complexation) [24-34]. Two limiting morphologies have been observed in SCNPs depending on the particular synthesis route employed and the hydrophobic/hydrophilic balance of the SCNP precursor chain. A sparse morphology resembling that displayed by intrinsically disordered proteins is often observed by means of intra-chain folding/collapse of the precursor under good solvent conditions [35, 36]. Conversely, a globular morphology more akin to that found in enzymes is typically obtained by single-chain self-folding in water of amphiphilic (neutral or charged) random copolymers of appropriate composition and molecular weight [37-41].

Recently, SCNPs have been used as enzyme-mimetic nanoreactors for the synthesis of a variety of chemical compounds [19], gold nanoparticles [42], quantum dots [43], and carbon nano-dots [44], as well as for ring-opening polymerization (ROP) [45] and living radical polymerization (LRP) [46, 47] processes. Hence, SCNPs containing entrapped $B(C_6F_5)_3$ molecules were found to display polymerase-like activity toward tetrahydrofuran via ring-opening polymerization in the presence of glycidyl phenyl ether that played the role of a co-catalyst [45]. Additionally, Sanchez-Sanchez and coworkers reported the metalloenzyme-mimic properties of copper (II)-containing SCNPs toward the controlled radical polymerization of water-soluble vinyl-type monomers under reductive conditions [46]. Very recently, efficient living radical polymerization of various alkyl methacrylate monomers using iron-containing SCNPs has been described by Azuma *et al.* [47].

However, to the best of our knowledge, the use of water-soluble self-folded metal-containing SCNPs as robust enzyme-mimic nanoreactors for the synthesis of intrinsically conducting polymers (ICPs) via step growth polymerization has not been investigated yet. In this Chapter, we disclose the use of water-soluble self-folded metal-containing single-chain nanoparticles (SCNPs) as robust enzyme-mimic nanoreactors for the synthesis of ICPs via step-growth polymerization. As a proof of concept, we report the first enzyme-mimetic synthesis of PEDOT: PSS dispersions at room temperature (r.t.) via oxidative polymerization using self-folded iron-containing SCNPs as efficient artificial pseudo-enzymes (Scheme 4.2).

Remarkably, this work paves the way to the synthesis of other types of intrinsically conducting polymers (e.g., polyaniline, polypyrrole) for a variety of potential applications using water-soluble SCNPs as robust enzyme-mimic nanoreactors operating at r.t. Moreover, it expands the use of SCNPs as bioinspired catalysts from chain-growth polymerization (i.e., ROP and LRP) to step-growth polymerization (i.e., polycondensation via oxidative polymerization).
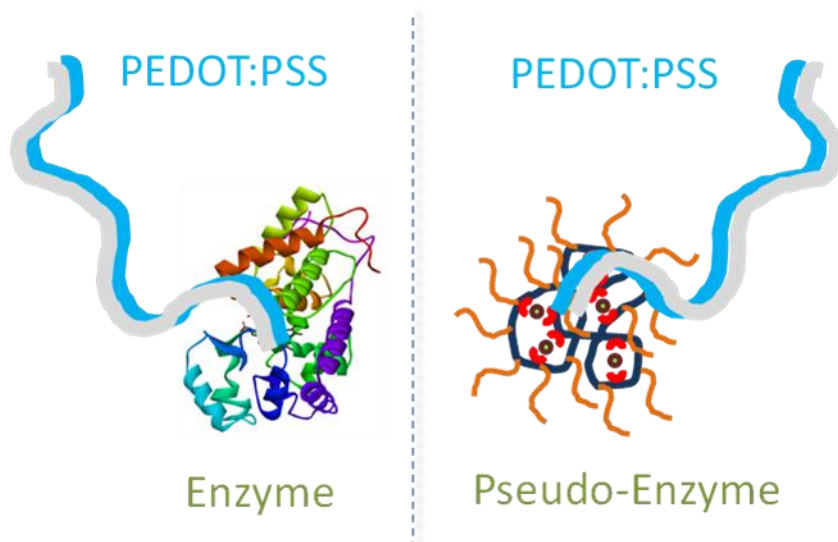
Scheme 4.2. *Synthesis of PEDOT: PSS by enzymes and artificial pseudo-enzymes.*

4.3. Experimental procedures

4.3.1. Materials

Oligo(ethylene glycol) methyl ether methacrylate (OEGMA) (average $M_n \sim 300$ g/mol), 2-acetoacetoxy ethyl methacrylate (AEMA) (95%), 3,4-ethylenedioxythiophene (EDOT) (97%), poly(sodium 4- styrenesulfonate) (PSS) (average $M_w \sim 77000$ g/mol), iron(II) acetate (Fe(OAc)$_2$) (95%), 2,2-azobis(2-methylpropionitrile) (AIBN) ($\geq$98%), hydrogen peroxide (H$_2$O$_2$) (30 wt% solution in water, ACS reagent), horseradish peroxidase (HRP) (type VI, essentially salt-free, lyophilized powder, $\geq$250 units/mg), poly(3,4-ethylenedioxythiophene)-poly(styrenesulfonate) (PEDOT:PSS) (3.0-4.0% in H$_2$O, high-conductivity grade), 1,4-dioxane (anhydrous, 99.8%), N,N-dimethyl formamide (DMF) (ACS reagent, 99.8%) and deuterated chloroform (CDCl$_3$) (99.96 atom % D, containing 0.03% (*v/v*) tetramethylsilane, TMS) were purchased from Sigma-Aldrich. Tetrahydrofuran (THF) (GPC grade), diethyl ether (Et$_2$O) (ACS reagent, anhydrous, > 99.0%), hexane (anhydrous, 95 %), and hydrochloric acid (extra pure, 37% in water) were supplied by Scharlau. 4-Cyanopentanoic acid dithiobenzoate (> 97%) was purchased from Strem Chemicals. Deionized water obtained from a Thermo Scientific apparatus (Barnstead TII Pure Water System) was employed in this work. AIBN was recrystallized from methanol. OEGMA and AEMA were purified by passing through basic and neutral alumina, respectively.

4.3.2. Techniques

Size exclusion chromatography (SEC) measurements were performed at 30 °C on an Agilent 1200 system equipped with PLgel 5 μm Guard and PLgel 5 μm MIXED-C columns and triple detection: a differential refractive index (RI) detector (Optilab Rex, Wyatt), a multi-angle laser light scattering (MALLS) detector (MiniDawn Treos, Wyatt), and a viscosimetric (VIS)

detector (ViscoStar-II, Wyatt). Data analysis was performed with ASTRA Software (version 6.1) from Wyatt. THF was used as eluent at a flow rate of 1 ml/min. A value of $dn/dc = 0.115$ was used for the precursor and the single-chain nanoparticles.

The freeze-drying system employed was a Telstar-Cryodos equipment.

[1]H nuclear magnetic resonance (NMR) spectra were recorded on a Bruker spectrometer operating at 400 MHz, using $CDCl_3$ as solvent. AEMA content was determined following the procedure described in section 4.4.1. [46].

Fourier transform infra-red (FTIR) measurements were performed at r.t. on a Jasco 3600 FTIR spectrometer.

Dynamic Light Scattering (DLS) measurements were carried out at 25 °C in a Zetasizer Nano-ZS apparatus.

Ultraviolet-visible (UV–vis) spectra were recorded on an Agilent 8453A apparatus equipped with a Peltier thermostatic cell holder (T-controller 89090A).

Metal content was determined by inductively coupled plasma (ICP) atomic emission spectroscopy performed on an Agilent 7700X spectrometer.

TGA Measurements were performed in a Q500, TA Instruments Thermogravimetric analysis. The sample was heated from 25ºC to 800ºC in an inert atmosphere.

Atomic Force Microscopy (AFM) measurements were performed using a Multimode AFM, equipped with a Nanoscope V controller (Bruker). All images were taken in tapping mode, using Multi300Al-G probes (Budgetsensors). Samples for AFM were prepared by spin coating (3000 rpm, 2 min) the PEDOT: PSS dispersions at 100 mg/ml concentration onto glass slides, allowing to obtain thin films. Prior coating, the glass substrates were washed in soapy solution with deionized water, rinsed with acetone and finally dried under a N_2 flow. Conductivity of PEDOT: PSS thin films was measured using a 4-point probe setup (HFS600-P, Linkam) and an Alpha impedance analyzer (Novocontrol).

4.3.3. Synthesis of OEGMA-AEMA copolymers

In a typical procedure, OEGMA (1.54 ml, 5.4 mmol), AEMA (0.34 ml, 1.8 mmol), CPADB (20 mg, 7×10^{-2} mmol) and AIBN (2.35 mg, 1.4×10^{-2} mmol) were dissolved in 1,4-dioxane (3 ml). The reaction mixture was degassed by passing argon for 15 min. The copolymerization reaction was carried out at 70 ºC for 24 h (Scheme 4.3). The resulting pink oil was isolated by precipitation in hexane. After that, the copolymer was redissolved in a minimal amount of THF and added to a large excess of hexane (twice), the residual solvent was concentrated and further drying at r.t. under dynamic vacuum. Poly(OEGMA-co-AEMA) copolymers were obtained as pink oils with 24-44 mol% of AEMA content, as determined by ^{1}H NMR spectroscopy [46].
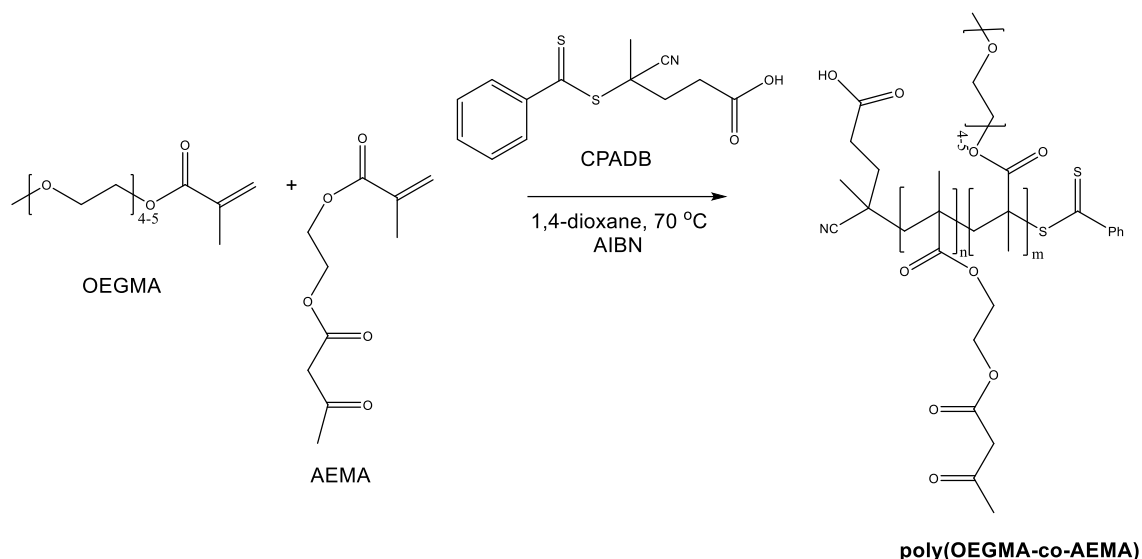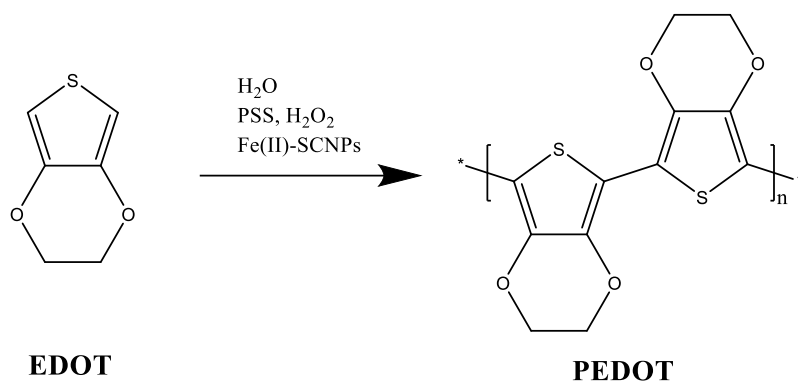
Scheme 4.3. *Representation of the synthesis of poly (OEGMA-co-AEMA) precursor copolymer* **P**.

4.3.4. Synthesis of artificial iron-containing pseudo-enzymes

In a typical procedure, 1000 mg of an amphiphilic random copolymer of oligo(ethyleneglycol) methyl ether methacrylate (OEGMA) and 2-acetoacetoxy ethyl methacrylate (AEMA) prepared following the experimental procedures reported the previous section [46] (**P**, M_w: 135 KDa, $Đ$: 1.10, AEMA content: 24 mol%) were dissolved in 1000 ml of THF at r.t. To this solution, 73.4 mg of Fe(OAc)$_2$ dissolved in 1 mL of DMF were added under stirring to induce intrachain folding/collapse via iron(II)/ (AEMA)$_2$ complexation (see Scheme 4.5). After 24 h of reaction time, solvent exchange to water was preformed and the mixture was dialyzed to remove unreacted Fe(OAc)$_2$ and residual organic compounds. The concentration of the final single-chain nanoparticles (**NP**) solution in water was 0.96 mg/ml. Finally, a fraction of the **NP** solution was isolated via freeze-drying for characterization and other fraction was keep in solution to be used as artificial iron-containing pseudo-enzymes. The average number of iron atoms per individual single-chain nanoparticle was found to be 48 by ICP atomic emission spectroscopy.

4.3.5. Synthesis of PEDOT using artificial iron-containing pseudo-enzymes

In a typical reaction, 0.512 mL of artificial iron-containing pseudo-enzymes aqueous solution (0.49 mg of **NP**), 226.6 mg of poly(sodium 4-styrenesulfonate) (PSS) and 0.117 mL of 3,4-ethylenedioxythiophene (EDOT) monomer were dissolved in water (20 ml) at r.t. under an argon atmosphere. To this mixture, 0.112 ml of a hydrogen peroxide solution (30 wt% H$_2$O$_2$ solution in water) was added (Scheme 4.4). The oxidative polymerization of EDOT was followed by UV–vis spectrometry by taken periodically samples from the polymerization medium. After reaction completion, conducting films (containing the artificial iron-containing pseudo-enzymes) were prepared from the resulting PEDOT: PSS dispersions via solvent casting.

**Scheme 4.4.** *Illustration of the synthesis of PEDOT: PSS.*

4.3.6. Synthesis of PEDOT using Fe(OAc)$_2$ (as control reaction)

In a typical reaction, 0.512 mL of a Fe(OAc)$_2$ aqueous solution (23.73 mg of Fe(OAc)$_2$), 226.6 mg of poly(sodium 4-styrenesulfonate) (PSS) and 0.117 ml of 3,4-ethylenedioxythiophene (EDOT) monomer were dissolved in water (20 ml) at r.t. under an argon atmosphere. This amount of Fe(OAc)$_2$ is the equimolar quantity used in the PEDOT synthesis using SCNPs. To this mixture, 0.112 ml of a hydrogen peroxide solution (30 wt% H$_2$O$_2$ solution in water) was added. The oxidative polymerization of EDOT was followed by UV-vis spectrometry, until a total time of 5 hours.

4.4. Results and discussion

4.4.1. Synthesis of iron-containing self-folded single-chain nanoparticles as artificial pseudo-enzymes

SCNPs were synthesized from poly(OEGMA-co-AEMA) copolymers. ^{1}H-NMR spectra of copolymers synthesized in this Chapter correspond to those found in the literature. OEGMA/AEMA ratios of the precursor polymers were calculated measuring the normalized integrated areas of the peaks (Figure 4.1) of the NMR spectrum of the OEGMA-co-AEMA copolymers.
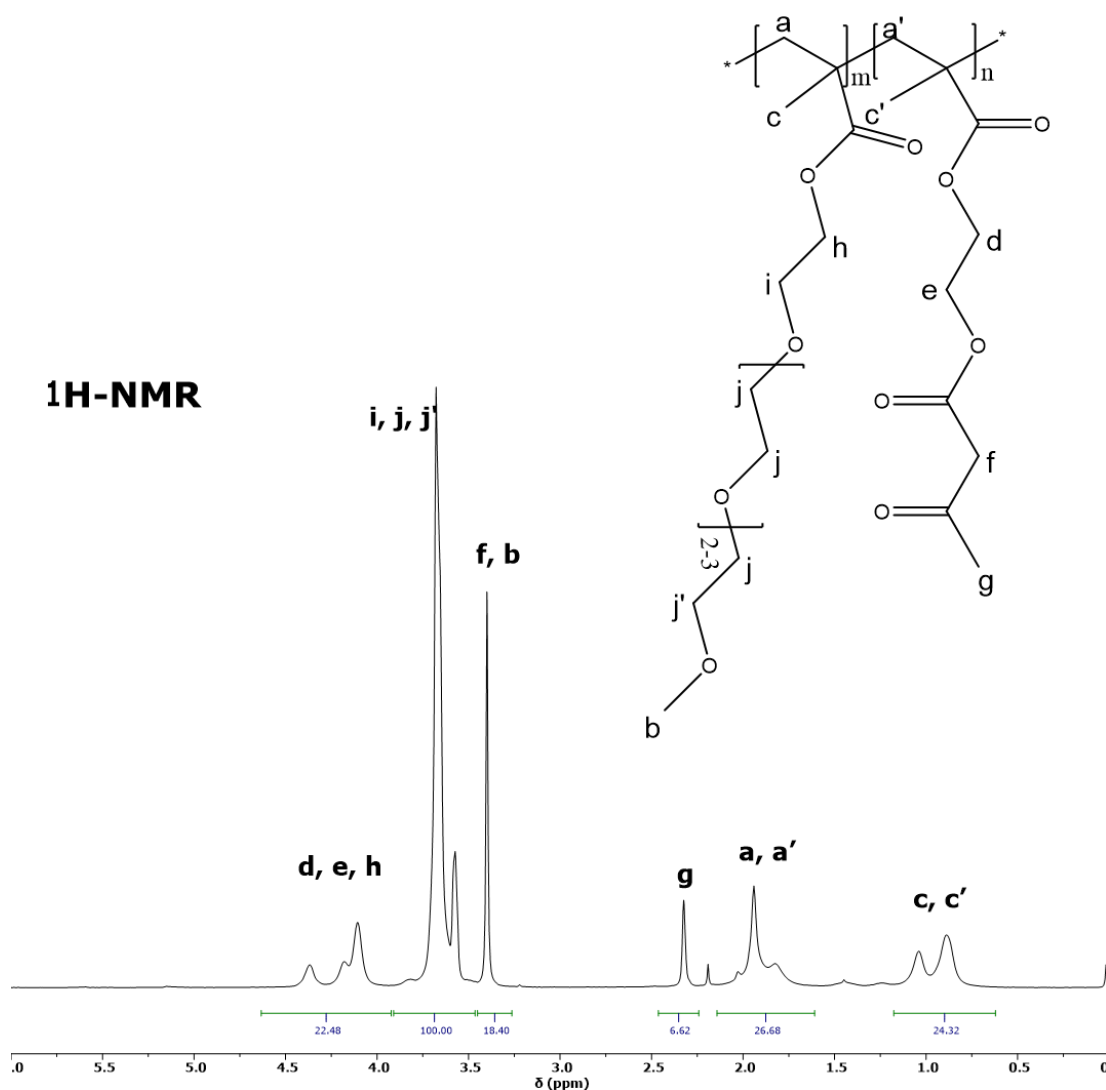
Figure 4.1. ¹H NMR spectrum of poly(OEGMA-co-AEMA) precursor copolymer **P**.
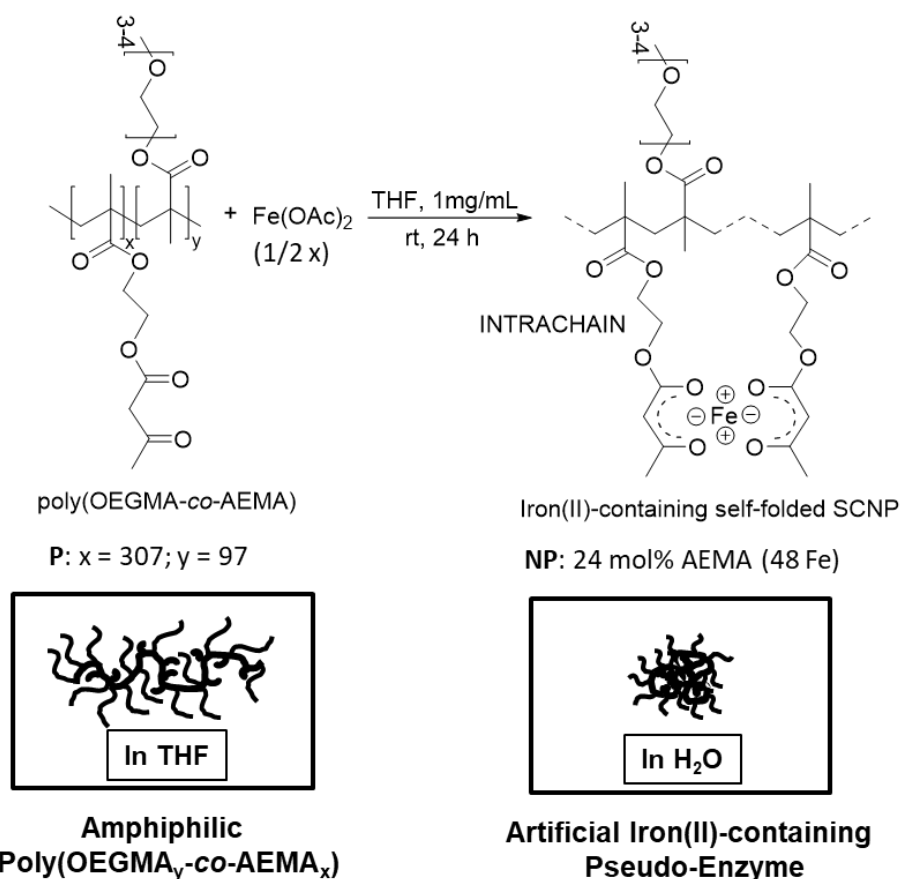
Copolymer compositions and molecular weights of copolymers synthesized in this project are shown on Table 4.1 below.

Table 4.1. Characterization data of poly(OEGMA-co-AEMA) precursor copolymers.

| OEGMA/AEMA ratio	M_w (kDa)	$Đ$
56.2% OEGMA/43.8% AEMA	29.2	1.01
76.4% OEGMA/23.6% AEMA	134.6	1.10

Scheme 4.5 illustrates the synthetic approach followed in this work to produce iron(II)-containing SCNPs as artificial pseudo-enzymes. Based on previous works [46], we synthesized a high molecular weight ($M_w = 135$ kDa, $Đ = 1.10$) amphiphilic random copolymer (**P**) composed of OEGMA (76 mol%) and AEMA (24 mol%) units to guarantee

the formation of single-chain core-shell globules in water with the hydrophobic AEMA units placed in the core and the hydrophilic OEGMA moieties in the shell, by working at highly diluted conditions (1 mg **P**/ ml). Metal complexation of AEMA units was carried out for 24 h at r.t. The resulting single-chain nanoparticles (**NP**) were purified from unreacted $Fe(OAc)_2$ and residual organic compounds by dialysis after solvent exchange to water, and isolated for characterization via freeze-drying.


poly(OEGMA-*co*-AEMA)

P: x = 307; y = 97

Iron(II)-containing self-folded SCNP

NP: 24 mol% AEMA (48 Fe)

In THF

In H₂O

Amphiphilic Poly(OEGMA$_y$-*co*-AEMA$_x$)

Artificial Iron(II)-containing Pseudo-Enzyme

Scheme 4.5. *Schematic illustration of the synthesis of self-folded iron (II)-containing single-chain nanoparticles* (**NP**) *as artificial pseudo-enzymes.*

The efficient formation of self-folded iron-containing SCNPs was confirmed by combined size exclusion chromatography (SEC) and dynamic light scattering (DLS) measurements. As depicted in Figure 4.2, the iron-containing SCNPs **NP** showed an increase in retention time (i.e. a reduction in hydrodynamic size) during SEC in THF when compared to the amphiphilic random copolymer precursor **P** due to the formation of intra-chain iron(II)/(AEMA)$_2$ complexes in the former case.
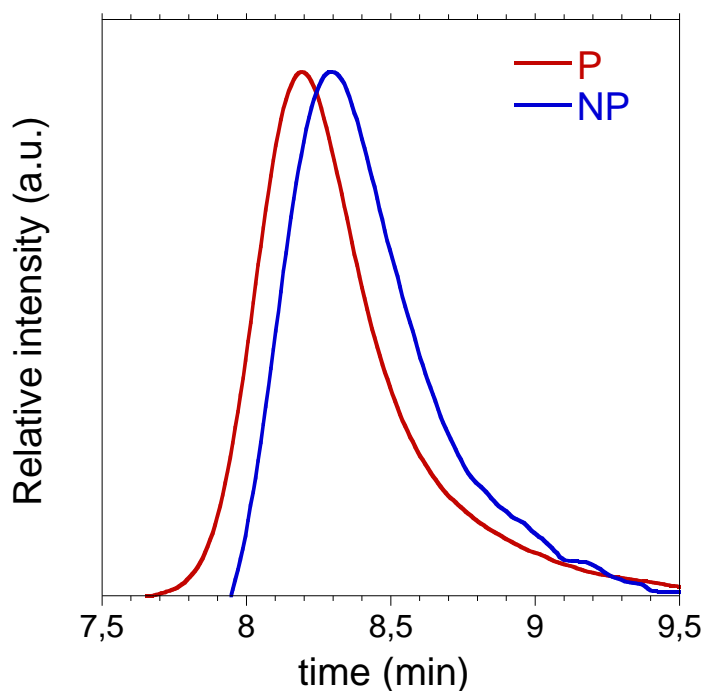
Figure 4.2. *Size-exclusion chromatography (SEC) traces in THF showing the typical reduction in hydrodynamic size of an amphiphilic random poly(OEGMA-co-AEMA) copolymer (P) (red line) upon intra-chain iron(II) complexation to give single-chain nanoparticles (NP) (blue line).*

The difference in hydrodynamic size of the iron-containing SCNPs when dissolved in water (good solvent for OEGMA units, bad solvent for AEMA moieties) and in THF (good solvent for both OEGMA and AEMA units) is shown in Figure 4.3, as determined by DLS measurements. The conformational change taking place on passing from THF to H_2O due to a modification in solvophilic/solvophobic balance promoting the self-folding of **P** to individual core-shell nanoparticles is illustrated schematically in Scheme 4.5. Further compaction is induced by intrachain iron(II)/(AEMA)$_2$ complexation. On average, self-folded iron-containing SCNPs were found to contain 48 Fe atoms per single-chain nanoparticle as determined by ICP atomic emission spectroscopy, which is a value similar to that found in copper-containing globular SCNPs prepared from amphiphilic random poly(OEGMA-co-AEMA) copolymers [46]. The above results support the efficient formation in water of individual SCNPs containing Fe(II)/(AEMA)$_2$ complexes placed in a hydrophobic core, which is stabilized by an external hydrophilic shell.
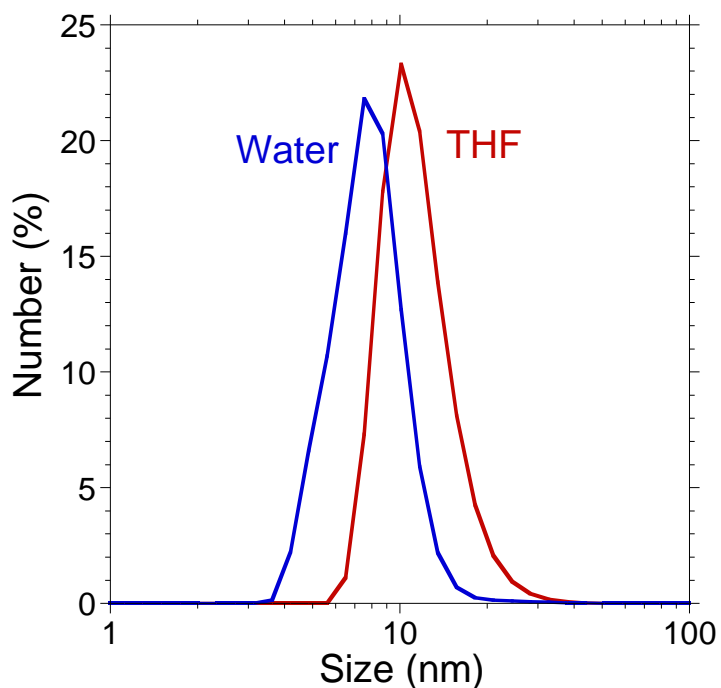
Figure 4.3. *Dynamic light scattering (DLS) results showing the different size of single-chain nanoparticles **NP** in H₂O, which is a good solvent for OEGMA units and a bad solvent for AEMA moieties (blue line) and in THF, which is a good solvent for both OEGMA and AEMA repeat units (red line).*

TGA measurements of iron-containing SCNPs left a residue of 8.48% of the original mass demonstrating SCNPs contain iron (Figure 4.4 B). The residual weight that can be assigned to FeO species due to the black colour of the residues. The precursor **P**, which was taken as a control, was totally decomposed at temperatures above 450ºC (Figure 4.4 A), so the residues observed for **NP** can be only attributed to metal oxide species.
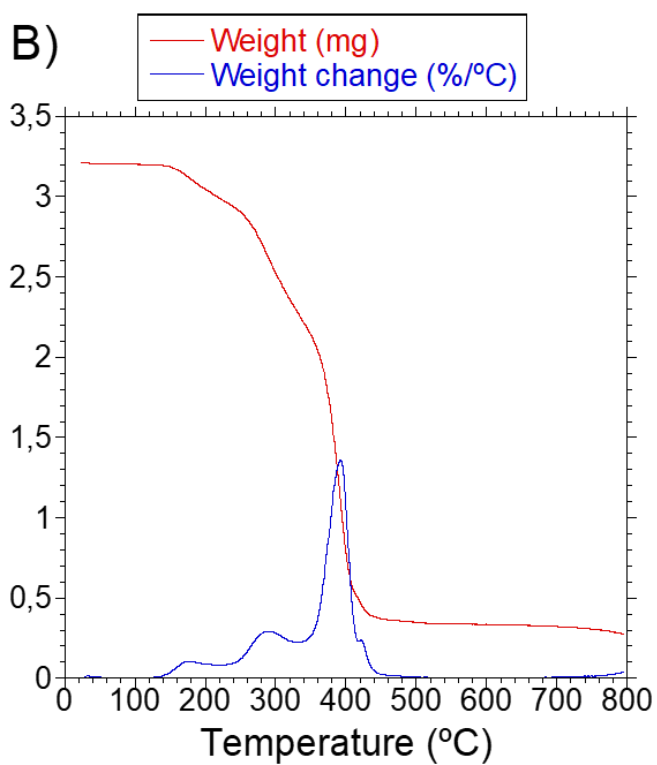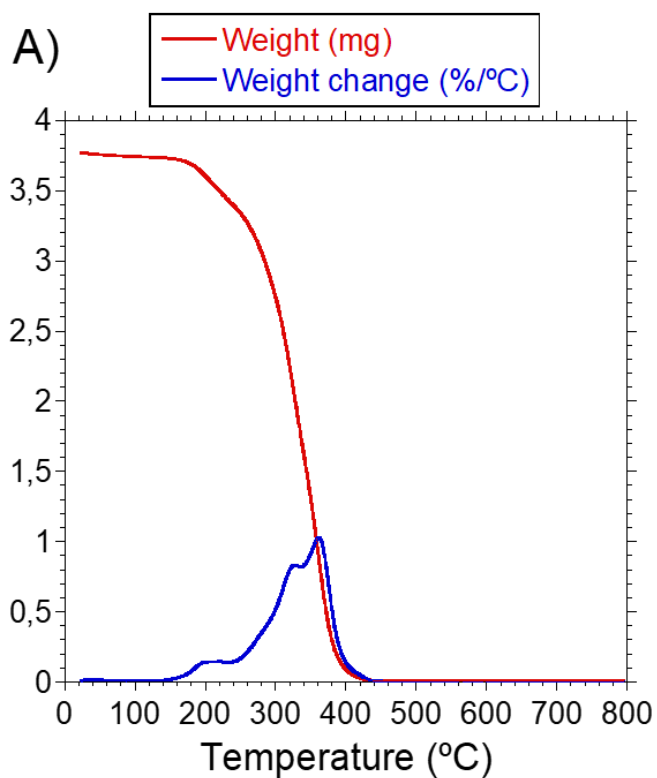
Figure 4.4. *Thermogram of the decomposition of poly (OEGMA-co-AEMA) precursor copolymer* **P (A)** *and iron(II) containing SCNPs* **NP (B)** *by thermogravimetric analysis showing the reduction of the mass (red line) of SCNPs with temperature and the mass loss rate (blue line).*

4.4.2. Synthesis and characterization of PEDOT using artificial iron-containing pseudo-enzymes

The enzyme-mimetic synthesis of PEDOT at r.t. using self-folded iron(II)-containing single-chain nanoparticles as artificial pseudo-enzymes is depicted in Scheme 4.6. We follow a recipe similar to that used during the first reported enzymatic synthesis of PEDOT [13] but totally replacing the horseradish peroxidase (HRP) enzyme by the self-folded iron(II)-containing SCNPs **NP** as artificial pseudo-enzymes, at a concentration of 0.96 mg **NP**/mL, (see Section 4.3.4 for technical details).
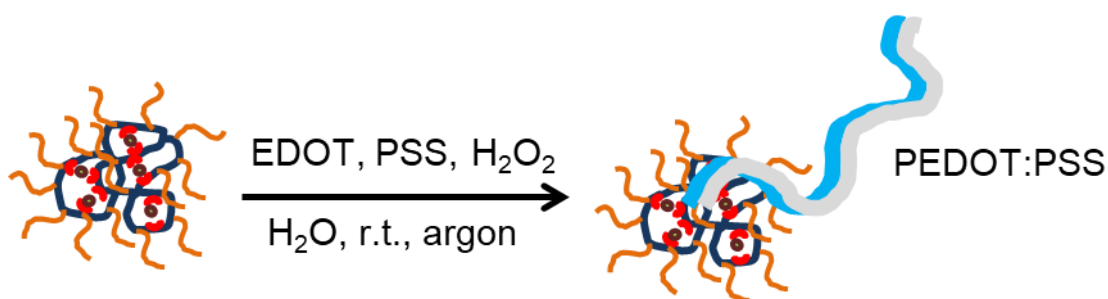
Scheme 4.6. *Schematic illustration of enzyme-mimetic synthesis of PEDOT: PSS dispersions at r.t. using self-folded iron(II)-containing SCNPs as artificial pseudo-enzymes.*

As illustrated in Figure 4.5, the initially transparent reaction medium takes a deep blue colour upon formation of the PEDOT: PSS dispersion at 3 h of reaction time, showing the ability of the self-folded iron(II)-containing SCNPs to perform as artificial pseudo-enzymes.
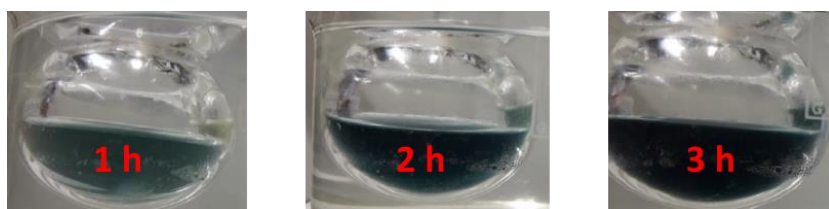
Figure 4.5. *Evolution of the colour of the reaction mixture with reaction time during the enzyme-mimetic synthesis of PEDOT.*

It should be noted that by using neat $Fe(OAc)_2$ instead of **NP**, the resulting PEDOT: PSS dispersion took a deep blue colour only after 5 h of reaction time. In Figure 4.6, we present

photographs of the reaction flask as a function of time. We observed an evolution of the solution's colour with time, from light to dark blue.


| 30 min | 1 h | 2 h | 3 h | 5 h |
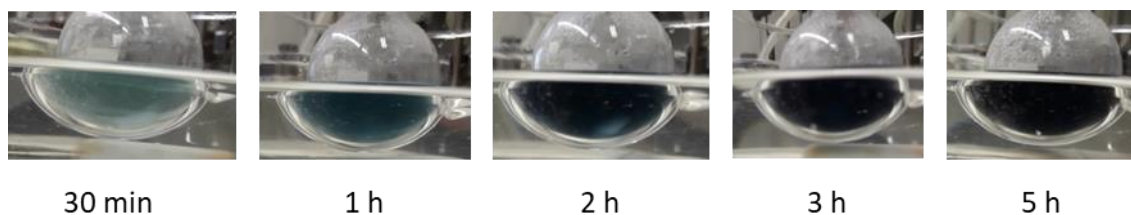
Figure 4.6. Photographs of the reaction flask as a function of time, for PEDOT synthesis using Fe(OAc)$_2$.

A comparison of the performance of the SCNPs versus HRP for the preparation of PEDOT: PSS dispersions is shown in Figure 4.7, as determined by UV–vis spectroscopy. Although for the HRP-mediated synthesis of PEDOT: PSS dispersions the reported optimum temperature was 4 °C [13], we found that the reaction temperature can be increased to r.t. by working under an inert argon atmosphere (Figure 4.7).
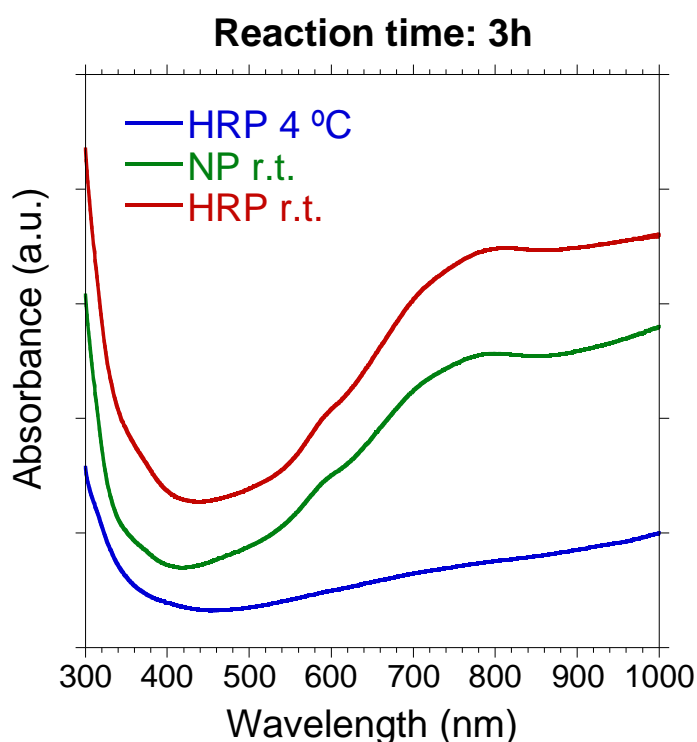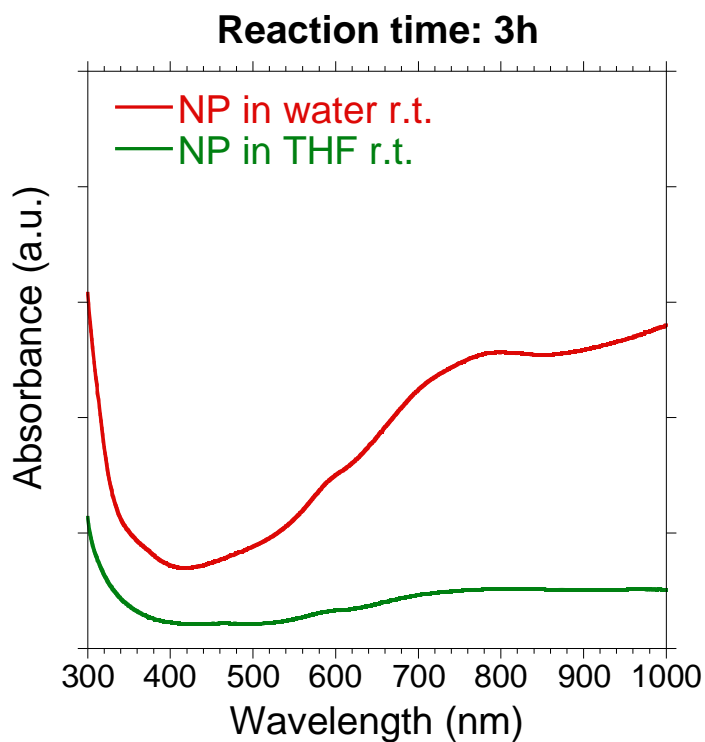

Figure 4.7. Comparison of the UV-vis spectra corresponding to PEDOT : PSS dispersions prepared at r.t. by using self-folded iron(II)-containing single-chain nanoparticles as artificial pseudo-enzymes (**NP**) or horseradish peroxidase (HRP) enzyme (also the spectrum obtained by using HRP at 4ºC is included for comparison).

Advantageously, the polymerization kinetics at r.t. is faster than at 4 °C. Remarkably, the characteristics of the PEDOT: PSS dispersions and PEDOT: PSS films synthesized using **NP** or HRP at r.t. for 3 h were very similar, as determined by UV–Vis (Figure 4.7) and FTIR spectrometry (Figure 4.8), respectively.
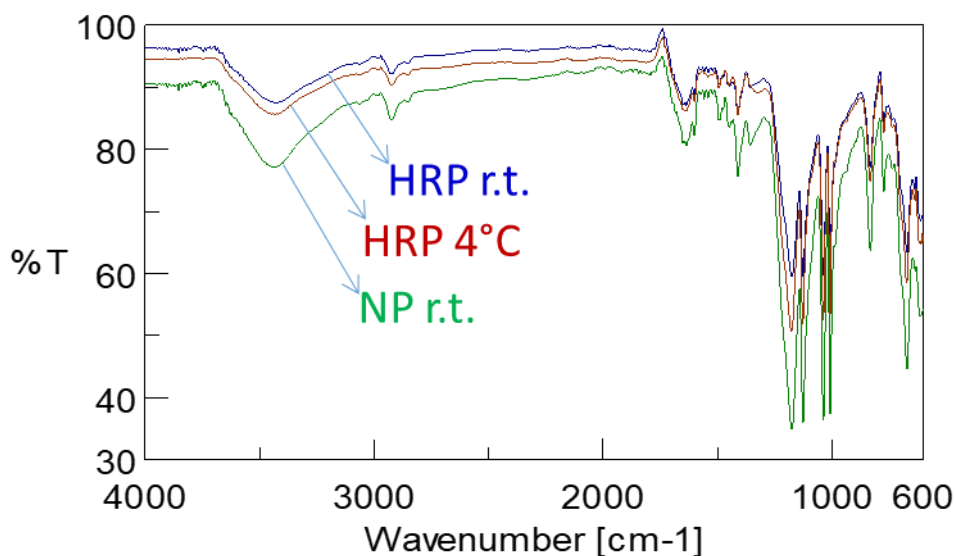
Figure 4.8. *FTIR spectra corresponding to PEDOT: PSS films prepared from the dispersions described in Figure 4.7.*

Hence, the characteristic bipolaron absorption band around 800 nm was observed in both the PEDOT: PSS dispersion prepared with the artificial pseudo-enzymes **NP** and the PEDOT: PSS dispersion synthesized using the horseradish peroxidase, HRP, enzyme (Figure 4.7). Such bipolaron absorption band which is a signature of the conductivity of the resulting PEDOT was absent when the synthesis was performed using **NP** dissolved in THF instead of water (see Figure 4.9).

Reaction time: 3h

*Figure 4.9. Comparison of the UV-vis spectra corresponding to PEDOT: PSS dispersions prepared with **NP** in water, and **NP** in THF.*

Thin films prepared form PEDOT: PSS dispersions synthesized at r.t. for 3 h using **NP** as artificial pseudo-enzymes were examined by atomic force microscopy (AFM) as illustrated in Figure 4.10. The bare glass slide showed a roughness of about 2.15 nm (Figure 4.10 A) that after coating with the PEDOT: PSS dispersion was significantly reduced to 0.35 nm (Figure 4.10 B). AFM images also showed that there were not any important presence of holes or discontinuities on the substrate after coating, indicating the homogeneous coverage of the PEDOT: PSS thin films.

A)

20.0 nm

Height   600.0 nm

B)

4.0 nm

Height   600.0 nm
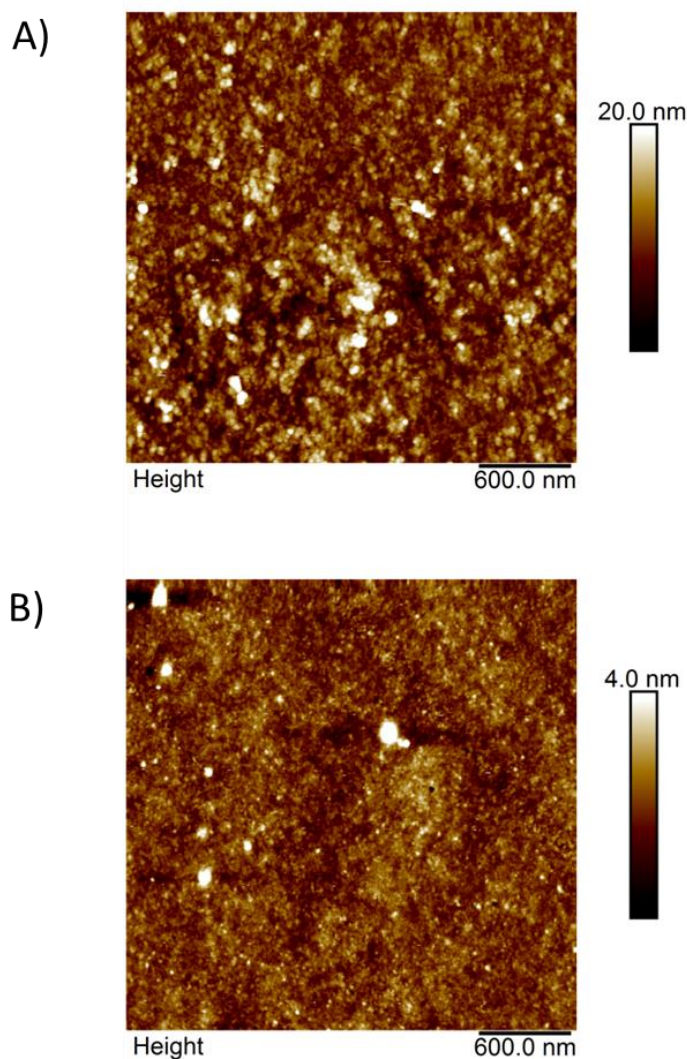
Figure 4.10. *AFM topography images (3 µm x 3 µm) of: (A) a bare glass slide, and (B) a PEDOT: PSS coated glass slide prepared from a PEDOT: PSS dispersion synthesized at r.t. for 3 h of reaction time by using self-folded iron(II)-containing single-chain nanoparticles NP as artificial pseudo-enzymes.*

Using sharp tweezers, we performed a scratch on the PEDOT: PSS thin film and its thickness was quantified via AFM by the step height presented in Figure 4.11, resulting in a film thickness of 250 ± 4 nm. Conductivity measurements on the PEDOT: PSS coated glass slide were performed using a 4 point probe setup. A mean electrical conductivity of $\sigma = 1 \times 10^{-4}$ S/cm was determined which was similar to that typically reported for PEDOT: PSS films prepared from PEDOT: PSS dispersions synthesized using iron-containing proteins like catalase ($\sigma = 1.3 \times 10^{-5}$ S/cm).
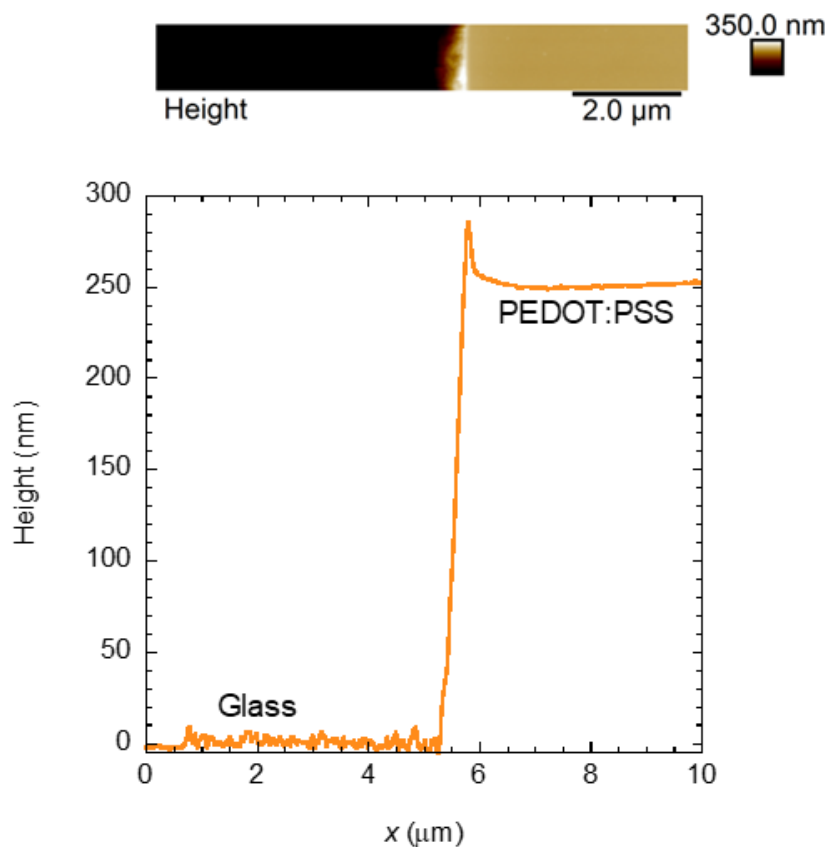
Figure 4.11. *Film thickness determination* via *AFM step height method.*

4.4.3. Characterisation of PEDOT Synthesised using Fe(OAc)$_2$ (control reaction)

In Figure 4.12 we show the UV-Vis spectrum after 5 h of synthesis time. The characteristic bipolaron absorption band around 800 nm (signature of the conductivity) was observed, indicating the successful synthesis of PEDOT: PSS.
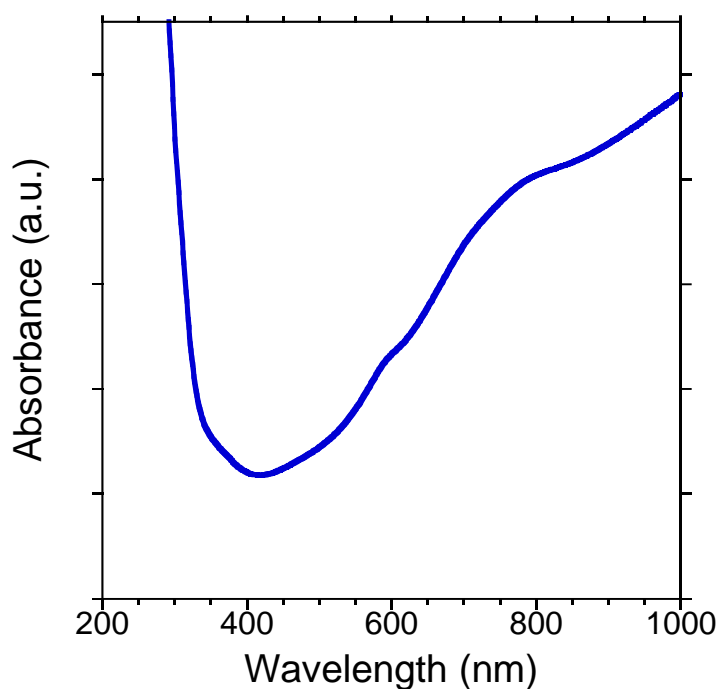
Figure 4.12. *UV-Vis spectrum of PEDOT: PSS prepared using Fe(OAc)₂.*

4.5. Conclusions

This Chapter we report the use of water-soluble self-folded metal-containing single-chain nanoparticles (SCNPs) as robust enzyme-mimic nanoreactors for the synthesis of intrinsically conducting polymers (ICPs) via step-growth polymerization. As a proof of concept, we performed the first enzyme-mimetic synthesis of poly(3,4-ethylenedioxythiophene): polystyrenesulfonate (PEDOT: PSS) dispersions via oxidative polymerization using self-folded iron(II)-containing SCNPs as efficient artificial pseudo-enzymes. The synthesis, which can be easily carried out in water at r.t for 3 h under argon atmosphere, provides with a PEDOT: PSS dispersion displaying the characteristic bipolaron UV–vis absorption band at 800 nm from conducting PEDOT. Thin films prepared from this PEDOT: PSS dispersion showed a value of electrical conductivity of $\sigma = 1\times10^{-4}$ S/cm, similar to that typically reported for PEDOT: PSS films prepared from PEDOT: PSS dispersions synthesized using iron-containing proteins like catalase ($\sigma = 1.3\times10^{-5}$ S/cm). This work opens the door to the synthesis of other types of ICPs (e.g., polyaniline, polypyrrole) using water-soluble metal-containing SCNPs as robust enzyme-mimic nanoreactors operating at r.t, and expands the use of SCNPs as bioinspired catalysts from chain-growth polymerization (i.e., ring-opening polymerization and living radical polymerization) to step-growth polymerization (i.e., polycondensation via oxidative polymerization).

4.6. References

[1] Z. Yu, Y. Xia, D. Du, J. Ouyang, PEDOT:PSS Films with Metallic Conductivity through a Treatment with Common Organic Solutions of Organic Salts and Their Application as a

Transparent Electrode of Polymer Solar Cells, ACS Applied Materials & Interfaces, 8 (2016) 11629-11638.

[2] I. Lee, G.W. Kim, M. Yang, T.-S. Kim, Simultaneously Enhancing the Cohesion and Electrical Conductivity of PEDOT:PSS Conductive Polymer Films using DMSO Additives, ACS Applied Materials & Interfaces, 8 (2016) 302-310.

[3] D. Mecerreyes, R. Marcilla, E. Ochoteco, H. Grande, J.A. Pomposo, R. Vergaz, J.M. Sánchez Pena, A simplified all-polymer flexible electrochromic device, Electrochimica Acta, 49 (2004) 3555-3559.

[4] Z. Hu, J. Zhang, Z. Hao, Y. Zhao, Influence of doped PEDOT:PSS on the performance of polymer solar cells, Solar Energy Materials and Solar Cells, 95 (2011) 2763-2767.

[5] E. Moczko, G. Istamboulie, C. Calas-Blanchard, R. Rouillon, T. Noguer, Biosensor employing screen-printed PEDOT:PSS for sensitive detection of phenolic compounds in water, Journal of Polymer Science Part A: Polymer Chemistry, 50 (2012) 2286-2292.

[6] K. Svennersten, M.H. Bolin, E.W.H. Jager, M. Berggren, A. Richter-Dahlfors, Electrochemical modulation of epithelia formation using conducting polymers, Biomaterials, 30 (2009) 6257-6264.

[7] K. Sun, S. Zhang, P. Li, Y. Xia, X. Zhang, D. Du, F.H. Isikgor, J. Ouyang, Review on application of PEDOTs and PEDOT:PSS in energy conversion and storage devices, Journal of Materials Science: Materials in Electronics, 26 (2015) 4438-4462.

[8] A.M. Nardes, M. Kemerink, M.M. de Kok, E. Vinken, K. Maturova, R.A.J. Janssen, Conductivity, work function, and environmental stability of PEDOT:PSS thin films treated with sorbitol, Organic Electronics, 9 (2008) 727-734.

[9] D. Alemu, H.-Y. Wei, K.-C. Ho, C.-W. Chu, Highly conductive PEDOT:PSS electrode by simple film treatment with methanol for ITO-free polymer solar cells, Energy & Environmental Science, 5 (2012) 9662-9671.

[10] L. Ouyang, C. Musumeci, M.J. Jafari, T. Ederth, O. Inganäs, Imaging the Phase Separation Between PEDOT and Polyelectrolytes During Processing of Highly Conductive PEDOT:PSS Films, ACS Applied Materials & Interfaces, 7 (2015) 19764-19773.

[11] T. Takano, H. Masunaga, A. Fujiwara, H. Okuzaki, T. Sasaki, PEDOT Nanocrystal in Highly Conductive PEDOT:PSS Polymer Films, Macromolecules, 45 (2012) 3859-3865.

[12] J.D. Morris, D. Khanal, J.A. Richey, C.K. Payne, Hemoglobin-mediated synthesis of PEDOT:PSS: enhancing conductivity through biological oxidants, Biomaterials Science, 3 (2015) 442-445.

[13] V. Rumbau, J.A. Pomposo, A. Eleta, J. Rodriguez, H. Grande, D. Mecerreyes, E. Ochoteco, First Enzymatic Synthesis of Water-Soluble Conducting Poly(3,4-ethylenedioxythiophene), Biomacromolecules, 8 (2007) 315-317.

[14] S. Nagarajan, J. Kumar, F.F. Bruno, L.A. Samuelson, R. Nagarajan, Biocatalytically Synthesized Poly(3,4-ethylenedioxythiophene), Macromolecules, 41 (2008) 3049-3052.

[15] J.D. Morris, K.M. Wong, C.D. Peñaherrera, C.K. Payne, Mechanism of the biomolecular synthesis of PEDOT:PSS: importance of heme degradation by hydrogen peroxide, Biomaterials Science, 4 (2016) 331-337.

[16] J.D. Morris, C.K. Payne, Tuning PEDOT:PSS conductivity with iron oxidants, Organic Electronics, 15 (2014) 1707-1710.

[17] S.M. Hira, C.K. Payne, Protein-mediated synthesis of the conducting polymer PEDOT:PSS, Synthetic Metals, 176 (2013) 104-107.

[18] J.J. Flores, C.K. Payne, J.D. Morris, Heme protein-mediated synthesis of PEDOT:PSS: enhancing conductivity by inhibiting heme degradation, RSC Advances, 7 (2017) 12017-12021.

[19] J.A. Pomposo, Single-Chain Polymer Nanoparticles: Synthesis, Characterization, Simulations, and Applications, John Wiley & Sons2017.

[20] J.A. Pomposo, Bioinspired single-chain polymer nanoparticles, Polymer International, 63 (2014) 589-592.

[21] M. Huo, N. Wang, T. Fang, M. Sun, Y. Wei, J. Yuan, Single-chain polymer nanoparticles: Mimic the proteins, Polymer, 66 (2015) A11-A21.

[22] A. Latorre-Sánchez, J.A. Pomposo, Recent bioinspired applications of single-chain nanoparticles, Polymer International, 65 (2016) 855-860.

[23] J. Rubio-Cervilla, E. González, J.A. Pomposo, Applications of Single-Chain Polymer Nanoparticles, in: J.A. Pomposo (Ed.) Single-Chain Polymer Nanoparticles: Synthesis, Characterization, Simulations, and Applications., Wiley-VCH, Weinheim, Germany, 2017, pp. 341-400.

[24] S. Mavila, O. Eivgi, I. Berkovich, N.G. Lemcoff, Intramolecular Cross-Linking Methodologies for the Synthesis of Polymer Nanoparticles, Chemical Reviews, 116 (2016) 878-961.

[25] O. Altintas, C. Barner-Kowollik, Single-Chain Folding of Synthetic Polymers: A Critical Update, Macromolecular Rapid Communications, 37 (2016) 29-46.

[26] A.M. Hanlon, C.K. Lyon, E.B. Berda, What Is Next in Single-Chain Nanoparticles?, Macromolecules, 49 (2016) 2-14.

[27] M. Gonzalez-Burgos, A. Latorre-Sanchez, J.A. Pomposo, Advances in single chain technology, Chemical Society Reviews, 44 (2015) 6122-6142.

[28] C.K. Lyon, A. Prasher, A.M. Hanlon, B.T. Tuten, C.A. Tooley, P.G. Frank, E.B. Berda, A brief user's guide to single-chain nanoparticles, Polymer Chemistry, 6 (2015) 181-197.

[29] A. Sanchez-Sanchez, J.A. Pomposo, Single-Chain Polymer Nanoparticles via Non-Covalent and Dynamic Covalent Bonds, Particle & Particle Systems Characterization, 31 (2014) 11-23.

[30] M. Artar, E. Huerta, E.W. Meijer, A.R.A. Palmans, Dynamic Single Chain Polymeric Nanoparticles: From Structure to Function, Sequence-Controlled Polymers: Synthesis, Self-Assembly, and Properties, American Chemical Society2014, pp. 313-325.

[31] A. Sanchez-Sanchez, I. Pérez-Baena, J.A. Pomposo, Advances in Click Chemistry for Single-Chain Nanoparticle Construction, Molecules, 18 (2013) 3339-3355.

[32] O. Altintas, C. Barner-Kowollik, Single Chain Folding of Synthetic Polymers by Covalent and Non-Covalent Interactions: Current Status and Future Perspectives, Macromolecular Rapid Communications, 33 (2012) 958-971.

[33] M.K. Aiertza, I. Odriozola, G. Cabañero, H.-J. Grande, I. Loinaz, Single-chain polymer nanoparticles, Cellular and Molecular Life Sciences, 69 (2012) 337-346.

[34] B.S. Murray, D.A. Fulton, Dynamic Covalent Single-Chain Polymer Nanoparticles, Macromolecules, 44 (2011) 7242-7252.

[35] A. Sanchez-Sanchez, S. Akbari, A.J. Moreno, F.L. Verso, A. Arbe, J. Colmenero, J.A. Pomposo, Design and Preparation of Single-Chain Nanocarriers Mimicking Disordered Proteins for Combined Delivery of Dermal Bioactive Cargos, Macromolecular Rapid Communications, 34 (2013) 1681-1686.

[36] J.A. Pomposo, I. Perez-Baena, F. Lo Verso, A.J. Moreno, A. Arbe, J. Colmenero, How Far Are Single-Chain Polymer Nanoparticles in Solution from the Globular State?, ACS Macro Letters, 3 (2014) 767-772.

[37] T. Terashima, T. Mes, T.F.A. De Greef, M.A.J. Gillissen, P. Besenius, A.R.A. Palmans, E.W. Meijer, Single-Chain Folding of Polymers for Catalytic Systems in Water, Journal of the American Chemical Society, 133 (2011) 4742-4745.

[38] T. Akagi, P. Piyapakorn, M. Akashi, Formation of Unimer Nanoparticles by Controlling the Self-Association of Hydrophobically Modified Poly(amino acid)s, Langmuir, 28 (2012) 5249-5256.

[39] M. Chen, C.J. Riddles, M.R. Van De Mark, Electroviscous Contribution to the Rheology of Colloidal Unimolecular Polymer (CUP) Particles in Water, Langmuir, 29 (2013) 14034-14043.

[40] T. Terashima, T. Sugita, K. Fukae, M. Sawamoto, Synthesis and Single-Chain Folding of Amphiphilic Random Copolymers in Water, Macromolecules, 47 (2014) 589-600.

[41] F. Lo Verso, J.A. Pomposo, J. Colmenero, A.J. Moreno, Simulation guided design of globular single-chain nanoparticles by tuning the solvent quality, Soft Matter, 11 (2015) 1369-1375.

[42] J. He, L. Tremblay, S. Lacelle, Y. Zhao, Preparation of polymer single chain nanoparticles using intramolecular photodimerization of coumarin, Soft Matter, 7 (2011) 2380-2386.

[43] G. Qian, B. Zhu, Y. Wang, S. Deng, A. Hu, Size-Tunable Polymeric Nanoreactors for One-Pot Synthesis and Encapsulation of Quantum Dots, Macromolecular Rapid Communications, 33 (2012) 1393-1398.

[44] B. Zhu, S. Sun, Y. Wang, S. Deng, G. Qian, M. Wang, A. Hu, Preparation of carbon nanodots from single chain polymeric nanoparticles and theoretical investigation of the photoluminescence mechanism, Journal of Materials Chemistry C, 1 (2013) 580-586.

[45] I. Perez-Baena, F. Barroso-Bujans, U. Gasser, A. Arbe, A.J. Moreno, J. Colmenero, J.A. Pomposo, Endowing Single-Chain Polymer Nanoparticles with Enzyme-Mimetic Activity, ACS Macro Letters, 2 (2013) 775-779.

[46] A. Sanchez-Sanchez, A. Arbe, J. Kohlbrecher, J. Colmenero, J.A. Pomposo, Efficient Synthesis of Single-Chain Globules Mimicking the Morphology and Polymerase Activity of Metalloenzymes, Macromolecular Rapid Communications, 36 (2015) 1592-1597.

[47] Y. Azuma, T. Terashima, M. Sawamoto, Self-Folding Polymer Iron Catalysts for Living Radical Polymerization, ACS Macro Letters, 6 (2017) 830-835.

Chapter 5: Fast and Efficient Synthesis of Highly Fluorescent Single-Chain Nanoparticles

5.1. Motivation

The development of highly fluorescent nanoparticles is of great interest for a variety of practical applications including new generation biological sensors, innovative chemical probes, improved optoelectronic devices, and intelligent materials. In this Chapter we report an original method toward the fast and efficient synthesis of highly fluorescent SCNPs based on the efficient use of aggregation-induced emission (AIE) cross-linking fluorophores.

5.2. Introduction

Single-chain polymer nanoparticles (SCNPs) are soft nanomaterials constructed via intra-chain cross-linking of individual precursor polymer chains [1-7], with promising prospects for nanomedicine [8-11], catalysis [12-19], sensing [20, 21], and other different application fields [22]. The SCNP local pockets formed upon chain collapse at high dilution provide a unique (and tunable) environment for attachment -either temporally or permanently- of active species, such as drugs, catalytic metal ions, or dyes [23, 24]. Moreover, SCNPs are promising building blocks for the construction of new fluorescent probes with ultra-small size, higher brightness, and better photostability than previous particle-based systems.

In general, fluorescent nano-probes are receiving enthusiastic pursuits from medical scientists because of their promising potential applications in cell imaging, targeting, tracing, and therapeutics [25]. Conventional luminescent nanoparticles are mainly based on inorganic quantum dots [26], lanthanide ion doped nanomaterials [27], and metallic nanoclusters [28] because of their excellent photostability with narrow emission, sub-nanometer size, and superior upconversion performance, although potential toxicity issues and poor biodegradability have largely hindered their common employment in biomedical applications [29].

Even if the field of SCNPs is still very incipient, a variety of fluorescent SCNPs have been synthesized through four different synthetic approaches based on common, traditional fluorophores [30]: (i) functionalization of the SCNP precursor polymer with a conventional fluorophore molecule before intra-chain cross-linking [31]; (ii) physical entrapment of an external traditional fluorophore molecule into non-fluorescent SCNPs [32] or in situ generation of this fluorophore molecule inside the SCNP [33]; (iii) post-functionalization of the SCNP surface via chemical reaction with appropriate, complementary reactive fluorophore molecules [34]; and (iv) generation of fluorophore functional moieties through intramolecular crosslinking [35].

In spite of recent advances in this field, to the best of our knowledge, the use of aggregation-induced emission (AIE) cross-linking fluorophores [36] to endow SCNPs with fluorescent properties has not been investigated yet. AIE compounds [37] are opposite to conventional fluorescent probes which often suffer from the well-known (and deleterious) aggregation-caused quenching (ACQ) effect [38]. On the contrary, AIE molecules- as first described by Tang and co-workers [39] in 2001-are nearly non-emissive compounds in solution but become highly fluorescent upon restriction of their intramolecular rotations (the so-called RIR mechanism [37]). In short, AIE fluorophores usually show very weak fluorescence or non-emissivity when molecularly dissolved in a good solvent, but are highly emissive when

aggregated -or after molecular immobilization- because of the restriction of the intramolecular rotation in the aggregate (immobilized) state leading the excitations to decay radiatively. There are several practical applications of AIE compounds in biological sensors, chemical probes, optoelectronic devices, and intelligent materials [36-38].

Currently, the development of fluorescent polymers and nanomaterials based on AIE probes is a field of intense activity [40-54]. Hexaphenyl silole (HPS) is the archetypal form of AIE luminogen. The HPS molecule consists of a silole core attached to six phenyl rings. Like in other AIEgens the phenyls (rotors) can rotate against the silole ring (stator) via the single-bond axes. In the solutions, the intramolecular rotation is active, which serves as a relaxation channel for the excited state to decay. In the aggregates, the rotation is restricted due to the physical constraint, which blocks the non-radiative path and activates the radiative decay. HPS is soluble organic solvents like acetonitrile, tetrahydrofuran (THF) and chloroform, but is insoluble in water [38].

This property can be generalized to other silole derivatives. Silole derivatives are non-polar hydrophobic molecules. They contain no polar moieties such as donor and acceptor functional groups. Some of these derivatives contain reactive functional groups that allow them to attach to polymers forming fluorescent SCNPs. One example is 1,1-dimethyl-2,5-bis(4-(azidomethyl)phenyl)-3,4-diphenylsilole (**Silole-N$_3$**). The **Silole-N$_3$** molecule is similar to HPS, but the two phenyl rings bound to the silicon are substituted by methyl groups and two of the four phenyl rings are functionalized by azides. These azides are very reactive under appropriate reaction conditions.

In this chapter, we will investigate a new photoactivation strategy developed for AIE cross-linking molecules containing azide moieties allowing the fast and efficient synthesis at room temperature (r.t.) of highly fluorescent SCNPs in solution showing excellent stability of the fluorescence emission intensity over time. A further motivation of this work is the synthesis of SCNPs showing fluorescent properties also in the solid state, i.e., free from ACQ effects often observed for SCNPs based on traditional fluorophores.

5.3. Experimental procedures

5.3.1. Materials

Methyl methacrylate (MMA) (99%), (2-acetoacetoxy)ethyl methacrylate (AEMA) (95%), 2.2′-azo(2-methylpropionitrile) (AIBN) (≥98%), p-carboxybenzenesulphonazide (p-CBSA) (97%), triethylamine (Et$_3$N) (>99%), HPS (98%), 1,1-dimethyl-2,5-bis(4-(azidomethyl)phenyl)-3,4-diphenylsilole (**Silole-N$_3$**) (96%), ethyl acetate (EtOAc) (anhydrous, 99.8%), diethyl ether (Et$_2$O) (ACS reagent, anhydrous, >99.0%), dichloromethane (CH$_2$Cl$_2$) (anhydrous, ≥99.8%), and deuterated chloroform (CDCl$_3$) (99.96 atom % D, containing 0.03% (*v/v*) tetramethylsilane) were purchased from Sigma-Aldrich and used, unless specified, as received. 2-Cyanoprop-2-yl-dithiobenzoate (CPDB) (≥97%) was purchased from Strem Chemicals. Methanol (MeOH) (synthesis grade) and tetrahydrofuran (THF) (HPLC grade) were purchased from Scharlab. AIBN was recrystallized from methanol. MMA was purified by distillation before use. AEMA was purified by passing through alumina.

5.3.2. Techniques

Experimental UV irradiation setup

UV irradiation experiments were performed using a Hamamatsu UV spot light source (LC8, Hg−Xe Lamp, UV intensity: 3.5 W/cm^2) equipped with an A9616-05 filter [transmittance wavelength: 300−400 nm (λ_{max} = 365 nm); transmitted intensity: 80%] and the corresponding UV-light guide. The distance from the guide to the solution containing the SCNP precursor was 10 cm. The open area during irradiation was 2 cm^2. A picture of the experimental setup is available in Figure 5.1.
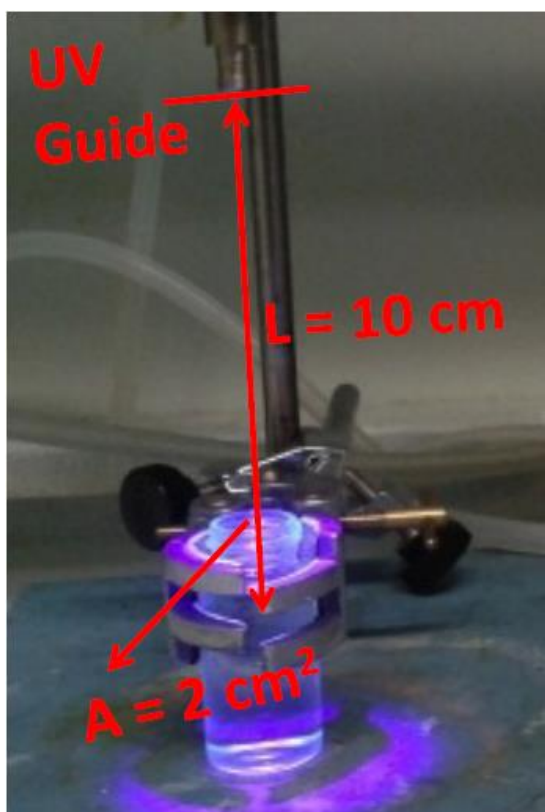
Figure 5.1. *Illustration of the experimental set-up employed for photoactivated synthesis of single-chain polymer nanoparticles (SCNPs) (SI from ref.[55]).*

Characterization techniques

Size exclusion chromatography (SEC) measurements were performed at 30 °C on an Agilent 1200 system equipped with PLgel 5 µm Guard and PLgel 5 µm MIXED-C columns, and triple detection: a differential refractive index detector (Optilab Rex, Wyatt), a MALLS detector (MiniDawn Treos, Wyatt), and a viscosimetric (VIS) detector (ViscoStar-II, Wyatt). Data analysis was performed with ASTRA Software (version 6.1) from Wyatt. THF was used as an eluent at a flow rate of 1 ml/min. A value of *dn/dc* = 0.083 was used for precursors and SCNPs.

^{1}H NMR spectra were recorded at r.t. on a Bruker spectrometer operating at 400 MHz, using CDCl$_3$ as a solvent. AEMA content was determined following the procedure described in the results section 5.4 [56].

Fourier-transform infrared (FTIR) spectra were recorded at r.t. on a JASCO 3600 FTIR spectrometer.

Elemental analysis (EA) measurements were performed in a Euro EA3000 elemental analyser (CHNS).

Photoluminescence spectra were recorded at r.t. on an Agilent Cary Eclipse spectrometer at an excitation wavelength of 364 nm.

Transmission electron microscopy (TEM) measurements were performed using a high-resolution transmission electron microscope TECNAI G220 TWIN. The measurements were carried out using an accelerating voltage of 200 kV under low dose conditions.

Ultraviolet-visible measurements were performed in an Agilent 8453A UV-Vis spectrometer with Peltier thermostatic cell holder T-controller 89096A.

Fluorescence Quantum Yield Determination

The Fluorescence Quantum Yield (Φ) of fluorescent nanoparticles **FNP** was determined by employing 2 different standards: Coumarin 1 in ethanol and 9,10-diphenylanthracene (DPA) in ethanol. The standards were cross-calibrated. The absorbance and fluorescence of **FNP** samples and standards were measured at different concentrations and Fluorescence vs. Absorbance plots were built. Absorbance was measured by UV-Vis spectroscopy.

5.3.3. Procedures

5.3.3.1. Synthesis of the copolymer

In a typical procedure [16], MMA (1 ml, 9.4 mmol), AEMA (0.6 ml, 3.1 mmol), CPDB (0.8 mg, 3×10^{-2} mmol) and (AIBN) (1 mg, 3×10^{-2} mmol) were dissolved in ethyl acetate (4.5 ml). The reaction mixture was degassed by passing argon for 15 min. The copolymerization reaction was carried out at 65 ºC for 18 h (see Scheme 5.1). The resulting poly(MMA-co-AEMA) copolymer **C** was isolated by precipitation in methanol and further drying (**C**: weight average molecular weight, M_w (SEC/ MALLS) = 189 kDa; polydispersity, $Đ$ = 1.25; molar fraction of AEMA units (^{1}H NMR) = 32%, x = 0.32). Reaction conditions of the synthesis of copolymers are annotated in Table 5.1.
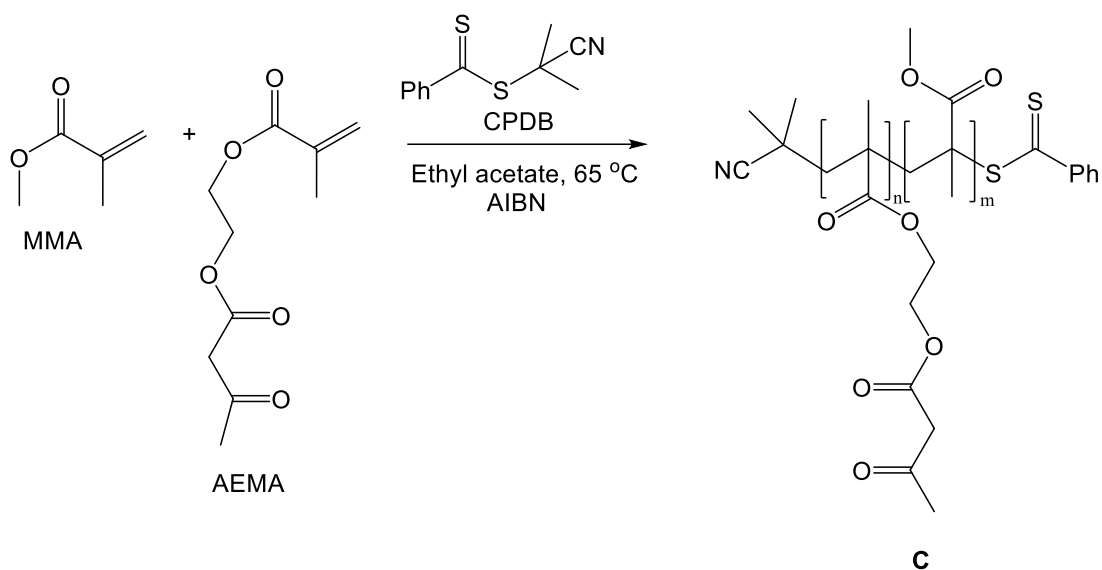
Scheme 5.1. *Representation of the synthesis of poly (MMA-co-AEMA) copolymer **C**.*

Table 5.1. *Amount of reagents (MMA, AEMA, CPDB, AIBN and EtOAc) used for the synthesis of poly(MMA-co-AEMA) copolymers and characterization data (M_w and AEMA content).*

MMA (ml)	1	1	1
AEMA (ml)	0.6	0.6	0.6
CPDB (mg)	7.5	1.6	0.8
AIBN (mg)	1.4	1	1
EtOAc (ml)	3	4	4.5
M_w (kDa)	52.8	104.2	188.8
AEMA content (mol %)	26.6	28.3	31.9

MMA = Methyl methacrylate; AEMA = 2-acetoacetoxy)ethyl methacrylate; CPDB = 2-cyanoprop-2-yl-dithiobenzoate; AIBN = 2.2′-azo(2-methylpropionitrile); EtOAc = ethyl acetate; M_w = molar mass; AEMA content = percentage of AEMA monomers in the copolymers.

5.3.3.2. Functionalization of the precursor

The whole functionalization reaction of copolymer **C** was performed protected from light. In a typical procedure, a random copolymer of MMA and AEMA (485 mg, 0.77 mmol) prepared according to the methodology reported in the previous section [16] (**C**: weight average molecular weight, M_w (SEC/MALLS) = 189 kDa; polydispersity, $Đ$ = 1.25; molar fraction of AEMA units (^{1}H NMR) = 32%, x = 0.32) was dissolved in CH_2Cl_2 (10 mL) at r.t. Then, p-CBSA (250 mg, 1.1 mmol) and Et_3N (0.4 mL, 2.87 mmol) were added, and the mixture was maintained under stirring for 24 h (see Scheme 5.2). After reaction, the solution was concentrated and precipitated in MeOH and the resulting nanoparticle

precursor **P** was dried in a vacuum oven in the dark [**P**: Yield = 73%; M_w (SEC/MALLS) = 289 kDa; $Đ$ = 1.24; molar fraction of α-diazo-β-ketoester units (EA) = 23%, y = 0.23; radius of gyration, R_g (SEC/MALLS) = 17.9 ± 1.0 nm; hydrodynamic radius, R_h (SEC/VIS) = 11.4 ± 0.1 nm].
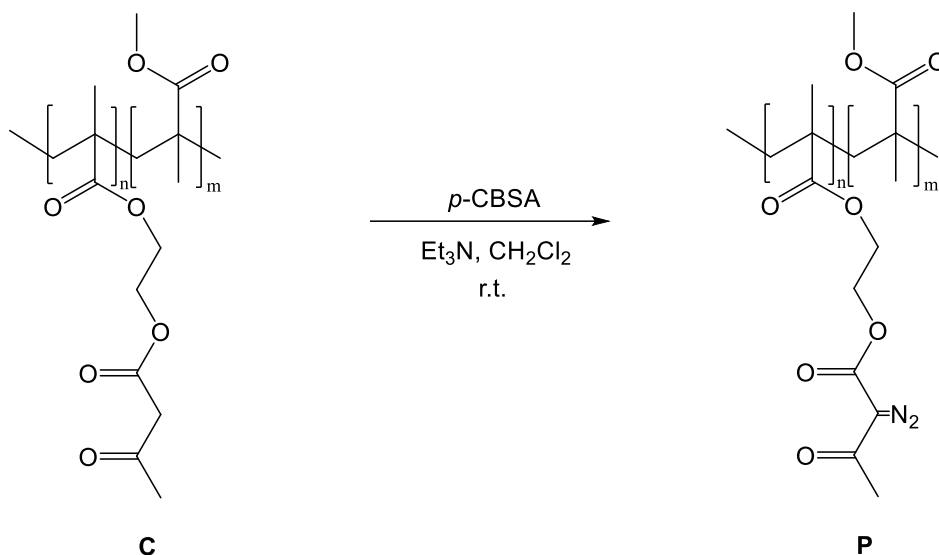
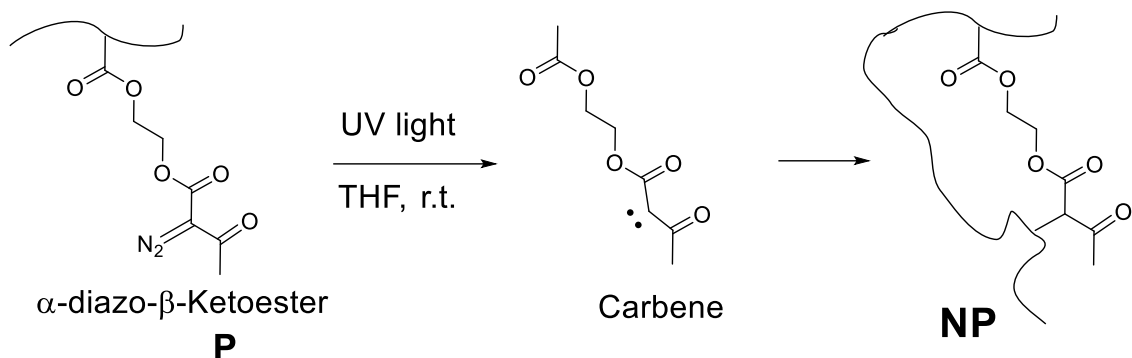**Scheme 5.2.** *Schematic illustration of the synthesis of precursors* **P**.

5.3.3.3. Synthesis of single-chain polymer nanoparticles in the presence of HPS

In a typical reaction, precursor **P** (6 mg, 9.5×10^{-3} mmol) and HPS (2.6 mg, 4.75×10^{-3} mmol, Scheme 5.3) were dissolved in CH_2Cl_2 (12 ml) at r.t. and the solution was subject to UV light irradiation through an open area of 2 cm^2 in the 300−400 wavelength range (λ_{max} = 365 nm) for 60 min (Scheme 5.4). The resulting (non-fluorescent) SCNPs **NP** were purified by precipitation in Et$_2$O and further drying in a vacuum oven [**NP**: Yield = 72%, M_w (SEC/MALLS) = 290 kDa; $Đ$ = 1.25; R_g (SEC/MALLS) = 7.3 ± 1.1 nm, R_h (SEC/VIS) = 9.5 ± 1.1 nm].
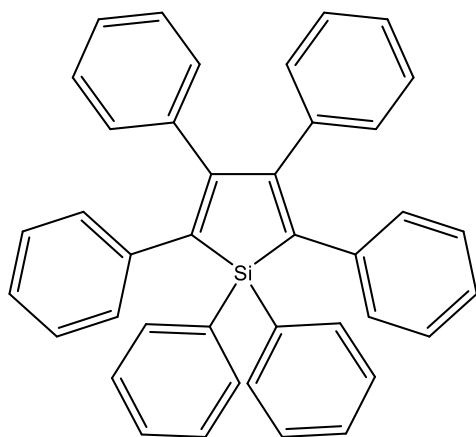
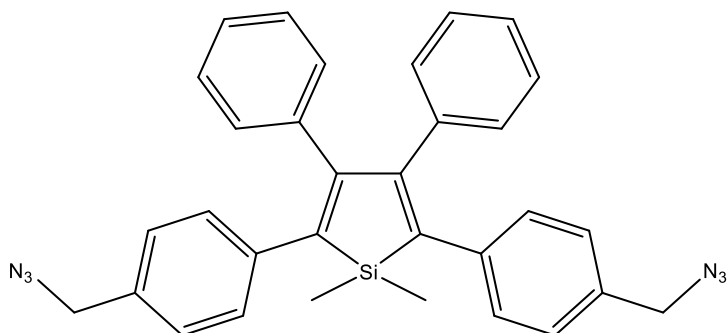**Scheme 5.3.** *Chemical structure of hexaphenyl silole* *(HPS).*

Scheme 5.4. *Illustration of the synthesis of single-chain nanoparticles* **NP**.

5.3.3.4. Synthesis of single-chain polymer nanoparticles in the presence of Silole-N₃

In a typical reaction, precursor **P** (6 mg, 9.5×10^{-3} mmol) and **Silole-N₃** (2.5 mg, 4.75×10^{-3} mmol, Scheme 5.5) were dissolved in CH_2Cl_2 (12 mL) at r.t. and the solution was subject to UV light irradiation ($\lambda_{max} = 365$ nm) for 60 min (Scheme 5.6). The resulting highly fluorescent SCNPs **FNP** were purified by precipitation in Et_2O and further drying in a vacuum oven [**FNP**: yield $= 78\%$, M_w (SEC/MALLS) $= 330$ kDa; $Đ = 1.26$; R_g (SEC/MALLS) $= 6.2 \pm 2.0$ nm, R_h (SEC/VIS) $= 9.0 \pm 0.3$ nm; fluorescent quantum yield, Φ (in THF) $= 0.065$ (see section 5.4.3 for details)].

Scheme 5.5. *Chemical structure of 1,1-dimethyl-2,5-bis(4-(azidomethyl)phenyl)-3,4-diphenylsilole (Silole-N₃).*
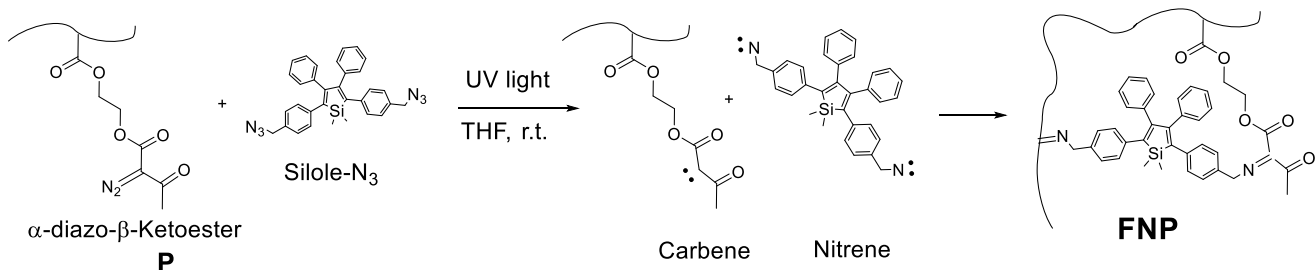

Scheme 5.6. *Illustration of the synthesis of fluorescent single-chain nanoparticles* **FNP**.

5.4. Results and discussion

We investigate in this work a new strategy toward highly fluorescent SCNPs based on the combined photoactivation of an AIE cross-linking compound containing azide functional groups, Silole-N_3, and a precursor **P** containing α-diazo-β-ketoester units (see Scheme 5.2).

Precursors **P** were prepared from copolymers **C** synthesized through reversible addition-fragmentation chain-transfer reaction (RAFT polymerization). Due to the similar reactivity of MMA and AEMA statistical copolymer ratios were obtained in all cases. Consequently, the β-ketoester functional groups of the AEMA monomer were randomly distributed in these copolymers [56]. ^{1}H NMR spectra of copolymers were in agreement with the chemical structure reported in the literature [16]. Copolymer composition was calculated based on the MMA/AEMA ratio of copolymers as measured by ^{1}H NMR. MMA/AEMA ratios were taken from the normalized integrated areas of the e, d and f, b peaks (Figure 5.2 A) of the ^{1}H NMR spectra.

Concerning precursor **P**, it was prepared from **C** via diazo transfer reaction (as described in the section 5.3.3.2: Functionalization of the precursor). Some broadening was observed in the ^{1}H NMR peaks of precursors **P** (Figure 5.2 B) compared to the copolymer **C**.
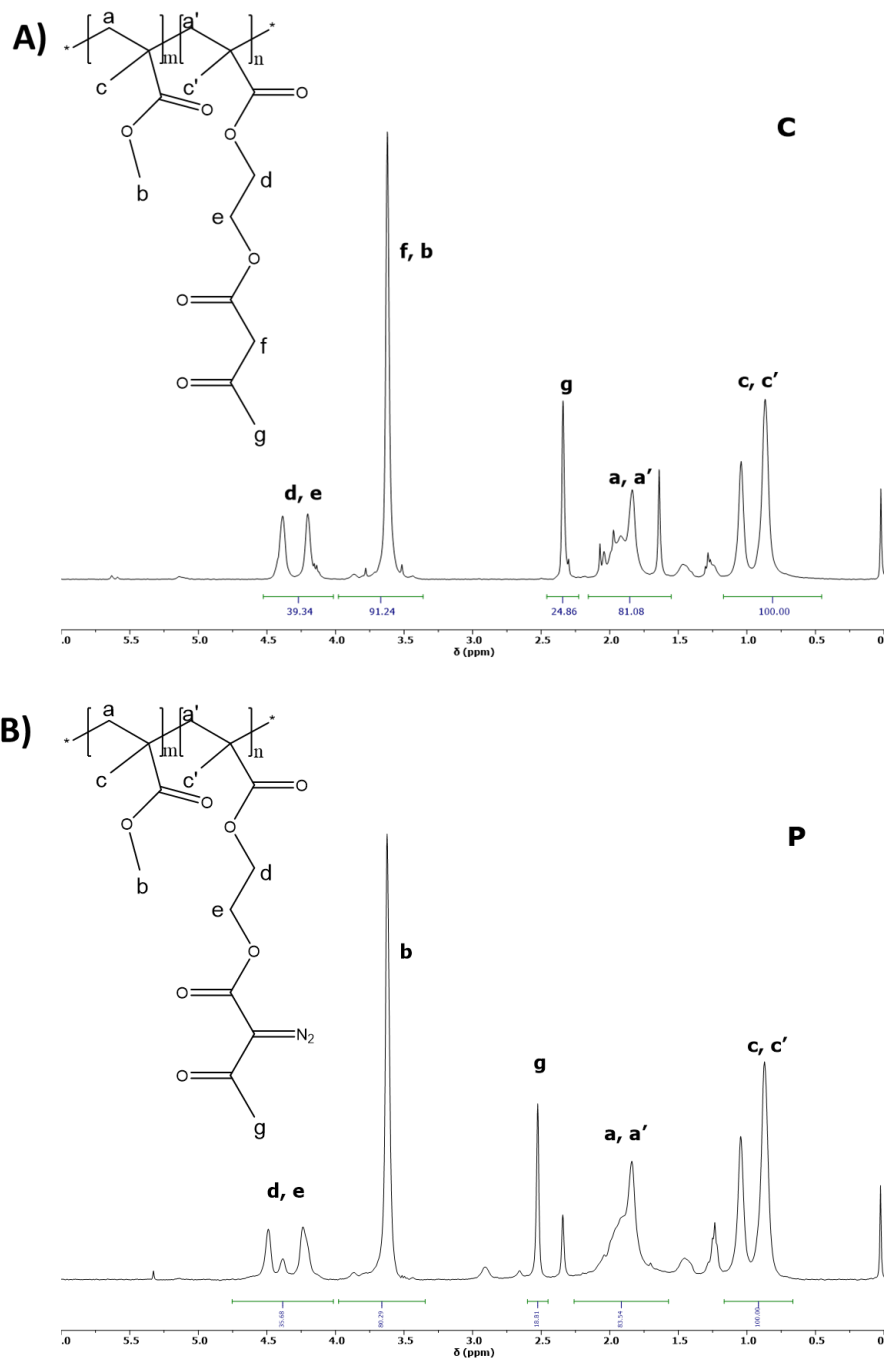
Figure 5.2. ¹H NMR spectra of **C** (A) and **P** (B), where **C** denotes the initial random copolymer of MMA and AEMA, and **P** is the precursor of the SCNPs prepared from **C** via diazo transfer reaction.

The elemental composition of copolymer **C** and precursor **P** containing α-diazo-β-ketoester functional groups was determined by microanalysis. The measured elemental composition was in all cases in good agreement with the theoretical one (Table 5.2).

Table 5.2. Comparison of theoretical (theo) and experimental (exp) content of carbon, hydrogen and nitrogen of copolymer **C** and precursor **P**.

Sample	Carbon (%)	Hydrogen (%)	Nitrogen (%)
Copolymer C (theo)	58.02	7.32	0
Copolymer C (exp)	57.86	7.20	0.01
Precursor P (theo)	54.70	6.45	6.17
Precursor P (exp)	54.78	6.47	4.37

Conversion of the diazo transfer reaction: $(4.37 / 6.17) \times 100 \approx 71$ %.

AIE compounds are a new kind of fluorophores that are nearly non-emissive molecules in solution but become highly emissive when aggregated or are immobilized because of the restriction of intramolecular rotations leading the excitations to decay radiatively [36-39]. We hypothesized that by generating a combination of both highly reactive nitrene [57] species (from **Silole-N₃**) and highly reactive carbene [58] species (from precursor **P**) via UV irradiation, the probability of efficient immobilization of the AIE compound in the resulting SCNP will increase considerably, when compared to the use of an AIE compound without azide functional groups (hexaphenylsilole, HPS). To confirm this hypothesis, we performed two complementary experiments (Figure 5.3).
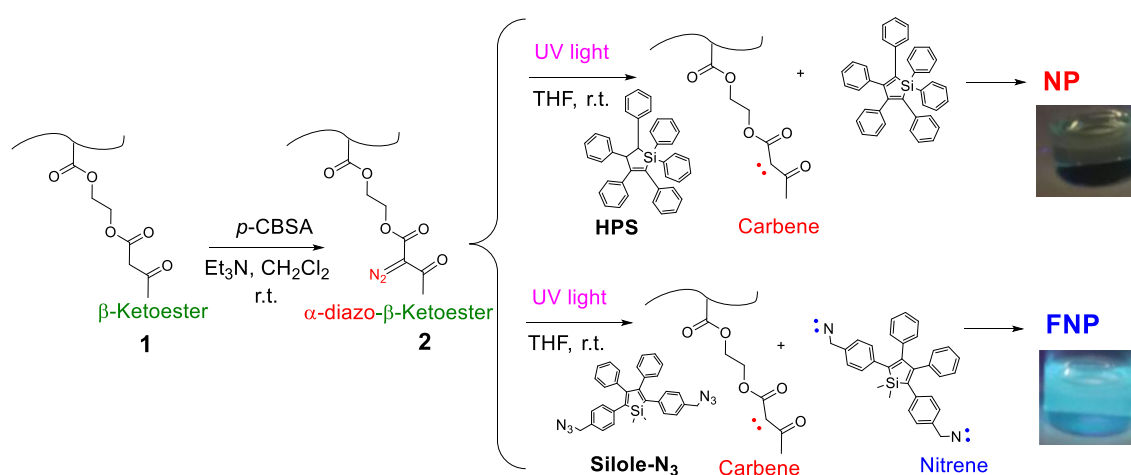

Figure 5.3. Synthesis of single-chain nanoparticles from precursor **P** in the presence a non-functional AIE molecule (HPS) gives to essentially non-fluorescent materials (**NP**), whereas using a bifunctional aggregation induced emission (AIE) compound (**Silole-N₃**) the resulting single-chain nanoparticles (**FNP**) displayed highly fluorescent properties.

5.4.1. Control reaction with HPS

In a control experiment, we placed precursor **P** in the CH_2Cl_2 solvent at high dilution (0.5 mg/mL) in the presence of HPS (AIE compound without azide functional groups). We employed a molar ratio of HPS to α-diazo-β-ketoester units of 1/2. As illustrated below,

even if efficient SCNP formation was observed by size exclusion chromatography (SEC) due to an increase in retention time upon chain compaction (Figure 5.4), the resulting SCNPs **NP** were found to be essentially non-fluorescent nanomaterials (Figure 5.8).
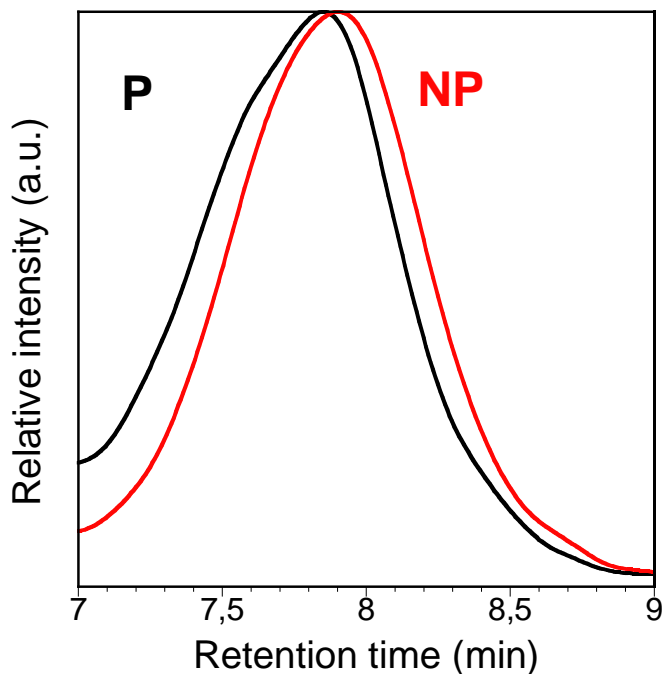
*Figure 5.4. Size exclusion chromatography (SEC) traces of **P** and **NP** showing an increase in retention time upon chain compaction, which supports the formation of SCNPs.*

In this case, upon irradiation of the α-diazo-β-ketoester units of precursor **P**, highly reactive carbene species were generated (see below) accompanied by N_2 formation and further N_2 release from the solution. The resulting carbenes -which have high tendency to react through many different pathways [58]- promoted intra-chain cross-linking reactions leading to the observed chain compaction.

Confirmation of successful photoinduced carbene generation from precursor **P** was obtained through complementary Fourier transform infrared (FTIR) spectroscopy and elemental analysis (EA) measurements, as illustrated in Figure 5.5 and summarized in Table 5.3.
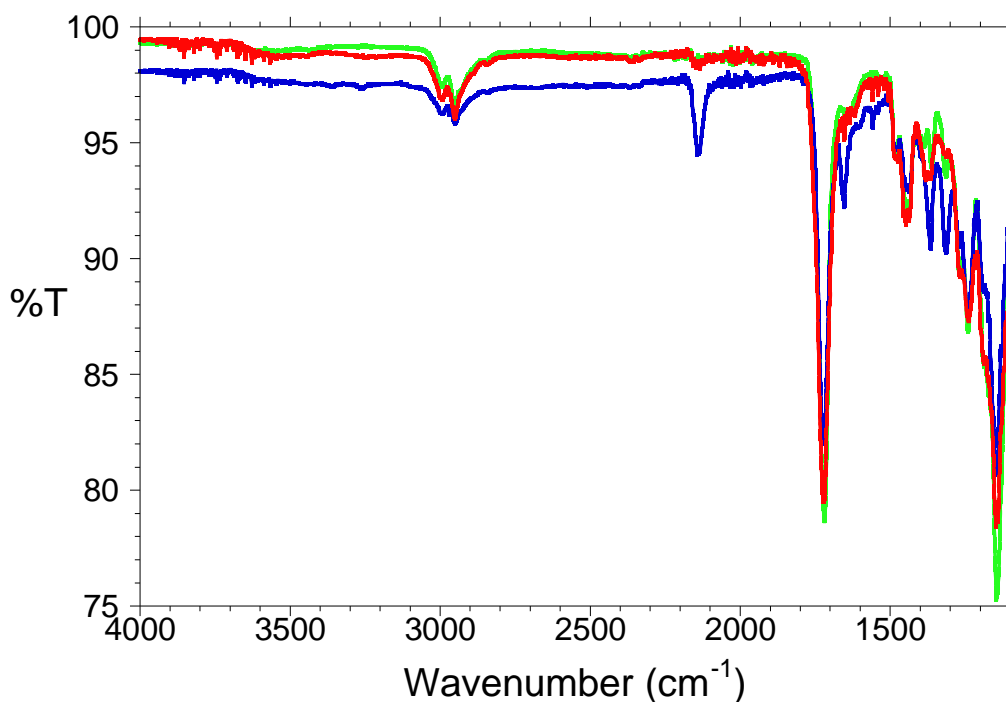
Figure 5.5. *FTIR spectra of precursor **P** (in blue colour) and **NP** (in red colour) showing the complete disappearance of the infra-red vibration band associated to the diazo moieties located at $v \approx 2200$ cm^{-1} upon carbene formation during UV irradiation of **P** in the presence of HPS for 60 min. The FTIR spectrum of the initial copolymer of MMA and AEMA units **C** used to synthesize **P** is also included (in green colour) for comparison.*

Table 5.3. Efficiency of Carbene Generation as Determined by Elemental Analysis (EA)

Sample	Nitrogen (wt %)
P (exp)	4.37
NP (theo)	0.00[a]
NP (exp)	0.42[b]

[a] By assuming an efficiency of carbene generation of 100 %.

[b] Efficiency of carbene generation: [(4.37 – 0.42) / 4.37] × 100 = 90.4 %.

Consequently, even if carbene generation was proved to be successful (efficiency of carbene generation >90%), most of the subsequent carbene C−H insertion reactions [58] were intra-chain reactions without allowing immobilization of a significant amount of external HPS molecules. To the best of our knowledge, this is the first report of SCNPs (although without fluorescence properties) synthesized through photo-activated carbene generation.

^{1}H-NMR spectra of SCNPs showed broadening of the peaks due to crosslinking.

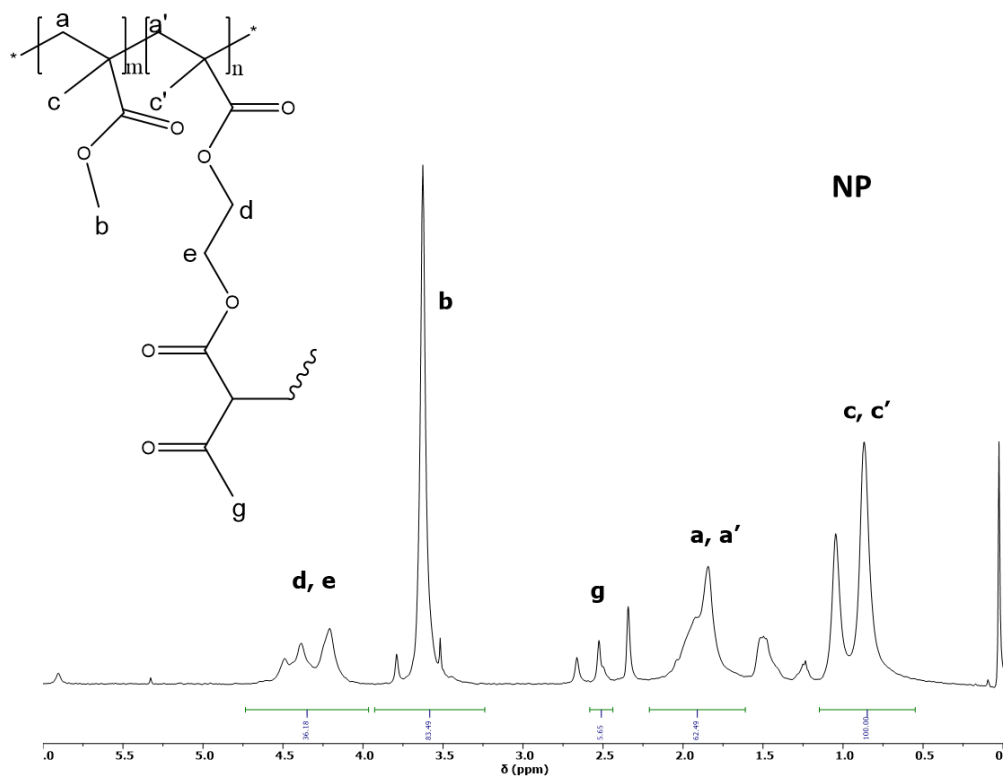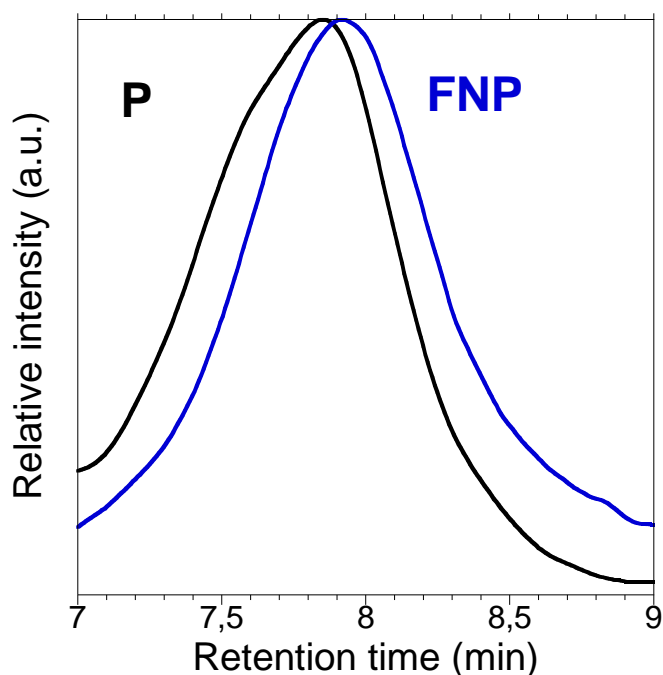*Figure 5.6. ¹H NMR spectrum SCNPs **NP** prepared from poly(MMA-co-AEMA) copolymers.*

5.4.2. Fluorescent SCNP synthesis

On the other hand, when the synthesis was performed under exactly the same conditions but replacing HPS by **Silole-N₃**, single-chain polymer nanoparticles endowed with highly fluorescent properties (FNP) were obtained (see Figure 5.3, Figure 5.7 and Figure 5.8).

*Figure 5.7. SEC traces of **P** and **FNP** showing an increase in retention time upon single-chain nanoparticle formation.*
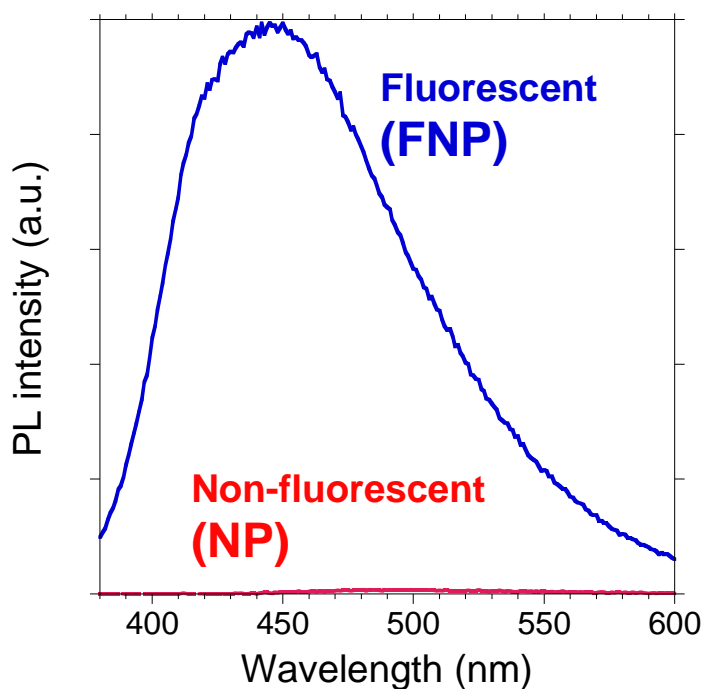
*Figure 5.8. Fluorescence emission spectra of **NP** and **FNP** in solution (solvent: THF, concentration: 1 mg/ml).*

These complementary experiments confirmed that the presence of the azide moiety in the AIE compound -that generates highly reactive nitrene species upon UV irradiation- is essential for **FNP** to display intense fluorescence emission. The progressive compaction of precursor **P** in the presence of **Silole-N₃** upon increasing the UV irradiation time is shown in Figure 5.9, as determined by SEC experiments.
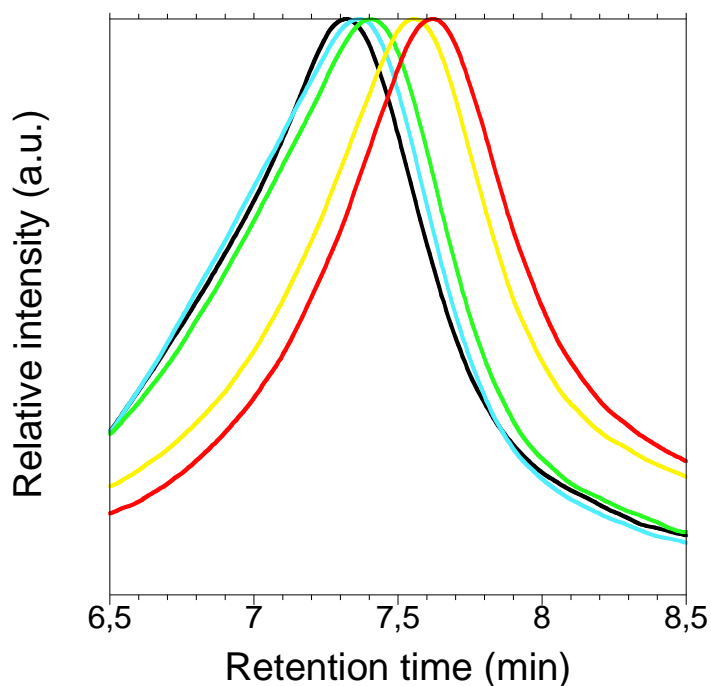
*Figure 5.9. SEC/MALLS traces of precursor **P** upon UV irradiation in the presence of **Silole-N₃** for: 0 (black line), 15 (blue line), 30 (green line), 60 (yellow line) and 120 (red line) min. showing its progressive chain compaction upon formation of **FNP**.*

The increase in retention time observed by SEC is a consequence of the reduction in hydrodynamic size of precursor **P** because of intramolecular cross-linking [59] upon the simultaneous generation of highly reactive nitrene and carbene species. The unimolecular (single-chain) nature of **FNP** was confirmed through absolute M_w measurements, using multi-angle laser light scattering (MALLS) detection during the SEC experiments [60] (see Table 5.4).

Table 5.4. Absolute weight average molecular weight, radius of gyration and hydrodynamic radius of precursor P as a function of UV Irradiation time, as determined by SEC with triple detection

UV irradiation time (min)	t_r (min)[a]	M_w (10^5 Da)[b]	R_g (nm)[b]	R_h (nm)[c]
0	7.348	2.89 ± 0.1	17.9 ± 1.0	11.4 ± 0.1
15	7.381	2.75 ± 0.1	11.4 ± 1.2	10.0 ± 0.2
30	7.413	3.95 ± 0.1	12.6 ± 1.0	10.6 ± 0.1
60	7.561	3.3 ± 0.1	6.2 ± 2.0	9.0 ± 0.3
120	7.626	3.23 ± 0.1	-	7.8 ± 0.5

[a]SEC retention time at peak maximum.

[b]As determined by GPC with MALLS detection.

[c]As determined by GPC with VIS detection.

Hence, upon SCNP formation, an increase in M_w was observed that can be attributed (within the experimental uncertainty of the MALLS technique) to the progressive immobilization of Silole-N_3 molecules in the nanoparticles. Concomitantly, a reduction in both the average values of radius of gyration (R_g) and hydrodynamic radius (R_h) of precursor **P** was observed (Table 5.4), as a consequence of its collapse to SCNPs. This behaviour is in good agreement with previous results reported in the literature [22].

Measurements of SCNPs with dynamic light scattering (DLS) measurements of precursor polymers **P** and SCNPs show particle sizes in agreement with those measured by SEC (Figure 5.10)
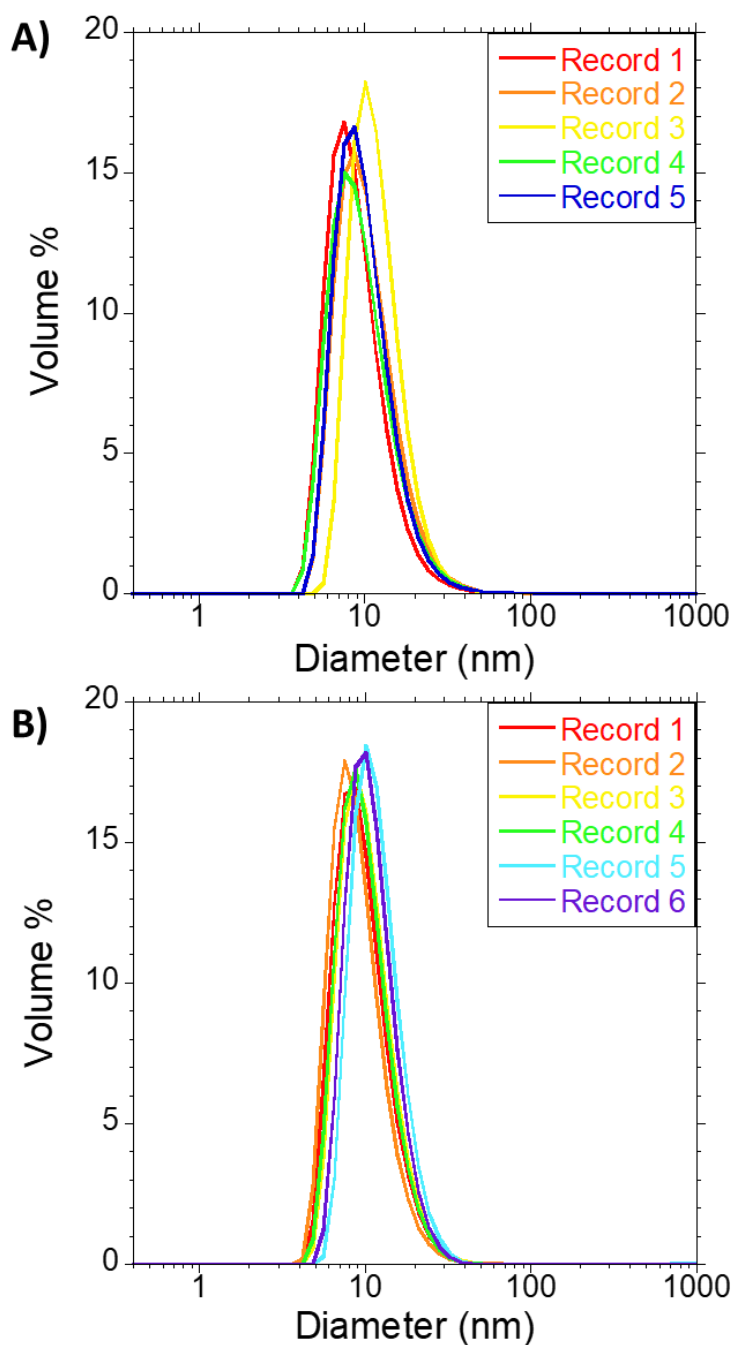
Figure 5.10. *Size distribution (volume distribution) of α-diazo-β-ketoester precursor **P** (**A**) and fluorescent SCNPs **FNP** after irradiation with UV light for 2h (**B**) in THF measured by dynamic light scattering.*

Figure 5.11 A illustrates the fluorescent properties of the resulting **FNP** in the tetrahydrofuran (THF) solution as determined by fluorescence spectroscopy (FS). The maximum fluorescence emission was obtained for nanoparticles generated after 60 min of UV irradiation time (Figure 5.11 B), and it was located at $\lambda_{em} \approx 455$ nm by using $\lambda_{ex} = 364$ nm, with a fluorescent quantum yield of $\Phi = 0.065$ (see section 5.4.3: Fluorescence quantum yield determination). Above this optimum photo-irradiation time during synthesis, a decrease in fluorescence emission intensity was observed that could be a consequence either of morphological transitions [61] or to photo-degradation of the AIE compound via secondary reactions.

117
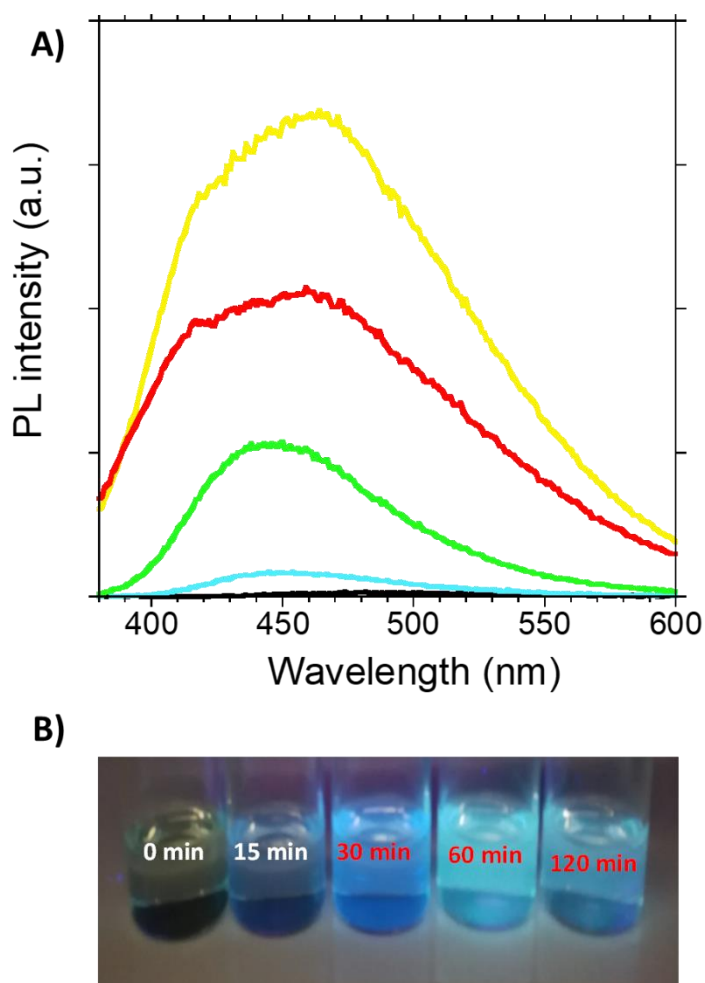
Figure 5.11. A) *Fluorescent properties of precursor* **P** *upon UV irradiation in the presence of* **Silole-N₃** *for: 0 (black line), 15 (blue line), 30 (green line), 60 (yellow line) and 120 (red line) min.* **B)** *The maximum fluorescence was observed for single-chain nanoparticles* **FNP** *synthesized after 60 min. of UV irradiation.*

To determine if a change in morphology was taking place at long UV irradiation times, SCNPs **FNP** obtained after 60 and 120 min of UV irradiation were visualized, after solvent removal, by transmission electron microscopy (TEM). It is worth of mention that characterization of SCNPs by TEM is a highly complicated task because of the change in conformation often observed upon solvent removal, the unavoidable nanoparticle—substrate interactions, and the presence of locally compact domains [62]. As illustrated in Figure 5.12, no significant change in the (near-spherical) SCNP shape was visible by TEM, so we can tentatively attribute the reduction in fluorescence emission intensity after prolonged UV irradiation to competitive photo-degradation reactions. Nevertheless, more studies-out of the scope of the current work-are required to confirm this assumption.
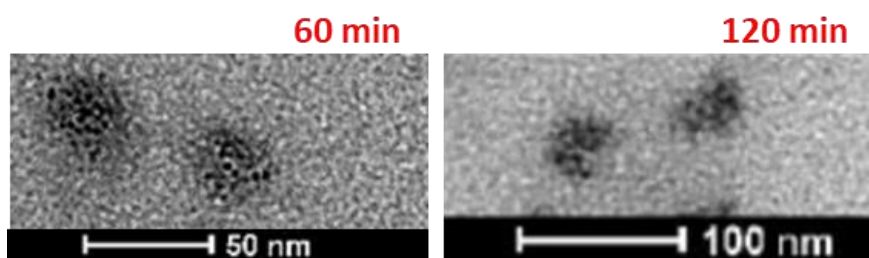
Figure 5.12. *TEM images of isolated SCNPs* **FNP** *synthesized after 60 min (scale bar: 50 nm) and 120 min (scale bar: 100 nm) of UV irradiation time.*

It is worth mentioning that purification of **FNP** from potentially unreacted Silole-N$_3$ molecules was highly facilitated by the excellent solubility of **Silole-N$_3$** in Et$_2$O (a precipitant for **FNP**). In addition to efficient nitrene generation from the azide-containing AIE compound, confirmation of successful carbene generation from α-diazo-β-ketoester units upon UV irradiation of precursor **P** was obtained from FTIR spectroscopy measurements, as illustrated in Figure 5.13. Hence, upon SCNP formation, the complete disappearance of the FTIR vibration band associated with the diazo moieties ($\nu \approx 2200$ cm^{-1}) was observed.
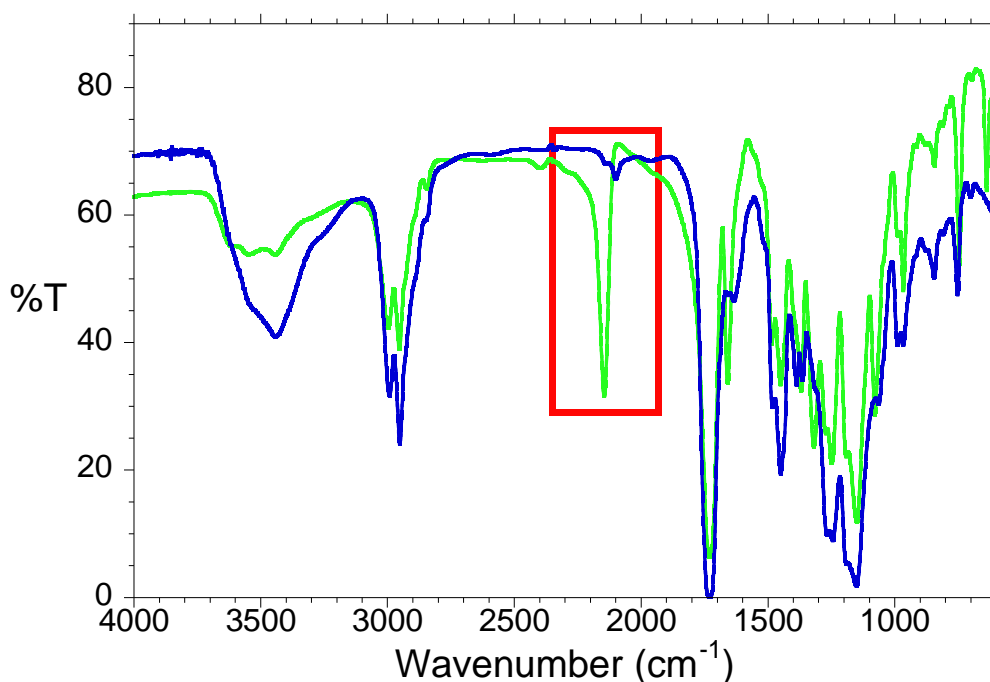
Figure 5.13. *Illustration of the disappearance of the infrared vibration band associated with the diazo moieties ($\nu \approx 2200$ cm^{-1}) of precursor* **P** *(green trace) after the formation of SCNP* **FNP** *(blue trace).*

Finally, the excellent stability of the fluorescence emission intensity of the purified **FNP** over time in solution is shown in Figure 5.14 A, whereas Figure 5.14 B illustrates the photoluminescence (PL) spectrum of FNP in bulk.
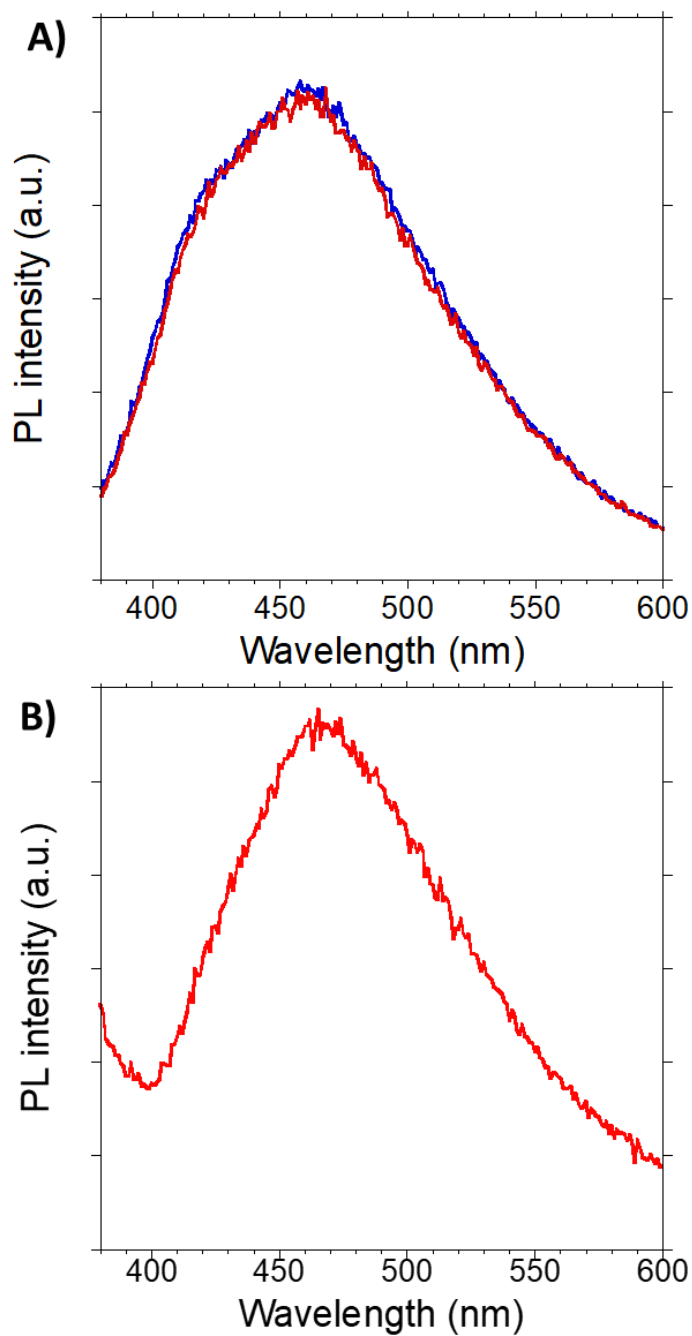
Figure 5.14. A) *Stability of the fluorescence properties of purified FNP over storage time: red curve is the PL spectrum of FNP in THF as synthesized; blue curve is the PL spectrum of FNP in THF after one week of storage.* **B)** *Fluorescence spectrum of FNP in the solid state (λ_{ex} = 364 nm).*

5.4.3. Fluorescence quantum yield determination.

The fluorescence quantum yield of the sample was calculated using the following equation [63]:

(5.1)

$$\Phi = \Phi_r(m/m_r) \ (n^2/n_r^2)$$

where Φ_r is the quantum yield of the standard (taken from the literature), m and m_r are the slopes of the Fluorescence vs. Absorbance plots of the sample and the standard respectively, and n and n_r are the refraction indexes of the sample and standard solvents.
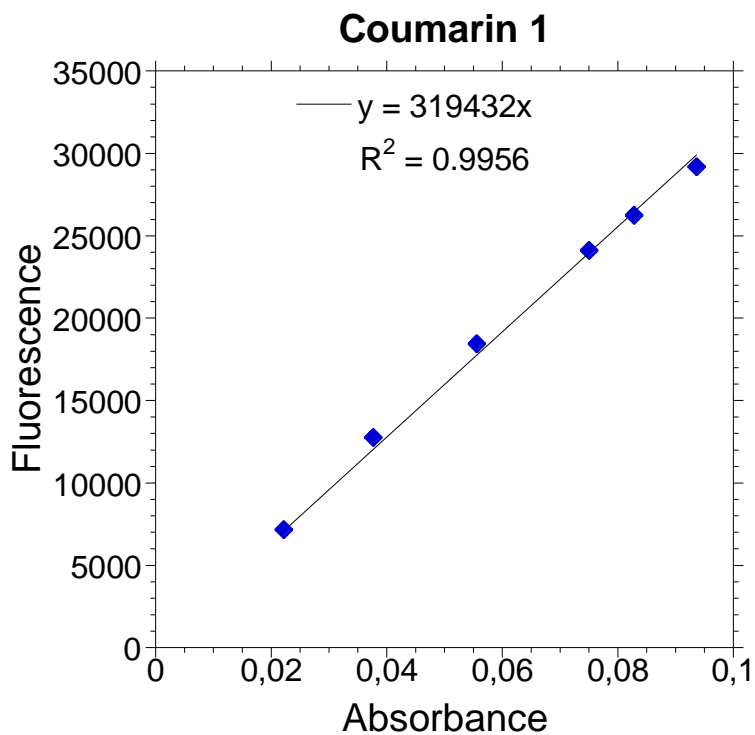
Figure 5.15. *Fluorescence vs. Absorbance plot of Coumarin 1 standard in ethanol. y=319432x. R²=0.9956.*

Coumarin 1:

Theoretical Φ_r (in ethanol): 0.732 [64]

Slope (m_r): 319432 (from Figure 5.15)

Refraction index of ethanol (n_r): 1.3571
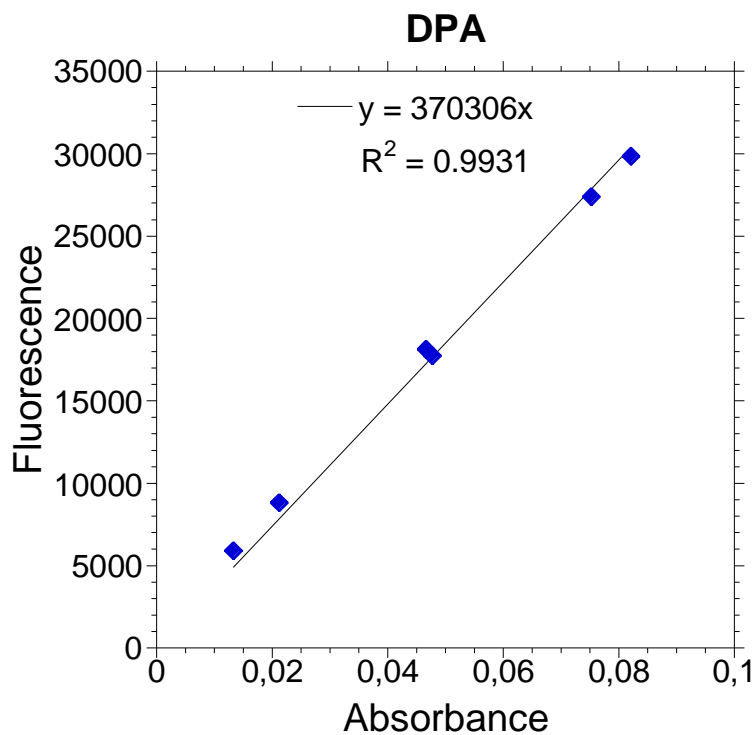
Figure 5.16. *Fluorescence vs. Absorbance plot of 9,10-diphenylanthracene (DPA) standard in ethanol. y=370306x. R²=0.9931.*

9, 10-diphenylanthracene (DPA):

Theoretical Φ_r (in ethanol): 0.90 [64]

Slope (m_r): 370306 (from Figure 5.16)

Refraction index of ethanol (n_r): 1.3571

Single-chain nanoparticles
FNP
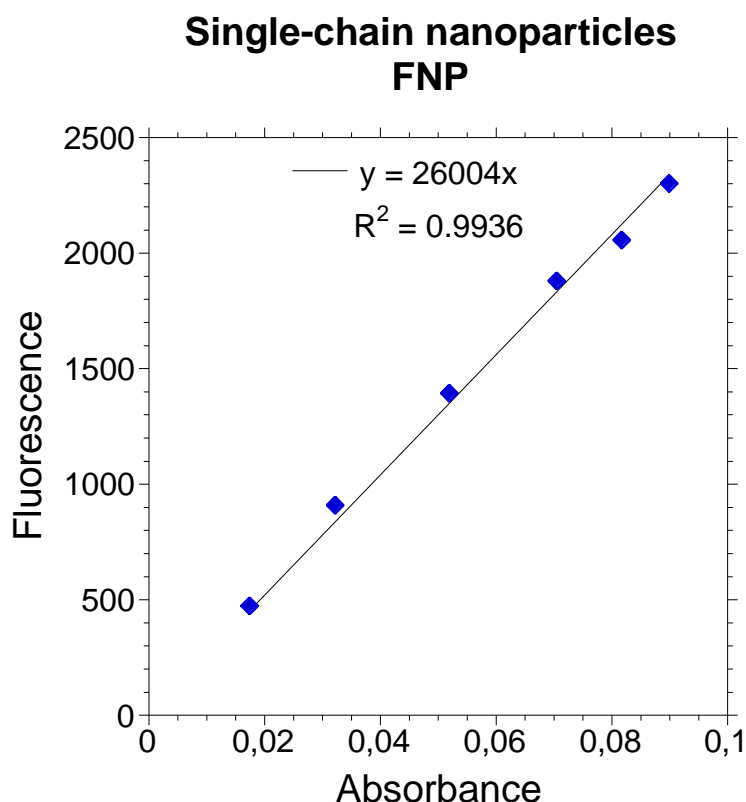
Figure 5.17. Fluorescence vs. Absorbance plot of single-chain nanoparticles FNP in THF. y=26004x. R²=0.9936.

Single-chain nanoparticles **FNP**:

Slope (*m*): 26004 (from Figure 5.17)

Refraction index of THF (*n*): 1.407

Fluorescence quantum yield of **FNP** with Coumarin 1 standard: $\Phi = 0.063$

Fluorescence quantum yield of **FNP** with DPA standard: $\Phi = 0.067$

Average Φ (single-chain nanoparticles **FNP** in THF): 0.065 ± 0.002

5.5. Conclusions

This chapter reports a new, fast, and efficient method to produce SCNPs with intense fluorescence emission in solution, which is based on the photoactivation of appropriate aggregation induced emission (AIE) cross-linking molecules containing azide functional groups. Hence, a new strategy based on photoactivation of appropriate AIE molecules containing azide functional groups for the fast and efficient generation of SCNPs with fluorescence emission in both solution and solid state is established. We have demonstrated that by the generation of a combination of both highly reactive nitrene species (from an azide-containing AIE cross-linking molecule, **Silole-N₃**) and highly reactive carbene species (from an appropriate polymeric precursor containing α-diazo-β-ketoester units, **P**) via UV irradiation, the probability of efficient immobilization of the AIE compound in the resulting

SCNP increases considerably, when compared to the use of an AIE compound without azide functional groups. Confirmation of successful single-chain compaction upon UV irradiation of precursor **P** in the presence of **Silole-N₃** at high dilution is obtained by SEC with multi-detection, including MALLS detector (for absolute M_w and R_g values) and VIS detector (for R_h data). The optimum UV irradiation time during the SCNP formation process is found to be 60 min. The resulting fluorescent SCNPs **FNP** ($R_h = 9$ nm) show a maximum emission peak in the THF solvent centred at $\lambda_{em} \approx 455$ nm and excellent stability of the fluorescence emission intensity over time, as determined by FS. Moreover, **FNP** retains its fluorescent properties in the solid state. To conclude, this work opens a new avenue to endow a variety of other nanostructured polymeric materials (e.g., block copolymers, microgels, dendrimers, and micelles) with intense fluorescence emission based on the new strategy of photo-activation of AIE molecules here disclosed.

5.6. References

[1] S. Mavila, O. Eivgi, I. Berkovich, N.G. Lemcoff, Intramolecular Cross-Linking Methodologies for the Synthesis of Polymer Nanoparticles, Chemical Reviews, 116 (2016) 878-961.
[2] O. Altintas, C. Barner-Kowollik, Single-Chain Folding of Synthetic Polymers: A Critical Update, Macromolecular Rapid Communications, 37 (2016) 29-46.
[3] C.K. Lyon, A. Prasher, A.M. Hanlon, B.T. Tuten, C.A. Tooley, P.G. Frank, E.B. Berda, A brief user's guide to single-chain nanoparticles, Polymer Chemistry, 6 (2015) 181-197.
[4] M. Artar, E. Huerta, E.W. Meijer, A.R.A. Palmans, Dynamic Single Chain Polymeric Nanoparticles: From Structure to Function, Sequence-Controlled Polymers: Synthesis, Self-Assembly, and Properties, American Chemical Society2014, pp. 313-325.
[5] M. Gonzalez-Burgos, A. Latorre-Sanchez, J.A. Pomposo, Advances in single chain technology, Chemical Society Reviews, 44 (2015) 6122-6142.
[6] A. Sanchez-Sanchez, J.A. Pomposo, Single-Chain Polymer Nanoparticles via Non-Covalent and Dynamic Covalent Bonds, Particle & Particle Systems Characterization, 31 (2014) 11-23.
[7] A. Sanchez-Sanchez, I. Pérez-Baena, J.A. Pomposo, Advances in Click Chemistry for Single-Chain Nanoparticle Construction, Molecules, 18 (2013) 3339-3355.
[8] T.-K. Nguyen, S.J. Lam, K.K.K. Ho, N. Kumar, G.G. Qiao, S. Egan, C. Boyer, E.H.H. Wong, Rational Design of Single-Chain Polymeric Nanoparticles That Kill Planktonic and Biofilm Bacteria, ACS Infectious Diseases, 3 (2017) 237-248.
[9] A. Sanchez-Sanchez, S. Akbari, A.J. Moreno, F.L. Verso, A. Arbe, J. Colmenero, J.A. Pomposo, Design and Preparation of Single-Chain Nanocarriers Mimicking Disordered Proteins for Combined Delivery of Dermal Bioactive Cargos, Macromolecular Rapid Communications, 34 (2013) 1681-1686.
[10] I. Perez-Baena, I. Loinaz, D. Padro, I. García, H.J. Grande, I. Odriozola, Single-chain polyacrylic nanoparticles with multiple Gd(iii) centres as potential MRI contrast agents, Journal of Materials Chemistry, 20 (2010) 6916-6922.
[11] S.K. Hamilton, E. Harth, Molecular Dendritic Transporter Nanoparticle Vectors Provide Efficient Intracellular Delivery of Peptides, ACS Nano, 3 (2009) 402-410.
[12] H. Rothfuss, N.D. Knöfel, P.W. Roesky, C. Barner-Kowollik, Single-Chain Nanoparticles as Catalytic Nanoreactors, Journal of the American Chemical Society, 140 (2018) 5875-5881.
[13] J. Rubio-Cervilla, E. González, J.A. Pomposo, Advances in Single-Chain Nanoparticles for Catalysis Applications, Nanomaterials, 7 (2017) 341.

[14] N.D. Knöfel, H. Rothfuss, J. Willenbacher, C. Barner-Kowollik, P.W. Roesky, Platinum(II)-Crosslinked Single-Chain Nanoparticles: An Approach towards Recyclable Homogeneous Catalysts, Angewandte Chemie International Edition, 56 (2017) 4950-4954.
[15] C.A. Tooley, S. Pazicni, E.B. Berda, Toward a tunable synthetic [FeFe] hydrogenase mimic: single-chain nanoparticles functionalized with a single diiron cluster, Polymer Chemistry, 6 (2015) 7646-7651.
[16] A. Sanchez-Sanchez, A. Arbe, J. Colmenero, J.A. Pomposo, Metallo-Folded Single-Chain Nanoparticles with Catalytic Selectivity, ACS Macro Letters, 3 (2014) 439-443.
[17] I. Perez-Baena, F. Barroso-Bujans, U. Gasser, A. Arbe, A.J. Moreno, J. Colmenero, J.A. Pomposo, Endowing Single-Chain Polymer Nanoparticles with Enzyme-Mimetic Activity, ACS Macro Letters, 2 (2013) 775-779.
[18] E. Huerta, P.J.M. Stals, E.W. Meijer, A.R.A. Palmans, Consequences of Folding a Water-Soluble Polymer Around an Organocatalyst, Angewandte Chemie International Edition, 52 (2013) 2906-2910.
[19] T. Terashima, T. Mes, T.F.A. De Greef, M.A.J. Gillissen, P. Besenius, A.R.A. Palmans, E.W. Meijer, Single-Chain Folding of Polymers for Catalytic Systems in Water, Journal of the American Chemical Society, 133 (2011) 4742-4745.
[20] A. Latorre-Sanchez, J.A. Pomposo, A simple, fast and highly sensitive colorimetric detection of zein in aqueous ethanol via zein–pyridine–gold interactions, Chemical Communications, 51 (2015) 15736-15738.
[21] M.A.J. Gillissen, I.K. Voets, E.W. Meijer, A.R.A. Palmans, Single chain polymeric nanoparticles as compartmentalised sensors for metal ions, Polymer Chemistry, 3 (2012) 3166-3174.
[22] J.A. Pomposo, Single-Chain Polymer Nanoparticles: Synthesis, Characterization, Simulations, and Applications, John Wiley & Sons2017.
[23] A. Latorre-Sánchez, J.A. Pomposo, Recent bioinspired applications of single-chain nanoparticles, Polymer International, 65 (2016) 855-860.
[24] J.A. Pomposo, Bioinspired single-chain polymer nanoparticles, Polymer International, 63 (2014) 589-592.
[25] X. He, J. Gao, S.S. Gambhir, Z. Cheng, Near-infrared fluorescent nanoprobes for cancer molecular imaging: status and challenges, Trends in Molecular Medicine, 16 (2010) 574-583.
[26] X. Michalet, F.F. Pinaud, L.A. Bentolila, J.M. Tsay, S. Doose, J.J. Li, G. Sundaresan, A.M. Wu, S.S. Gambhir, S. Weiss, Quantum Dots for Live Cells, in Vivo Imaging, and Diagnostics, Science, 307 (2005) 538.
[27] W. Yin, L. Zhou, Z. Gu, G. Tian, S. Jin, L. Yan, X. Liu, G. Xing, W. Ren, F. Liu, Z. Pan, Y. Zhao, Lanthanide-doped GdVO4 upconversion nanophosphors with tunable emissions and their applications for biomedical imaging, Journal of Materials Chemistry, 22 (2012) 6974-6981.
[28] L. Shang, S. Brandholt, F. Stockmar, V. Trouillet, M. Bruns, G.U. Nienhaus, Effect of Protein Adsorption on the Fluorescence of Ultrasmall Gold Nanoclusters, Small, 8 (2012) 661-665.
[29] Y. Zhang, Y. Bai, J. Jia, N. Gao, Y. Li, R. Zhang, G. Jiang, B. Yan, Perturbation of physiological systems by nanoparticles, Chemical Society Reviews, 43 (2014) 3762-3809.
[30] J. De-La-Cuesta, E. González, J.A. Pomposo, Advances in Fluorescent Single-Chain Nanoparticles, Molecules, 22 (2017).
[31] P. Wang, H. Pu, J. Ge, M. Jin, H. Pan, Z. Chang, D. Wan, Fluorescence-labeled hydrophilic nanoparticles via single-chain folding, Materials Letters, 132 (2014) 102-105.
[32] C. Song, L. Li, L. Dai, S. Thayumanavan, Responsive single-chain polymer nanoparticles with host–guest features, Polymer Chemistry, 6 (2015) 4828-4834.
[33] Y. Liu, T. Pauloehrl, S.I. Presolski, L. Albertazzi, A.R.A. Palmans, E.W. Meijer, Modular Synthetic Platform for the Construction of Functional Single-Chain Polymeric Nanoparticles: From Aqueous Catalysis to Photosensitization, Journal of the American Chemical Society, 137 (2015) 13096-13105.

[34] A.P.P. Kröger, R.J.E.A. Boonen, J.M.J. Paulusse, Well-defined single-chain polymer nanoparticles via thiol-Michael addition, Polymer, 120 (2017) 119-128.

[35] C. Heiler, J.T. Offenloch, E. Blasco, C. Barner-Kowollik, Photochemically Induced Folding of Single Chain Polymer Nanoparticles in Water, ACS Macro Letters, 6 (2017) 56-61.

[36] B. Yang, X. Zhang, X. Zhang, Z. Huang, Y. Wei, L. Tao, Fabrication of aggregation-induced emission based fluorescent nanoparticles and their biological imaging application: recent progress and perspectives, Materials Today, 19 (2016) 284-291.

[37] Y. Hong, J.W.Y. Lam, B.Z. Tang, Aggregation-induced emission, Chemical Society Reviews, 40 (2011) 5361-5388.

[38] Y. Hong, J.W.Y. Lam, B.Z. Tang, Aggregation-induced emission: phenomenon, mechanism and applications, Chemical Communications, (2009) 4332-4353.

[39] J. Luo, Z. Xie, J.W.Y. Lam, L. Cheng, H. Chen, C. Qiu, H.S. Kwok, X. Zhan, Y. Liu, D. Zhu, B.Z. Tang, Aggregation-induced emission of 1-methyl-1,2,3,4,5-pentaphenylsilole, Chemical Communications, (2001) 1740-1741.

[40] X. Zhang, K. Wang, M. Liu, X. Zhang, L. Tao, Y. Chen, Y. Wei, Polymeric AIE-based nanoprobes for biomedical applications: recent advances and perspectives, Nanoscale, 7 (2015) 11486-11508.

[41] X. Zhang, S. Wang, L. Xu, L. Feng, Y. Ji, L. Tao, S. Li, Y. Wei, Biocompatible polydopamine fluorescent organic nanoparticles: facile preparation and cell imaging, Nanoscale, 4 (2012) 5581-5584.

[42] R. Jiang, H. Liu, M. Liu, J. Tian, Q. Huang, H. Huang, Y. Wen, Q.-y. Cao, X. Zhang, Y. Wei, A facile one-pot Mannich reaction for the construction of fluorescent polymeric nanoparticles with aggregation-induced emission feature and their biological imaging, Materials Science and Engineering: C, 81 (2017) 416-421.

[43] D. Wei, Y. Xue, H. Huang, M. Liu, G. Zeng, Q. Wan, L. Liu, J. Yu, X. Zhang, Y. Wei, Fabrication, self-assembly and biomedical applications of luminescent sodium hyaluronate with aggregation-induced emission feature, Materials Science and Engineering: C, 81 (2017) 120-126.

[44] R. Jiang, M. Liu, C. Li, Q. Huang, H. Huang, Q. Wan, Y. Wen, Q.-y. Cao, X. Zhang, Y. Wei, Facile fabrication of luminescent polymeric nanoparticles containing dynamic linkages via a one-pot multicomponent reaction: Synthesis, aggregation-induced emission and biological imaging, Materials Science and Engineering: C, 80 (2017) 708-714.

[45] Q.-y. Cao, R. Jiang, M. Liu, Q. Wan, D. Xu, J. Tian, H. Huang, Y. Wen, X. Zhang, Y. Wei, Microwave-assisted multicomponent reactions for rapid synthesis of AIE-active fluorescent polymeric nanoparticles by post-polymerization method, Materials Science and Engineering: C, 80 (2017) 578-583.

[46] L. Mao, M. Liu, R. Jiang, Q. Huang, Y. Dai, J. Tian, Y. Shi, Y. Wen, X. Zhang, Y. Wei, The one-step acetalization reaction for construction of hyperbranched and biodegradable luminescent polymeric nanoparticles with aggregation-induced emission feature, Materials Science and Engineering: C, 80 (2017) 543-548.

[47] Q.-y. Cao, R. Jiang, M. Liu, Q. Wan, D. Xu, J. Tian, H. Huang, Y. Wen, X. Zhang, Y. Wei, Preparation of AIE-active fluorescent polymeric nanoparticles through a catalyst-free thiol-yne click reaction for bioimaging applications, Materials Science and Engineering: C, 80 (2017) 411-416.

[48] Q. Wan, R. Jiang, L. Guo, S. Yu, M. Liu, J. Tian, G. Liu, F. Deng, X. Zhang, Y. Wei, Novel Strategy toward AIE-Active Fluorescent Polymeric Nanoparticles from Polysaccharides: Preparation and Cell Imaging, ACS Sustainable Chemistry & Engineering, 5 (2017) 9955-9964.

[49] J. Tian, R. Jiang, P. Gao, D. Xu, L. Mao, G. Zeng, M. Liu, F. Deng, X. Zhang, Y. Wei, Synthesis and cell imaging applications of amphiphilic AIE-active poly(amino acid)s, Materials Science and Engineering: C, 79 (2017) 563-569.

[50] Y. Liu, L. Mao, X. Liu, M. Liu, D. Xu, R. Jiang, F. Deng, Y. Li, X. Zhang, Y. Wei, A facile strategy for fabrication of aggregation-induced emission (AIE) active fluorescent

polymeric nanoparticles (FPNs) via post modification of synthetic polymers and their cell imaging, Materials Science and Engineering: C, 79 (2017) 590-595.

[51] D. Xu, M. Liu, H. Zou, Q. Huang, H. Huang, J. Tian, R. Jiang, Y. Wen, X. Zhang, Y. Wei, Fabrication of AIE-active fluorescent organic nanoparticles through one-pot supramolecular polymerization and their biological imaging, Journal of the Taiwan Institute of Chemical Engineers, 78 (2017) 455-461.

[52] H. Huang, D. Xu, M. Liu, R. Jiang, L. Mao, Q. Huang, Q. Wan, Y. Wen, X. Zhang, Y. Wei, Direct encapsulation of AIE-active dye with β cyclodextrin terminated polymers: Self-assembly and biological imaging, Materials Science and Engineering: C, 78 (2017) 862-867.

[53] S. Yu, D. Xu, Q. Wan, M. Liu, J. Tian, Q. Huang, F. Deng, Y. Wen, X. Zhang, Y. Wei, Construction of biodegradable and biocompatible AIE-active fluorescent polymeric nanoparticles by Ce(IV)/HNO3 redox polymerization in aqueous solution, Materials Science and Engineering: C, 78 (2017) 191-197.

[54] Z. Long, M. Liu, R. Jiang, G. Zeng, Q. Wan, H. Huang, F. Deng, Y. Wan, X. Zhang, Y. Wei, Ultrasonic-assisted Kabachnik-Fields reaction for rapid fabrication of AIE-active fluorescent organic nanoparticles, Ultrasonics Sonochemistry, 35 (2017) 319-325.

[55] I. Perez-Baena, I. Asenjo-Sanz, A. Arbe, A.J. Moreno, F. Lo Verso, J. Colmenero, J.A. Pomposo, Efficient Route to Compact Single-Chain Nanoparticles: Photoactivated Synthesis via Thiol–Yne Coupling Reaction, Macromolecules, 47 (2014) 8270-8280.

[56] A. Sanchez-Sanchez, S. Akbari, A. Etxeberria, A. Arbe, U. Gasser, A.J. Moreno, J. Colmenero, J.A. Pomposo, "Michael" Nanocarriers Mimicking Transient-Binding Disordered Proteins, ACS Macro Letters, 2 (2013) 491-495.

[57] S. Bräse, C. Gil, K. Knepper, V. Zimmermann, Organic Azides: An Exploding Diversity of a Unique Class of Compounds, Angewandte Chemie International Edition, 44 (2005) 5188-5240.

[58] M.P. Doyle, R. Duffy, M. Ratnikov, L. Zhou, Catalytic Carbene Insertion into C—H Bonds, Chemical Reviews, 110 (2010) 704-724.

[59] A. Latorre-Sánchez, A. Alegría, F. Lo Verso, A.J. Moreno, A. Arbe, J. Colmenero, J.A. Pomposo, A Useful Methodology for Determining the Compaction Degree of Single-Chain Nanoparticles by Conventional SEC, Particle & Particle Systems Characterization, 33 (2016) 373-381.

[60] J.A. Pomposo, I. Perez-Baena, L. Buruaga, A. Alegría, A.J. Moreno, J. Colmenero, On the Apparent SEC Molecular Weight and Polydispersity Reduction upon Intramolecular Collapse of Polydisperse Chains to Unimolecular Nanoparticles, Macromolecules, 44 (2011) 8644-8649.

[61] M. Huo, Q. Ye, H. Che, X. Wang, Y. Wei, J. Yuan, Polymer Assemblies with Nanostructure-Correlated Aggregation-Induced Emission, Macromolecules, 50 (2017) 1126-1133.

[62] J.A. Pomposo, A.J. Moreno, A. Arbe, J. Colmenero, Local Domain Size in Single-Chain Polymer Nanoparticles, ACS Omega, 3 (2018) 8648-8654.

[63] S. Ramesan, S. Vyas, Abid, Determination of Relative Fluorescence Quantum Yield Using The Agilent Cary Eclipse, Agilent Technologies, Inc., Solutions for Your Analytical Business, Markets and Applications Programs, 2016.

[64] Methods for the determination of photoluminescence quantum yield, Nanoco Technologies Limited, Nanoco Technologies Limited, 2013.

Chapter 6: Self-Reporting of Folding and Aggregation Phenomena in Single-Chain Nanoparticles

6.1. Motivation

Self-reporting fluorescence methods for monitoring folding and aggregation of proteins have a long history in biochemistry. Placing orthogonal luminophores within individual synthetic polymer chains for self-reporting both folding (i.e., its intramolecular compaction to isolated single-chain nanoparticles, SCNPs) and unbidden aggregation (i.e., the intermolecular association of SCNPs) remains a great challenge. In this Chapter, we introduce a simple and efficient platform to identify both single-chain compaction and intermolecular aggregation phenomena of discrete, individual synthetic polymer chains.

6.2. Introduction

The folding of some polypeptides, especially enzymes, into perfectly defined three-dimensional (3D) architectures is critical to their function. The specific spatial arrangement of residues ultimately dictates function in 3D-structured proteins [1]. Protein misfolding and aggregation are involved in the onset of many neurodegenerative aged-related human disorders. Well-known examples are Alzheimer´s, Parkinson´s and Huntington´s diseases [2]. To better understand diseases and design drugs, a variety of methods -from biochemical assays to time-resolved microscopy- have been developed to investigate protein folding [3] and to monitor the self-assembly of defective proteins into pathogenic protein aggregates [4]. Among them, photoluminescence techniques are highly valuable due to their high sensitivity and the possibility to select, synthesize and optimize a diversity of photoluminescence probes (luminophores). These compounds allow visualizing protein folding, misfolding and aggregation in vitro and in living cells [5].

Trying to mimic the outstanding functionalities of proteins, the research field of folding functionalized synthetic polymers to single-chain nanoparticles (SCNPs) has flourished in recent years [6][7]. The folded conformations of SCNPs produce robust nano-objects when stabilized by covalent bonds as surrogates of disulphide bonds in proteins [8, 9]. Conversely, when folding of discrete, individual chains arises from noncovalent interactions such as hydrogen bonds, host-guest interactions, metal complexation, $\pi-\pi$ stacking and hydrophobic interactions, dynamic SCNPs are obtained.[6, 10-13] Current single-chain technology [14-16] still lacks the nature´s exquisite degree of control to generate sophisticated 3D nanoentities. Nevertheless, some SCNPs do already mimic the outstanding properties of certain antimicrobial polypeptides as well as both the size and function of some metalloenzymes, intrinsically disordered proteins (IDPs) and structural proteins. For instance, Wong et al. described antimicrobial SCNPs against Gram-negative bacteria (e.g., Pseudomonas aeruginosa) at micromolar concentrations (e.g., 1.4 µM) able to kill $\geq$ 99.99% of both planktonic cells, and biofilm within only 1 hour [17]. Ravi and co-workers developed biomimetic SCNPs that closely match the properties of β_{high} lens crystallins in size, refractive index, and dynamic viscosity [18]. He *et al.* synthesized catalytic SCNPs containing Ni-thiolate complexes with excellent thermal stability under aerobic conditions and remarkable activity and selectivity for the photocatalytic reduction of CO_2 to CO [19]. More recently, Zimmerman *et al.* reported copper-based SCNPs that function as "clickases", showing enzyme-like click catalysis in vivo and enabling efficient cell surface glycan editing [20]. Previously, our team demonstrated enzyme-mimetic substrate selectivity of copper-containing SCNPs in oxidative coupling of mixtures of terminal alkynes [21], and pH-

regulated kinetics of IDP-like SCNPs during simultaneous controlled delivery of folic acid and hinokitiol [22].

However, as observed in the case of defective proteins, some SCNPs systems are not free from multi-SCNPs aggregation phenomena -arising during synthesis or after long-term storage trough inter-chain reactions- that negatively affect its performance, e.g., in catalysis, drug delivery and sensing applications [23-25]. In the case of SCNPs, single-chain compaction, and competitive multi-SCNPs assembly phenomena are mainly detected after synthesis ("ex-situ") by means of light, X-ray and neutron scattering techniques [26]. Self-reporting, fluorescence methods for monitoring folding and aggregation of proteins have a long history in biochemistry. Placing orthogonal luminophores within individual synthetic polymer chains for self-reporting both folding (i.e., its intra-molecular compaction to isolated single-chain nanoparticles, SCNPs) and unbidden aggregation (i.e., the inter-molecular association of SCNPs) remains as a great challenge. To the best of our knowledge, no techniques exist yet for self-reporting -via photoluminescence- both intra-molecular compaction and inter-molecular aggregation phenomena in SCNPs. Previously, Palmans, Meijer *et al.* developed SCNPs showing fluorescence upon intra-molecular self-assembly of BiPy groups [27, 28]. Raymo *et al.* investigated a variety of biocompatible and photo-switchable fluorescent multi-chain assemblies [29-31]. More recently, two different methods for self-reporting of single-chain folding during synthesis have been reported by Barner-Kowollik *et al.* based on: i) annihilation of paramagnetic nitroxide radicals [32], or ii) release of a pyrene chromophore [33]. Critically, a visual, self-reporting method to distinguish by the naked eye between individual SCNPs and unbidden multi-SCNPs assemblies, and in the former case the degree of single-chain compaction, would be invaluable in further advancing this field of bioinspired research.

SCNPs will be prepared from MMA/AEMA copolymers via the Hantzsch pyridine synthesis reaction. This reaction was reported in 1881 by Arthur Rudolf Hantzsch [34]. In the Hantzcsh reaction an aldehyde, two equivalents of a β-ketoester and a nitrogen donor (such as ammonium acetate) react to form a dihydropyridine ring, which can be oxidized to pyridine. The 1,4-dihydropyridine (1,4-DHP) product of the reaction is called Hantzsch ester. Hantzsch esters have been often used as reductants in catalytic hydrogenation reactions, acting as electron donors and proton sources [35]. These products also have many biological applications as calcium channel blockers and the 1,4-DHP structure is contained in commercial drugs; for instance, nifedipine, amlodipine or nimodipine. Shen *et al.* [36] developed a one pot method for the synthesis of 1,4-DHPs under mild conditions.
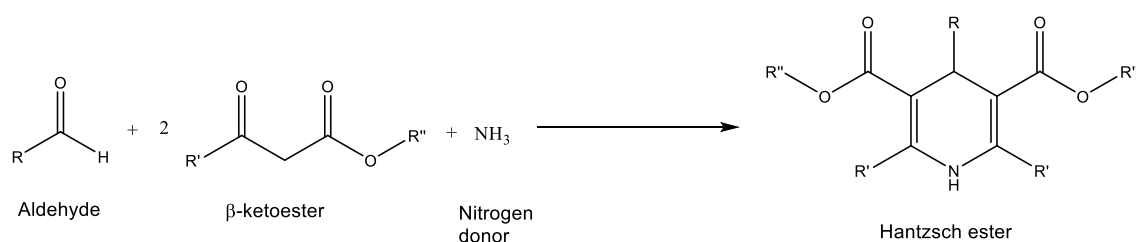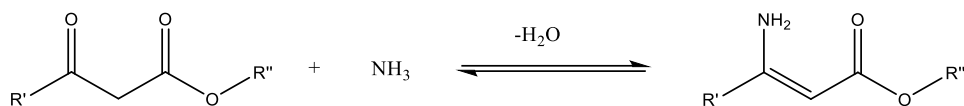

Scheme 6.1. *Schematic representation of the synthesis of Hantzsch esters.*

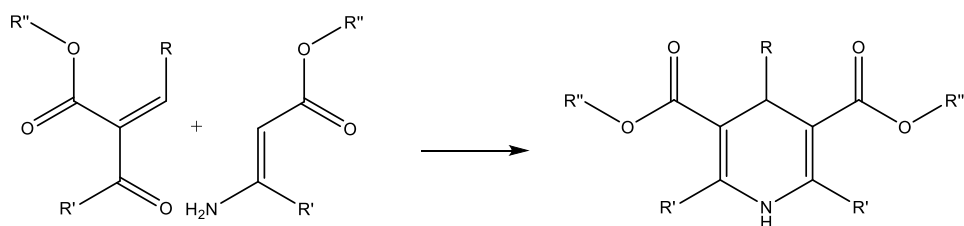The Hantzsch reaction mechanism is the following:

Knoevenagel condensation between the aldehyde and a β-ketoester gives the following intermediate.
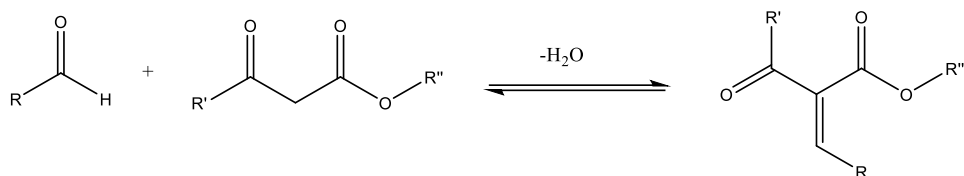
Condensation of the second equivalent β-ketoester with ammonia produces an ester enamine.

Condensation between the two intermediate products results in the formation of a dihydroxipyridine ring.

In this chapter we introduce a new, straightforward strategy to bridge the gap between single-chain folding and inter-molecular aggregation self-reporting methods for proteins and synthetic polymers relying on efficient placement within individual chains of orthogonal self-reporting luminophores (Scheme 6.2). The strategy is exemplified through generation of two complementary luminophores via Hantzsch ester formation [34] for efficient visualization of single-chain folding [37] and, when present or externally induced, multi-SCNPs aggregation. The key points of the present method are: i) starting from non-luminescent β-ketoester-decorated chains, single-chain intramolecular compaction is visually detected through fluorescence arising from the Hantzsch fluorophores acting as intra-chain connectors generated progressively during folding of individual chains, so -in absence of aggregation phenomena at high dilution- the fluorescence intensity grows with the compaction degree, as measured by the reduction in chain size (see below); ii) multi-chain aggregation -when present or intentionally induced- is detected by intense photoluminescence at redshifted wavelengths arising from orthogonal aggregation-induced emission (AIE) luminophores after formation of multi-SCNPs assemblies [38-40]; and iii) both kind of self-reporting probes are installed, concurrently, within the same polymer chain via the multicomponent Hantzsch reaction [41-43]. This strategy holds promise to

perceive with the naked eye the aggregation state / compaction degree of SCNPs during functional applications.
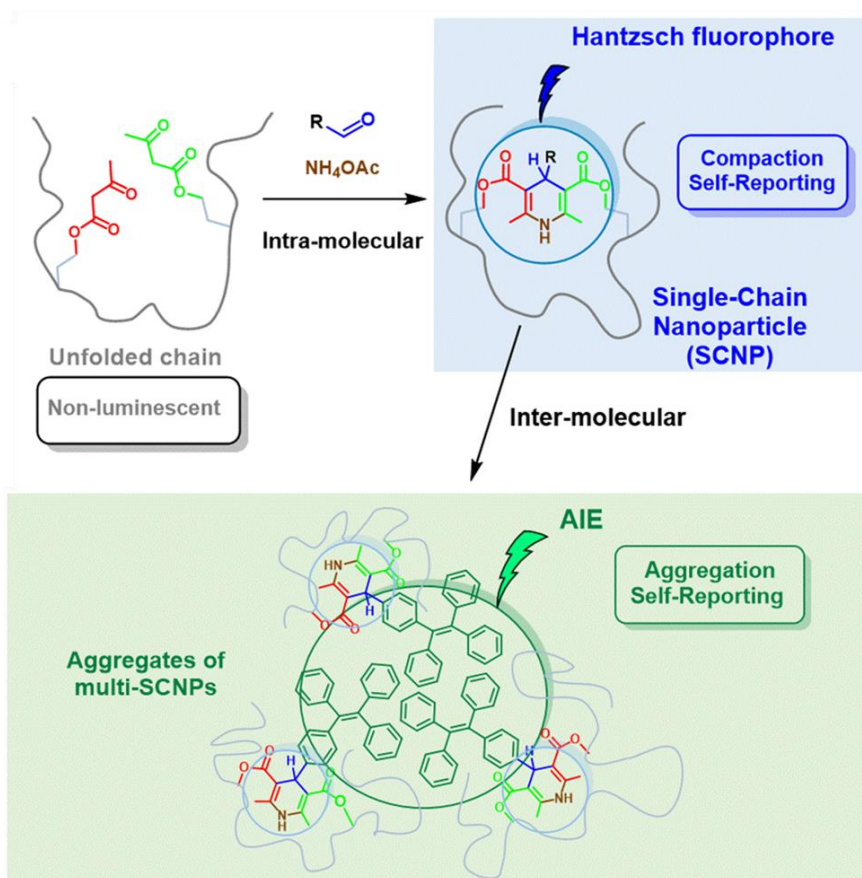
Scheme 6.2. *Schematic illustration of the strategy for the synthesis of orthogonal luminophores based on Hantzsch ester formation within a β-ketoester-decorated chain for self-reporting of intra-molecular compaction (folding) and inter-molecular association (aggregation).*

6.3. Materials and Techniques

6.3.1. Materials

Methyl methacrylate (MMA) (99%), (2-acetoacetoxy)ethyl methacrylate (AEMA) (95%), 2.2′-azo(2-methylpropionitrile) (AIBN) (≥98%), ammonium acetate (NH₄OAc) (99.999% trace metals basis), benzaldehyde (**A1**) (≥99%), terephthalaldehyde (**A2**) (99%), 4-(1,2,2-triphenylethenyl)benzaldehyde (**A3**) (≥95%), 2,2-dimethoxy-2-phenylaceto-phenone (DMPA) (99%), 3,6-dioxa-1,8-octane-dithiol (DODT) (95%), piperidine (PIP) (99%), ethyl acetate (EtOAc) (anhydrous, 99.8 %), diethyl ether (Et₂O) (ACS reagent, anhydrous, >99.0%), ethanol (EtOH) (anhydrous, denatured) and deuterated chloroform (CDCl₃) (99.96 atom % D, containing 0.03 % (*v/v*) tetramethylsilane, TMS) were purchased from Sigma-Aldrich and used, unless specified, as received. 2-Cyanoprop-2-yl-dithiobenzoate (CPDB) (≥97%) was purchased from Strem Chemicals. Methanol (MeOH) (synthesis grade) and tetrahydrofuran (THF) (HPLC grade) were purchased from Scharlab. AIBN was

recrystallized from MeOH. MMA was purified by distillation before use. AEMA was purified by passing through alumina.

6.3.2. Techniques

Size-Exclusion Chromatography / Multi-Angle Light Scattering (SEC/MALS): SEC / MALS measurements were performed at 30 °C on an Agilent 1200 system equipped with PLgel 5μm Guard and PLgel 5μm MIXED-C columns, and triple detection: a differential refractive index (RI) detector (Optilab Rex, Wyatt), a multi-angle laser light scattering (MALS) detector (MiniDawn Treos, Wyatt), and a viscosimetric (VIS) detector (ViscoStar-II, Wyatt). Data analysis was performed with ASTRA Software (version 6.1) from Wyatt. THF was used as eluent at a flow rate of 1 ml/min. A value of $dn/dc = 0.083$ was used for **P1-P3**, **N1f-N3f** and **N1fa-N3fa**.

^{1}H Nuclear Magnetic Resonance (^{1}H NMR): ^{1}H NMR spectra were recorded at room temperature on a Bruker spectrometer operating at 400 MHz, using CDCl$_3$ as solvent. AEMA content of **P1-P3** was determined following the procedure described in section 5.3 and ref. [44].

Fourier Transform Infra-Red (FTIR) spectroscopy: FTIR spectra were recorded at room temperature on a JASCO 3600 FTIR spectrometer.

Elemental Analysis (EA): EA measurements were performed in a Euro EA3000 elemental analyser (CHNS).

Fluorescence spectroscopy (FS): Photoluminiscence spectra were recorded at room temperature on an Agilent Cary Eclipse spectrometer at an excitation wavelength of 365 nm.

Dynamic light scattering (DLS): DLS measurements (intensity distribution) were carried out at room temperature on a Malvern Zetasizer Nano ZS apparatus.

Small-angle X-ray scattering (SAXS): SAXS experiments were conducted on the Rigaku 3-pinhole PSAXS-L equipment of the Materials Physics Center operating at 45 kV and 0.88 mA. The MicroMax-002+ X-Ray Generator System is composed by a microfocus sealed tube source module and an integrated X-Ray generator unit which produces CuKα transition photons of wavelength $\lambda = 1.54$ Å. The flight path and the sample chamber in this equipment are under vacuum. The scattered X-Rays are detected on a two-dimensional multiwire X-Ray Detector (Gabriel design, 2D-200X) and converted to one-dimensional scattering curves by radial averaging. This gas-filled proportional type detector offers a 200 mm diameter active area with ca. 200 μm resolution. After radial integration, the scattered intensities were obtained as a function of momentum transfer $q = 4\pi\lambda^{-1}sin\,\theta$, where θ is half the scattering angle. Reciprocal space calibration was done using silver behenate as standard. The sample to detector distance was 2 m, covering a q-range between 0.008 and 0.20 Å^{-1}. The measurements were performed at r.t. on THF solutions in capillaries of 2 mm thickness. The concentration was 1 mg/ml in order to avoid interference effects between different macromolecules and reproduce the usual synthesis conditions in the kinetic experiments. Note that with laboratory SAXS instruments the concentration range usually explored for this kind of systems is around 8 mg/ml. The low concentration here investigated required long measuring times, of at least 1 hour, for each sample. The data were carefully corrected for background scattering (due to capillary and solvent), measured

for each sample on the same capillary for the same time. Scattering cross-sections were obtained in absolute units by using water as calibration standard.

The generalized Gaussian coil function [45] given by:

<div align="right">*(6.1)*</div>

$$P(Q) = \frac{1}{\nu U^{1/2\nu}} \gamma\left(\frac{1}{2\nu}, U\right) - \frac{1}{\nu U^{1/\nu}} \gamma\left(\frac{1}{\nu}, U\right)$$

Where $U = \frac{(2\nu+1)(2\nu+2)}{6} Q^2 R_G^2$

and $\gamma(a, x) = \int_0^X t^{a-1} exp(-t)dt$

was employed for a precise determination of the values of radius of gyration, R_g, and scaling exponent, ν.

A series of measurements were performed on **P1-P3**, **N1f-N3f** and **N1fa-N3fa**, where the nanoparticles had previously been synthesized (Figure 6.6 A, B and C). Figure 6.6 D compares the radii of gyration obtained by fitting equation (6.1) to the results.

In addition, we carried out a kinetic experiment following in situ the nanoparticle formation process as a function of reaction time during single-chain compaction of **P1** (1.2 eq) in THF (1 mg/ml) via intra-chain Hantzsch ester formation involving **A2** (0.25 eq), NH_4OAc (4 eq) and piperidine (0.05 eq). Immediately after mixing all reagents, the capillary was filled with a small amount of the solution and placed within the SAXS instrument. SAXS measurements were performed on this sample as function of reaction time, with 1 hour duration, along a full week, keeping the sample exactly in the same position and under vacuum. The resulting evolution of the radius of gyration and scaling exponent obtained by fitting equation (6.1) are shown in Figure 6.11 A. In parallel, photoluminescence experiments were performed on the rest of the solution which was kept in a vial. A sample from this solution was also measured by SAXS at the end of the kinetic experiment (results represented by squares in Figure 6.11 A).

UV irradiation experiments: UV irradiation experiments were performed in a Penn PhD Photoreactor M2 (Penn Photon Devices, LLC).

6.3.3. Synthetic procedures

6.3.3.1. Synthesis of precursor copolymers P1-P3

Copolymers **P1-P3** were synthesized by RAFT copolymerization following procedures similar to those reported in section 5.2.3.1 and ref. [44]. In a typical procedure, MMA (2 ml, 18.7 mmol), AEMA (1.5 ml, 8 mmol), 2-cyanoprop-2-yl-dithiobenzoate (7.9 mg, 3.6×10^{-2} mmol) and 2,2-azobis(2-methylpropionitrile) (1.5 mg, 9×10^{-3} mmol) were dissolved in ethyl acetate (8.8 ml). The reaction mixture was degassed by passing argon for 15 min. The copolymerization reaction was carried out at 65ºC for 18 h. (**P3**: Yield (%) = 42, M_w

(SEC/SLS) = 56.2 kDa, M_w/M_n = 1.08, R_g = 7.8 nm, composition (^{1}H NMR) = 34.9 mol% AEMA). The resulting copolymers **P1-P3** were isolated by precipitation in methanol and further drying under vacuum. The molar fraction of β-ketoester groups in **P1-P3**, x, was determined by ^{1}H NMR spectroscopy following the procedure reported in section 5.3 and ref. [44] from the normalized areas of peaks d, e and f of Figure 6.8. The absolute molecular weight, M_w, and the dispersity of the molecular weight distribution, $Đ$, of copolymers **P1-P3** were determined by SEC/MALS. The values of x, M_w, and $Đ$ for copolymers **P1-P3** are provided in Table 6.1.

6.3.3.2. Synthesis of fluorescent SCNPs **N1f-N3f**

After screening of reaction conditions with aldehydes **A1** and **A2**, **N1f-N3f** were synthesized at r.t. from **P1-P3**, respectively, by intra-chain Hantzsch ester formation at high dilution using aldehyde compound **A2**. In a typical reaction, **P2** (100 mg, 0.21 mmol), **A2** (7.1 mg, 0.053 mmol), NH$_4$OAc (48.8 mg, 0.63 mmol), and PIP (2 μL, 0.02 mmol) were dissolved in THF (100 ml). Samples were taken periodically to monitor the single-chain folding reaction through SEC/MALS and FS, respectively. After reaction completion, the solution was concentrated, precipitated in Et$_2$O and dried under vacuum, prior to further characterization by SEC/MALS, ^{1}H NMR, FTIR, EA, FS, DLS and SAXS.

6.3.3.3. Synthesis of fluorescent SCNPs with AIE **N1fa-N3fa**

After screening of reaction conditions with aldehydes **A2** and **A3**, **N1fa-N3fa** were synthesized at r.t. from **P1-P3**, respectively, by intra-chain Hantzsch ester formation at high dilution using a blend of aldehyde compounds **A2** and **A3** at a molar ratio of 1/2. In a typical reaction, **P2** (100 mg, 0.21 mmol), **A2** (3.6 mg, 0.027 mmol), **A3** (19.1 mg, 0.053 mmol), NH$_4$OAc (48.8 mg, 0.63 mmol), and PIP (2 μl, 0.02 mmol) were dissolved in THF (100 ml). Samples were taken periodically to monitor the single-chain folding reaction through SEC/MALS and FS, respectively. After reaction completion, the solution was concentrated, precipitated in Et$_2$O and dried under vacuum, prior to further characterization by SEC/MALS, ^{1}H NMR, FTIR, EA, FS, DLS and SAXS.

6.3.3.4. Self-reporting of multi-SCNPs aggregation by **N1fa-N3fa** in good solvent

Aggregation of SCNPs **N1fa-N3fa** was induced through photoactivated radical-mediated thiol-ene coupling (TEC) reaction involving a homobifunctional cross-linker (DODT) and the 1,4-dihidropyridine groups of SCNPs **N1fa-N3fa**, in the presence of DMPA as photoinitiator. Reactions were carried out in THF at r.t. under UV irradiation. In a typical reaction, **P2** (3 mg, 6.3 x 10^{-3} mmol), DODT (1 μl, 6.3 x 10^{-3} mmol) and DMPA (0.6 mg, 2.4 x 10^{-3} mmol) were dissolved in THF (0.12 mL) and subject to UV light irradiation (λ_{exc} = 365 nm) for 90 min in a Penn PhD Photoreactor M2 (Penn Photon Devices, LLC). The multi-SCNPs aggregates obtained were analysed by DLS and FS.

6.3.3.5. Self-reporting of multi-SCNPs aggregation by **N1fa-N3fa** in solvent / non-solvent mixtures

For experiments about self-reporting of multi-SCNPs aggregation in solvent / non-solvent mixtures, mixtures of THF and EtOH of varying composition were employed. The multi-SCNPs aggregates obtained were analysed by DLS and FS.

6.4. Results

6.4.1. Self-reporting of folding within a single polymer chain via Hantzsch reaction

Following the strategy depicted in Scheme 6.2, we first synthesized non-fluorescent polymers randomly decorated with β-ketoester moieties via RAFT copolymerization [44, 46] of methyl methacrylate (MMA) and 2-(acetoacetoxy)ethyl methacrylate (AEMA) monomers. Random placement of pendant reactive groups along the copolymer chains to participate in the Hantzsch reaction was guaranteed by similar reactivity ratios of MMA ($r_{MMA} = 0.89$) and AEMA ($r_{AEMA} = 0.98$) [47]. Several representative poly(MMA-r-AEMA) copolymers of varying molecular weight (M_w) and composition (molar fraction of β-ketoester groups, x) were prepared and characterized by ^{1}H NMR spectroscopy and SEC/MALS (see Table 6.1). Copolymers **P1**–**P3** showed low values of dispersity ($Đ < 1.25$).

Table 6.1. *Characterization data for poly(MMA-r-AEMA) copolymers with β-ketoester pendant reactive groups.*

Polymer	M_w (kDa)[a]	$Đ$[a]	x (mol %)[b]
P1	43.6	1.13	54.6
P2	288.6	1.22	33.2
P3	56.2	1.08	34.9

[a] Weight average molecular weight and dispersity determined by SEC/MALS.

[b] Molar fraction of β-ketoester groups determined via ^{1}H NMR.

Initial experiments about self-reporting of single-chain compaction were performed using benzaldehyde (**A1**) (Scheme 6.3) and copolymer **P1** containing 55 mol % of β-ketoester reactive groups. Single-chain compaction of **P1** was induced at r.t. in THF at high dilution (1 mg/ml) via intra-chain Hantzsch reaction between β-ketoester pendants of **P1** (1 eq), **A1** (0.5 eq) and ammonium acetate (NH_4OAc, 0.5 eq), in the presence of piperidine (0.1 eq) as catalyst [48]. At high dilution, the intra-chain reaction leading to single-chain compaction is favoured over the inter-chain reaction giving to aggregation of multiple chains. Importantly, the Hantzsch ester resulting from **A1** and ethyl acetoacetate is known to display fluorescence in organic solvents such as dimethylsulfoxide ($\lambda_{em} = 421$ nm, quantum yield $\Phi_F = 1.2$ %) [49]. The generation of Hantzsch luminophores as intra-chain connectors could be therefore a very suitable strategy for self-reporting of single-chain compaction.
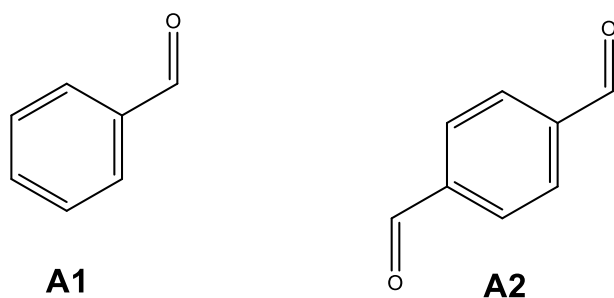
Scheme 6.3. *Aldehyde compounds allowing to monitor the compaction of individual polymer chains to single-chain nanoparticles (SCNPs). Benzaldehyde (**A1**) and terephthalaldehyde (**A2**).*

As revealed by SEC / MALS measurements, the intra-chain Hantzsch ester formation reaction was found to proceed very smoothly and SEC retention time (t_R) of **P1** -taken at the maximum of the SEC trace- slightly increased during single-chain compaction as a consequence of the induced reduction in hydrodynamic size [6] (Figure 6.1).
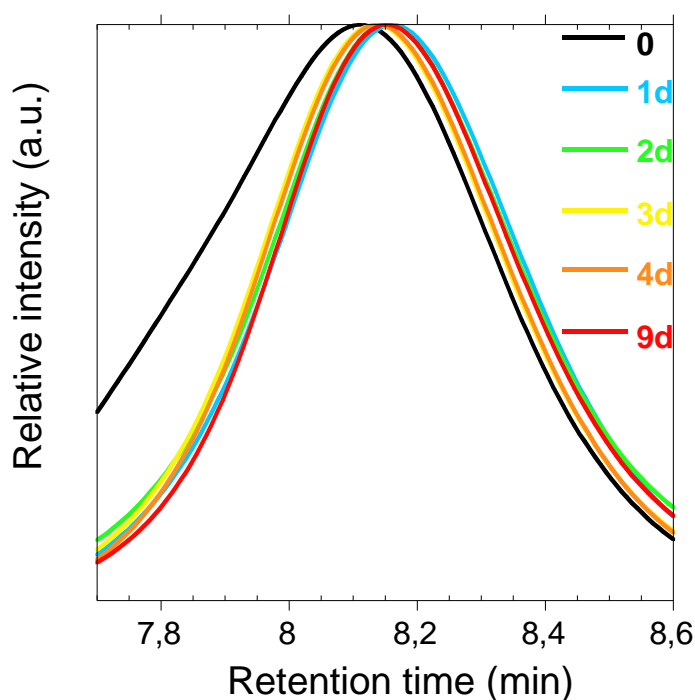
Figure 6.1. *SEC/MALS elugrams as a function of reaction time (0, 1, 2, 3, 4 and 9 days) during single-chain folding of **P1** (1.2 eq) via intra-chain Hantzsch ester formation involving **A1** (0.5 eq), NH₄OAc (0.5 eq) and piperidine (0.05 eq). Initial SEC/MALS trace of unfolded **P1** displayed in black. Final SEC/MALS trace of **P1** after 9 days of reaction time displayed in red.*

In order to improve the degree of single-chain compaction, we replaced **A1** (0.5 eq) by bifunctional terephthalaldehyde (**A2**) (0.25 eq) although with limited success under the above reaction conditions (see Figure 6.2).
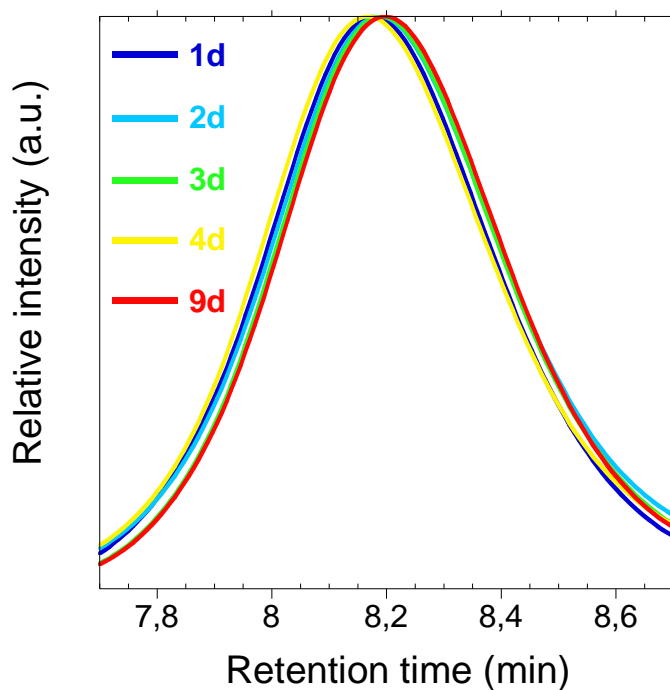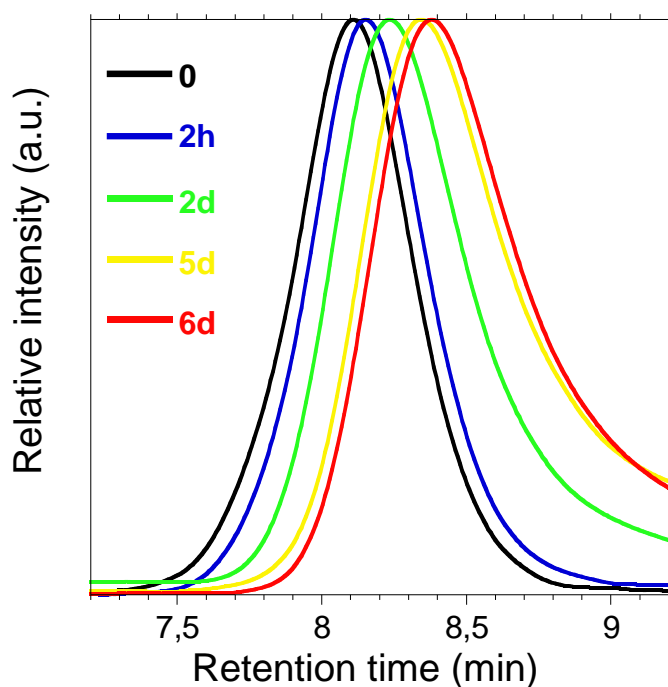
Figure 6.2. *SEC/MALS elugrams as a function of reaction time (1, 2, 3, 4 and 9 days) during single-chain folding of **P1** (1.2 eq) via intra-chain Hantzsch ester formation involving **A2** (0.25 eq), NH₄OAc (0.5 eq) and piperidine (0.05 eq). Final SEC/MALS trace of **P1** after 9 days of reaction time displayed in red.*

Unexpectedly, we found that by increasing the amount of NH$_4$OAc from 0.5 eq to 3 eq, the degree of single-chain compaction of **P1** to SCNP **N1f** [50] improved notably, as observed by SEC (see Figure 6.3).

Figure 6.3. *Normalized SEC/MALS elugrams as a function of reaction time (h = hours, d = days) during single-chain compaction of **P1** (1.2 eq) via intra-chain Hantzsch ester formation involving **A2** (0.25 eq), NH₄OAc (3 eq) and piperidine (0.05 eq).*

Due to the presumably formation of an excess of enamine adduct under such conditions, the kinetics of the Hantzsch ester formation reaction substantially slows down when compared to classical procedures [51]. Slow kinetics, however, should be beneficial for attaining equilibrium conformations of the resulting SCNPs, although it could increase the probability of inter-chain reactions. After 6 days of reaction time, corresponding to a shift of SEC retention time of $\Delta t_R = 0.28$ min, the yield of the Hantzsch ester formation reaction was found to be 92% as calculated from elemental analysis data (Table 6.2).

Table 6.2. Elemental analysis data and yield of the intra-chain Hantzsch ester formation reaction calculated thereof.

Experimental				Theoretical	Yield[b] (%)
Sample	C (wt. %)	H (wt. %)	N (wt. %)	N_{max}[a] (wt. %)	
P1	57.01	7.02	-	-	-
P2	58.47	7.20	-	-	-
P3	57.41	7.17	-	-	-
N1f	58.01	7.01	2.06	2.24	92.0
N2f	59.71	7.27	1.60	1.63	98.1
N2fa	59.11	7.92	1.25	1.39	90.0
N3fa	58.64	7.05	1.19	1.43	83.2

[a]Maximum amount of nitrogen from the theoretical molecular formula by assuming a yield of the intra-chain Hantzsch ester formation reaction of 100 %.

[b]Yield (%) = (N / N_{max}) x 100.

The evolution of SEC traces for copolymer **P2** of higher molecular weight and lower β-ketoester content is shown in Figure 6.4. The shift towards longer retention times (Δt_R = 0.32 min) was indicative of the progressive compaction of **P2** to SCNPs **N2f** via intra-chain Hantzsch ester formation, which amounted to 98 % after 7 days of reaction time (Table 6.2).
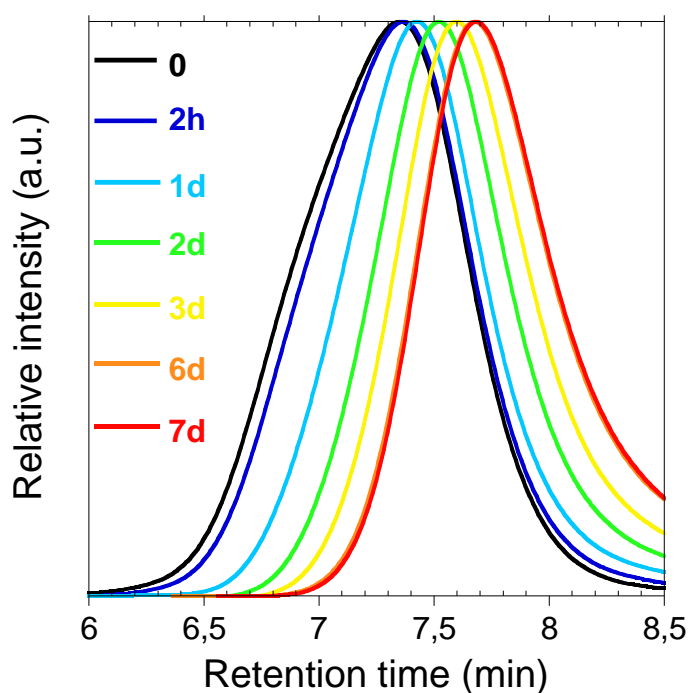
Figure 6.4. *SEC/MALS elugrams of **P2** (1.2 eq) during reaction with **A2** (0.25 eq), NH₄OAc (3 eq) and piperidine (0.05 eq).*

No further significant shift of the SEC trace of **P2** was observed at longer reaction time. Similar observation of single-chain compaction of **P3** to SCNPs **N3f** (Figure 6.5) revealed the general scope of this method for chains randomly decorated with β- ketoester moieties.
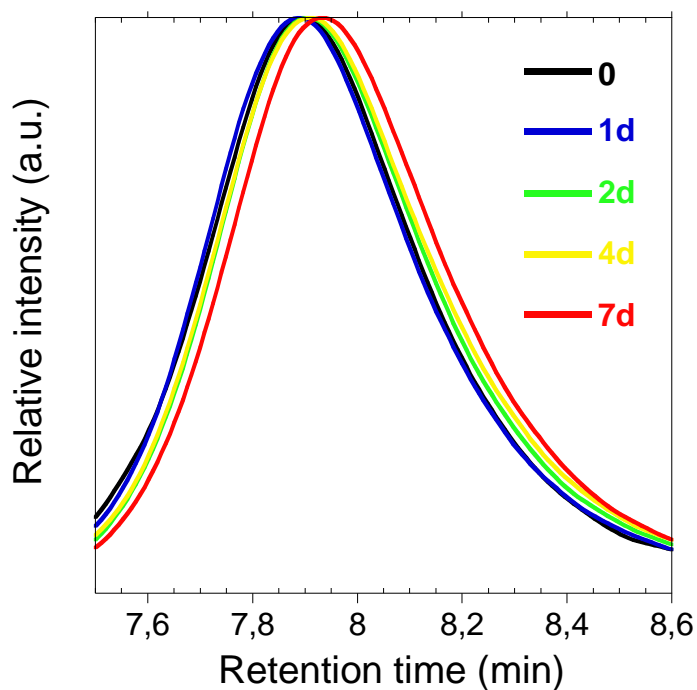
Figure 6.5. *SEC/MALS elugrams as a function of reaction time (0, 1, 2, 4 and 7 days) during single-chain folding of **P3** (1.2 eq) via intra-chain Hantzsch ester formation involving **A2** (0.25 eq), NH₄OAc (3 eq) and piperidine (0.05 eq). Final SEC/MALS trace of **P3** after 7 days of reaction time displayed in red.*

It is worth mentioning the high yield of the Hantzsch ester achieved, even involving a very slow reaction kinetics arising from both the excess of NH$_4$OAc used and the macromolecular environment of the β-ketoester groups in **P1–P3** when compared to the Hantzsch reaction kinetics of low molecular weight organic molecules [41-43]. Actual M_w data of **P1–P3** and **N1f–N3f** derived from SEC/MALS measurements confirmed the successful intra-chain reaction without signs of significant multi-chain aggregation (Table 6.3).

Table 6.3. *Absolute M_w data of precursors **P1-P3**, SCNPs **N1f-N3f** and SCNPs **N1fa-N3fa** as determined from static multi-angle light scattering (MALS) measurements.*

Sample	M_w (kDa)	Sample	M_w (kDa)	Sample	M_w (kDa)
P1	43.6	N1f	56.1	N1fa	78.9
P2	288.6	N2f	346.3	N2fa	357.9
P3	56.2	N3f	71.4	N3fa	84.3

Additional support of single-chain compaction was obtained from small angle X-ray scattering (SAXS) measurements in solution showing a decrease of the radius of gyration from R_g = 6.5, 23.4 and 7.8 nm (unfolded **P1- P3** chains) to R_g = 4.6, 10.7 and 5.9 nm (SCNPs **N1f-N3f**) and Flory exponents from v = 0.59 in the unfolded state to v = 0.46, 0.42 and 0.44 (SCNPs **N1f-N3f**) (see Figure 6.6).
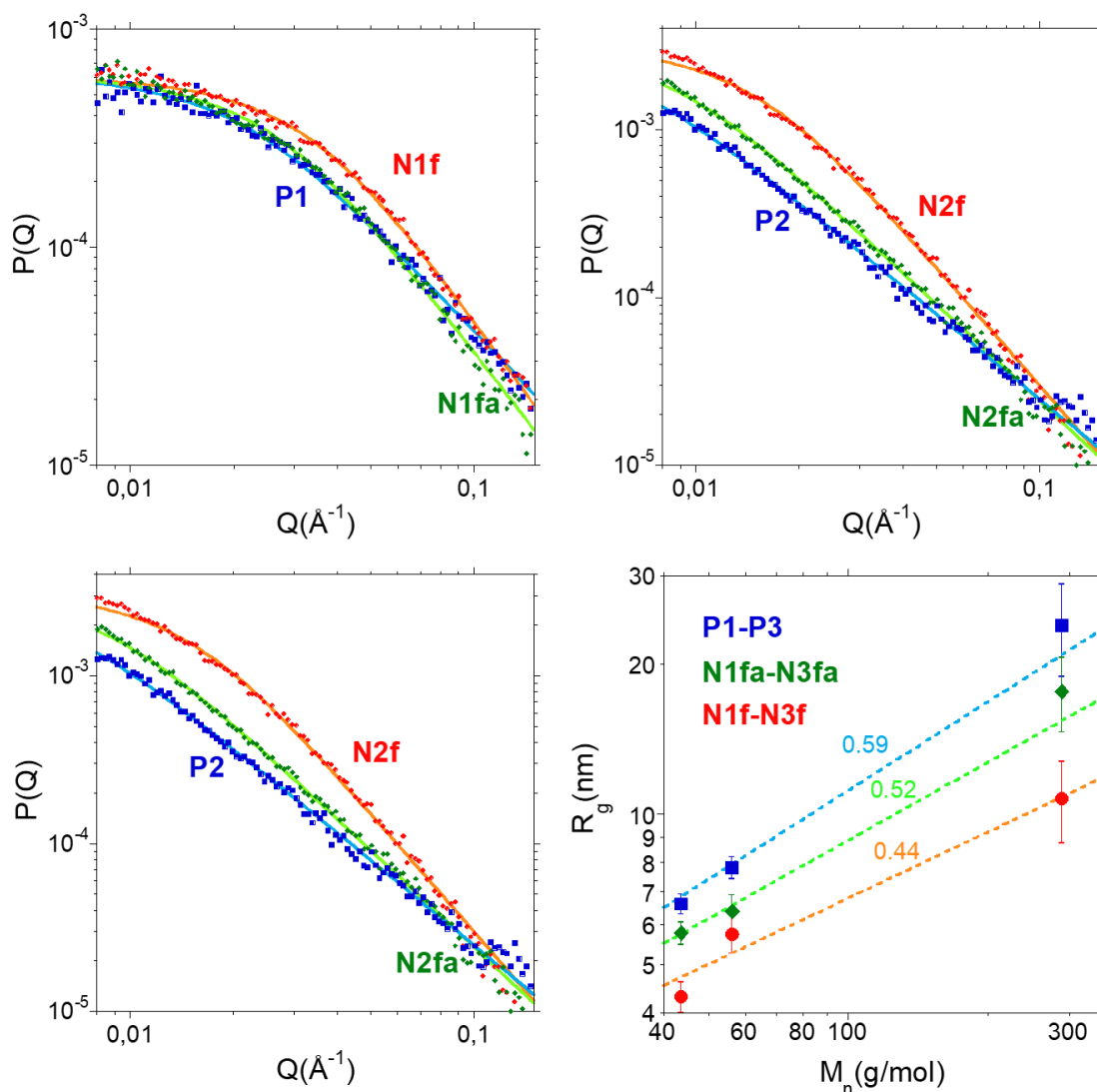
Figure 6.6. A) *SAXS results revealing the form factor of **P1**, **N1f** and **N1fa**. Values of R_g and ν were obtained through fits of the experimental P(Q) vs Q data to a generalized Gaussian coil function (equation (6.1). **P1**: R_g = 6.5 nm, ν = 0.59. **N1f**: R_g = 4.6 nm, ν = 0.46. **N1fa**: R_g = 5.8 nm, ν = 0.48. **B)** SAXS results revealing the form factor of **P2**, **N2f** and **N2fa**. Values of R_g and ν were obtained through fits of the experimental P(Q) vs Q data to a generalized Gaussian coil function (equation (6.1). **P2**: R_g = 23.8 nm, ν = 0.59. **N2f**: R_g = 10.7 nm, ν = 0.42. **N2fa**: R_g = 17.6 nm, ν = 0.52. **C)** SAXS results revealing the form factor of **P3**, **N3f** and **N3fa**. Values of R_g and ν were obtained through fits of the experimental P(Q) vs Q data to a generalized Gaussian coil function (equation (6.1). **P3**: R_g = 7.8 nm, ν = 0.59. **N3f**: R_g = 5.7 nm, ν = 0.44. **N3fa**: R_g = 6.4 nm, ν = 0.51. **D)** Scaling laws ($R_g \sim M_w{}^\nu$) corresponding to **P1-P3**, SCNPs **N1f-N3f** and SCNPs **N1fa-N3fa** as determined from SAXS measurements.*

These values are in agreement with previous results concerning single-chain folding of synthetic polymers to SCNPs [26, 52]. Complementary to elemental analysis data, infra-red (IR) spectroscopy revealed the appearance of a new, broad band between 3300 and 3500 cm⁻¹ arising from the stretching vibrations of -NH- groups (Figure 6.7).
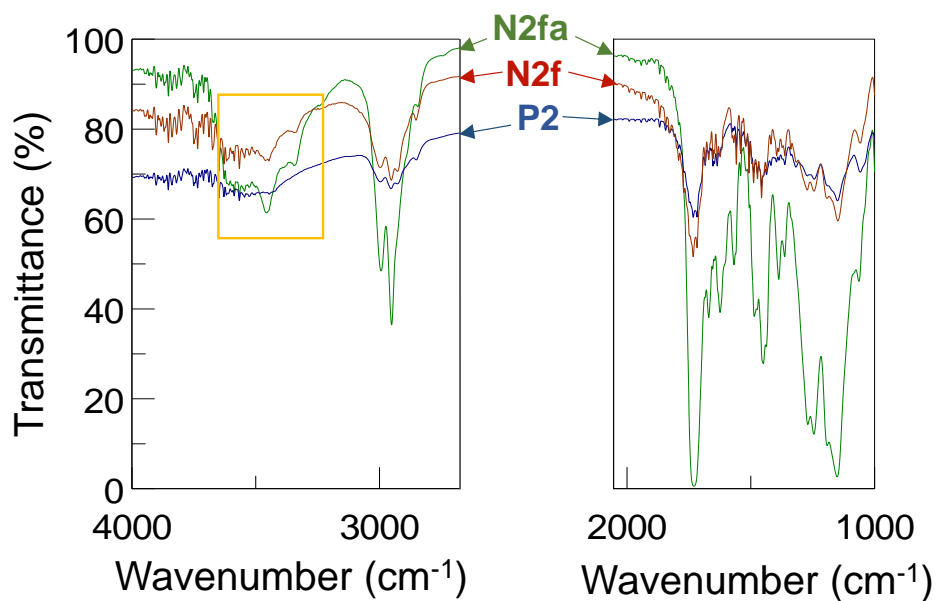
Figure 6.7. *FTIR spectra of **P2**, **N2f** and **N2fa** in the wavenumber regions of 3000-4000 cm⁻¹ and 2000-1000 cm⁻¹. The appearance of a new, broad band -when compared to **P2**- arising from the stretching vibrations of –NH– groups in **N2f** and **N2fa** is highlighted in yellow.*

Also, the ^{1}H NMR spectrum was in agreement with the expected structure of SCNPs **N2f** (Figure 6.8).
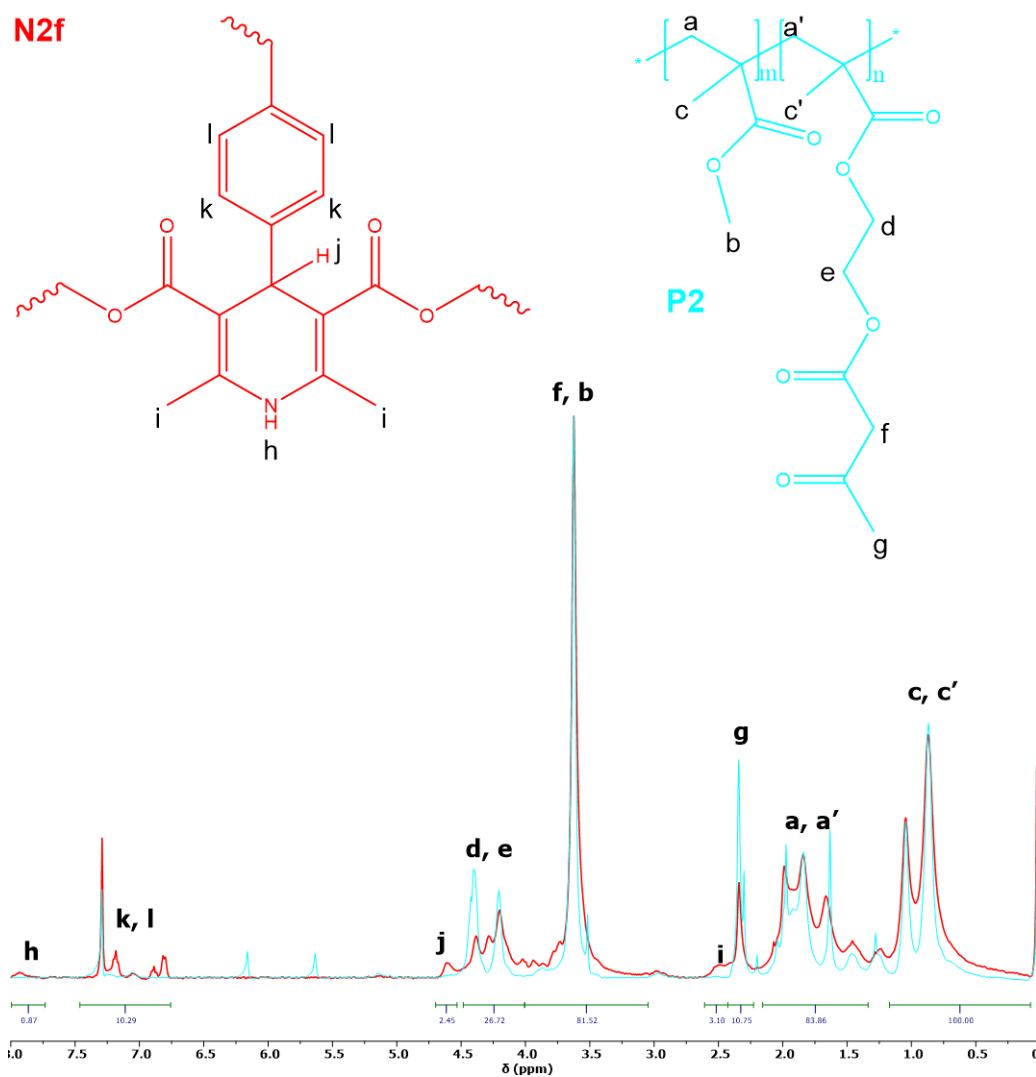
Figure 6.8. *¹H NMR spectra of **P2** (displayed in blue) and **N2f** (in red).*

Fluorescence spectroscopy measurements further supported the successful, progressive formation of intra-chain connectors via Hantzsch reaction. As illustrated in Figure 6.9, the intensity of the fluorescence band corresponding to the emission of intra-chain Hantzsch fluorophores increases progressively with reaction time.
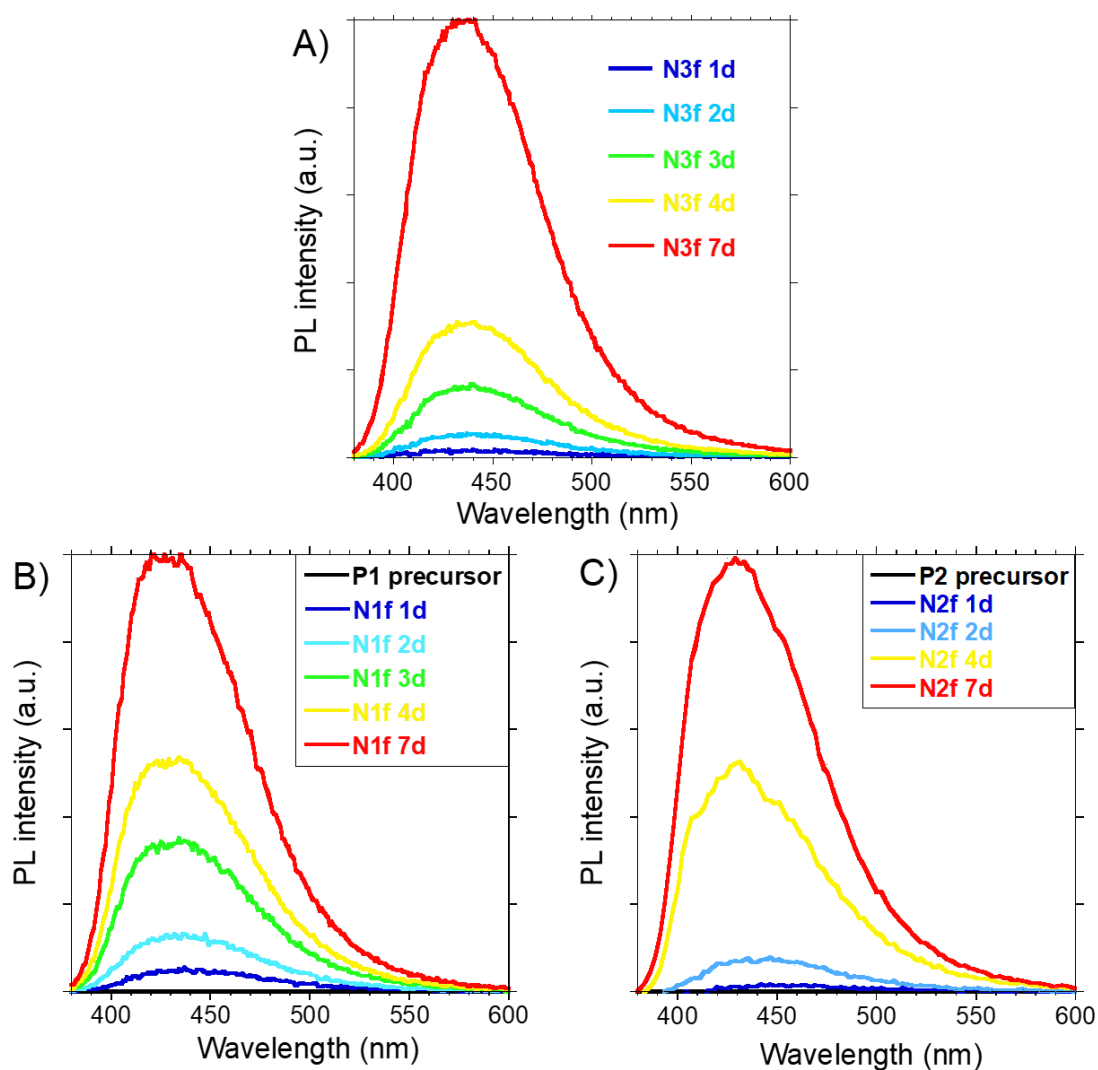
Figure 6.9. A) *Photoluminescence emission spectra of **P3** during single-chain compaction as a function of reaction time (λ_exc = 365 nm).* **B)** *Results of FS experiments showing the increase in photoluminescence emission during "in-situ" generation of SCNPs **N1f** from **P1**.* **C)** *Results of FS experiments showing the increase in photoluminescence emission during "in-situ" generation of SCNPs **N2f** from **P2**.*

Consequently, single-chain compaction was visually detected under UV illumination at λ_{exc} = 365nm through photoluminescence arising from Hantzsch luminophores progressively generated as intra-chain connectors (Figure 6.10).

Figure 6.10. *Photographs of **P2** in THF (1 mg/ml) under 365 nm UV illumination after 2h and 7d of single-chain compaction.*

An inverse relationship between single-chain size reduction as monitored by in situ SAXS kinetic experiments (Figure 6.11 A) and photoluminescence emission (Figure 6.9 B) was found, as illustrated in Figure 6.11 B. Altogether, the above experimental data provide support of the visual detection of single-chain folding of **P1–P3** to SCNPs **N1f–N3f** via intra-chain Hantzsch fluorophore generation.
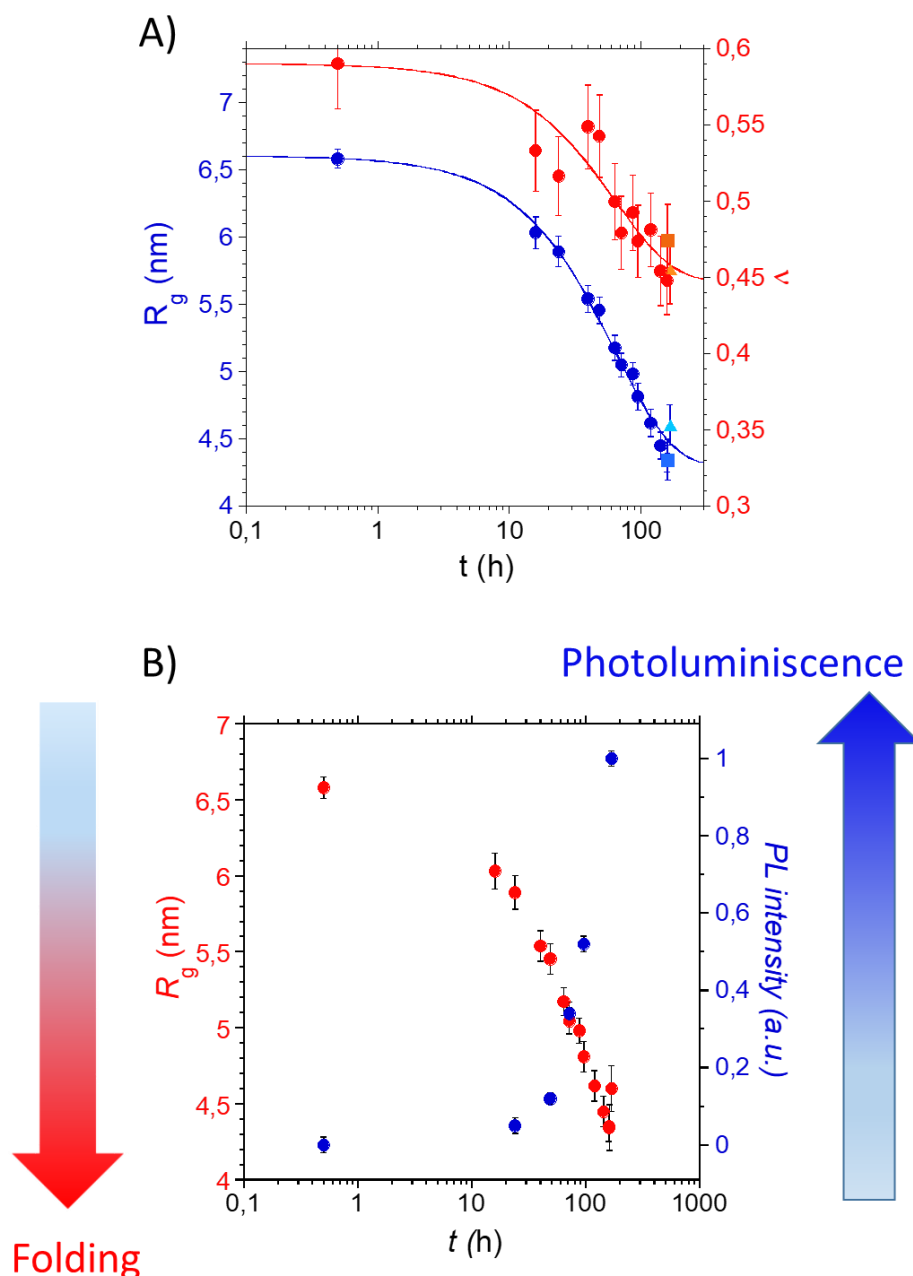
Figure 6.11. A) *Results of SAXS experiments showing the single-chain size reduction ($R_g \sim M_w{}^v$) during "in-situ" generation of SCNPs **N1f** from **P1** (circles). Data from other two independent measurements are also included for comparison (triangles and squares). **B)** Inverse relationship between single-chain size reduction, as determined by SAXS measurements, and photoluminescence emission observed during single-chain compaction of **P1**.*

6.4.2. Self-reporting of folding and aggregation within a single polymer chain by orthogonal luminophores via Hantzsch reaction

Next, to endow the synthetic polymers **P1–P3** with orthogonal intra-molecular compaction and inter-molecular aggregation self-reporting characteristics, we investigated replacement of bifunctional terephthalaldehyde **A2** by 4-(1,2,2-triphenylethenyl)benzaldehyde **A3** (see Scheme 6.4) with the aim of visual detection of

multi-chain aggregates (when formed) via aggregation-induced emission (AIE) [38-40] from tetraphenylethene (TPE) moieties.

A)
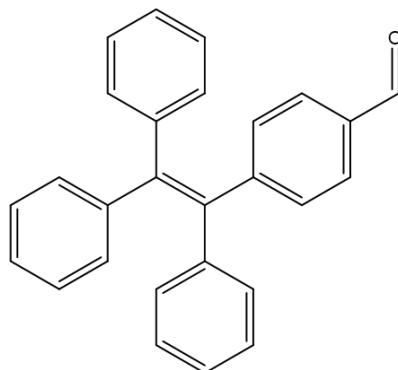
A3

B)
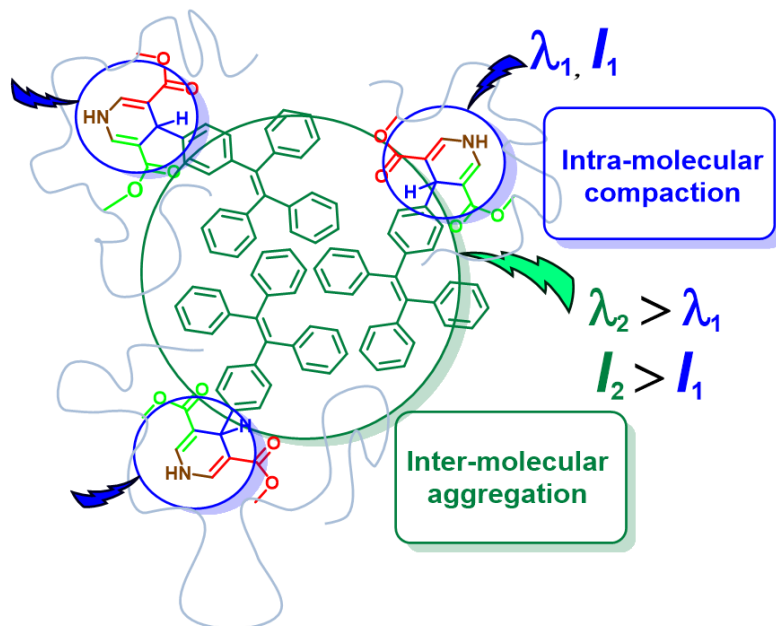
Scheme 6.4. A) Aldehyde compound to report, additionally, the assembly of SCNPs into multi-SCNPs aggregates via aggregation-induced emission (AIE) 4-(1,2,2- triphenylethenyl)benzaldehyde (A3). B) Illustration of self-reporting of folding and aggregation by orthogonal Hantzsch luminophores within a single polymer chain.

Remarkably, TPE molecules show almost no photoluminescence in diluted solutions (e.g., $\Phi_F = 0.24$ % in acetonitrile) whereas in a non-solvent medium and in the solid state they display intense AIE-type photoluminescence (e.g., $\lambda_{em} = 475$ nm and $\Phi_F = 49$ % in amorphous film) [53]. We hypothesized that photoluminescence arising from aggregation of TPE-containing SCNPs should be more intense than that coming from Hantzsch fluorophores, and should be located at redshifted wavelengths. Moreover, installation of TPE pendants based on aldehyde **A3** can be carried out also through Hantzsch ester formation. Hence, placement of an orthogonal (AIE-type) luminophore within a synthetic

polymer chain via Hantzsch ester formation could be a very suitable strategy for additional self-reporting of multi-SCNPs aggregation. Unfortunately, total replacement of **A2** by **A3** resulted in a significant reduction of the degree of single-chain compaction, presumably due to the large steric hindrance introduced by **A3** within the macromolecular environment of the reactive β-ketoester groups (Figure 6.12). The degree of single-chain compaction increased by only partial replacement of **A2** by **A3**.
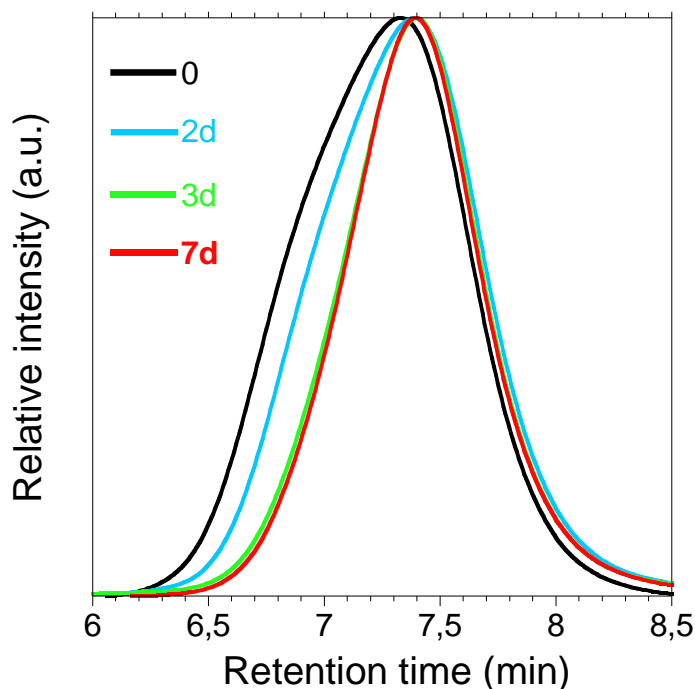
Figure 6.12. SEC/MALS elugrams as a function of reaction time (0, 2, 3 and 7 days) during single-chain folding of **P2** (1.2 eq) via intra-chain Hantzsch ester formation involving **A3** (0.5 eq), NH₄OAc (3 eq) and piperidine (0.05 eq). Initial SEC/MALS trace of unfolded **P2** displayed in black. Final SEC/MALS trace of **P2** displayed in red.

Figure 6.13 shows the evolution of the SEC / MALS traces as a function of reaction time during single-chain folding of **P2** to SCNPs **N2fa** [54] using a **A2** / **A3** molar ratio of 1/2. Even involving a slower Hantzsch reaction kinetics due to the presence of **A3**, the yield of the Hantzsch ester product was 90 % for SCNPs **N2fa** after 13 days of reaction time (Table 6.2).
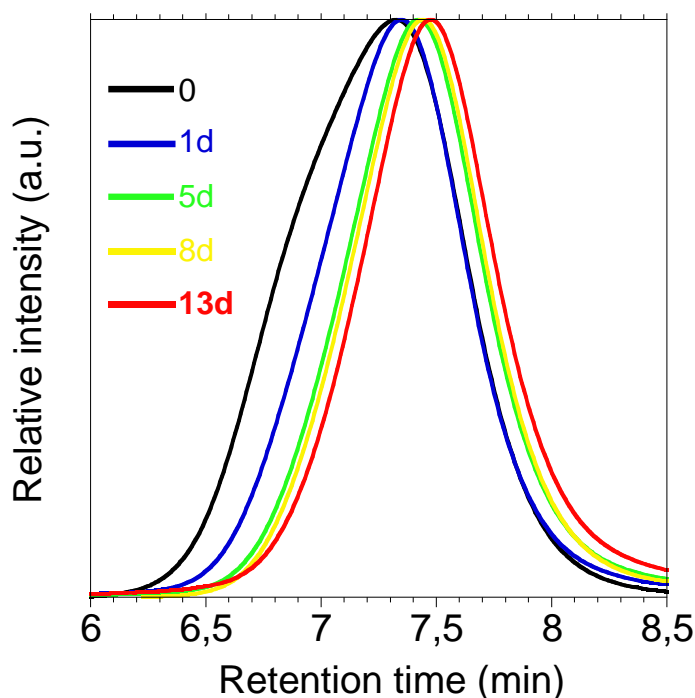
Figure 6.13. *Normalized SEC/MALS elugrams as a function of reaction time during single-chain compaction via intra-chain Hantzsch ester formation involving* **P2** *(1.2 eq),* **A2** *(0.125 eq),* **A3** *(0.25 eq), NH4OAc (3 eq) and piperidine (0.05 eq).*

SAXS measurements provide solid support of the single-chain compaction of **P2** to SCNPs **N2fa**, revealing a reduction in size from $R_g = 23.8$ nm to $R_g = 17.6$ nm, and a decrease of the scaling exponent from $\nu = 0.59$ to $\nu = 0.52$, respectively (Figure 6.6 B). Due to the severe steric hindrance introduced by **A3** the degree of single-chain compaction was lower, however, than that observed for SCNPs **N2f** ($R_g = 10.7$ nm, $\nu = 0.42$). Structural characterization by ^{1}H NMR and IR spectroscopy -complemented with elemental analysis data- revealed both generation of intra-chain connectors via Hantzsch reaction and successful incorporation of TPE moieties into SCNPs **N2fa** (Figure 6.7, Figure 6.14, Table 6.2).

Moreover, absolute M_w data (Table 6.3) and SAXS results (Figure 6.6) corroborated the single-chain nature of nanoparticles **N1fa–N3f**.
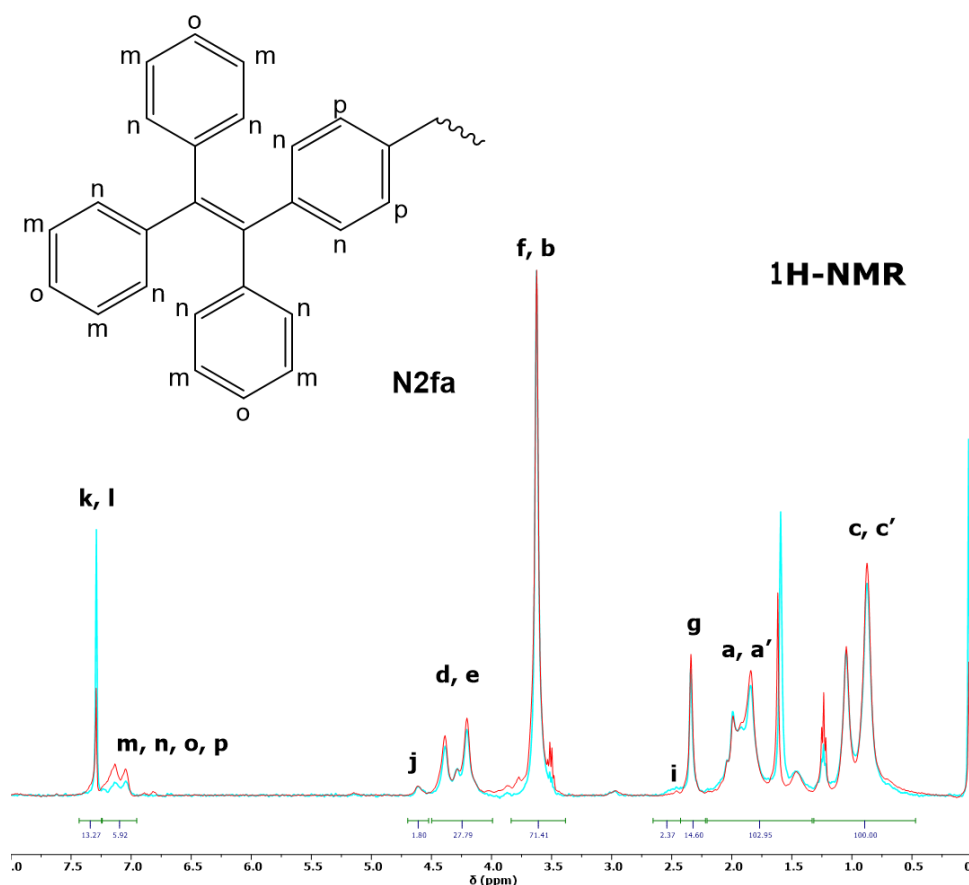
Figure 6.14. *^{1}H NMR spectrum of **N2fa** synthesized using a **A2** / **A3** molar ratio = 1 / 2 (displayed in red) compared to that obtained by using neat **A3** (in blue).*

6.4.3. Self-reporting of (intentionally induced) multi-SCNPs aggregation

Two model experiments were performed to investigate self-reporting of (intentionally induced) multi-SCNPs aggregation by SCNPs **N1fa–N3fa**. First, inter-particle association was promoted in good solvent via photo-activated radical-mediated thiol-ene coupling (TEC) reaction under UV irradiation in the presence of 2,2-dimethoxy-2-phenylacetophenone, as photo-initiator, and 3,6- dioxa-1,8-octane-dithiol, as homobifunctional cross-linker. Before UV irradiation of SCNPs **N1fa** in THF, photoluminescence arising exclusively from the Hantzsch luminophores generated as intra-chain connectors was observed (Figure 6.15 A, i). After 90 min of UV irradiation (λ_{exc} = 365 nm), the formation of multi-SCNPs aggregates, that was confirmed by dynamic light scattering (DLS) measurements (see Figure 6.15 B and C), was successfully accompanied by a significant increase in photoluminescence at redshifted wavelengths (Figure 6.15 A, ii).
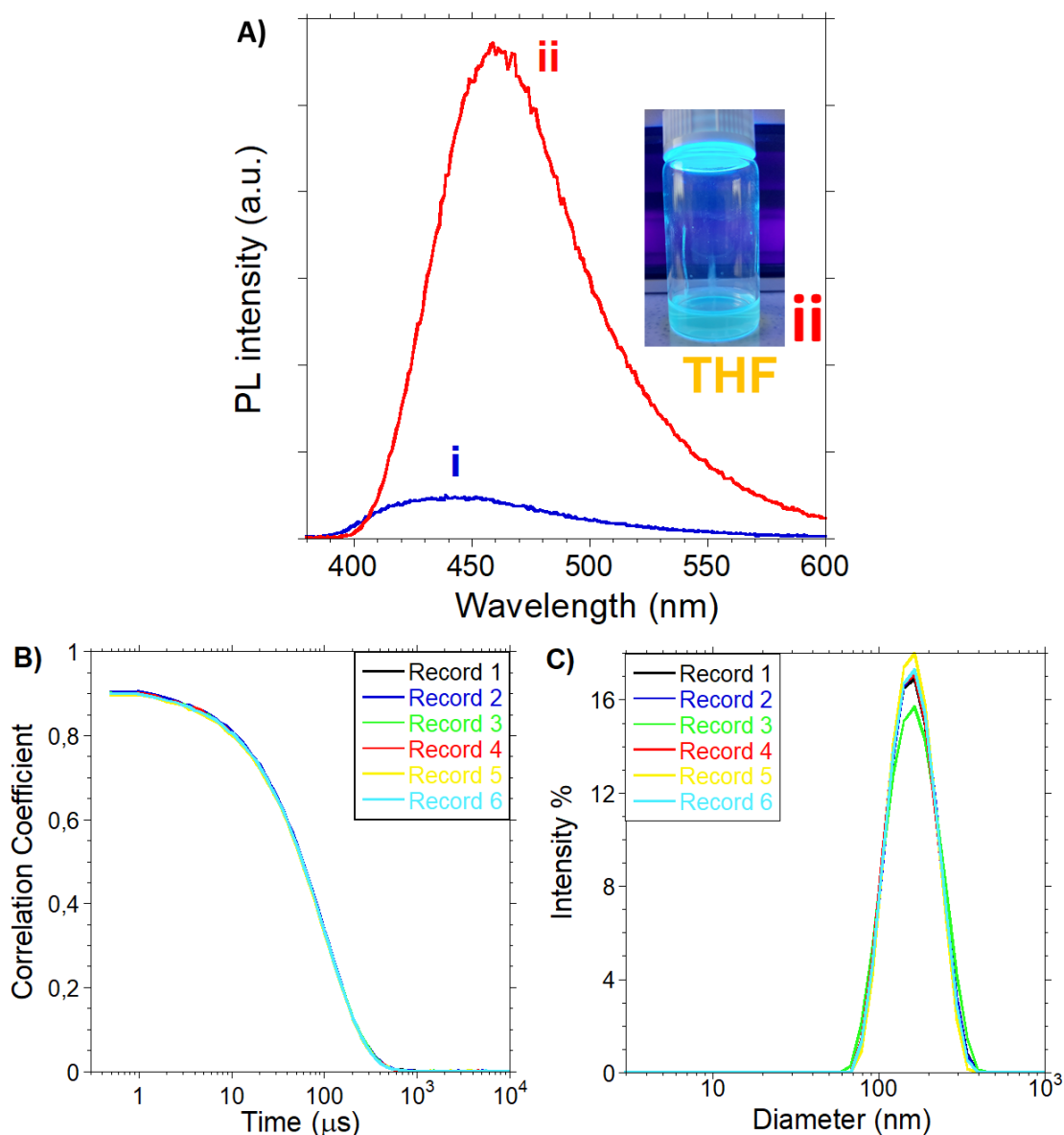
Figure 6.15. A) *Increase in photoluminescence at redshifted wavelengths upon formation in THF of multi-SCNPs aggregates (ii) via UV irradiation (λ$_{exc}$ = 365 nm) of SCNPs **N2fa** (i) in the presence of 3,6-dioxa-1,8-octane-dithiol as homobifunctional cross-linker and 2,2-dimethoxy-2-phenylacetophenone as photoinitiator. **B)** Correlation function of multi-SCNPs aggregates of SCNPs **N2fa** (1 mg ml^{-1}) generated in THF (1 mg ml^{-1}) through photoactivated radical-mediated thiol-ene coupling reaction. The corresponding DLS intensity distribution is given in **C)** showing that the hydrodynamic size of the multi-SCNPs aggregates is > 100 nm. Results from 6 consecutive measurement are shown.*

Next, inter-molecular association of SCNPs **N1fa–N3fa** in mixtures of THF and EtOH -which is a precipitant of SCNPs **N1fa–N3fa**- was investigated. As a representative example, SCNPs **N3fa** developed intense AIE-type photoluminescence at redshifted wavelengths in THF / EtOH mixtures upon decreasing the THF / EtOH volume ratio (Figure 6.16).
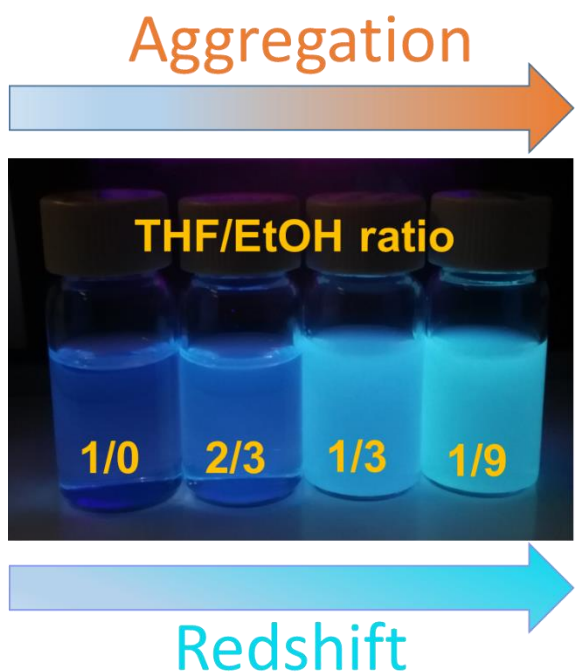
Figure 6.16. *Photographs of SCNPs **N2fa** (1 mg/ml) in solvent (THF) / non-solvent (EtOH) mixtures at different volume ratios under 365 nm UV illumination.*

The presence of multi-SCNPs aggregates was confirmed by DLS experiments. Hence, DLS (intensity distribution) results of SCNPs **N3fa** in THF / EtOH mixtures at volume ratios of 2/3 and 1/3 revealed the presence of multi-SCNPs aggregates with hydrodynamic size larger than 100 nm (Figure 6.17).
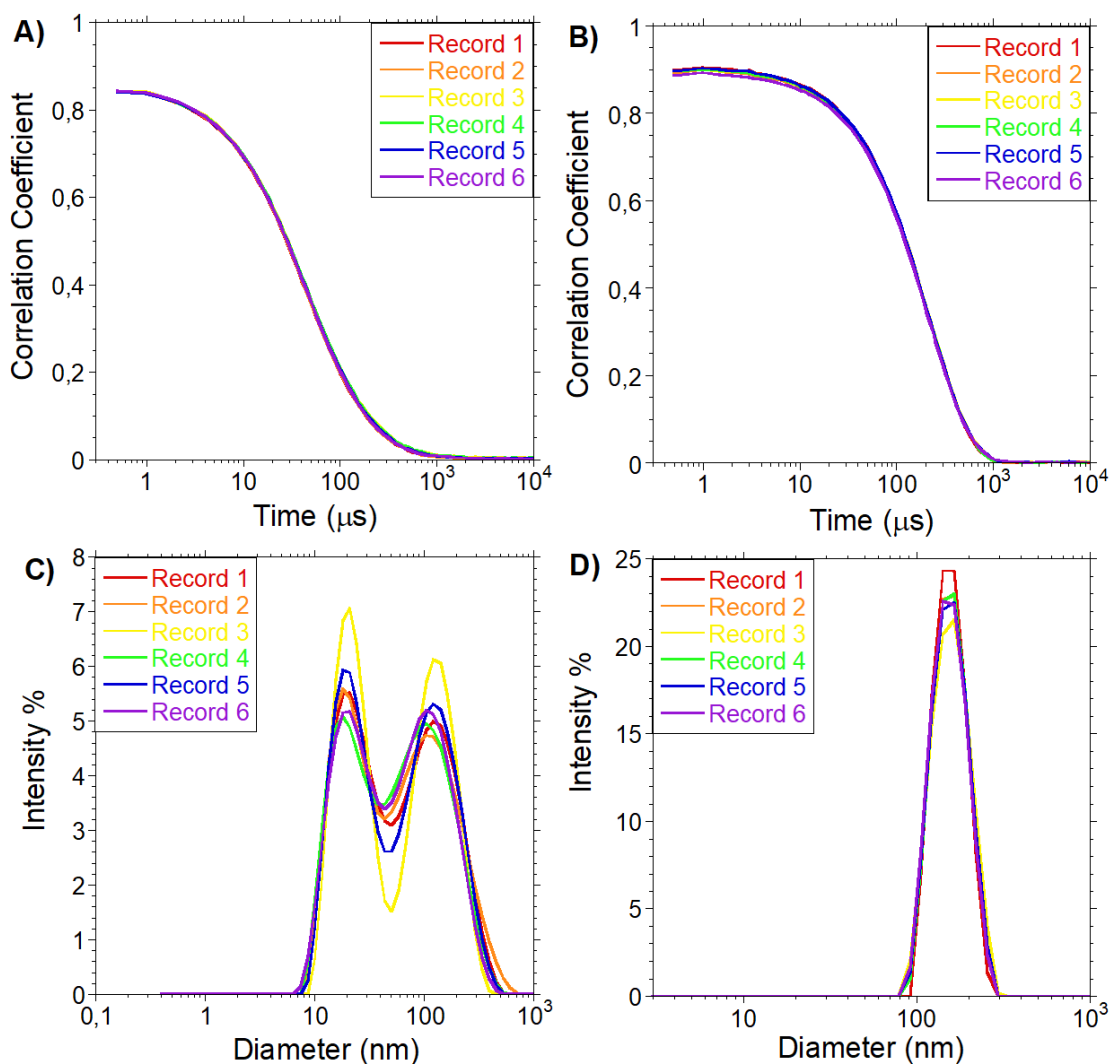
Figure 6.17. *Correlation function of multi-SCNPs aggregates of SCNPs **N2fa** (1 mg/ml) generated in THF / EtOH mixtures with a THF / EtOH ratio of 2/3 **(A)** and 1/3 **(B)**. The corresponding DLS intensity distributions are given in **C)** and **D)**, respectively. Results from 6 consecutive measurement are shown.*

Macroscopic precipitation was visually observed at a THF / EtOH volume ratio of 1/9. Although in the latter case a certain contribution from conformational changes induced by preferential solvation [55] could be involved, taken together, the above model experiments certified that SCNPs **N1fa–N3fa** were indeed successfully equipped with orthogonal luminophores for visualizing intramolecular compaction and inter-molecular aggregation phenomena.

Finally, the high sensitivity of this method via changes in both photoluminescence intensity and wavelength was applied to establish an accurate diagram of states of the SCNPs in THF / EtOH mixtures. Figure 6.18 shows the photoluminescence emission spectra of SCNPs **N3fa** in THF / EtOH mixtures (1 mg/ml) at different volume ratios.
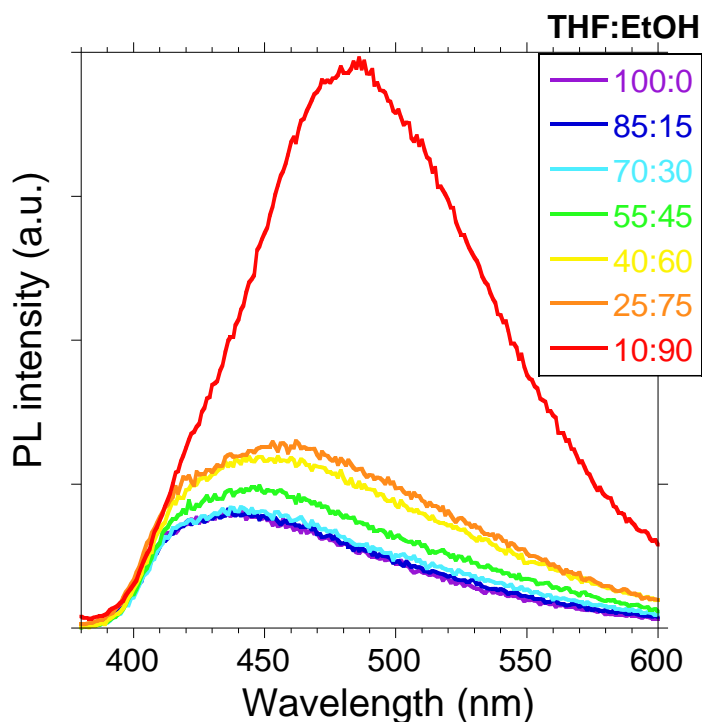
*Figure 6.18. Photoluminescence emission spectra of SCNPs **N3fa** in THF / EtOH mixtures (1 mg/ml) at different volume ratios (λ_{exc} = 365 nm).*

At low EtOH content ($\leq$ 15 vol. %) the photoluminescence emission spectrum of the single-chain nanoparticles was equivalent to that recorded in neat THF, revealing the absence of significant aggregation phenomena. Upon increasing the EtOH content in the mixture, the photoluminescence emission intensity grew (Figure 6.19 A) and the wavelength at peak maximum shifted towards higher values (Figure 6.19 B). Macroscopic precipitation -which was observed at high EtOH content (90 vol. %)- was accompanied by a 5-fold increase in photoluminescence emission intensity, which was found to shift to λ_{em} = 485nm. Based on the above consistent changes in photoluminescence intensity and wavelength, a reliable diagram of states reporting intra-molecular compaction (**C**), inter-molecular aggregation (**A**) and macroscopic precipitation (**P**) of SCNPs **N3fa** in THF / EtOH mixtures emerged (see Figure 6.19).
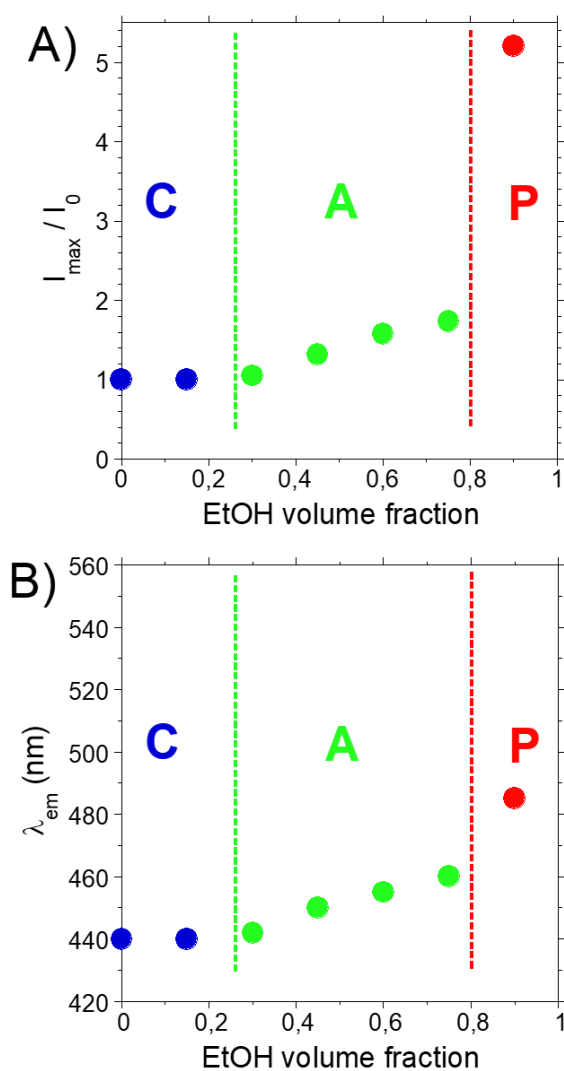
Figure 6.19. A) *Ratio of photoluminescence emission intensity at peak maximum to that in neat THF (I_{max}/I_0) as a function of EtOH volume fraction, and diagram of states of SCNPs **N3fa**: "intra-molecular compaction" zone (**C**, blue solid circles), "inter-molecular aggregation" region (**A**, green solid circles) and "macroscopic-precipitation" zone (**P**, red solid circles). **B)** Photoluminescence emission wavelength at peak maximum (l_{em}) as a function of EtOH volume fraction (blue, green and red circles), and **C-A-P** diagram.*

6.5. Conclusions

In conclusion, we have developed a strategy for self-reporting both intra-molecular compaction and inter-molecular aggregation through installation of orthogonal luminophores based on Hantzsch ester formation within a single polymer chain. We have demonstrated that this method permits to detect visually the degree of single-chain compaction of a synthetic polymer chain containing β-ketoester moieties via generation of Hantzsch luminophores as intra-chain connectors taking the role of surrogates of covalent disulphide bonds in folded proteins. We have shown that orthogonal AIE-type luminophores placed also through intra-chain Hantzsch reaction allow complementary self-reporting of inter-molecular aggregation via photoluminescence at redshifted wavelengths. Multi-chain aggregation, in the case of SCNPs, would play a role equivalent to the self-assembly of defective proteins into pathogenic aggregates. The method is simple and highly

accurate e.g. to establish reliable single-chain compaction-aggregation-precipitation diagrams of SCNPs in solvent / non-solvent mixtures. Since introduction of β-ketoester moieties in synthetic polymer chains is relatively straightforward and a variety of functional SCNPs have indeed been constructed from precursors containing these pendants, this strategy holds promise to perceive at a glance the presence / absence of detrimental multi-chain aggregates affecting the performance of SCNPs in catalysis, sensing, recognition, and so on.

6.6. References

[1] M. Gruebele, K. Dave, S. Sukenik, Globular Protein Folding In Vitro and In Vivo, Annual Review of Biophysics, 45 (2016) 233-251.

[2] V. Armiento, A. Spanopoulou, A. Kapurniotu, Peptide-Based Molecular Strategies To Interfere with Protein Misfolding, Aggregation, and Cell Degeneration, Angewandte Chemie International Edition, 59 (2020) 3372-3384.

[3] J.R. Lakowicz, Principles of fluorescence spectroscopy, Springer science & business media2013.

[4] A. Aliyan, N.P. Cook, A.A. Martí, Interrogating Amyloid Aggregates using Fluorescent Probes, Chemical Reviews, 119 (2019) 11819-11856.

[5] C.W. Bertoncini, M.S. Celej, Small Molecule Fluorescent Probes for the Detection of Amyloid Self-Assembly In Vitro and In Vivo, Current Protein & Peptide Science, 12 (2011) 206-220.

[6] J.A. Pomposo, Single-Chain Polymer Nanoparticles: Synthesis, Characterization, Simulations, and Applications, John Wiley & Sons2017.

[7] We use the term "folding" referred to the process by which a functionalized polymer chain assumes its final shape or conformation as individual single-chain nanoparticle (SCNP) via non-covalent, or covalent, or dynamic covalent intra-chain interactions at high dilution. Folding, single-chain compaction and intra-molecular compaction are utilized as synonyms along the chapter. Note, however, that "unfolding" of SCNPs is reserved to SCNPs with non-covalent or dynamic covalent intra-chain interactions.

[8] S. Mavila, O. Eivgi, I. Berkovich, N.G. Lemcoff, Intramolecular Cross-Linking Methodologies for the Synthesis of Polymer Nanoparticles, Chemical Reviews, 116 (2016) 878-961.

[9] C.K. Lyon, A. Prasher, A.M. Hanlon, B.T. Tuten, C.A. Tooley, P.G. Frank, E.B. Berda, A brief user's guide to single-chain nanoparticles, Polymer Chemistry, 6 (2015) 181-197.

[10] M. ter Huurne Gijs, R.A. Palmans Anja, E.W. Meijer, Supramolecular Single-Chain Polymeric Nanoparticles, CCS Chemistry, 1 (2019) 64-82.

[11] T.S. Fischer, D. Schulze-Sünninghausen, B. Luy, O. Altintas, C. Barner-Kowollik, Stepwise Unfolding of Single-Chain Nanoparticles by Chemically Triggered Gates, Angewandte Chemie International Edition, 55 (2016) 11276-11280.

[12] E. Huerta, P.J.M. Stals, E.W. Meijer, A.R.A. Palmans, Consequences of Folding a Water-Soluble Polymer Around an Organocatalyst, Angewandte Chemie International Edition, 52 (2013) 2906-2910.

[13] E.A. Appel, J. Dyson, J. del Barrio, Z. Walsh, O.A. Scherman, Formation of Single-Chain Polymer Nanoparticles in Water through Host–Guest Interactions, Angewandte Chemie International Edition, 51 (2012) 4185-4189.

[14] E. Verde-Sesto, A. Arbe, A.J. Moreno, D. Cangialosi, A. Alegría, J. Colmenero, J.A. Pomposo, Single-chain nanoparticles: opportunities provided by internal and external confinement, Materials Horizons, 7 (2020) 2292-2313.

[15] M. Gonzalez-Burgos, A. Latorre-Sanchez, J.A. Pomposo, Advances in single chain technology, Chemical Society Reviews, 44 (2015) 6122-6142.

[16] M. Ouchi, N. Badi, J.-F. Lutz, M. Sawamoto, Single-chain technology using discrete synthetic macromolecules, Nature Chemistry, 3 (2011) 917-924.

[17] T.-K. Nguyen, S.J. Lam, K.K.K. Ho, N. Kumar, G.G. Qiao, S. Egan, C. Boyer, E.H.H. Wong, Rational Design of Single-Chain Polymeric Nanoparticles That Kill Planktonic and Biofilm Bacteria, ACS Infectious Diseases, 3 (2017) 237-248.

[18] J. Liang, J.J. Struckhoff, P.D. Hamilton, N. Ravi, Preparation and Characterization of Biomimetic β-Lens Crystallins Using Single-Chain Polymeric Nanoparticles, Langmuir, 33 (2017) 7660-7668.

[19] S. Thanneeru, J.K. Nganga, A.S. Amin, B. Liu, L. Jin, A.M. Angeles-Boza, J. He, "Enzymatic" Photoreduction of Carbon Dioxide using Polymeric Metallofoldamers Containing Nickel–Thiolate Cofactors, ChemCatChem, 9 (2017) 1157-1162.

[20] J. Chen, J. Wang, K. Li, Y. Wang, M. Gruebele, A.L. Ferguson, S.C. Zimmerman, Polymeric "Clickase" Accelerates the Copper Click Reaction of Small Molecules, Proteins, and Cells, Journal of the American Chemical Society, 141 (2019) 9693-9700.

[21] A. Sanchez-Sanchez, A. Arbe, J. Colmenero, J.A. Pomposo, Metallo-Folded Single-Chain Nanoparticles with Catalytic Selectivity, ACS Macro Letters, 3 (2014) 439-443.

[22] A. Sanchez-Sanchez, S. Akbari, A.J. Moreno, F.L. Verso, A. Arbe, J. Colmenero, J.A. Pomposo, Design and Preparation of Single-Chain Nanocarriers Mimicking Disordered Proteins for Combined Delivery of Dermal Bioactive Cargos, Macromolecular Rapid Communications, 34 (2013) 1681-1686.

[23] B.T. Tuten, D. Chao, C.K. Lyon, E.B. Berda, Single-chain polymer nanoparticles via reversible disulfide bridges, Polymer Chemistry, 3 (2012) 3068-3071.

[24] G. Hattori, Y. Hirai, M. Sawamoto, T. Terashima, Self-assembly of PEG/dodecyl-graft amphiphilic copolymers in water: consequences of the monomer sequence and chain flexibility on uniform micelles, Polymer Chemistry, 8 (2017) 7248-7259.

[25] G.M. ter Huurne, I.K. Voets, A.R.A. Palmans, E.W. Meijer, Effect of Intra- versus Intermolecular Cross-Linking on the Supramolecular Folding of a Polymer Chain, Macromolecules, 51 (2018) 8853-8861.

[26] A. Arbe, J.A. Pomposo, A.J. Moreno, F. LoVerso, M. González-Burgos, I. Asenjo-Sanz, A. Iturrospe, A. Radulescu, O. Ivanova, J. Colmenero, Structure and dynamics of single-chain nano-particles in solution, Polymer, 105 (2016) 532-544.

[27] M.A.J. Gillissen, I.K. Voets, E.W. Meijer, A.R.A. Palmans, Single chain polymeric nanoparticles as compartmentalised sensors for metal ions, Polymer Chemistry, 3 (2012) 3166-3174.

[28] G.M. ter Huurne, M.A.J. Gillissen, A.R.A. Palmans, I.K. Voets, E.W. Meijer, The Coil-to-Globule Transition of Single-Chain Polymeric Nanoparticles with a Chiral Internal Secondary Structure, Macromolecules, 48 (2015) 3949-3956.

[29] M. Tomasulo, E. Deniz, R.J. Alvarado, F.M. Raymo, Photoswitchable Fluorescent Assemblies Based on Hydrophilic BODIPY—Spiropyran Conjugates, The Journal of Physical Chemistry C, 112 (2008) 8038-8045.

[30] I. Yildiz, S. Impellizzeri, E. Deniz, B. McCaughan, J.F. Callan, F.M. Raymo, Supramolecular Strategies To Construct Biocompatible and Photoswitchable Fluorescent Assemblies, Journal of the American Chemical Society, 133 (2011) 871-879.

[31] S. Swaminathan, C. Fowley, B. McCaughan, J. Cusido, J.F. Callan, F.M. Raymo, Intracellular Guest Exchange between Dynamic Supramolecular Hosts, Journal of the American Chemical Society, 136 (2014) 7907-7913.

[32] T.S. Fischer, S. Spann, Q. An, B. Luy, M. Tsotsalas, J.P. Blinco, H. Mutlu, C. Barner-Kowollik, Self-reporting and refoldable profluorescent single-chain nanoparticles, Chemical Science, 9 (2018) 4696-4702.

[33] J.T. Offenloch, E. Blasco, S. Bastian, C. Barner-Kowollik, H. Mutlu, Self-reporting visible light-induced polymer chain collapse, Polymer Chemistry, 10 (2019) 4513-4518.

[34] A. Hantzsch, Condensationsprodukte aus Aldehydammoniak und ketonartigen Verbindungen, Berichte der deutschen chemischen Gesellschaft, 14 (1881) 1637-1638.

[35] D. Pi, H. Zhou, P. Cui, R. He, Y. Sui, Silver-Catalyzed Biomimetic Transfer Hydrogenation of N-Heteroaromatics with Hantzsch Esters as NADH Analogues, ChemistrySelect, 2 (2017) 3976-3979.

[36] L. Shen, S. Cao, J. Wu, J. Zhang, H. Li, N. Liu, X. Qian, A revisit to the Hantzsch reaction: Unexpected products beyond 1,4-dihydropyridines, Green Chemistry, 11 (2009) 1414-1420.

[37] We use the term "folding" referred to the process by which a functionalized polymer chain assumes its final shape or conformation as individual single-chain nanoparticle (SCNP) via non-covalent, or covalent, or dynamic covalent intra-chain interactions at high dilution. Folding, single-chain compaction and intra-molecular compaction are utilized as synonyms along the chapter. Note, however, that "unfolding" of SCNPs is reserved to SCNPs with non-covalent or dynamic covalent intra-chain interactions.

[38] Z. Zhao, H. Zhang, J.W.Y. Lam, B.Z. Tang, Aggregation-Induced Emission: New Vistas at the Aggregate Level, Angewandte Chemie International Edition, 59 (2020) 9888-9907.

[39] K. Kokado, K. Sada, Consideration of Molecular Structure in the Excited State to Design New Luminogens with Aggregation-Induced Emission, Angewandte Chemie International Edition, 58 (2019) 8632-8639.

[40] J. Luo, Z. Xie, J.W.Y. Lam, L. Cheng, H. Chen, C. Qiu, H.S. Kwok, X. Zhan, Y. Liu, D. Zhu, B.Z. Tang, Aggregation-induced emission of 1-methyl-1,2,3,4,5-pentaphenylsilole, Chemical Communications, (2001) 1740-1741.

[41] R. Kakuchi, Multicomponent Reactions in Polymer Synthesis, Angewandte Chemie International Edition, 53 (2014) 46-48.

[42] H.G.O. Alvim, E.N. da Silva Júnior, B.A.D. Neto, What do we know about multicomponent reactions? Mechanisms and trends for the Biginelli, Hantzsch, Mannich, Passerini and Ugi MCRs, RSC Advances, 4 (2014) 54282-54299.

[43] J. Zhu, H. Bienaymé, Multicomponent reactions, John Wiley & Sons 2006.

[44] A. Sanchez-Sanchez, S. Akbari, A. Etxeberria, A. Arbe, U. Gasser, A.J. Moreno, J. Colmenero, J.A. Pomposo, "Michael" Nanocarriers Mimicking Transient-Binding Disordered Proteins, ACS Macro Letters, 2 (2013) 491-495.

[45] B. Hammouda, Small-Angle Scattering From Branched Polymers, Macromolecular Theory and Simulations, 21 (2012) 372-381.

[46] C. Barner-Kowollik, Handbook of RAFT polymerization, John Wiley & Sons 2008.

[47] A. Zoller, K.B. Kockler, M. Rollet, C. Lefay, D. Gigmes, C. Barner-Kowollik, Y. Guillaneuf, A complete kinetic study of a versatile functional monomer: acetoacetoxyethyl methacrylate (AAEMA), Polymer Chemistry, 7 (2016) 5518-5525.

[48] E.F.V. Scriven, Pyridines: from lab to production, Academic Press 2013.

[49] P. Pávez, M.V. Encinas, Photophysics and Photochemical Studies of 1,4-Dihydropyridine Derivatives, Photochemistry and Photobiology, 83 (2007) 722-729.

[50] We use the code "f" for denoting folding self-reporting, whereas "fa" is reserved to denote both folding and aggregation self-reporting.

[51] A.R. Katritzky, D.L. Ostercamp, T.I. Yousaf, The mechanism of the hantzsch pyridine synthesis: A study by 15N and 13C NMR spectroscopy, Tetrahedron, 42 (1986) 5729-5738.

[52] J.A. Pomposo, I. Perez-Baena, F. Lo Verso, A.J. Moreno, A. Arbe, J. Colmenero, How Far Are Single-Chain Polymer Nanoparticles in Solution from the Globular State?, ACS Macro Letters, 3 (2014) 767-772.

[53] Q. Miao, Polycyclic Arenes and Heteroarenes: Synthesis, Properties, and Applications, John Wiley & Sons 2015.

[54] We use the code "f" for denoting folding self-reporting, whereas "fa" is reserved to denote both folding and aggregation self-reporting.

[55] A.K. Laha, P.K. Das, S. Bagchi, Study of Preferential Solvation in Mixed Binary Solvent as a Function of Solvent Composition and Temperature by UV—Vis Spectroscopic Method, The Journal of Physical Chemistry A, 106 (2002) 3230-3234.

Chapter 7: Conclusions

7.1. Conclusions

This Thesis has contributed to increase our understanding of single-chain polymer nanoparticles (SCNPs) as complex soft nano-objects with potential applications in a variety of fields, specially catalysis and sensing. The main conclusions of this work are the following:

1) A simple elastic SCNP model, as introduced in Chapter 3, provides a useful framework for connecting -in the case of covalent-bonded SCNPs- the amount of reactive groups (x) and precursor molar mass (M) with the SCNP size (R) upon intra-chain cross-linking in a variety of solvents of different quality and on substrates of different surface free energy. Force versus stretching curves for SCNPs of different values of x -at low deformation- would allow determining experimentally the effective elastic constant of the model.

2) Water-soluble self-folded iron-containing SCNPs can be used as enzyme-mimic nanoreactors for the synthesis of intrinsically conducting polymers (ICPs) via step-growth polymerization, as reported in Chapter 4. PEDOT: PSS dispersions generated through this method showed the characteristic bipolaron UV–Vis absorption band at 800 nm from conducting PEDOT. Thin films prepared from these PEDOT: PSS dispersions revealed an electrical conductivity value of $\sigma = 1 \times 10^{-4}$ S/cm, similar to that typically reported for films prepared from PEDOT: PSS dispersions synthesized using iron-containing proteins.

3) Photoactivation of aggregation induced emission (AIE) molecules containing azide functional groups in the presence of precursor polymers developing highly reactive carbene species under such conditions is a new strategy for the generation of SCNPs with intense fluorescence emission in both solution and solid state ($\lambda_{em} \approx 455$ nm), as described in Chapter 5. This strategy opens a new avenue to endow a variety of other nanostructured polymeric materials with intense fluorescence emission.

4) An original platform for self-reporting both intra-molecular compaction and inter-molecular aggregation through installation of orthogonal luminophores based on Hantzsch ester formation within a single polymer chain has been developed. As reported in Chapter 6, the degree of single-chain compaction of a synthetic polymer chain containing β-ketoester moieties can be detected visually via the generation of Hantzsch luminophores at high dilution. Orthogonal AIE-type luminophores placed also through intra-chain Hantzsch reaction allows self-reporting of inter-molecular aggregation -when present- via photoluminescence at redshifted wavelengths.

7.2. Publications

This thesis has contributed to the following publications:

- J. De-La-Cuesta, E. González, A.J. Moreno, A. Arbe, J. Colmenero, J.A. Pomposo, Size of Elastic Single-Chain Nanoparticles in Solution and on Surfaces, Macromolecules, 50 (2017) 6323-6331.

- J. De-La-Cuesta, E. González, J.A. Pomposo, Advances in Fluorescent Single-Chain Nanoparticles, Molecules, 22 (2017).

- J. De-La-Cuesta, J.A. Pomposo, Photoactivation of Aggregation-Induced Emission Molecules for Fast and Efficient Synthesis of Highly Fluorescent Single-Chain Nanoparticles, ACS Omega, 3 (2018) 15193-15199.

- J. De-La-Cuesta, I. Asenjo-Sanz, A. Latorre-Sánchez, E. González, D.E. Martínez-Tong, J.A. Pomposo, Enzyme-mimetic synthesis of PEDOT from self-folded iron-containing single-chain nanoparticles, European Polymer Journal, 109 (2018) 447-452.

- J. De-La-Cuesta, E. Verde-Sesto, A. Arbe, J.A. Pomposo, Self-Reporting of Folding and Aggregation by Orthogonal Hantzsch Luminophores Within a Single Polymer Chain, Angewandte Chemie International Edition, 60 (2021) 3534-3539.

Resumen

Esta tesis profundiza en la comprensión de las nanopartículas poliméricas unimoleculares (SCNPs, por sus siglas en inglés) como nano-objetos blandos complejos con aplicaciones potenciales en varios campos, especialmente catálisis y detección. En particular, este trabajo cubre diferentes aspectos relacionados con la estructura y propiedades de las SCNPs como: i) el desarrollo de un modelo teórico de SCNPs elásticas que permita comprender el comportamiento de estas nanopartículas en solución y sobre superficies; ii) el diseño de SCNPs como nanoreactores avanzados para la síntesis de un polímero intrínsecamente conductor como el poli(etilendioxitiofeno) (PEDOT); iii) el diseño de SCNPs altamente fluorescentes por fotoactivación de copolímeros que contienen grupos funcionales diazo y un fluoróforo de emisión inducida por agregación (AIE) decorado con grupos azida; y iv) la síntesis de SCNPs que contienen fluoróforos ortogonales para autoreportar compactación intra-molecular y, cuando está presente o es inducida externamente, agregación inter-molecular.

El Capítulo 1, como capítulo introductorio, resume varios conceptos relevantes para la comprensión de los resultados reportados en los Capítulos 3-6.

El Capítulo 2 explica las técnicas e instrumentos utilizados en la caracterización de polímeros, SCNPs y productos utilizados o sintetizados en la tesis.

El Capítulo 3 presenta un nuevo modelo para el cálculo del tamaño, la masa molar aparente y el factor de contracción de las SCNP elásticas en función de la longitud de la cadena del polímero, la fracción de monómero reactivo y la calidad del disolvente. El modelo se utiliza para estimar el tamaño de las SCNPs en diferentes superficies.

El modelo trata con SCNP con enlaces intracadena covalentes permanentes.

El plegamiento de cadenas de polímeros sintéticos individuales (precursores) a nanopartículas de polímeros de cadena única (SCNP) recuerda al plegamiento de proteínas a su estado nativo funcional y ha atraído un interés significativo en los últimos años. El proceso de autoplegado puede ser impulsado por diferentes interacciones intramoleculares, tales como enlaces de tipo no covalente, covalente y covalente dinámico, mediante el uso de precursores bien definidos decorados con grupos funcionales apropiados y condiciones experimentales tales que los eventos de acoplamiento entre cadenas se minimizan en gran medida. Las SCNP resultantes son nano-objetos blandos con aplicaciones potenciales en nanomedicina, biosensores y catálisis, entre otros campos. Los modelos teóricos que proporcionan una conexión entre la cantidad de grupos funcionales, x, y la masa molar precursora, M, con el tamaño de las SCNP resultantes son de gran interés para establecer relaciones estructura-propiedades útiles. En particular, los parámetros relevantes para las aplicaciones finales, como el área superficial, la viscosidad intrínseca y el coeficiente de difusión, dependen del tamaño de las SCNPs.

Recientemente, se ha introducido un modelo que proporciona la reducción de tamaño esperada al plegar cadenas simples de tamaño R_0 a SCNPs de tamaño R mediante interacciones reversibles (enlaces no covalentes) en función de x y M. Este modelo simple proporciona una valiosa estimación a priori de la reducción de tamaño al plegar cadenas simples a SCNPs convencionales a través de interacciones reversibles ($\sim$7% de la desviación promedio de los datos calculados de los experimentales; 72 SCNPs y 22 interacciones reversibles analizadas). A pesar de tal avance en la provisión de relaciones estructura-

propiedades útiles para desarrollar aplicaciones prácticas de SCNPs sensibles, hasta donde sabemos, no se ha reportado todavía ningún modelo equivalente para el caso de SCNPs con enlaces covalentes.

En comparación con las SCNPs reversibles, la estructura de las SCNPs con enlaces covalentes incluye entrecruzamientos intramoleculares permanentes que afectan en gran medida el grado de compactación final alcanzado y les proporcionan una estabilidad térmica superior. Por lo tanto, las SCNPs con enlaces covalentes en solución con una naturaleza similar y parámetros M y x similares a las SCNP reversibles, muestran, en promedio, un nivel más alto de compactación de la cadena. En este trabajo, presentamos un modelo simple de SCNPs unidas covalentemente considerando estos nano-objetos con entrecruzamientos intracadena como redes elásticas unimoleculares compuestas de hebras elásticas conectadas por entrecruzamientos. Derivamos expresiones de la ley de escala para el tamaño, el coeficiente de difusión, la masa molar aparente y el factor de contracción de los SCNP elásticos en solventes buenos, theta y malos. Además, obtenemos leyes de escala para la altura de las SCNP elásticas depositadas en sustratos de energía libre de superficie alta y baja.

En el Capítulo 4 se reporta la síntesis de SCNPs enzimo-miméticas, solubles en agua, compuestas por copolímeros de poli(oligo(etilenglicol)-metil-éter metacrilato y 2-acetoacetoxietil metacrilato) [poli(OEGMA-co-AEMA)], por coordinación con iones ferrosos (Fe^{2+}). Estas SCNPs se utilizan -por primera vez- como catalizadores para la síntesis de dispersiones del polímero intrínsecamente conductor PEDOT: PSS mediante polimerización oxidativa.

En este capítulo, se investiga el diseño de SCNPs como pseudoenzimas artificiales que contienen hierro para la síntesis de un polímero intrínsecamente conductor (ICP) como el poli (3,4-etilendioxitiofeno), PEDOT.

La primera síntesis enzimática de una dispersión PEDOT: PSS se reportó en 2007, mediante el uso de peroxidasa de rábano como catalizador y en presencia de PSS como plantilla soluble en agua y como dopante para equilibrar la carga. La síntesis tradicional de dispersiones de PEDOT: PSS implica el uso de sales que contienen hierro y oxidantes como el persulfato de amonio. Con el objetivo de introducir alternativas respetuosas con el medio ambiente en lugar de catalizadores químicos convencionales, en los últimos años se ha desarrollado una variedad de síntesis de PEDOT: PSS mediada por enzimas mediante la introducción de proteínas que contienen hierro en un complejo hemo (peroxidasa de rábano, peroxidasa de soja, catalasa y hemoglobina, citocromo c) y peróxido de hidrógeno como oxidante. Las propiedades de las películas PEDOT: PSS resultantes dependen de la enzima específica empleada durante la síntesis. Curiosamente, como lo demostraron Hira y Payne, incluso las proteínas simples que enlazan con el hierro que muestran actividad no enzimática (por ejemplo, transferrina) pueden usarse como oxidantes para la síntesis de dispersiones de PEDOT: PSS. Este hecho expande significativamente el catálogo de oxidantes biomoleculares disponibles para la síntesis de películas basadas en PEDOT con un conjunto deseado de propiedades, ya que en la actualidad se conocen más de 800 proteínas hemo diferentes.

El uso de nanopartículas poliméricas monocatenarias (SCNP) como construcciones que imitan las enzimas ha atraído un interés significativo. Las SCNPs dotadas de morfología y actividad enzimo-mimética a menudo muestran una mayor estabilidad frente a los cambios térmicos y una degradabilidad reducida en comparación con las enzimas naturales. Las SCNP se construyen mediante el auto-plegado de una sola cadena polimérica lineal

mediante enlaces covalentes intracadena o interacciones supramoleculares (p. Ej., Enlaces de hidrógeno, enlaces covalentes dinámicos, complejación de metales). Se han observado dos morfologías limitantes en SCNP dependiendo de la ruta sintética empleada y el equilibrio hidrófobo / hidrófilo de la cadena precursora de las SCNPs. Una morfología esparsa que se asemeja a la mostrada por proteínas intrínsecamente desordenadas se observa a menudo por medio del plegamiento / colapso intracadena del precursor en buenas condiciones de disolvente. Por el contrario, una morfología globular más parecida a la que se encuentra en las enzimas se obtiene típicamente por auto-plegado intramolecular en agua de copolímeros aleatorios anfifílicos (neutros o cargados) de composición y peso molecular apropiados.

En este capítulo se revela el uso de nanopartículas monocatenarias (SCNP) autoplegadas, solubles en agua y que contienen metales como nano-reactores que imitan a las enzimas para la síntesis de polímeros intrínsecamente conductores (ICP) a través de la polimerización por etapas. Como prueba de concepto, se realiza la primera síntesis enzimo-mimética de dispersiones de poli (3,4-etilendioxitiofeno): poliestirenosulfonato (PEDOT: PSS) mediante polimerización oxidativa utilizando SCNPs auto-plegadas que contienen hierro (II) como pseudo- enzimas artificiales. Las SCNPs fueron sintetizadas mediante conplejación por hierro del polímero precursor OEGMA-co-AEMA. La compactación de las SCNPs se midió mediante cromategrafía de exclusión por tamaño (SEC) y dispersión de luz dinámica (DLS). La síntesis, que puede llevarse a cabo fácilmente en agua a temperatura ambiente durante 3 h bajo atmósfera de argón, proporciona una dispersión PEDOT: PSS que muestra la banda de absorción UV-vis a $\lambda = 800$ nm característica del bipolarón del PEDOT conductivo. Las películas delgadas preparadas a partir de esta dispersión PEDOT: PSS mostraron un valor de conductividad eléctrica de $\sigma = 1 \times 10^{-4}$ S/cm, similar al reportado típicamente para películas PEDOT: PSS preparadas a partir de dispersiones PEDOT: PSS sintetizadas usando proteínas que contienen hierro como catalasa ($\sigma = 1,3 \times 10^{-5}$ S/cm). Este capítulo abre la puerta a la síntesis de otros tipos de ICP (p. Ej., Polianilina, polipirrol) utilizando SCNP que contienen metales solubles en agua como nanoreactores que imitan a las enzimas que operan a temperatura ambiente, y amplía el uso de SCNP como catalizadores bioinspirados para la polimerización en cadena (es decir, polimerización por apertura de anillo y polimerización por radicales vivos) a la polimerización por etapas (es decir, policondensación mediante polimerización oxidativa).

El Capítulo 5 muestra la síntesis y caracterización de SCNPs fluorescentes mediante la fotoactivación de copolímeros de poli(metil metacrilato-co-2-acetoacetoxietil metacrilato) [poli (MMA-co-AEMA)] funcionalizados con grupos funcionales diazo. La emisión de fluorescencia se produce mediante la adición de un fluoróforo de emisión inducida por agregación (AIE) con grupos azida. El entrecruzamiento en las SCNPs se logra mediante la activación de los grupos azida y diazo al irradiarlos con luz ultravioleta.

El desarrollo de nanopartículas altamente fluorescentes es de gran interés para una variedad de aplicaciones prácticas que incluyen sensores biológicos de nueva generación, sondas químicas innovadoras, dispositivos optoelectrónicos mejorados y materiales inteligentes. En este capítulo presentamos un método original para la síntesis rápida y eficiente de SCNP altamente fluorescentes basado en el uso eficiente de fluoróforos entrecruzantes con emisión inducida por agregación (AIE).

En el capítulo, se investiga una nueva estrategia de fotoactivación rápida y eficiente para producir SCNPs con emisión de fluorescencia intensa en solución, que se basa en la fotoactivación de moléculas entrecruzantes de emisión inducida por agregación (AIE) apropiadas que contienen grupos funcionales azida para la generación rápida y eficiente de

SCNPs con emisión de fluorescencia tanto en solución como en estado sólido. Se ha demostrado que la generación de una combinación de especies de nitreno altamente reactivas (de una molécula AIE entrecruzante que contiene azida, Silole-N$_3$) y especies de carbeno altamente reactivas (de un precursor polimérico apropiado de MMA-co-AEMA que contiene unidades α-diazo-β-cetoéster, **P**) mediante irradiación UV, la probabilidad de una inmovilización eficaz del compuesto AIE en el SCNP resultante aumenta considerablemente, en comparación con el uso de un compuesto AIE sin grupos funcionales azida. Se obtiene la confirmación del éxito de la compactación de cadenas individuales tras la irradiación UV del precursor P en presencia de Silole-N$_3$ a una dilución alta por la reducción del tamaño de las cadenas medida por cromatografía de exclusión por tamaño (SEC) con detección múltiple. El tiempo óptimo de irradiación UV durante el proceso de formación de SCNP es de 60 min. Medida por espectrografía de fluorescencia, las SCNP fluorescentes FNP ($R_h = 9$ nm) resultantes muestran un pico de emisión máximo en el disolvente THF centrado en $\lambda_{em} \approx$ 455 nm y una excelente estabilidad de la intensidad de emisión de fluorescencia a lo largo del tiempo, según lo determinado por espectroscopía de fluorescencia. Además, las FNPs conservan sus propiedades fluorescentes en estado sólido, libres de los efectos de ACQ que a menudo se observan en las SCNPs basadas en fluoróforos tradicionales. También de midió el rendimiento cuántico de las FNPs. Para concluir, este trabajo abre una nueva vía para dotar a una variedad de otros materiales poliméricos nanoestructurados (por ejemplo, copolímeros de bloque, microgeles, dendrímeros y micelas) con una emisión de fluorescencia intensa basada en la nueva estrategia de fotoactivación de moléculas de AIE.

El Capítulo 6 presenta una ruta para la síntesis y caracterización de SCNPs de poli(MMA-co-AEMA) fluorescentes basada en la reacción de síntesis de dehidropiridinas de Hantzsch. El empleo de fluoróforos ortogonales permite reportar tanto el plegado, como la agregación de estas SCNPs. La compactación intramolecular que da lugar a las SCNPs se identifica mediante la formación de ésteres de Hantzsch fluorescentes, mientras que la detección de agregación intermolecular se produce a través de la incorporación de luminóforos AIE con fluorescencia en longitudes de onda desplazadas al rojo.

En este capítulo se presenta una estrategia nueva y sencilla para cerrar la brecha entre el plegamiento intramoleclular de cadenas simples y los métodos autoreportantes de agregación intermolecular para proteínas y polímeros sintéticos que se basan en la colocación eficiente dentro de cadenas individuales de luminóforos ortogonales autoreportantes. La estrategia se ejemplifica mediante la generación de dos luminóforos complementarios a través de la formación de éster de Hantzsch para la visualización del plegamiento dentro de cadenas individuales y, cuando está presente o inducida externamente, la agregación de múltiples SCNPs. Los puntos clave del presente método son: i) partiendo de cadenas decoradas con β-cetoésteres no luminiscentes, la compactación intramolecular monocatenaria se detecta visualmente a través de la fluorescencia que surge de los fluoróforos de Hantzsch, que actúan como conectores intracadena equivalentes a los enlaces disulfuro covalentes en proteínas plegadas, generados progresivamente durante el plegado de las cadenas individuales, por lo que -en ausencia de fenómenos de agregación a alta dilución- la intensidad de la fluorescencia crece con el grado de compactación, medida por la reducción en el tamaño de la cadena; ii) la agregación de cadenas múltiples -cuando está presente o inducida intencionalmente- es detectada por una fotoluminiscencia intensa a longitudes de onda desplazadas al rojo que surge de luminóforos ortogonales de emisión inducida por agregación (AIE) debido a la formación de conjuntos de múltiples SCNPs; y iii) ambos tipos de sondas de autoreportantes se instalan, al mismo tiempo, dentro de la misma cadena polimérica a través de la reacción de Hantzsch multicomponente. Esta estrategia

permite percibir a simple vista el estado de agregación / grado de compactación de las SCNPs.

Se midió en diferentes tiempos la fluorescencia de las SCNPs por espectrografía de fluorescencia, y su tamaño por cromategrafía de exclusión por tamaño (SEC) y dispersión de luz dinámica (DLS). El grado de compactación de las SCNPs se midió mediante dispesión de rayos X de ángulo reducido (SAXS).

La agregación de múltiples cadenas, en el caso de las SCNPs, desempeñaría un papel equivalente al autoensamblaje de proteínas defectuosas en agregados patógenos. Es un método es simple y muy preciso para, por ejemplo, establecer diagramas fiables de compactación intra-cadena -agregación-precipitación de SCNPs en mezclas de disolventes / no disolventes. Dado que la introducción de restos β-cetoéster en cadenas de polímeros sintéticos es relativamente sencilla y una variedad de SCNPs funcionales se han construido a partir de precursores que contienen estos grupos funcionales, esta estrategia promete percibir de un vistazo la presencia / ausencia de agregados de multi-cadena perjudiciales que afectan el rendimiento de SCNPs en catálisis, detección, reconocimiento, etc.

Las principales conclusiones de la tesis se recogen en el Capítulo 7.

Acknowledgements

En primer lugar, me gustaría agradecer al Prof. Juan Colmenero por darme la oportunidad de incorporarme al grupo "Polymers and Soft Matter" del Centro de Física de Materiales. También quisiera agradecer a la Universidad de País Vasco (UPV/EHU) por darme la oportunidad de realizar la tesis, al Centro de Física de Materiales (CFM) por permitirme utilizar sus instalaciones y al Ministerio de Ciencia e Innovación por concederme la beca PREDOC.

Me gustaría agradecer especialmente al director de esta tesis, el Prof. José A. Pomposo, por confiar en mi para este proyecto, por su ayuda y por guiarme a lo largo de la tesis.

Además, quiero agradecer a los demás profesores del grupo. Especialmente a la Prof. Arantxa Arbe por su ayuda haciendo las medidas de SAXS. Al Prof. Ángel Alegría le agradezco su ayuda en las cuestiones y trámites relacionados con el doctorado. Y quisiera agradecer al personal del CFM por su ayuda cuando la he necesitado.

I would like to thank Prof. Reidar Lund from the University of Oslo (UiO) for allowing me to work in the Bio[3] - Soft Matter group of the Department of Chemistry of the UiO during my stay in Oslo and for his help, support and guidance in a new city far from home. Special thanks to Nico for teaching me how to use the equipment and for inviting me to the parties. I am also grateful to the rest of the team (Victoria, Mikkel, Mirna, Synne…) for their support and help.

Muchas gracias a la gente del grupo "Polymers and Soft Matter" del CFM. Sobre todo a Isabel, por estar dispuesta a ayudar cuando se lo piden y por mantener en funcionamiento todos los equipos del laboratorio. También agradezco a Ester su ayuda en el laboratorio y orientándome en la tesis. Y gracias a Dani por las medidas de AFM. Quiero expresar mi gratitud al resto de los compañeros que siguen en el grupo (Jokin, Agustín, Numera, Davide, Jon, Amaia, Paula, Jorge, Mariarita, Javier, Matteo…) o que han pasado por el (Ali, Xavi, Amaia, Bea, Jordan, Maud, Dani, Ander, Thomas, Jon, Marina, Edurne, Natalia, Izaskun, Lucia, Alex, Ana Lucia…) por su ayuda y por los momentos que hemos pasado juntos estos años.

Y finalmente quisiera agradecer a toda mi familia el apoyo que me han dado todo este tiempo y por haber confiado en mí. Eskerrik asko denoi.